

A Numerical Framework for Fluid-Acoustic-Structure Interaction in Clarinet-like Instruments

Shi Yong



Computational Acoustic Modeling Laboratory
McGill University
Montreal, Quebec, Canada

August 2016

A thesis submitted to McGill University in partial fulfillment of the requirements for
the degree of PhD in Music Technology.

© 2016 Shi Yong

Abstract

This thesis presents numerical investigations of the aeroacoustic aspects of clarinet-like instruments. A customized simulation system based on the two-dimensional lattice Boltzmann method is developed to address acoustic problems involving complex boundary conditions carrying a low Mach number mean flow. The simulation is accelerated by means of GPU parallel computing.

The accuracy and stability of the modeling system are substantiated by benchmark acoustic problems involving static boundaries, which include the acoustic transmission and radiation characteristics of axisymmetric waveguides terminated by different geometries, as well as the aeroacoustic behavior of whistles with complicated curved geometries. The effect of non-zero subsonic mean flow is investigated. The numerical results agree well with those provided by available theories and experimental data. The accuracy of the 32-bit representation of floating-point numbers in the GPU-accelerated computations is also verified.

Aspects of fluid-acoustic-structure interaction of a clarinet that comprises a dynamic mouthpiece-reed structure and an acoustic resonator are investigated in both a quasi-stationary regime and a dynamic regime. The effect of different lay geometries is investigated as well. For the case of a fixed reed, the vena contracta factor varies very little over approximately 80% of the duration, which is in general agreement with the current theory. For the case of a slowly moving reed, hysteresis is found in the numerical flow due to the inertia of the fluid volume. The vena contracta factor is greater than unity in the region of high pressure differences, which is in contrast with the theoretical assumption and is due to the non-uniform height across the reed channel. In simulations carried out for a dynamic regime with acoustic feedback, the phenomenon of flow separation / reattachment in a reed channel, as well as the vena contracta factors, are significantly different from the theoretical expectations. The acoustic perturbation of the pressure and velocity fields in a mouthpiece chamber and reed channel are visualized with high resolution. The effect of different lay geometries is observable in many aspects, including the earlier acceleration of volume flow in the short channel and the extra energy dissipation in the long channel with a ditch at the end.

Sommaire

Cette thèse présente des analyses de simulations numériques de certains aspects aéroacoustiques d'instrument de musique à anche simple ressemblant à la clarinette. Un système de simulation sur mesure basé sur la méthode de Lattice-Boltzmann à 2 dimensions est développé pour résoudre des problèmes acoustiques avec des conditions frontière complexes et un écoulement fluide subsonique à faible nombre de Mach. La simulation est accélérée par du calcul en parallèle sur un GPU.

La précision et la stabilité du système de simulation sont évaluées avec des simulations de référence ayant des conditions frontière statiques, incluant la transmission et la radiation dans des guides d'onde axisymétrique se terminant par des géométries connues, ainsi que le comportement aéroacoustique de sifflets avec différentes géométries courbes. L'effet d'un écoulement subsonique moyen non nul est analysé. Les résultats numériques sont en accord avec les résultats théoriques et expérimentaux disponibles. La précision de la représentation sur 32-bit des nombres flottants dans les calculs accélérés sur le GPU est aussi vérifiée.

Les aspects fluid-acoustique-structure interaction de la clarinette comprenant une structure dynamique anche-bec et un résonateur acoustique sont analysés en régime quasi stationnaire et en régime dynamique. L'effet de la géométrie de la table est analysé. Dans le cas d'une anche fixe, le facteur de vena contracta varie très peu pour 80% de la durée de la simulation, ce qui est en accord avec la théorie actuelle. Dans le cas d'une anche en mouvement lent, nous trouvons de l'hystérésis dans les résultats numériques en conséquence de l'inertie du volume fluide. Le facteur de vena contracta est supérieur à 1 dans la région de grande différence de pression, ce qui contraste avec les hypothèses théoriques et est une conséquence de la hauteur non uniforme du canal le long de l'anche. Dans les simulations en régime dynamique avec retour d'onde acoustique, le phénomène de séparation / attachement de la couche limite dans le canal d'anche, de même que le facteur de vena contracta sont significativement différent des attentes théoriques. Les perturbations des champs de pression et de vitesse acoustiques dans la chambre du bec et dans le canal d'anche sont visualisées en haute résolution. L'effet de changement dans la géométrie de la table du bec est observable selon plusieurs aspects, incluant une accélération antérieure du débit dans un canal court et une augmentation de la dissipation d'énergie dans un canal long.

Acknowledgments

Firstly, I would like to sincerely thank my supervisor, Prof. Gary P. Scavone, for his constant support, advice, guidance, encouragement, recommendations and great patience throughout the long journey of my studies at McGill University.

I would like to sincerely thank Prof. Andrey R. da Silva for co-advising this thesis and inviting me to Federal University of Santa Maria in Brazil for a research internship. Without his valuable advice and comments this research would have been impossible. Thanks also go to Dr. Eric Brandao and Dr. Stephan Paul for their precious support during my stay in Brazil.

I would like to thank the professors of the Music Technology area, in particular Prof. Philippe Depalle, for his helpful suggestions on signal processing. I am grateful to Prof. Luc Mongeau from the department of Mechanical Engineering for his valuable advice on acoustic topics. Also thanks Dr. Alireza Najafi-Yazdi and Dr. Kaveh Habibi for their suggestions on boundary conditions.

I wish to thank Prof. Jean Kergomard from Aix-Marseille University in France for his valuable suggestions on several topics of my thesis. I wish to thank Prof. Anna Snakowska and Dr. Lukasz Gorazd from AGH University of Science and Technology in Poland for sharing their experimental data, and thank Prof. Gwenael Gabard from University of Southampton in UK for providing his theoretical results of sound radiation. I wish to thank Dr. Liao Wei and Dr. Peng Yan from Old Dominion University for their helpful suggestions and discussions on several topics in computational fluid dynamics and lattice Boltzmann methods.

I wish to thank Prof. Xie Bosun from South China University of Technology and Prof. Guan Shanqun from Beijing University of Posts and Telecommunications in China for their precious encouragement and recommendations that motivated me to pursue a Ph.D. after I have left the university for many years.

I wish to thank the people in Yamaha Corp. in Japan, in particular Mr. Toshi Kunitomo, Mr. Hirofumi Onitsuka and Mr. Akira Miki, for offering me the research internship, which is helpful to part of this research.

I would like to thank Johnty Wang and Connor Kemp for their kind help on English writing, and Dr. Antoine Lefebvre for his help on the French translation.

I am grateful to my colleagues, Charalampos Saitis, Vincent Freour, Hossein Man-

sour, Pauline Eveno, Jason Leung, Loic Jeanson, Esteban Maestre, Quim Llimona, Fu Lei, Jung Suk Lee, Avrum Hollinger, Corey Kereliuk, Bertrand Scherrer, Andrew Hankinson, Marlon Schumacher, Sven-Amin Lembke, Marcello Giordano, Renato Baldas, Cao Yinan, Lu Ye, Qin Ying, Gabriel Vigliensoni, Yang Lingxiao, Johnny Venom, Xiao Wen, for their friendship and assistance throughout my stay in the Music Technology community. Special thanks go to Darryl Cameron for his constant help in the laboratory.

I gratefully acknowledge the financial support of Fonds Québécois de la Recherche sur la Nature et les Technologies (FQRNT) for a doctoral research scholarship. Also, I am extremely thankful to the Schulich School of Music and Centre for Interdisciplinary Research in Music Media and Technology (CIRMMT) for their essential financial support.

Finally, the greatest thanks go to every member of my family, my parents, my sister and my girl friend, for their love, patience and constant support throughout this endeavor.

Contribution of authors

This thesis, and the research to which it refers, is the candidate's own original work (except for commonly understood and accepted ideas or where explicit reference to the work of other people, published or otherwise, is made). The dissertation is formatted as a monograph comprising six chapters and includes contents from the following publications:

1. A. da Silva, Y. Shi, and G. Scavone, "Computational analysis of the dynamic flow in single-reed woodwind instruments.", *Proceedings of Meetings on Acoustics*, Vol. 19, No. 1, Acoustical Society of America, 2013.
2. Y. Shi, A. da Silva, G. Scavone, "Numerical analysis of the mean flow effect on the sound directivity pattern of cylindrical ducts.", *Proceedings of the Stockholm Music Acoustics Conference (SMAC 2013)*, Stockholm, Sweden, 2013.
3. Y. Shi, A. da Silva, G. Scavone, "Lattice Boltzmann Simulations of Sound Directivity of a Cylindrical Pipe with Mean Flow.", *Journal of Physics A: Mathematical and Theoretical* 46(31), 315501, 2013.
4. Y. Shi, A. da Silva, G. Scavone, "Numerical Simulation of Whistles Using Lattice Boltzmann Methods.", *International Symposium on Musical Acoustics (ISMA 2014)*, Le Mans, France, 2014.
5. Y. Shi, A. da Silva, G. Scavone, "LBM Simulation of the Quasi-static Flow in a Clarinet.", *Proceedings of the Third Vienna Talk on Music Acoustics* 16 (2015): 19, 2015.

The candidate was responsible for the numerical simulation, data analysis, and preparing manuscripts for all the publications listed above (with the exception of the manuscript of the first paper, which was written by Andrey R. da Silva). The above articles present some preliminary results of the model that will be thoroughly discussed throughout this thesis. Andrey R. da Silva and Gary P. Scavone provided the original prototype of the numerical model, which was re-implemented and improved by the candidate. They also provided feedback, supervision and helped in the review of the manuscripts. Gary P. Scavone provided necessary funding, laboratory equipment and space.

Contents

1	Introduction	1
1.1	Background	1
1.2	Objectives and Scope	2
1.3	Outline	5
2	Theoretical Background	7
2.1	The Scale of Fluid Flow	7
2.2	Fundamentals of Fluid Dynamics	8
2.2.1	Conservation of Mass	10
2.2.2	Conservation of Momentum	12
2.2.3	Adiabatic Approximation	14
2.2.4	Navier-Stokes Equations	16
2.3	Acoustic Wave Equations	17
2.3.1	Harmonic Plane Waves	19
2.4	Boundary Conditions and Boundary Layer	20
3	Lattice Boltzmann Method	24
3.1	Introduction	24
3.2	Fundamental Theory of LBM	26
3.2.1	From LGA to LBE	26
3.2.2	From BE to LBE	27
3.2.3	LBGK models	30
3.2.4	Multiple Relaxation Times	32
3.3	Initial and Boundary Conditions	33
3.3.1	Initial Conditions	33

3.3.2	Boundary Conditions	34	
3.3.3	No-Slip Condition	35	
3.3.4	Free-Slip Condition	36	
3.3.5	Curved Boundary	37	
3.3.6	Moving Boundary	39	
3.3.7	Non-Reflecting Boundary	39	
	3.3.7.1 Ideal Non-Reflecting Boundary	39	
	3.3.7.2 Non-Reflecting Boundaries for LBM	41	
3.4	Numerical Procedure of LBGK model	43	
	3.4.1 Procedure of LBGK-SRT Model	43	
	3.4.2 Procedure of LBGK-MRT Model	45	
	3.4.3 Software Implementation	46	
3.5	Parallel LBGK Model on GPU	46	
	3.5.1 Previous Work	47	
	3.5.2 GPU Programming Model	47	
	3.5.3 Software Implementation	49	
4	Numerical Modeling of Acoustic Systems with Static Boundaries	54	
4.1	Overview	54	
4.2	Acoustic Transmission in Pipes	56	
	4.2.1 Introduction	56	
	4.2.2 A Pipe Carrying a Quiescent Flow	62	
		4.2.2.1 LBM Scheme	63
		4.2.2.2 Representing a 3D Axisymmetric Flow in a 2D Model . .	64
		4.2.2.3 Source Signal	66
		4.2.2.4 Signal Probing and Post-Processing	68
		4.2.2.5 Results	69
	4.2.3 A Pipe Carrying a Mean Flow	72	
		4.2.3.1 LBM Scheme	72
		4.2.3.2 Source Signal	72
		4.2.3.3 Signal Probing and Post-Processing	74
		4.2.3.4 Results	76
	4.2.4 Pipes with Horn Extension	81	

4.2.4.1	Horns with a Quiescent Flow	83
4.2.4.2	Horns Carrying a Mean Flow	86
4.2.5	Summary	89
4.3	Acoustic Radiation Out of Pipes	90
4.3.1	Introduction	90
4.3.2	Numerical Scheme	92
4.3.3	A Pipe Carrying a Quiescent Flow	94
4.3.4	A Pipe Carrying a Mean Flow	100
4.3.5	Pipes with Horn Extension	104
4.3.6	Influence of Bit Depth	108
4.3.7	Summary	111
4.4	Aeroacoustic Behavior of Whistles	112
4.4.1	Introduction	112
4.4.2	Previous Works	114
4.4.3	Numerical Scheme	115
4.4.4	Results	118
4.4.4.1	Jet Formation and Oscillation	118
4.4.4.2	Sound Oscillation	119
4.4.4.3	Change of Frequency and Amplitude with Jet Speed	120
4.4.5	Summary	125
4.5	Conclusion	125
5	Numerical Modeling of Acoustic Systems with Moving Boundaries	128
5.1	Overview	128
5.2	Previous Flow Behaviour Studies	131
5.3	Numerical Scheme	133
5.3.1	The Reed Model	134
5.3.2	The LBM Scheme	136
5.4	Investigations of the Quasi-stationary Regime	139
5.4.1	Setup of Simulations	139
5.4.2	Results of Static Reed	141
5.4.3	Results of Moving Reed	144
5.4.4	Discussions	147

5.5	Investigations of the Dynamic Regime	151
5.5.1	Setup of Simulations	151
5.5.2	Waveform and Spectrum	154
5.5.3	Field Visualizations in One Duty Cycle	158
5.5.3.1	Pressure Field in Mouthpiece	158
5.5.3.2	Velocity Field in Mouthpiece	161
5.5.3.3	Zoomed-In Field Visualization in the Reed Channel . . .	165
5.5.4	Characteristics of Dynamic Flows in One Duty Cycle	171
5.5.4.1	Dynamic Flow Behaviors in the Reed Channel	174
5.5.5	Discussions	180
5.6	Conclusion	183
6	Conclusions and Future Research	186
6.1	Conclusions	186
6.2	Future Research	189
A	Benchmarks	191

List of Figures

2.1	Differential control volume.	9
2.2	Boundary layer on a semi-infinite flat plate.	21
3.1	D2Q9 structure.	31
3.2	Explicit boundary nodes (black nodes).	35
3.3	Implicit boundary curve.	35
3.4	No-slip condition.	36
3.5	Free-slip condition.	37
3.6	Curved boundary.	38
3.7	nVidia CUDA programming model. (source nVidia).	48
3.8	Flowcharts of CPU model and GPU model.	49
3.9	Mapping lattice grid to thread grid on the GPU.	51
4.1	LB model of the axisymmetric pipe with a quiescent flow for the measurements of reflectance and length correction.	63
4.2	Source signal.	67
4.3	CPU SRT model, comparison between numerical results (solid) and analytical predictions (---) of the reflection coefficient and length correction of an unflanged cylindrical pipe in the absence of a mean flow ($M = 0$).	70
4.4	GPU SRT model, comparison between numerical (solid) and analytical predictions (---) of the reflectance and length correction of an unflanged cylindrical pipe in the absence of a mean flow ($M = 0$).	71
4.5	LB model of an axisymmetric pipe carrying a subsonic mean flow for the measurement of reflection coefficient and length correction at the open end.	73

4.6	GPU SRT model, comparison between complex wavenumbers calculated from the simulations of an unflanged cylindrical pipe in the presence of a mean flow: (a) Mach=0.05, (b) Mach=0.1, (c) Mach=0.15.	77
4.7	GPU SRT model, comparison between numerical results, analytical predictions and experimental measurements of the magnitude of the reflectance at the open end of an unflanged cylindrical pipe in the presence of a mean flow: (a) (b) Mach=0.05, (c) (d) Mach=0.1, (e) (f) Mach=0.15.	78
4.8	GPU SRT model, comparison between numerical results, analytical predictions and experimental measurements of the length correction at the open end of an unflanged cylindrical pipe in the presence of a mean flow: (a) (b) Mach=0.05, (c) (d) Mach=0.1, (e) (f) Mach=0.15.	80
4.9	LB model of the axisymmetric pipe terminated by a horn for the measurements of reflectance and length correction.	83
4.10	GPU SRT model, comparison between LBM and BEM results (da Silva, 2008) of the magnitude of the reflectance $ R $ as a function of ka for horns with different curvature radii in the absence of a mean flow ($M = 0$): (a) $r = 2a$, (b) $r = 4a$. The $ R $ of the unflanged pipe without a horn extension (Levine and Schwinger, 1948) is plotted for comparison.	84
4.11	GPU SRT model, comparison between LBM and BEM results (da Silva, 2008) of the length correction l/a as a function of ka for horns with different curvatures in the absence of a mean flow ($M = 0$): (a) $r = 2a$, (b) $r = 4a$	85
4.12	GPU SRT model, comparison of the magnitude of the reflectance $ R $ as a function of ka for horns with different curvatures in the presence of a mean flow with different Mach numbers: (a) $r = 2a$, (b) $r = 4a$	87
4.13	GPU SRT model, comparison of the length correction l/a as a function of ka for horns with different curvatures in the presence of a mean flow with different Mach numbers: (a) $r = 2a$, (b) $r = 4a$	88
4.14	LB model of the axisymmetric pipe for the measurements of radiation directivity.	92

- 4.15 CPU SRT 64-bit model, comparison between numerical (solid) and analytical predictions Levine and Schwinger (1948) (- - -) of the acoustic pressure directivity as a function of the angle in the absence of a mean flow: (a) $ka = 0.48$, (b) $ka = 1$, (c) $ka = 2$, (d) $ka = 2.5$, (e) $ka = 3$, (f) $ka = 3.5$ 95
- 4.16 GPU SRT 32-bit model, comparison between numerical (solid) and analytical predictions Levine and Schwinger (1948) (- - -) of the acoustic pressure directivity as a function of the angle in the absence of a mean flow: (a) $ka = 0.48$, (b) $ka = 1$, (c) $ka = 2$, (d) $ka = 2.5$, (e) $ka = 3$, (f) $ka = 3.5$ 96
- 4.17 Evaluation of the far-field condition in terms of acoustic impedance in the radiation domain: (a) amplitude of acoustic impedance, (b) phase of acoustic impedance. The measuring distance is $d = 250$ cells from the outlet. 97
- 4.18 GPU SRT model, comparison between numerical (solid), analytical predictions (- - -) and experimental measurements (red dot) of the acoustic pressure directivity as a function of the angle in the absence of a mean flow ($M = 0$): (a) $ka = 0.74$, (b) $ka = 1.48$, (c) $ka = 2.96$ 98
- 4.19 GPU SRT model, comparison between numerical (solid), analytical predictions (- - -) and experimental measurements (red dot) of the acoustic pressure directivity as a function of the angle in the presence of a mean flow at $M = 0.036$: (a) $ka = 0.74$, (b) $ka = 1.48$, (c) $ka = 2.96$. The zone of relative silence is indicated by a grey arrow. 101
- 4.20 GPU SRT model, comparison between numerical (solid), analytical predictions (- - -) of the acoustic pressure directivity as a function of the angle in the presence of a mean flow at $M = 0.15$: (a) $ka = 0.74$, (b) $ka = 1.48$, (c) $ka = 2.96$, (d) $ka = 3.77$. The zone of relative silence is indicated by a grey arrow. 102
- 4.21 LB model of the axisymmetric pipe terminated by a horn for the measurements of radiation directivity. 104

- 4.22 GPU SRT 32-bit model, comparison between analytical predictions Levine and Schwinger (1948) (unflanged pipe, ----) and numerical (horn radius= $2a$) of the acoustic pressure directivity as a function of the angle in various mean flow: (a) $ka = 0.48$, (b) $ka = 1$, (c) $ka = 2$, (d) $ka = 2.5$, (e) $ka = 3$, (f) $ka = 3.5$ 106
- 4.23 GPU SRT 32-bit model, comparison between analytical predictions Levine and Schwinger (1948) (unflanged pipe, ----) and numerical (horn radius= $4a$) of the acoustic pressure directivity as a function of the angle in various mean flow: (a) $ka = 0.48$, (b) $ka = 1$, (c) $ka = 2$, (d) $ka = 2.5$, (e) $ka = 3$, (f) $ka = 3.5$ 107
- 4.24 Comparison the results of three LBM-SRT models (CPU SRT 64-bit, CPU SRT 32-bit and GPU SRT 32-bit), Acoustic density signals are probed at a distance of 250 cells and angle of 32 degree from the open end. 109
- 4.25 Comparison of numerical results between three LBM-SRT models (CPU 64-bit, CPU 32-bit, GPU 32-bit) and analytical predictions Levine and Schwinger (1948) (- - -) of the acoustic pressure directivity as a function of the angle in the absence of a mean flow: (a) $ka = 0.48$, (b) $ka = 1$, (c) $ka = 2$, (d) $ka = 2.5$, (e) $ka = 3$, (f) $ka = 3.5$ 110
- 4.26 Whistles of different size. 116
- 4.27 Boundaries of the whistles. 117
- 4.28 The formation of the jet during start-up. The colors represent the absolute value of velocity ($\sqrt{u_x^2 + u_y^2}$). The red color corresponds to the highest speed and the dark blue to the lowest speed. For the simulation the jet speed at the center of the flue exit is $U_{jet} = 30 \text{ m/s}$ 119
- 4.29 Images of the air speed near the flue channel exit and labium of Whistle I during one cycle. The colors represent the absolute value of velocity ($\sqrt{u_x^2 + u_y^2}$). The red color corresponds to the highest speed and the dark blue to the lowest speed. For the simulation the jet speed at the center of the flue channel is $U_{jet} = 30 \text{ m/s}$ 120
- 4.30 Numerical density of whistle I with various jet speed. Jet speed: (a), $U_{jet} = 10 \text{ m/s}$. (b), $U_{jet} = 20 \text{ m/s}$. (c), $U_{jet} = 30 \text{ m/s}$. (d), $U_{jet} = 40 \text{ m/s}$. . . 121
- 4.31 Normalized spectrum of whistle I with various jet speeds: (a), $U_{jet} = 20 \text{ (m/s)}$. (b), $U_{jet} = 30 \text{ (m/s)}$. (c), $U_{jet} = 40 \text{ (m/s)}$ 122

4.32	Peak frequency and normalized magnitude of whistle I for various jet speeds. 4.32(a): peak frequency and frequency of edge tone (fb1, fb2, fb3 and fb4, see Eq. 4.38), (b) normalized magnitude.	123
4.33	Peak frequency and normalized magnitude of whistle II for various jet speeds. (a): peak frequency and frequencies of edge tone (fb1, fb2, fb3 and fb4, see Eq. 4.38), (b) normalized magnitude.	124
5.1	Geometry of the distributed reed model.	134
5.2	Hybrid clarinet model.	136
5.3	Three different lay geometries used in the simulations.	138
5.4	Results of static reed, short channel ($L/h = 1$).	141
5.5	Results of static reed, long channel ($L/h = 4$).	142
5.6	Results of moving reed, short channel ($L/h = 1$).	145
5.7	Results of moving reed, long channel ($L/h = 4$).	146
5.8	Visualization of the velocity field, short channel.	148
5.9	Visualization of the velocity field, long channel.	149
5.10	Three probing points in reed channel.	154
5.11	Time histories of displacements of reed tips (left) and pressures (right) for different geometries.	155
5.12	Normalized waveforms (left) and spectrum (right) of reed tips (yr) and acoustic pressures (pa in mouthpiece, rad in radiation domain) for different geometries.	156
5.13	Instances selected for visualization in one ducy cycle.	157
5.14	Short channel: pressure field (background) and profile of averaged pressure (thick black dashed line) in mouthpiece.	159
5.15	Long channel: pressure field (background) and profile of averaged pressure (thick black dashed line) in mouthpiece.	160
5.16	Long channel with a ditch: pressure field (background) and profile of averaged pressure (thick black dashed line) in mouthpiece.	161
5.17	Short channel: absolute velocity field u (background) and velocity vectors (white arrows) in mouthpiece.	162
5.18	Long channel: absolute velocity field u (background) and velocity vectors (white arrows) in mouthpiece.	163

5.19	Long channel with a ditch: absolute velocity field u (background) and velocity vectors (white arrows) in mouthpiece.	164
5.20	Short channel: the curl of velocity field (background), the velocity profile (white arrows), the pressure profile (thick dashed line) and the aerodynamic force profile on the reed (green arrows). Zoomed in in the vicinity of reed channel.	166
5.21	Long channel: the curl of velocity field (background), the velocity profile (white arrows), the pressure profile (thick dashed line) and the aerodynamic force profile on the reed (green arrows). Zoomed in in the vicinity of reed channel.	167
5.22	Long channel with a ditch: the curl of velocity field (background), the velocity profile (white arrows), the pressure profile (thick dashed line) and the aerodynamic force profile on the reed (green arrows). Zoomed in in the vicinity of reed channel.	168
5.23	One duty cycle selected from time histories of reed tip for different geometries (a: short channel, b: long channel, c: long channel with a ditch).	171
5.24	Opening, Normalized energy flow and Reynolds number in one cycle for different geometries (a: short channel, b: long channel, c: long channel with a ditch).	172
5.25	Displacement of reed tip (top) and volume flow per unit width (bottom) probed at three locations (x_0, x_1, x_2) during one cycle for different geometries.	174
5.26	Pressure difference for different geometries.	175
5.27	Compare the numerical results with the theoretical predictions in terms of volume flow and vena contracta factor in one duty cycle for different geometries.	181
A.1	2D Poiseuille flow channel.	192
A.2	Time history of <i>Reynolds number</i> for different collision modes (SRT vs. MRT) and relaxation parameters (Ω) . Simulation parameters: $a = 5.5$, $M = 0.1$	193
A.3	Time history of <i>Diff</i> for different collision modes (SRT vs. MRT) and relaxation parameters (Ω) . Simulation parameters: $a = 5.5$, $M = 0.1$	194

A.4	Time history of <i>Error</i> for different collision modes (SRT vs. MRT) and relaxation parameters (Ω). Simulation parameters: $a = 5.5, M = 0.1$	195
A.5	Negative feedback loop for velocity correction.	195
A.6	The mean value of Error as a function of Reynolds number. Simulation parameters: $a = 5.5, \Omega = 1.99$	196
A.7	The mean value of Error as a function of grid resolution. Simulation parameters: $\Omega = 1.6, Re = 10$	197

List of Tables

3.1	Velocity weights for three lattice models.	31
3.2	Features of the nVidia GeForce GTX 670.	47
3.3	Performance of CPU model compared to GPU model (a D2Q9 LBGK model with a 1000×1000 lattice).	52
4.1	Relaxation parameter Ω for different Mach numbers.	73
4.2	Valid ka range of the two-microphone method for $\Delta_{12} = 1.5a$	81
4.3	Height (H) and width (W) of the two whistles.	116
4.4	Size of the two LB models.	117
5.1	Geometric and mechanic parameters of the reed.	135
5.2	Geometric parameters of the clarinet.	137
5.3	Number of cells corresponding to different spatial resolutions.	138
5.4	Mouth pressures prescribed for different lay geometries.	152
5.5	Instances selected for sequential field visualizations in one duty cycle. . .	158
5.6	Mean value of pm and dynamic range of pa in one duty cycle for different lay geometries.	158
5.7	Five steps during one duty cycle for the cases of long channel.	176
5.8	Five steps during one duty cycle for the case of short channel.	178

Chapter 1

Introduction

1.1 Background

Woodwind music instruments such as the clarinet have largely remained in their present form for more than a century. The sound production of a clarinet depends on flow-induced vibrations, with the reed modulating the air flow entering into the instrument by opening and closing a narrow channel defined between the reed tip and the lay of the mouthpiece. There are still many aspects of their playing behavior that are not completely understood from a scientific perspective.

Besides traditional theoretical and experimental approaches, computational simulations have become popular in the field of musical acoustics thanks to the development of new numerical algorithms and inexpensive computation resources. Numerical simulations have many advantages when it comes to performing faster, better and with cheaper computations, as well as in certain situations where theoretical modeling and experimental measurements are either very difficult or impossible.

The methods of computational modeling of woodwind music instruments vary from realtime simulations, such as the digital waveguide modeling of virtual woodwind instruments (Smith, 1992; Välimäki, 1995; Scavone, 1997), to non-realtime numerical methods that can provide high accuracy, such as the computational analysis and computer aided design of woodwind instruments based on the finite element method (Lefebvre and Scavone, 2010, 2012), to the direct numerical simulations of the physical behaviors of fully coupled woodwind instruments on the microscopic scale (da Silva et al., 2007; Obikane, 2011; Giordano, 2013, 2014).

On the macroscopic scale and without considering aeroacoustic effects, the acoustic behavior of a woodwind musical instrument is governed by the acoustic wave equation. For problems involving aerodynamic phenomenon, such as turbulences, vortex shedding and interactions between an aerodynamic field and an acoustic field, the wave equation is inadequate and more fundamental governing equations such as the Euler equations or the Navier-Stokes equations should be explored. In this sense, the acoustic solution is considered as a perturbation to a more complicated aerodynamic flow problem, for which the modern computational fluid dynamics (CFD) methods have been very successful. But since *“the nature, characteristics, and objectives of aeroacoustic problems are also quite different from the commonly encountered CFD problems”* (Tam, 1995), issues pertinent to aeroacoustics must be studied separately when we apply CFD methods to the analysis of related aeroacoustic problems (Tam, 1995; Wells and Renaut, 1997).

In addition to other traditional CFD techniques, a relatively new tool called the lattice Boltzmann method (LBM) has attracted much attention over the last three decades. The main advantage of the LBM is represented by its simplicity in simulating the fluid field and acoustic field involving complicated boundary conditions directly and simultaneously in one single step. Also, the LBM is by nature well suited for parallel computation, which is advantageous for computationally intensive problems that require high spatial resolutions and large temporal scales.

The LBM simulation of woodwind music instruments was pioneered by Skordos (1995), who worked on recorders and organ pipes, and by Kühnelt (2007), who worked on flutes. However, their models were limited to rather simplified static geometries with low spatial resolutions. A more interesting LBM simulation of an isolated clarinet mouthpiece without an acoustic resonator was reported by da Silva et al. (2007), who successfully solved the fluid-structure interaction associated with the mouthpiece-reed system in the dynamic regime.

1.2 Objectives and Scope

The main objective of this thesis is to develop a numerical framework that is capable of simulating the fully coupled fluid-acoustic-structure interaction in clarinet-like instruments with geometrical changes. This work is a continuation of the PhD thesis research conducted by da Silva (2008). The simulation of a dynamic clarinet is char-

acterized by a vibrating structure (the reed) interacting with an isentropic viscous flow at the limit of low compressibility and low acoustic amplitude shaped by static boundary conditions, including complex solid walls and anechoic boundaries. Instead of using traditional continuum-based computational aeroacoustic (CAA) methods (either decoupled approaches or direct numerical simulation) to solve the compressible Navier-Stokes equations, the particle-based LBM was chosen because of its several advantages, which include its simplicity and capability of solving the acoustic and flow field simultaneously under a reasonable computational cost, a good robustness for complex boundary conditions and a second-order accuracy.

With respect to the software implementation of a LBM-based numerical simulation system, a researcher can either utilize one of many existing commercial or open-source packages, such as PowerFlow, Palabos, Sailfish, openLBMflow, CFDEM, waLBerla, etc., or build a customized simulation system using a general programming language suitable for scientific computation, such as Matlab, Python or C++. Either option comes with its own advantages and disadvantages. From a user's point of view, a closed-source commercial software such as PowerFlow is not only expensive but also hides implementation details that a researcher may be interested in or need for further processing, thus it is less preferred in a scientific investigation compared to other open-source alternatives. This is especially true for the implementation of a moving boundary coupled with the finite difference scheme of a distributed reed model, which requires a fully coupled interaction of acoustic-fluid-structure fields that is essential to the simulation of a dynamic clarinet. Unfortunately, this feature is not directly supported by PowerFlow. Moreover, even in the versions of PowerFlow available in 2016, coupling the standard rigid wall prescribed by a velocity with another numerical solver of a vibrating reed model seems very difficult if not impossible. Likewise, the fully coupled moving boundary and the distributed reed model are not immediately included in any other existing open-source LBM solvers. Therefore, it is justifiable that da Silva chose to develop a customized Matlab code from scratch to address the simulation problems throughout his PhD thesis research.

In the present thesis research, for the same reason, we also chose to develop a new customized simulation system using a general programming language rather than using an existing software package. The new system is partly evolved from the Matlab code of the old system used by da Silva. Due to computational limits, the old system did not

include acoustic resonator and radiation domain components in the dynamic clarinet implementation. Also, the stability of the old system in simulations involving a fluid with a very low viscosity, as well as the efficiency of the numerical procedure representing a moving boundary or a complex curved boundary needed to be improved. To solve these problems, we found that it was more efficient to re-implement a new framework rather than to modify or tweak the Matlab code of the old system. Compared to the old system, the new system is significantly improved in terms of robustness, efficiency and flexibility. Since a new system is potentially open to new bugs, it must be verified or validated before we can perform any useful simulations and trust its outcome. Therefore, a significant part of this research is engaged in validating the new simulation system in a number of different situations.

This thesis research has been organized in three sequential steps.

- The first step is to re-implement a customized LBM-based simulation system, which is capable of modeling acoustic systems with arbitrarily shaped solid boundaries.
- The second step is to verify the simulation system by addressing various benchmark acoustic problems featured by various static boundaries. The accuracy, stability and efficiency of this system are of particular concern. Furthermore, the verified model is used to investigate problems where the analytical solutions or experimental results are not available yet.
- The last step is to develop a complete clarinet model that comprises an acoustic resonator coupled to a dynamic mouthpiece-reed system. The aero-dynamic aspects of the dynamic flow and its dependency on the reed channel geometry are investigated.

There are several major differences between the present thesis research and the previous work conducted by da Silva (2008). In addition to the reimplementation, improvement and validation of the new LBM-based numerical simulation system, the contributions of this thesis research are also exhibited in the following aspects:

- The numerical investigation of the radiation directivity pattern of an axisymmetric waveguide has been extended to cases including the effects of both flow parameters (non-zero mean flow with different velocities) and geometrical parameters (horn extension with different curvature radius).

- The numerical investigation of realistic whistles has been carried out, which examines the stability of the new system simulating an acoustic problem involving a complicated geometry and a jet with relative high speed in a low viscosity fluid field during a long simulation time.
- In the simulations of a clarinet in the quasi-stationary regime, the complete non-linear characteristic curves including cases of both a fixed reed and a slowly moving reed have been investigated.
- In the numerical simulations of a clarinet in the dynamic regime, acoustic oscillations have been initiated and the flow behaviors in the reed channel as well as in the mouthpiece chamber have been visualized with high fidelity, which has never been reported in prior literature. Moreover, a noticeable inverse flow due to the influence of acoustic coupling, which cannot be predicted in the old system (da Silva, 2008), has been discovered.
- A preliminary numerical investigation has been carried out on the influence of minor geometrical changes of the internal mouthpiece shape on the timbre and playability of a dynamic clarinet in soft playing condition, including a rapid expansion of the reed channel at the end and two different channel lengths.

1.3 Outline

The presentation of this research work is outlined as follows.

Chapter 2 presents an elementary review of the theoretical background of fluid dynamics and acoustics that are useful for the discussions in the subsequent chapters. This chapter does not attempt to provide many details or comprehensive discussions, for which one can refer to textbooks dedicated to their respective fields.

Chapter 3 presents an introduction to the fundamental concepts of the LBM theory as well as its numerical procedures. A comprehensive discussion of various boundary conditions used in this study are provided. The software implementation and the parallel programming procedure are provided as well. The models discussed in this chapter provide the fundamental simulation tools for the subsequent numerical investigations.

The objectives of Chpt. 4 are twofold. First, the validity of the LB models built in the previous chapter is verified by solving benchmark acoustic problems associated with

various static solid boundaries, which include acoustic waveguides with different open-ended geometrical terminations and whistles with complicated geometries. The effects of subsonic mean flow conditions on the radiation properties of the acoustic systems are discussed. Second, the verified models are used to investigate phenomena that have not yet been solved analytically.

In Chpt. 5, the LB model is extended to a clarinet-like system comprising a dynamic mouthpiece-reed system and a fully coupled acoustic resonator with one end open in the radiation domain. The interface integrating the moving solid boundary (the reed) and the fluid dynamic and acoustic domains is developed from the technique proposed by da Silva et al. (2007), but the present simulation system is different and improved in several important aspects, including an acoustic component, an improved pressure source procedure, improved numerical stability and an efficient parallel computing scheme. The flow behavior of the new clarinet model in the quasi-stationary regime is investigated first. Then under a soft playing condition, the aeroacoustic aspects of the flow in the dynamic regime are investigated. The effects of the reed channel geometry on the flow behavior in both quasi-stationary and dynamic regimes are analyzed and compared to those predicted by a theoretical model (van Zon et al., 1990).

Finally, the general conclusions and suggestions for future research are provided in Chpt. 6.

Chapter 2

Theoretical Background

This chapter provides a short review of theoretical concepts useful for subsequent discussions of the lattice Boltzmann methods in Chpt. 3 and the investigations of the acoustic and aeroacoustic behaviors of the acoustic structures and wind instruments presented in Chpts. 4 and 5.

The forthcoming sections are organized as follows: Section 2.1 briefly discusses fluid dynamics from different scales, which helps us distinguish the theoretical models based on the continuum hypothesis from those based on the particle level. Section 2.2 discusses the fundamental governing equations of fluid dynamics, including the conservation laws of mass and momentum as well as the derivation of the famous Navier-Stokes equations. In addition, the adiabatic relation between pressure and density is derived based on the adiabatic approximation. For a comprehensive discussion on fluid dynamics, one can refer to the textbooks of Batchelor (1967), Fox et al. (2004), White (2011) and Kundu et al. (2012). Section 2.3 shows how the acoustic wave equations are derived from the Navier-Stokes equations. Plane wave propagation in ducts is also discussed. General discussions of acoustics can be found in books written by Pierce (1989) and Kinsler et al. (2000). Finally, an elemental discussion of boundary conditions and boundary layers are presented in Sec. 2.4.

2.1 The Scale of Fluid Flow

A fluid, including both liquids and gases, can be investigated on different scales. From a macroscopic point of view, a fluid is continuous and is different from a solid due to

the fact that it deforms continuously under a shear stress, which can be observed by a layperson in everyday life. From a microscopic and discrete point of view, a fluid is formed from an aggregation of a large number of moving molecules, which are either widely spaced (for the case of a gas) or closely spaced (for the case of a liquid). In principle, the behavior and properties of molecules themselves can be studied at the microscopic level and be related to the macroscopic bulk properties of materials using probability theory, as is done in the branch of physics known as *kinetic theory* or *statistical mechanics*.

For most engineering problems, however, the underlying motion of discrete molecules is not considered directly. Rather, a fluid is modeled as a continuum in a much larger scale and is characterized by its macroscopic properties such as fluid pressure, density, velocity, temperature, etc. In other words, the state of a fluid is described by a continuous function of space and time that represents the appropriate averages of molecular characteristics in a small area surrounding the point of interest. This *continuum hypothesis* holds if the ratio of the mean free path l (average traveling distance of a molecule between collisions) to the length scale L of the system, known as the *Knudsen number* ($Kn = l/L$), is much less than unity. Let's consider air at room temperature and atmospheric pressure with a mean free path of the order $5 \times 10^{-8} m$ (Kundu et al., 2012, pp. 5). In this case the length scale associated with a Knudsen number of 0.01 is $5 \times 10^{-6} m$, which is very small compared to the characteristic geometry size of a typical woodwind instrument.

2.2 Fundamentals of Fluid Dynamics

Given the continuum hypothesis based on the low Knudsen condition, any property of a fluid is a continuous function of space and time. From a Eulerian point of view, we observe the fluid as if it passes by the coordinate fixed in space. The most important variable in fluid dynamics is the velocity field:

$$\mathbf{u}(\mathbf{x}, t) = \mathbf{i}u_x(x, y, z, t) + \mathbf{j}u_y(x, y, z, t) + \mathbf{k}u_z(x, y, z, t). \quad (2.1)$$

The acceleration vector field \mathbf{a} of the flow is derived by the total time derivative of the velocity vector field:

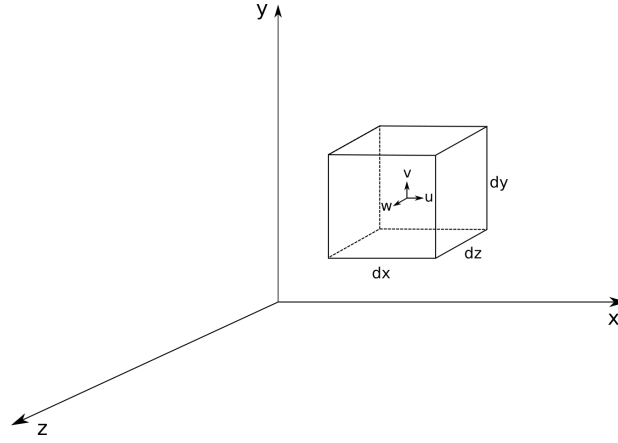


Figure 2.1 Differential control volume.

$$\mathbf{a} = \frac{D\mathbf{u}}{Dt} = \frac{\partial\mathbf{u}}{\partial t} + (\mathbf{u} \cdot \nabla)\mathbf{u}, \quad (2.2)$$

where the gradient operator is given as $\nabla = \mathbf{i} \frac{\partial}{\partial x} + \mathbf{j} \frac{\partial}{\partial y} + \mathbf{k} \frac{\partial}{\partial z}$.

Now we can consider an infinitesimal but macroscopic fixed control volume (dx, dy, dz) of a specific collection of neighboring fluid particles called a *differential control volume*, as depicted in Fig. 2.1. If we confine our analysis to classical Newton's laws and set aside nuclear reactions and relativistic effects, the basic laws of conservation of mass, momentum and energy apply directly to the differential control volume, from which we can derive the governing equations of fluid dynamics describing the fluid behaviours at the macroscopic level. This is the top-down approach, in contrast to the bottom-up approach based on kinetic theory.

In order to apply basic physical laws to a control volume, we must convert the mathematics to a specific region instead of individual masses. The *Reynolds transport theorem* is used for the conversion which can be applied to all the basic laws involving the time derivative of fluid properties.

For an arbitrary fixed control volume V enclosed by the control surface A , the Reynolds transport theorem is written as (White, 2011, pp. 144–146)

$$\frac{d}{dt} B_{\text{sys}} = \frac{d}{dt} \left(\int_{CV} \beta \rho dV \right) + \int_{CS} \beta \rho (\mathbf{u} \cdot \mathbf{n}) dA, \quad (2.3)$$

where B is any fluid property (mass, density, momentum, energy, etc.) of a local system,

$\beta = dB/dm$ is the intensive value of B per unit mass in any small portion of the fluid, dV is the elemental volume, ρdV is a differential mass of the fluid, dA is the differential area of the surface enclosing the system, $\mathbf{u} \cdot \mathbf{n}$ is the flux term, where \mathbf{u} is the flow velocity and \mathbf{n} is the outward normal unit vector on the control surface.

The Reynolds transport theorem relates the time derivative of fluid property B within the control volume V to the rate of change of B of the control surface A . Alternatively, we can rewrite the flux term $\mathbf{u} \cdot \mathbf{n}$ explicitly as the combination of a positive outflow and a negative inflow, and in this way the expanded form of the Reynolds transport theorem is given by

$$\frac{d}{dt} B_{syst} = \frac{d}{dt} \left(\int_{CV} \beta \rho dV \right) + \int_{CS} \beta \rho u \cos \theta dA_{out} - \int_{CS} \beta \rho u \cos \theta dA_{in}, \quad (2.4)$$

where θ is the angle between the local velocity \mathbf{u} and the local normal vector \mathbf{n} , $u \cos \theta dA_{in}$ and $u \cos \theta dA_{out}$ represent the inflow volume and the outflow volume, respectively.

2.2.1 Conservation of Mass

The basic conservation law of mass is given by:

$$\frac{dm}{dt} = 0. \quad (2.5)$$

This basic law can be applied to a differential control volume (dx, dy, dz) depicted in Fig. 2.1, which states that the fluid mass does not change.

Then we apply the Reynolds transport theorem to the differential control volume. Letting $B = m$ and $\beta = dm/dm = 1$, and combining the equation of mass conservation (Eq. 2.5) and the Reynolds transport theorem (Eq. 2.4), the integral form of the mass conservation relation results:

$$\frac{dm}{dt} = 0 = \frac{d}{dt} \left(\int_{CV} \rho dV \right) + \int_{CS} \rho (\mathbf{u} \cdot \mathbf{n}) dA. \quad (2.6)$$

Since the flow through each side of the control volume is approximately one-dimensional, Eq. 2.6 can be written as:

$$\int_{CV} \frac{\partial \rho}{\partial t} dV + \sum_i (\rho_i A_i u_i)_{out} - \sum_i (\rho_i A_i u_i)_{in} = 0, \quad (2.7)$$

where $\rho_i A_i u_i$ is the mass flow term on all six faces (three inlets and three outlets).

The volume integral of an infinitesimal element can be simply approximated by a differential term:

$$\int_{CV} \frac{\partial \rho}{\partial t} dV \approx \frac{\partial \rho}{\partial t} dx dy dz. \quad (2.8)$$

The inlet mass flow on the left face of the infinitesimal control volume can be written as $\rho u dx dy$, and the slightly different outlet mass flow on the right face can be written as $[\rho u + (\partial \rho u / \partial x) dx] dy dz$. Similarly, we can write the mass flow terms for the up / down and front / back face pairs. Introducing the mass flow terms on all six faces as well as Eq. 2.8 into Eq. 2.7, we obtain the partial differential equation of mass conservation, or the equation of continuity:

$$\frac{\partial \rho}{\partial t} + \frac{\partial}{\partial x}(\rho u_x) + \frac{\partial}{\partial y}(\rho u_y) + \frac{\partial}{\partial z}(\rho u_z) = 0. \quad (2.9)$$

Using the vector gradient operator, the equation of continuity can be written in the compact form:

$$\frac{\partial \rho}{\partial t} + \nabla \cdot (\rho \mathbf{u}) = 0. \quad (2.10)$$

It should be noted that we only assume that the density and velocity are continuum functions during the derivation of the equation of continuity. In fact, the equation of continuity is quite general and is valid for various flows, be they steady or unsteady, viscous or inviscid, compressible or incompressible.

If the density variation of a flow is very small, i.e., $\partial \rho / \partial t \approx 0$, the flow is considered incompressible. In such a case, the density term can be neglected and the equation of continuity reduces to

$$\nabla \cdot \mathbf{u} = 0. \quad (2.11)$$

By using some density approximations (White, 2011, pp 235), the explicit criterion for an incompressible flow is given as

$$\frac{u^2}{c_s^2} = M^2 \ll 1, \quad (2.12)$$

where c_s is the speed of sound and the dimensionless number $M = u/c_s$ is called the *Mach number*. A flow with a Mach number less than 0.3 is commonly considered incompressible (Kundu et al., 2012, pp. 99). For problems studied throughout this thesis, this condition is usually satisfied, i.e., the air flow at standard conditions with a velocity less than about 100 m/s.

2.2.2 Conservation of Momentum

Conservation of momentum can be derived by applying Newton's second law and the Reynolds transport theorem to a differential control volume (dx, dy, dz). First we recall the Newton's second law in terms of the time derivative of momentum:

$$d\mathbf{F} = \frac{d}{dt}(m\mathbf{u}). \quad (2.13)$$

Let $B = m\mathbf{u}$ and $\beta = dB/dm = \mathbf{u}$, and combine Eq. 2.13 and the Reynolds transport theorem Eq. 2.4, we obtain the linear momentum relation as:

$$d\mathbf{F} = \frac{\partial}{\partial t} \left(\int_{CV} \mathbf{u} \rho dV \right) + \sum_i (\dot{m}_i \mathbf{u}_i)_{out} - \sum_i (\dot{m}_i \mathbf{u}_i)_{in}, \quad (2.14)$$

where $d\mathbf{F}$ is the net force on the differential control volume and $\dot{m} = \int_{CS} \rho \mathbf{u} \cdot \mathbf{n} dA$ is the mass flux.

Given that the inlet momentum flux on the left face of the infinitesimal control volume is $\rho u \mathbf{u} dy dz$, the outlet mass flow on the right face would be $[\rho u_x \mathbf{u} + \frac{\partial}{\partial x}(\rho u_x \mathbf{u} dx)] dy dz$. The momentum flux terms for other faces can be derived in a similar way.

The volume integral of an infinitesimal element can be simply reduced to the differential term:

$$\frac{\partial}{\partial t}(\mathbf{u} \rho dV) \approx \frac{\partial}{\partial t}(\rho \mathbf{u} dx dy dz). \quad (2.15)$$

Introducing Eq. 2.15 and the momentum flux terms on all six faces into Eq. 2.14, with some simplifications by cancelling out redundant terms and using the notation of the total acceleration, we can obtain the intermediate result:

$$d\mathbf{F} = \rho \frac{D\mathbf{u}}{Dt} dx dy dz. \quad (2.16)$$

The net force $d\mathbf{F}$ includes the body forces due to external fields (gravity, magnetism

and electric potential) and surface forces due to the stresses on the sides of the control surface. For the problems investigated throughout this thesis, the body forces can be neglected. The surface forces include both normal forces due to the hydrostatic pressure and the viscous shear stresses that arise from the frictional forces due to the velocity gradients in the motion of fluid elements. If the hydrostatic stress on the faces normal to x-axis is σ_{xx} , the shear viscous stresses in y- and z-direction on a face normal to x-axis are τ_{yx} and τ_{zx} , respectively, and assuming each of the component is proportional to the element volume $dV = dx dy dz$, then the x-component of the net force is written as

$$dF_x = \left(\frac{\partial \sigma_{xx}}{\partial x} + \frac{\partial \tau_{yx}}{\partial y} + \frac{\partial \tau_{zx}}{\partial z} \right) dx dy dz. \quad (2.17)$$

Likewise, the y- and z-components of the net force are derived as:

$$dF_y = \left(\frac{\partial \tau_{xy}}{\partial x} + \frac{\partial \sigma_{yy}}{\partial y} + \frac{\partial \tau_{zy}}{\partial z} \right) dx dy dz, \quad (2.18a)$$

$$dF_z = \left(\frac{\partial \tau_{xz}}{\partial x} + \frac{\partial \tau_{yz}}{\partial y} + \frac{\partial \sigma_{zz}}{\partial z} \right) dx dy dz. \quad (2.18b)$$

The compact form of the differential momentum equation can be obtained by substituting the net force term in Eq. 2.16 by the stress tensors given in Eq. 2.17 and 2.18:

$$\rho \frac{D\mathbf{u}}{Dt} = -\nabla p + \nabla \cdot \boldsymbol{\tau}_{ij}. \quad (2.19)$$

The derivation of the stress tensor σ and τ is beyond the scope of this work, but the results can be found in standard textbooks of fluid dynamics (e.g. Fox et al., 2004; White, 2011). The shear stress tensor τ_{ij} stands for a viscous stress in the j direction on a face normal to the i axis, which may be expressed in terms of velocity gradients and fluid properties as follows:

$$\tau_{xy} = \tau_{yx} = \mu \left(\frac{\partial u_y}{\partial x} + \frac{\partial u_x}{\partial y} \right), \quad (2.20a)$$

$$\tau_{yz} = \tau_{zy} = \mu \left(\frac{\partial u_z}{\partial y} + \frac{\partial u_y}{\partial z} \right), \quad (2.20b)$$

$$\tau_{zx} = \tau_{xz} = \mu \left(\frac{\partial u_x}{\partial z} + \frac{\partial u_z}{\partial x} \right), \quad (2.20c)$$

where μ is the dynamic viscosity.

The normal stress tensor σ corresponding to friction from bulk-expanding motion is expressed as:

$$\sigma_{xx} = -p - \frac{2}{3}\mu\nabla \cdot \mathbf{u} + 2\mu\frac{\partial u_x}{\partial x}, \quad (2.21a)$$

$$\sigma_{yy} = -p - \frac{2}{3}\mu\nabla \cdot \mathbf{u} + 2\mu\frac{\partial u_y}{\partial y}, \quad (2.21b)$$

$$\sigma_{zz} = -p - \frac{2}{3}\mu\nabla \cdot \mathbf{u} + 2\mu\frac{\partial u_z}{\partial z}. \quad (2.21c)$$

Introducing the shear and normal stress tensor (Eq. 2.20 and Eq. 2.21) into Eq. 2.19, one can write the compact form of the differential momentum equation in terms of basic fluid properties (density, pressure, velocity and viscosity) as

$$\rho\frac{D\mathbf{u}}{Dt} = -\nabla p + \mu\left[\nabla^2\mathbf{u} + \frac{1}{3}\nabla(\nabla \times \mathbf{u})\right], \quad (2.22)$$

where $\nabla \times \mathbf{u}$ is the curl of the velocity field.

2.2.3 Adiabatic Approximation

The problems studied throughout this thesis are characterized by an acoustic wave propagation superimposed on a viscous air flow at a low Mach number ($M < 0.3$). The amplitude of the acoustic waves is represented in terms of variations of the fluid density. Along with the acoustic wave oscillation, the internal energy of the fluid is changed by the quick compression and expansion of the air due to the vibrations of the fluid molecules. The coupling between the variations of temperature and the variations of density and momentum of the flow is described by the partial differential equation of energy conservation.

When the air flow is at room temperature and atmospheric pressure, the amplitude of the acoustic wave is several orders smaller than the nominal density of the fluid and the coupling between the density and the variation of momentum and temperature is extremely small and can be neglected. In this case, we can assume that the heat is not transferred between different parts of the flow but rather the small local temperature oscillations are confined in local heat reservoirs in every point in space. Instead of us-

ing the equation of energy conservation, the relation between the pressure, density and temperature of a homentropic flow can be approximated by the exact Laplacian relation, also known as the adiabatic law:

$$\frac{p}{p_0} = \left(\frac{\rho}{\rho_0}\right)^\gamma = \left(\frac{T}{T_0}\right)^{\left(\frac{\gamma}{\gamma-1}\right)}, \quad (2.23)$$

where p , ρ and T are the instantaneous value of pressure, density and absolute temperature degree in Kelvin, respectively, and γ is the ratio of the specific heats of the gas. The sub-index 0 indicates the value before an adiabatic change. The relation between the instantaneous variables p , ρ and T , and the associated small variations, namely p' , ρ' and T' , are expressed as:

$$p = p_0 + p', \quad (2.24a)$$

$$\rho = \rho_0 + \rho', \quad (2.24b)$$

$$T = T_0 + T'. \quad (2.24c)$$

Introducing the above small variations in Eq. 2.24 into the adiabatic law and expanding it to first order in small quantities, we can obtain

$$\frac{p}{p_0} = 1 + \frac{p'}{p_0} = \left(1 + \frac{\rho'}{\rho_0}\right)^\gamma \simeq 1 + \gamma \frac{\rho'}{\rho_0}. \quad (2.25)$$

So the small variations of pressure and density are related by:

$$p' = \left(\gamma \frac{p_0}{\rho_0}\right) \rho'. \quad (2.26)$$

On the other hand, the mean values of the thermodynamic variables are related by the equation of state for gases,

$$p_0 = \rho_0 R T_0, \quad (2.27)$$

where R is the gas constant, which is equal to $287 \text{ J kg}^{-1} \text{ K}^{-1}$ for dry air (Kundu et al., 2012, p. 17). Equations 2.26 and 2.28 give

$$p' = c_s^2 \rho', \quad (2.28)$$

where $c_s = \sqrt{\gamma RT_0}$ is the speed of sound.

The precise adiabatic relation between pressure and density is derived from Eq. 2.24 and Eq. 2.28 as

$$p = c_s^2 \rho + (p'_0 - c_s^2 \rho_0), \quad (2.29)$$

which is commonly simplified to the following relation by removing the offset term on the right hand side:

$$p = \rho c_s^2. \quad (2.30)$$

The adiabatic approximation holds as long as the variations of pressure and density are small and the flow is below the explicit criterion for an incompressible flow, i.e. $M < 0.3$.

2.2.4 Navier-Stokes Equations

The Navier-Stokes equations are a set of non-linear partial differential equations that describe the fluid motion. To solve them numerically, the number of equations should be no less than the number of unknowns. The compressible form of the Navier-Stokes equations is composed of the continuity equation (Eq. 2.10) and the equation of momentum conservation (Eq. 2.22). For three-dimensional flows, there are four unknowns, i.e., u_x, u_y, u_z and ρ , where the pressure p is mapped to the density ρ by the adiabatic relation (Eq. 2.30).

The subsonic air flows investigated throughout this thesis can be described as slightly-compressible and almost isothermal. The variations of viscosity with the temperature is very small such that it can be assumed constant. The convective term $\nabla \times \mathbf{u} = 0$ in Eq. 2.22 can be omitted, and the equation of momentum conservation is reduced to

$$\rho \frac{D\mathbf{u}}{Dt} = -\nabla p + \mu \nabla^2 \mathbf{u}. \quad (2.31)$$

By expanding the compact form of the continuity equation and the equation of momentum conservation, the Navier-Stokes equations for incompressible flow are written as follows:

$$\frac{\partial \rho}{\partial t} + \frac{\partial(\rho u_x)}{\partial x} + \frac{\partial(\rho u_y)}{\partial y} + \frac{\partial(\rho u_z)}{\partial z} = 0, \quad (2.32a)$$

$$\rho \left(\frac{\partial u_x}{\partial t} + u_x \frac{\partial u_x}{\partial x} + u_y \frac{\partial u_x}{\partial y} + u_z \frac{\partial u_x}{\partial z} \right) + c_s^2 \frac{\partial \rho}{\partial x} - \mu \left(\frac{\partial^2 u_x}{\partial x^2} + \frac{\partial^2 u_x}{\partial y^2} + \frac{\partial^2 u_x}{\partial z^2} \right) = 0, \quad (2.32b)$$

$$\rho \left(\frac{\partial u_y}{\partial t} + u_x \frac{\partial u_y}{\partial x} + u_y \frac{\partial u_y}{\partial y} + u_z \frac{\partial u_y}{\partial z} \right) + c_s^2 \frac{\partial \rho}{\partial y} - \mu \left(\frac{\partial^2 u_y}{\partial x^2} + \frac{\partial^2 u_y}{\partial y^2} + \frac{\partial^2 u_y}{\partial z^2} \right) = 0, \quad (2.32c)$$

$$\rho \left(\frac{\partial u_z}{\partial t} + u_x \frac{\partial u_z}{\partial x} + u_y \frac{\partial u_z}{\partial y} + u_z \frac{\partial u_z}{\partial z} \right) + c_s^2 \frac{\partial \rho}{\partial z} - \mu \left(\frac{\partial^2 u_z}{\partial x^2} + \frac{\partial^2 u_z}{\partial y^2} + \frac{\partial^2 u_z}{\partial z^2} \right) = 0. \quad (2.32d)$$

2.3 Acoustic Wave Equations

An acoustic wave in a compressible fluid medium is a mechanical oscillatory motion of the fluid particles in small amplitude. When the fluid is deformed (compressed or expanded) by an external disturbance, individual infinitesimal elements of the fluid move back and forth in the direction of the force and initiate a propagation of a wave on the macroscopic scale. The partial differential equations governing the propagation of acoustic waves are called the *acoustic wave equations*, which describe mathematically the spatial-temporal evolutions of the acoustical variables of interest (velocity, density, pressure, etc.).

The acoustic wave equations can be derived directly from the Navier-Stokes equations (Kinsler et al., 2000). Assuming the mean flow is zero and the acoustic disturbance (the deviation of each flow variable from its equilibrium value in comparison to the equilibrium value) is very small, we decompose the variables of interest into the sum of an equilibrium value and a perturbed value:

$$p = p_0 + p', \quad (2.33a)$$

$$\mathbf{u} = \mathbf{0} + \mathbf{u}' = \mathbf{u}', \quad (2.33b)$$

$$\rho = \rho_0 + \rho'. \quad (2.33c)$$

Since the viscosity has a negligible effect on the acoustic waves, the viscous stress term can be omitted from the momentum conservation equation (Eq. 2.31), which reduces to Euler's equation:

$$\rho \frac{D\mathbf{u}}{Dt} = -\nabla p. \quad (2.34)$$

Substituting Eq. 2.33 to the continuity equation (Eq. 2.10) and Euler's equation, we can obtain the linearized form (omitting some small quadratic terms):

$$\frac{\partial \rho'}{\partial t} + \rho_0 \nabla \cdot \mathbf{u}' = 0 \quad (2.35)$$

and

$$\frac{\partial \mathbf{u}'}{\partial t} + \frac{c_s^2}{\rho_0} \nabla \rho' = 0. \quad (2.36)$$

We have used the approximation $\rho_0 + \rho' \approx \rho_0$ in the above derivations.

To obtain a single differential equation with one dependent variable, we need some further manipulations. Taking the time derivative of Eq. 2.35 and assuming that ρ_0 is a weak function of time, we obtain

$$\frac{\partial^2 \rho'}{\partial t^2} + \rho_0 \nabla \cdot \left(\frac{\partial \mathbf{u}'}{\partial t} \right) = 0. \quad (2.37)$$

Then taking the divergence of the Euler equation (Eq. 2.36), we have

$$\nabla \cdot \left(\frac{\partial \mathbf{u}'}{\partial t} \right) + \frac{c_s^2}{\rho_0} \nabla^2 \rho' = 0. \quad (2.38)$$

Eliminating the divergence term between these two equations gives the linear lossless wave equation for the acoustic density

$$\frac{\partial^2 \rho'}{\partial t^2} - c_s^2 \nabla^2 \rho' = 0, \quad (2.39)$$

where ∇^2 is the three-dimensional spatial Laplacian operator.

Actually, the wave equation is applicable to any acoustics variables. The linear lossless wave equation for velocity and pressure are expressed respectively as

$$\frac{\partial^2 \mathbf{u}'}{\partial t^2} - c_s^2 \nabla^2 \mathbf{u}' = 0 \quad (2.40)$$

and

$$\frac{\partial^2 p'}{\partial t^2} - c_s^2 \nabla^2 p = 0. \quad (2.41)$$

Since we have used the irrotational approximation that the curl of particle velocity is zero, i.e., $\nabla \times \mathbf{u} = 0$, the acoustic velocity can be expressed as the gradient of a scalar potential function,

$$\mathbf{u}' = \nabla \phi, \quad (2.42)$$

where ϕ is identified as the velocity potential, which satisfies the wave equation within the same approximations:

$$\frac{\partial^2 \phi}{\partial t^2} - c_s^2 \nabla^2 \phi = 0. \quad (2.43)$$

A real fluid is not curl-free everywhere (especially in the vicinity of boundaries), but Eq. 2.43 still holds because the rotational effects are very small for most part of the sound propagation.

2.3.1 Harmonic Plane Waves

A simple but interesting case of the acoustic wave is the plane wave, where each acoustic variable has constant amplitude and phase on the plane perpendicular to the direction of propagation. The propagation of a plane pressure wave in the x-direction is described by the one-dimensional wave equation

$$\frac{\partial^2 p'}{\partial t^2} - c_s^2 \frac{\partial^2 p'}{\partial x^2} = 0, \quad (2.44)$$

whose harmonic solution in complex form is given by a sum of two traveling waves in opposite directions

$$p' = \mathbf{A}e^{j(\omega t - kx)} + \mathbf{B}e^{j(\omega t + kx)}, \quad (2.45)$$

where the complex constants \mathbf{A} and \mathbf{B} are independent of position, and we have the following relations:

$$c_s = \omega/k = 2\pi f/k = f\lambda, \quad (2.46)$$

where ω is the frequency in radians per second, f is the frequency in Hz, k is the spatial frequency (wavenumber) and λ is the wavelength. The associated particle velocity in the direction of propagation is given by

$$\mathbf{u}' = \frac{1}{\rho_0 c_s} [\mathbf{A}e^{j(\omega t - kx)} - \mathbf{B}e^{j(\omega t + kx)}]. \quad (2.47)$$

2.4 Boundary Conditions and Boundary Layer

Throughout this thesis, we are dealing with fluids interacting with either a static solid boundary or a moving boundary, so it is necessary to discuss the boundary conditions.

If the velocity on the surface of a solid boundary is \mathbf{u}_b at a point \mathbf{x} , and the fluid velocity is \mathbf{u} , since the normal component of the fluid velocity must be equivalent to the normal component of the boundary velocity, we have

$$\mathbf{u} \cdot \mathbf{n} = \mathbf{u}_b \cdot \mathbf{n}, \quad (2.48)$$

where \mathbf{n} is the unit vector normal to the solid surface. For a static solid boundary, Eq. 2.48 reduces to

$$\mathbf{u} \cdot \mathbf{n} = 0. \quad (2.49)$$

In the case of a reed on a clarinet's mouthpiece, the boundary location may change over time. If the solid surface is described by the equation $\chi(\mathbf{x}, t) = 0$, the boundary condition taking the deformation of the surface into account is called the *kinematic boundary condition*, which is expressed as (da Silva, 2008)

$$\frac{D\chi}{Dt} = \frac{\partial\chi}{\partial t} + \mathbf{u} \cdot \nabla\chi = 0. \quad (2.50)$$

The boundary condition presented above only discusses the normal component of the fluid velocity. For viscous fluids, the influence of the tangential component of the fluid velocity must be taken into account. The condition of continuity of the velocity requires that the tangential component of the velocity is continuous across the solid boundary. Actually, no matter how small the viscosity ν may be, the *no-slip* condition must be satisfied such that the tangential component of the fluid velocity at the solid boundary is equivalent to that of the boundary velocity. Due to the viscous stress, the tangential movement of the fluid particles in the vicinity of the solid wall is retarded by the stagnant fluid particles at the wall. The thin shear layer where the viscous effects are dominant is called the *boundary layer*, which was first introduced by Ludwig Prandtl in 1904.

Figure 2.2 illustrates a uniform viscous flow with a constant upstream velocity of U over a semi-infinite sharp flat plate parallel to the flow direction. A shear layer of

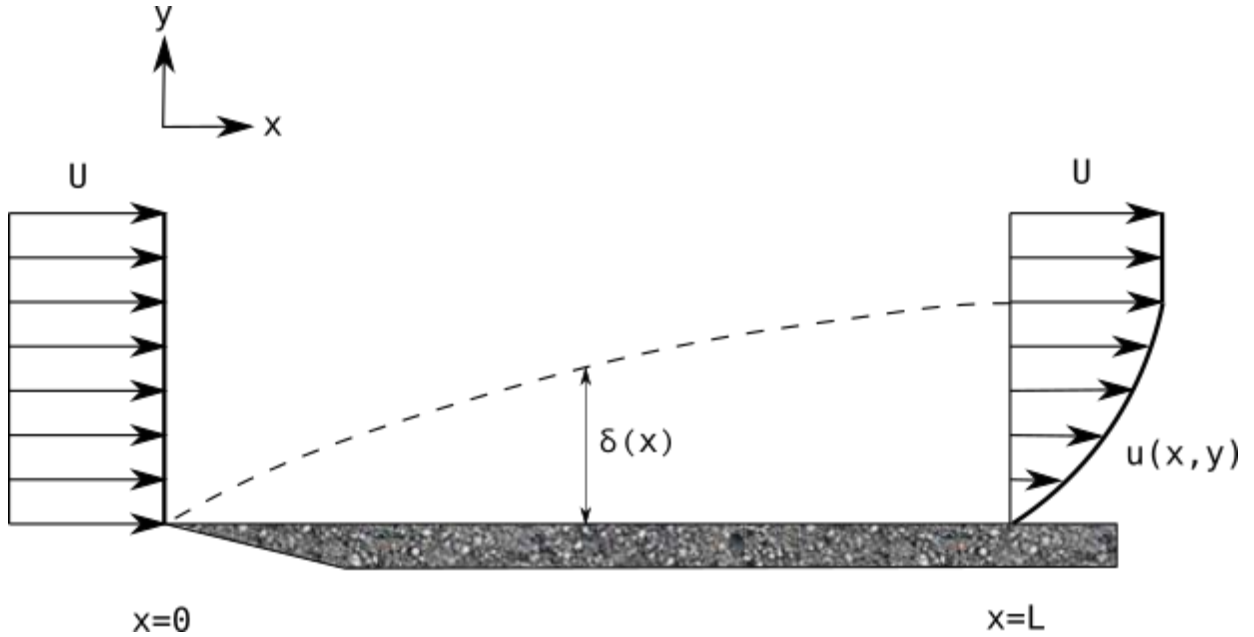


Figure 2.2 Boundary layer on a semi-infinite flat plate.

unknown thickness grows along the downstream direction. The flow is retarded by the no-slip wall condition and its velocity profile $u(y)$ is rounded, which merges into the external velocity U at a thickness $y = \delta(x)$. Practically, the disturbance thickness δ is defined as the distance from the surface at which the velocity is within 1% of the constant free stream, $u(x, y) \approx 0.99U$, because the location of the boundary layer edge (where the velocity gradient equals to zero) is not obvious to find.

The boundary layer equations for a steady incompressible viscous flow over a flat plane surface can be derived from the mass and momentum conservation equations of the incompressible Navier-Stokes equations (Eq. 2.32). For a flow characterized by a large Reynolds number ($Re_x = U_x/\nu \gg 1$), the shear layer must be very thin, hence some approximations apply, such that $u_y \ll u_x$, $\partial u_x/\partial x \ll \partial u_x/\partial y$ and $\partial u_y/\partial x \ll \partial u_y/\partial y$. Thus, the y-momentum equation can be neglected entirely and the pressure gradient on the y-direction is negligible. Prandtl's boundary layer equations for two-dimensional incompressible flow is then given by

$$\frac{\partial u_x}{\partial x} + \frac{\partial u_y}{\partial y} = 0 \quad (2.51)$$

and

$$u_x \frac{\partial u_x}{\partial x} + u_y \frac{\partial u_x}{\partial y} \approx U \frac{dU}{dx} + \frac{1}{\rho} \frac{\partial \tau}{\partial y}, \quad (2.52)$$

where the shear stress is given by:

$$\tau = \begin{cases} \mu \frac{\partial u}{\partial y} & \text{for laminar flow,} \\ \mu \frac{\partial u}{\partial y} - \overline{\rho u'_x u'_y} & \text{for turbulent flow,} \end{cases}$$

where the tensor $\overline{\rho u'_x u'_y}$ plays the role of a stress and is called the Reynolds stress tensor (Kundu et al., 2012, pp. 556).

For most flow problems, the boundary layer equations cannot be solved exactly. But for simple cases such as the laminar flow past a semi-infinite flat plate, the exact solution is given by Blasius (Blasius, 1907; Tani, 1977) based on the insight that the laminar boundary layer velocity profile is self-similar. To avoid difficulties, an approximate method known as the *Karman momentum integral* can be used to obtain approximate information on boundary layer growth (thickness δ as a function of x) in general cases (laminar or turbulent boundary layers, with or without a pressure gradient). This approach is achieved by applying the basic continuity equation and momentum equations to a differential control volume enclosing a short section of the flow on the plate. The Karman equation presents

$$\frac{\tau_w}{\rho} = \frac{d}{dx}(U^2 \theta) + \delta^* U \frac{dU}{dx}, \quad (2.53)$$

where τ_w is the wall shear stress along the plate, the displacement thickness δ^* is defined as

$$\delta^* = \int_0^\delta \left(1 - \frac{u}{U}\right) dy, \quad (2.54)$$

and the momentum thickness θ is defined as

$$\theta = \int_0^\delta \frac{u}{U} \left(1 - \frac{u}{U}\right) dy. \quad (2.55)$$

The Karman equation is restricted to two-dimensional steady incompressible flow with no body forces parallel to the surface, and is valid for either a laminar or turbulent boundary layer flow.

One of the interesting predictions made by the boundary layer theory is the flow separation phenomenon. As we will see in Chpt. 5, the reed's oscillatory behavior is strongly influenced by the flow separation, which is observable in the visualized velocity fields during the oscillation period.

Chapter 3

Lattice Boltzmann Method

3.1 Introduction

We have discussed the Navier-Stokes equations in Chpt. 2, which are macro-scale level descriptions based on the continuous mechanics approach and have been widely used in the majority of the macroscopic fluid problems. However, macroscopic models are not able to capture the micro-flows related to complex physical effects such as turbulence, multiphase flows, etc.

If we study the fluid flow on the particle level, i.e., the motion of each molecule is tracked individually and the interaction of molecules is described by Newtonian formulation, this is called the *Molecular Dynamics* approach (MD). Theoretically, one can obtain the position and velocity of each molecule at any time by solving the equations based on Newton's second law applied to each particle. The macroscopic quantities of the fluid, such as density, velocity and temperature, are no more than the ensemble average of the corresponding microscopic quantities. The transport coefficients of the fluid, such as viscosity, thermal conductivity, diffusivity, etc., can also be obtained from the microscopic quantities through linear transformation. The main problem, though, is that the number of unknowns is extremely large. The number of molecules N for a small volume of fluid in practice is on the order of Avogadro's number 10^{23} , and for a N-body system, the number of unknowns is $6N$. Thus, it is impractical to solve the whole system for even a tiny volume of fluid with the most advanced computer resources available nowadays. Also, for most problems, we are interested in the collective behaviors of the system rather than the motion of every individual molecular constituent.

Besides the molecular dynamics model at the microscopic level and the continuum models at the macroscopic level, one can also model the fluid behavior on a mesoscopic level, less straightforwardly, using the kinetic theory. The kinetic theory attempts to study a fluid from a statistical point of view, i.e., the evolution of the fluid is formulated to a transport equation in terms of particle distribution functions. One particularly important transport equation is the *Boltzmann equation*, which is difficult to solve directly but which can be solved numerically using the *lattice Boltzmann method* (LBM).

The LBM originated from a simplified molecular dynamical model simulating the fluid flow effects on a microscopic scale called *Lattice Gas Automata* (LGA), from which the incompressible Navier-Stokes equations in the limit of a small Knudsen number can be recovered (Frisch et al., 1986, 1987). Instead of handling single particles, the LBM handles particle distributions and treats collisions in a manner different from the LGA. The equations of the LBM can also be derived from the continuum Boltzmann Equation (BE) (Sterling and Chen, 1996; Wolf-Gladrow, 2004). In the limit of a small Knudsen number, the Navier-Stokes equations can be recovered from the lattice Boltzmann equation using the Chapman-Enskog expansion (Chapman and Cowling, 1960).

Compared to traditional computational fluid dynamics and aeroacoustic techniques, the LBM has several advantages: solving both scales associated with the acoustic and flow fields in a single time-step, the direct acquisition of the pressure field, the straightforward boundary condition schemes and the relatively easy programming and parallelization. Over the last few decades, the LBM has developed quickly and has attracted significant attention in the industrial and academic communities. Nowadays, the LBM has become a viable numerical tool for modeling fluid flows in computational fluid dynamics (CFD), computational aeroacoustics (CAA) and beyond. For an in-depth description of the LBM, one can refer to textbooks by Succi (2001), Wolf-Gladrow (2004), Sukop and Thorne (2006), Guo and Shu (2013), or excellent review papers (Chen and Doolen, 1998; Aidun and Clausen, 2010).

This chapter aims to provide the fundamental concepts of the LBM theory as well as its software implementation. The sections are organized as follows: Section 3.2 briefly introduces the two different approaches leading to the generic lattice Boltzmann equations and the LBGK model used in the forthcoming chapters. Section 3.3 discusses the initial conditions as well as various boundary conditions involved in this study. Section 3.4 deals with the numerical procedures of the lattice Boltzmann models. Section 3.5 ex-

plores the GPU parallel programming that greatly accelerates the LBM's computations.

3.2 Fundamental Theory of LBM

3.2.1 From LGA to LBE

The Lattice Gas Automata (LGA) simulates the fluid as a set of particles residing on a regular lattice. The processes of collision and propagation of these particles are based on some physical laws such that the mass, momentum, and energy are conserved. A LGA comprises a regular lattice, where the nodes on the lattice can take a certain number of different state variables $\{n_i\}$, $i \in \{1, \dots, M\}$, which describes the population of M given velocities c_i . In LGA, the time and space are discrete and the state variables are Boolean (0 or 1). The evolution equation of the LGA is given by

$$n_i(\mathbf{x} + \mathbf{e}_i, t + 1) = n_i(\mathbf{x}, t) + \Omega_i(\mathbf{x}, t), \quad (i = 0, 1, \dots, M), \quad (3.1)$$

where \mathbf{e}_i are the local particle velocities, $\Omega_i(\mathbf{x}, t)$ is the collision operator that depends on $n_i(\mathbf{x}, t)$.

The evolution of the LGA model is divided into two steps: streaming and collision. In the streaming step, the state variables propagate from node to node according to the velocity c_i . In the collision step, the particles arrive at a node interact and change their velocity directions, and the state of the node is determined by collision rules that are based on conservation laws of physical quantities (mass, momentum, energy). After each evolution step, the state of a given node is determined by the previous state of both this node and its neighbouring nodes.

The LGA has the advantages of straightforward boundary conditions, simple coding and inherent parallel nature. But there are several intrinsic defects when it is used in fluid flow simulations, such as statistical noise, lack of Galilean invariance and a velocity-dependent pressure.

A fix to the statistical noise problem of LGA is proposed by McNamara and Zanetti (1988). They replaced the Boolean occupation variables n_i with the mean population of particles, which are real numbers between 0 and 1. The evolution equation of the LGA

then becomes

$$f_i(\mathbf{x} + \mathbf{e}_i\Delta x, t + \Delta t) = f_i(\mathbf{x}, t) + \Omega_i(\mathbf{x}, t), \quad (i = 0, 1, \dots, M), \quad (3.2)$$

where f_i is the particle velocity distribution function along the i th direction, and Δx and Δt are time and space increments, respectively. This is an important step that translates the LGA into the lattice Boltzmann model. Equation 3.2 is called the lattice Boltzmann equation (LBE). The collision operator $\Omega_i(\mathbf{x}, t)$, which represents the rate of change of f_i in collisions, is required to satisfy the conservation of mass and momentum at each node:

$$\sum_{i=1}^M \Omega_i = 0, \quad (3.3)$$

$$\sum_{i=1}^M \Omega_i \mathbf{e}_i = 0. \quad (3.4)$$

The macroscopic quantities of density and momentum can be recovered from the moments of the distribution function f_i as

$$\rho = \sum_{i=1}^M f_i \quad (3.5)$$

and

$$\rho \mathbf{u} = \sum_{i=1}^M f_i \mathbf{e}_i. \quad (3.6)$$

The collision operator Ω_i in the LBE can be obtained in various ways, but here we focus on the most simple and popular one. Inspired by the method of relaxation that is well known in computational fluid dynamics and many physical problems, Qian et al. (1992) used the relaxation process to replace the collision term in the LBE, which is written as

$$f_i(\mathbf{x} + \mathbf{e}_i\Delta x, t + \Delta t) = (1 - \omega)f_i(\mathbf{x}, t) + \omega f_i^{eq}(\mathbf{x}, t), \quad (3.7)$$

where ω is the relaxation parameter. This scheme is linearly stable for $0 < \omega < 2$.

3.2.2 From BE to LBE

Aside from the MD approach, the N-body fluid system can be alternatively described by the Hamiltonian formulation

$$\mathcal{H} = \mathcal{H}(\mathbf{q}, \mathbf{p}, t), \quad (3.8)$$

where \mathcal{H} is the total sum of the kinetic energy and the potential energy of the system, \mathbf{q} is the $3N$ spatial coordinates of the N molecules and \mathbf{p} is the $3N$ conjugate momenta.

Following the Hamiltonian approach, and using the concept of *probability distribution function* (PDF) $f_N(\mathbf{q}, \mathbf{p}, t)$, the state of an infinitesimal volume in the $6N$ dimensional phase space is described by the probability $f_N d\mathbf{q} d\mathbf{p}$. The partial differential equation describing the evolution of f_N is called the Liouville equation:

$$\frac{\partial f_N}{\partial t} - \sum_{j=1}^N \left[\frac{\partial \mathcal{H}}{\partial \mathbf{q}_j} \frac{\partial f_N}{\partial \mathbf{p}_j} - \frac{\partial \mathcal{H}}{\partial \mathbf{p}_j} \frac{\partial f_N}{\partial \mathbf{q}_j} \right] = 0. \quad (3.9)$$

The Liouville equation can be represented by a chain of evolution equations in terms of reduced s-particle probability distribution functions $F_s (1 \leq s \leq N)$ defined as

$$F_s(\mathbf{q}_1, \mathbf{p}_1, \dots, \mathbf{q}_s, \mathbf{p}_s) = \int f_N(\mathbf{q}_1, \mathbf{p}_1, \dots, \mathbf{q}_s, \mathbf{p}_s) d\mathbf{q}_{s+1} d\mathbf{p}_{s+1} \dots d\mathbf{q}_N d\mathbf{p}_N. \quad (3.10)$$

The chain of PDFs, called the BBGKY hierarchy (Bogoliubov et al., 1962), is identical to the Liouville equation and is fully coupled. Both the Liouville equation and the BBGKY hierarchy are difficult to solve. The strategy to simplify the problem is to truncate the BBGKY to certain orders that approximate the original chain under some assumptions. The simplest case would be to define a PDF by truncating the BBGKY chain to the first order:

$$f(\mathbf{x}, \mathbf{e}, t) = mN F_1(\mathbf{q}_1, \mathbf{p}_1, t), \quad (3.11)$$

where $\mathbf{x} = \mathbf{q}_1$ is the particle position and $\mathbf{e} = \mathbf{p}_1/m$ is the particle velocity. The single particle velocity distribution function f represents the population of particles within the velocity volume element $d\mathbf{e}$ with velocity \mathbf{e} inside the infinitesimal volume element $d\mathbf{x}$ at position \mathbf{x} and at time t . The evolution of f is described by the Boltzmann equation,

which is written as

$$(\partial_t + \mathbf{e} \cdot \nabla)f(\mathbf{e}, \mathbf{x}, t) = J(f), \quad (3.12)$$

where $J(f)$ represents the effect of intermolecular collisions, which is given, based on Boltzmann's assumptions of collision of two particles, by

$$J(f) = \int [(f_{1'}f_{2'} - f_1f_2)|\mathbf{e}_1 - \mathbf{e}_2|\sigma(\theta)d\theta]d\mathbf{e}_2, \quad (3.13)$$

where f_{12} is the two-body distribution function prior to the molecules' collision and $f_{1'2'}$ is the distribution function after, \mathbf{e}_1 and \mathbf{e}_2 are the velocities of molecules 1 and 2, $\sigma(\theta)$ is the differential cross-section of the volume where the collision takes place and θ is the scattering angle.

Bhatnagar et al. (1954) proves that the collision term in Eq. 3.13 can be approximated by an operator that contains a single relaxation parameter ω_c . The well known BGK collision operator is given by

$$J(f) = -\frac{1}{\tau}(f - f^{eq}), \quad (3.14)$$

where $\tau = 1/\omega_c$ is the single relaxation time of the disturbance f to the equilibrium state f^{eq} . The BGK operator describes that $f - f^{eq}$ decays exponentially as $e^{-t/\tau}$.

The Boltzmann equation with BGK approximation is written as

$$(\partial_t + \mathbf{e} \cdot \nabla)f(\mathbf{e}, \mathbf{x}, t) = -\frac{1}{\tau}(f(\mathbf{e}, \mathbf{x}, t) - f^{eq}(\mathbf{e}, \mathbf{x}, t)), \quad (3.15)$$

where f^{eq} is the Maxwellian distribution function

$$f^{eq}(\mathbf{e}, \mathbf{x}, t) = \frac{\rho}{(2\pi RT)^{3/2}} \exp\left[-\frac{(\mathbf{e} - \mathbf{u})^2}{2RT}\right], \quad (3.16)$$

where R is the gas constant given by the ratio of the Boltzmann constant to the particle mass.

In the limit of low Mach number flow, f^{eq} can be expanded into a Taylor series:

$$f^{eq} = \frac{\rho}{(2\pi RT)^{D/2}} \exp\left(-\frac{\mathbf{e}^2}{2RT}\right) \left[1 + \frac{(\mathbf{e} \cdot \mathbf{u})}{RT} + \frac{(\mathbf{e} \cdot \mathbf{u})^2}{2RT} - \frac{u^2}{2RT}\right]. \quad (3.17)$$

The discretization starts from the velocity space, \mathbf{e} , which is represented by a finite

set of velocities, e_i . To determine the correct discretization scheme, the conservation law of mass and momentum requires the following quadratures to hold:

$$\int e^k f^{eq} de = \sum_i w_i e_i^k f^{eq}(e_i), \quad 0 \leq k \leq 3, \quad (3.18)$$

where w_i are the weights and e_i are the lattice velocities. Then by defining $f_i(\mathbf{x}, t) = w_i f(\mathbf{x}, e_i, t)$ and $f_i^{eq}(\mathbf{x}, t) = w_i f^{eq}(\mathbf{x}, e_i, t)$, the discrete-velocity BGK Boltzmann equation is given as

$$(\partial_t + e_i \cdot \nabla) f_i = -\frac{1}{\tau} (f_i - f_i^{eq}). \quad (3.19)$$

Assuming a Lagrangean behavior such that the lattice velocity $e_i = \Delta \mathbf{x} / \Delta t$, Eq. 3.19 can be discretized in space and time using a first order finite difference scheme, which leads to the BGK lattice Boltzmann equation (BGK-LBE):

$$f_i(\mathbf{x} + e_i \Delta t, t + \Delta t) - f_i(\mathbf{x}, t) = -\frac{1}{\tau} (f_i - f_i^{eq}). \quad (3.20)$$

Equation 3.20 is identical to Eq. 3.7 derived from the LGA, where $\tau = 1/\omega$ is the relaxation time. The left hand side of Eq. 3.20 represents the propagation process of the distribution functions f_i . The right hand side represents the collision operator, which determines the change rate of f_i due to intermolecular collisions.

The kinematic viscosity in lattice units is related to the relaxation parameter by

$$\nu = \frac{2/\omega - 1}{6}. \quad (3.21)$$

Equation 3.21 shows the kinematic viscosity of a fluid is in proportion to the relaxation time, or the averaged collision period of the molecules.

The discrete form of the equilibrium function f_i^{eq} is given by (Qian et al., 1992)

$$f_i^{eq}(\mathbf{x}, t) = w_i \rho \left[1 + \frac{\mathbf{u} \cdot \mathbf{e}_i}{c_s^2} + \frac{(\mathbf{u} \cdot \mathbf{e}_i)^2 - c_s^2 \mathbf{u}^2}{2c_s^4} \right], \quad (3.22)$$

where c_s is the speed of sound in lattice units. The velocity weights w_i are used to guarantee the isotropy of the fourth-order tensor of velocities and Galilean invariance, which is important for recovering the Navier-Stokes equations.

He and Luo (1997) show that the incompressible Navier-Stokes equations can be recovered from the lattice Boltzmann model by using the Chapman-Enskog procedure, as long as the fluid flow is in the low Mach number limit.

3.2.3 LBGK models

According to the standard DdQn (d -dimensional, n -velocity) nomenclature of the types of lattice geometries (Qian et al., 1992), the weight w_i of the three popular LB models, D1Q3, D2Q9 and D3Q19, are given in Table 3.1. The speed of sound c_s is model dependent, but for these three models $c_s = 1/\sqrt{3}$.

model	static	vert. / hort.	diag.
D1Q3	2/3	1/6	0
D2Q9	4/9	1/9	1/36
D3Q19	1/3	1/18	1/36

Table 3.1 Velocity weights for three lattice models.

The D2Q9 lattice model has been used throughout this study due to its simplicity, numerical stability and computational efficiency.

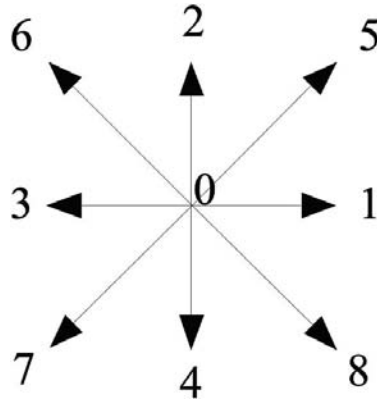


Figure 3.1 D2Q9 structure.

Figure 3.1 illustrates the D2Q9 lattice structure used in this thesis, where the non-diagonal directions are indexed by 1, 2, 3, 4 and the diagonal directions are indexed by 5, 6, 7, 8. Index 0 is reserved to the rest site. Using this indexing scheme, the equilibrium distribution function in each direction i can be written explicitly as:

$$f_i^{eq} = \frac{4}{9}\rho \left[1 - 1.5 \frac{\mathbf{u}^2}{c_s^2} \right], \quad \text{for } i = 0, \quad (3.23a)$$

$$f_i^{eq} = \frac{1}{9}\rho \left[1 + 3 \frac{\mathbf{e}_i \cdot \mathbf{u}}{c_s^2} + 4.5 \frac{(\mathbf{e}_i \cdot \mathbf{u})^2}{c_s^4} - 1.5 \frac{\mathbf{u}^2}{c_s^2} \right], \quad \text{for } i = 1, 2, 3, 4, \quad (3.23b)$$

$$f_i^{eq} = \frac{1}{36}\rho \left[1 + 3 \frac{\mathbf{e}_i \cdot \mathbf{u}}{c_s^2} + 4.5 \frac{(\mathbf{e}_i \cdot \mathbf{u})^2}{c_s^4} - 1.5 \frac{\mathbf{u}^2}{c_s^2} \right], \quad \text{for } i = 5, 6, 7, 8, \quad (3.23c)$$

where the lattice velocities \mathbf{e}_i are given by

$$\mathbf{e}_0 = (0, 0), \quad (3.24a)$$

$$\mathbf{e}_{1,3}, \mathbf{e}_{2,4} = (\pm 1, 0), (0, \pm 1), \quad (3.24b)$$

$$\mathbf{e}_{5,6,7,8} = (\pm 1, \pm 1). \quad (3.24c)$$

3.2.4 Multiple Relaxation Times

The LBGK model in Eq. 3.20 is called a Single Relaxation Time (SRT) model because it has a single relaxation rate for all of the modes. Due to its simplicity, the LBGK-SRT model is probably one of the most popular lattice Boltzmann models and it generally performs well. However, for simulations dealing with fluids that have very small kinematic viscosities such as air, numerical instabilities may arise from the SRT model because of the strong anisotropy of the dispersion relations dictated by the lattice symmetry (Lallemand and Luo, 2000).

A Multiple Relaxation Time (MRT) collision scheme is proposed by d’Humières (1994), where the single relaxation parameter is replaced by a relaxation matrix and the collision is performed in *moment space* while the propagation is still executed in *velocity space*. Lallemand and Luo (2000) prove that the numerical stability of the LBGK model can be greatly improved by carefully separating the kinetic modes with different relaxation rates in the MRT collision scheme.

The LBE with a MRT is obtained by using a multiple relaxation time matrix in the collision operator:

$$\mathbf{f}(\mathbf{x} + \mathbf{e}_i \Delta t, t + \Delta t) - \mathbf{f}(\mathbf{x}, t) = -\Lambda(\mathbf{f} - \mathbf{f}^{eq}), \quad (3.25)$$

where $\mathbf{f} = (f_0, f_1, \dots, f_{q-1})^T$ is the vector of distribution functions in the velocity space \mathbb{V} , Λ is the multiple relaxation time matrix. The collision process in the moment space \mathbb{M} is expressed as

$$\mathbf{m}(\mathbf{x} + \mathbf{e}_i \Delta t, t + \Delta t) - \mathbf{m}(\mathbf{x}, t) = -\mathbf{S}(\mathbf{m} - \mathbf{m}^{eq}), \quad (3.26)$$

where \mathbf{m} are the moments of the distribution functions, \mathbf{m}^{eq} are the moments of the equilibrium distribution functions and \mathbf{S} is a diagonal matrix. \mathbf{f} is mapped to the moment space through a transformation matrix \mathbf{M} ,

$$\mathbf{m} = \mathbf{M}\mathbf{f} = (m_0, m_1, \dots, m_{q-1})^T, \quad (3.27)$$

and \mathbf{S} is given by

$$\mathbf{S} = \mathbf{M}\Lambda\mathbf{M}^{-1}. \quad (3.28)$$

The transformation matrix of a standard D2Q9 LBGK-MRT model is given as

$$\mathbf{M} = \begin{bmatrix} 1 & 1 & 1 & 1 & 1 & 1 & 1 & 1 & 1 \\ -4 & -1 & -1 & -1 & -1 & 2 & 2 & 2 & 2 \\ 4 & -2 & -2 & -2 & -2 & 1 & 1 & 1 & 1 \\ 0 & 1 & 0 & -1 & 0 & 1 & -1 & -1 & 1 \\ 0 & -2 & 0 & 2 & 0 & 1 & -1 & -1 & 1 \\ 0 & 0 & 1 & 0 & -1 & 1 & 1 & -1 & -1 \\ 0 & 0 & -2 & 0 & 2 & 1 & 1 & -1 & -1 \\ 0 & 1 & -1 & 1 & -1 & 0 & 0 & 0 & 0 \\ 0 & 0 & 0 & 0 & 0 & 1 & -1 & 1 & -1 \end{bmatrix}. \quad (3.29)$$

In a MRT model, although the collision step is executed in the moment space, the streaming step is still executed in the velocity space. Generally, the MRT model is implemented by a more efficient approach that combines the two steps into one single step of evolution:

$$\mathbf{f}(\mathbf{x} + \mathbf{e}_i \Delta t, t + \Delta t) - \mathbf{f}(\mathbf{x}, t) = -\mathbf{M}^{-1}\mathbf{S}(\mathbf{m} - \mathbf{m}^{eq}). \quad (3.30)$$

3.3 Initial and Boundary Conditions

3.3.1 Initial Conditions

The initial states of the distribution function $\mathbf{f}(t = 0)$ can be approximated by its equilibrium states $\mathbf{f}^{eq}(t = 0)$. This scheme is straightforward and works well for systems not sensitive to initial conditions, i.e., systems with steady or quasi-steady flows. This scheme is called the *equilibrium scheme*.

For systems involving unsteady or strong nonlinear flows, the final results may contain large errors evolving from tiny initial errors. In this case, the accuracy of the initial value of $\mathbf{f}(t = 0)$ can be further improved using the more complicated *non-equilibrium scheme*, which is first proposed by Skordos (1993). In this scheme, the distribution function \mathbf{f} is decomposed to the equilibrium part \mathbf{f}^{eq} and the non-equilibrium part \mathbf{f}^{neq} , where the latter is expanded to a Taylor series and the higher-order terms are omitted. The distribution function itself is also expanded into a series using the Chapman-Enskog method. Using some mathematical manipulations and ignoring small higher-order terms, \mathbf{f}^{neq} can be explicitly expressed as functions of velocity \mathbf{u} and ρ , from which the initial states of the distribution function $\mathbf{f}(t = 0)$ can be obtained.

Since the results of this study are not sensitive to initial conditions, the equilibrium scheme is chosen for the initialization of the distribution functions.

3.3.2 Boundary Conditions

The boundary operator in a lattice Boltzmann model describes the interaction between the fluid particles and the particles of the boundary wall. The implementation of a boundary condition can be either straightforward, such as in the case that a physical wall is aligned with the grid coordinates, or relatively complicated in the case of arbitrary shaped boundaries or moving boundaries.

A solid wall boundary can be implemented using two schemes. The *explicit boundary scheme* uses special boundary nodes, also called dry nodes, to represent boundaries, contrary to those nodes representing fluids or wet nodes. This scheme is depicted in Fig. 3.2, where the black nodes represent dry nodes and the white nodes represent wet nodes.

In the *implicit boundary scheme*, the boundary curves are not defined directly on the

nodes. Rather, the propagation of fluid nodes near the boundary curves are changed by a predefined procedure associated with the boundaries. In Fig. 3.3, a solid wall is defined by the line AB which passes through the mid-points of links between two arrays of nodes. All the neighboring nodes close to the line AB, i.e., all the nodes inside the dashed rectangular area, must be treated properly after the propagation.

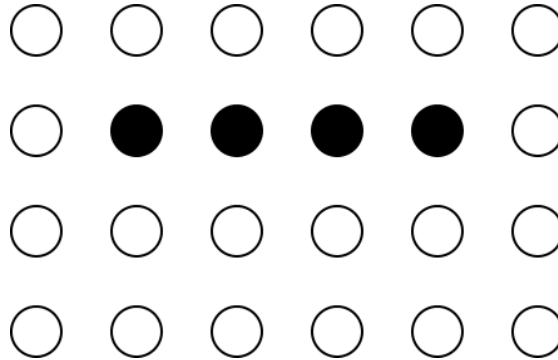


Figure 3.2 Explicit boundary nodes (black nodes).

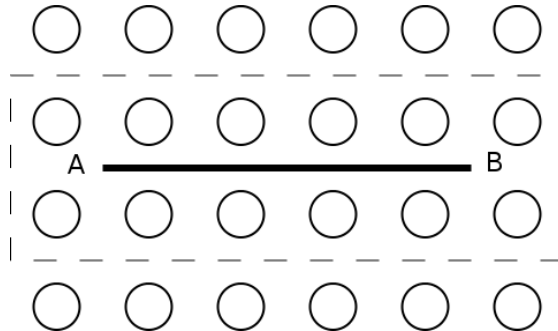


Figure 3.3 Implicit boundary curve.

Since the implicit boundary scheme provides better accuracy and can be extended to complicated non-aligned geometries using an interpolation or extrapolation scheme, it is used throughout this study. The boundary conditions used in this research are discussed in the following sub-sections.

3.3.3 No-Slip Condition

Perhaps the simplest approach to describe the solid walls of a wind instrument is the no-slip boundary condition. This approach assumes the solid wall has a sufficient ru-

gosity such that the tangential advection of solid particles is refrained and the tangential component of the fluid particles at the solid wall is zero.

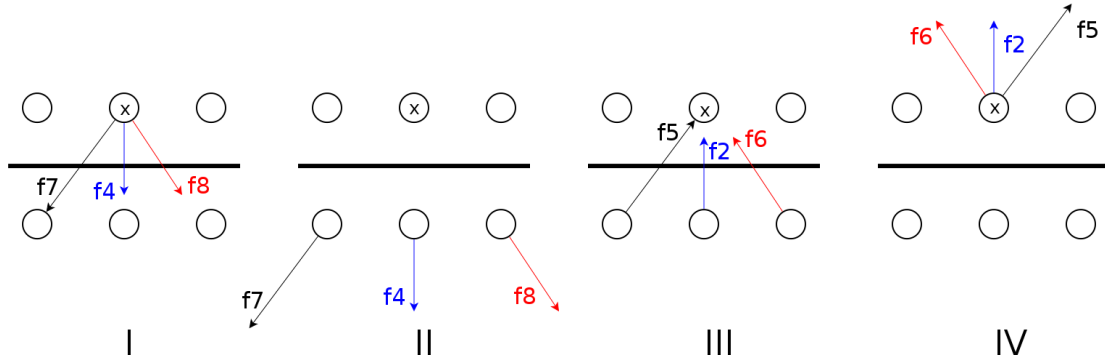


Figure 3.4 No-slip condition.

Figure 3.4 depicts the procedure of the no-slip condition in four steps. Step I shows the states of f_4 , f_7 and f_8 of a grid node at position \mathbf{x} at time t in the pre-streaming stage. In step II, the traveling particles pass through the solid boundary and arrive at the neighboring sites. In step III, a bounce-back scheme is applied to all three particles that have crossed the solid wall by inverting their directions. In step IV, the particles propagate along their new directions at time $t + \Delta t$. This procedure can be described by the following formulas:

$$\begin{aligned} f_6(\mathbf{x}, t + \Delta t) &= f_8(\mathbf{x}, t), \\ f_2(\mathbf{x}, t + \Delta t) &= f_4(\mathbf{x}, t), \\ f_5(\mathbf{x}, t + \Delta t) &= f_7(\mathbf{x}, t). \end{aligned}$$

For boundaries aligned with the grid coordinates, the no-slip condition provides a second-order accuracy of representing the viscous boundary layer phenomena. Non-aligned boundaries and curved boundaries can also be handled by no-slip conditions using an interpolation or extrapolation procedure.

3.3.4 Free-Slip Condition

The free-slip condition is useful for simulating smooth walls where the tangential components of the flow velocities at the wall are untouched and the effects of the viscous

boundary layers are minimized. It is also useful in the case of representing a vertically symmetric 2D system by a half plane, where the axis of symmetry is numerically identical to a free-slip condition.

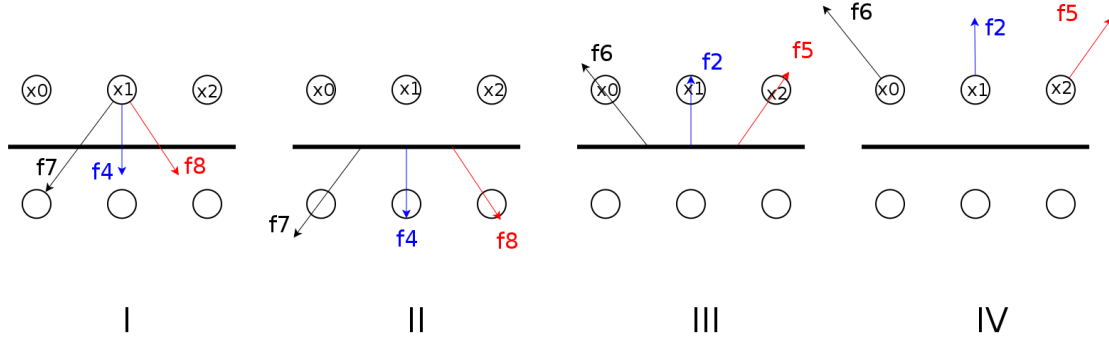


Figure 3.5 Free-slip condition.

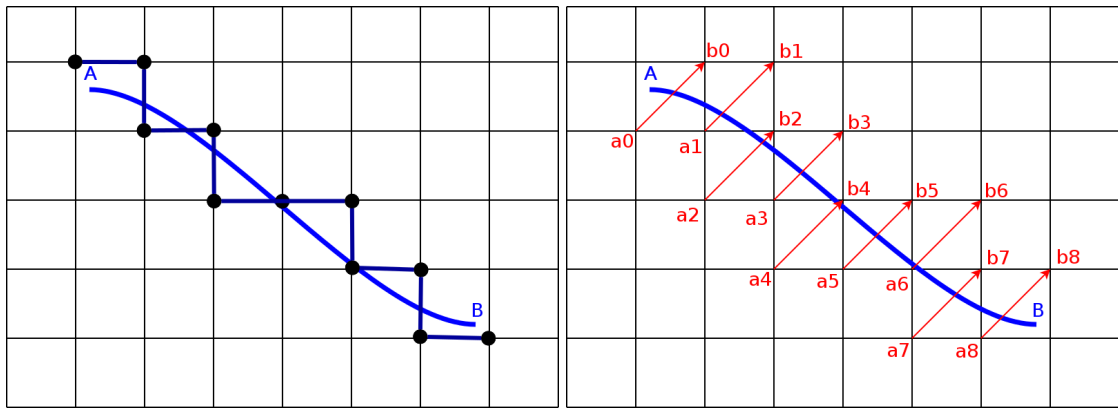
Figure 3.5 depicts the procedure of the free-slip condition in four steps. Step I shows the states of f_4 , f_7 and f_8 of a grid node x_1 at time t in the pre-streaming stage. In step II, the particles propagate and arrive at the solid boundary. In step III, the vertical components of the velocity are flipped while the horizontal components are unchanged. In step IV, the particles propagate in their new directions at time $t + \Delta t$ and arrive at new destinations. This procedure can be described by the following formulas:

$$\begin{aligned} f_6(\mathbf{x}_0, t + \Delta t) &= f_7(\mathbf{x}_1, t), \\ f_2(\mathbf{x}_1, t + \Delta t) &= f_4(\mathbf{x}_1, t), \\ f_5(\mathbf{x}_2, t + \Delta t) &= f_8(\mathbf{x}_1, t). \end{aligned}$$

3.3.5 Curved Boundary

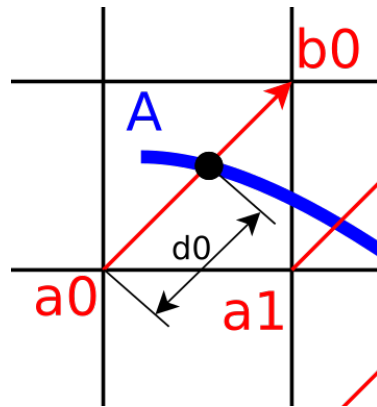
The no-slip boundary condition works for either simple straight walls or arbitrarily shaped walls. However, the implementation can be tricky when the boundary is a non-aligned wall or an arbitrary curved wall.

The simplest curved boundary scheme uses a staircase to approximate the curved wall \overline{AB} , as shown in Fig. 3.6(a). The staircase can be either defined on the lattice grids using the explicit boundary scheme or represented by a set of line sections using the implicit boundary scheme (which gives slightly better accuracy). The no-slip boundary



(a) Curve AB and the staircase (shown as an explicit boundary scheme).

(b) Crossing vectors for direction 5.



(c) Intersection point and crossing distance d_0 .

Figure 3.6 Curved boundary.

condition is implemented directly on the staircase. This scheme provides first-order accuracy and works well as long as the spatial resolution of the lattice is high enough.

For the case of complicated curved walls, it is time consuming to manually find all the boundary nodes shaping the staircase. A new searching procedure was developed in this research which can more efficiently find the curved boundary nodes in all directions. This procedure is exemplified for direction 5 in Fig. 3.6(b) and described in the following steps:

1. Find a rectangular lattice that completely encloses the curved wall and enumerate all the vectors for direction 5 inside the rectangular box.

2. Keep track of vectors crossing the curve \overline{AB} , such as $\overrightarrow{a_0b_0}, \overrightarrow{a_1b_1}, \dots, \overrightarrow{a_8b_8}$. A crossing vector is found if there is an intersection between the vector and the curve.
3. The boundary nodes can be derived from the intersection points. For example, for vector $\overrightarrow{a_0b_0}$, either point a_0, b_0 or the middle point of line $\overline{a_0b_0}$ can be defined as a boundary node for the no-slip boundary condition.

This procedure should be performed for all 8 directions. Practically, an arbitrary curved wall can be well approximated by a set of line-segments, where the length of each segment must be shorter than the spatial resolution of the lattice. Then, the problem of searching the intersection between a vector and a curve is reduced to searching the intersection between a vector and each line-segment of the curve, which is a very simple analytical geometry problem.

Essentially, other than the automatic searching procedure, this alternative scheme works in the same way as the simple staircase scheme. When the points of a_i or b_i are selected as the boundary nodes, the curved boundary is implemented as the explicit boundary scheme. If the middle points of the crossing lines are selected, the implicit boundary scheme is implemented, which gives slightly better accuracy.

To achieve second-order accuracy, the interpolation scheme proposed by Bouzidi et al. (2001) and Lallemand and Luo (2003) or extrapolation scheme proposed by Guo et al. (2002) can be used. For such a case, the distance measured from the end of the crossing vector to the intersection, depicted as d_0 in Fig. 3.6(c), is required.

3.3.6 Moving Boundary

A moving boundary condition can be implemented based on the curved boundary condition by incorporating the effects of interaction between the boundary wall and the fluid particles surrounding the boundary. To improve the accuracy, the fractional distance between the lattice nodes and the curved boundary should be handled by an interpolation or extrapolation procedure, and the effects of momentum transfer between the solid wall nodes and fluid nodes should be included. In Chpt. 5, the oscillating reed in the mouthpiece of a hybrid clarinet scheme is represented by a moving curved boundary.

3.3.7 Non-Reflecting Boundary

3.3.7.1 Ideal Non-Reflecting Boundary

In the context of computational acoustics / aeroacoustic simulations, an ideal non-reflecting boundary allows the aerodynamic field to pass freely, such that the incident acoustic waves coming from any angle and carrying any frequency components or any transient features are absorbed completely. Therefore, the numerical simulation is not contaminated by any wave reflections.

The effectiveness of a non-reflecting boundary can be evaluated by its frequency-dependent transmission and reflection coefficients. This can be explained intuitively in the case of 1D plane wave propagation. If the complex pressure amplitude of the incident wave is P_i , that of the reflected wave P_r , and that of the transmitted wave P_t , then the pressure transmission and reflection coefficients are defined as:

$$T = P_t/P_i, \quad (3.31)$$

$$R = P_r/P_i. \quad (3.32)$$

When the plane wave reaches the interface of an ideal non-reflecting boundary, all of its components are transmitted and nothing is reflected, so $P_r = 0$ and $P_t = P_i$. Therefore, the transmission coefficient $T = 1$ and the reflection coefficient $R = 0$ at all frequencies.

Let's consider a cylindrical pipe with a characteristic impedance Z_1 that is terminated by an unknown boundary at an open end, where the impedance is defined as the ratio of acoustic pressure to acoustic volume flow at a particular frequency. The discontinuity is described by a change of acoustic impedance, say, Z_2 . The reflection coefficient at the boundary is given by (Kinsler et al., 2000):

$$R = \frac{Z_2 - Z_1}{Z_2 + Z_1}. \quad (3.33)$$

If there is an ideal non-reflecting boundary at the open end, $R = 0$, which implies $Z_2 = Z_1$, meaning the pipe terminated by an ideal non-reflecting boundary at one end is equivalent to a semi-infinite pipe. For a pipe with a uniform cross-sectional area S filled with a homogeneous fluid, the impedance is purely resistive, i.e. $Z_1 = \rho_0 c_s / S$. There-

fore, an ideal non-reflecting boundary condition should demonstrate a purely resistive impedance for all frequencies.

The characteristic impedance discussed above does not take the viscous and thermal losses into account. In a 1D lossy tube, the characteristic impedance is not purely resistive but related to r_v , the ratio of the tube radius a to the viscous boundary layer thickness, and r_t , the ratio of a to the thermal boundary layer thickness. Thus, in a simulation of a wave propagating in a lossy pipe, an ideal non-reflecting boundary should have some dissipation and dispersion behavior such that the thermoviscous losses are taken into account. This requirement also holds for the 2D and 3D cases.

3.3.7.2 Non-Reflecting Boundaries for LBM

The LBM is relatively new and robust non-reflecting boundary schemes are still in development. On the other hand, users of the direct numerical simulation (DNS), which is another one-step aeroacoustics simulation tool, have proposed many non-reflecting boundary schemes, such as the zero f gradients (ZFG) methods (Li et al., 2006), extrapolation method (EM) (Chen et al., 1996; Maier et al., 1996), the characteristic boundary conditions (Thompson, 1987, 1990; Giles, 1990), the perfectly matched layer method (PML) (Hu, 1996, 2001, 2005, 2006; Hu et al., 2006), the C^l continuous method (Loh, 2003) and the absorbing boundary condition (ABC) (Kam et al., 2006), etc. Some of the non-reflecting boundaries developed for the DNS can be extended to the LBM, while others may not be appropriate. One challenge of implementing open boundaries for the LBM scheme is that the macroscopic conditions, such as velocity and pressure, cannot be directly specified. Rather, they need to be converted into the distribution function f , which is not a trivial task.

Some of the non-reflecting boundaries that can be extended to the LBM are briefly introduced in the following paragraphs.

3.3.7.2.1 Zero f Gradients Methods (ZFG) This method is implemented by setting the gradient of the distribution function along the direction normal to the boundary to zero. Li et al. (2006) used this method in LBM simulations to calculate benchmark aeroacoustic problems and obtained acceptable agreement with the reference DNS solution. Najafi-Yazdi and Mongeau (2012) recently compared the ZFG with the PML in aeroacoustic simulations and found that boundaries using the ZFG scheme result in many

more reflections than that using the PML scheme.

3.3.7.2.2 Extrapolation Method (EM) and Filtering Method (FM) The extrapolation method is first proposed by Chen et al. (1996). In this scheme, the lattice Boltzmann model is treated as a special finite difference scheme of the kinetic equation for the discrete velocity distribution functions. An additional layer of sites is attached to the outside wall boundaries and the distribution functions are calculated by extrapolation in each time step before the streaming operations are performed. The extrapolation method can be arranged for either the distribution function f or its first gradient ∇f in all the directions, and can be used with a low-pass filter to reduce the high-frequency reflections.

3.3.7.2.3 Perfectly Matched Layer (PML) The PML technique was first proposed for the Maxwell's equation in the field of electromagnets (Berenger, 1994). Then it was extended to the linearized Euler equations (Hu, 1996, 2001, 2005) and the nonlinear Euler and Navier-Stokes equations (Hu, 2006; Hu et al., 2008). More recently, two groups, Najafi-Yazdi and Mongeau (2012) and Craig (2011), applied the PML technique to the LBGK model in the presence of a non-zero mean flow. In their models, an additional PML layer is attached to the outer boundary of the LBM lattice. The outgoing waves decay exponentially in the PML layer before they reach the outer boundaries.

3.3.7.2.4 Absorbing Boundary Condition (ABC) The concept of the ABC was first extended from the DNS to the LBM by Kam et al. (2006). It is implemented by adding an extra damping term to the governing equation of the LBGK-SRT model:

$$\frac{\partial f}{\partial t} + \xi \cdot \nabla f = -\frac{1}{\tau}(f - f^{eq}) - \sigma(f^{eq} - f^T), \quad (3.34)$$

where f^T are the target distribution functions, $\sigma = \sigma_m(\delta/D)^2$ is the absorption coefficient, where σ_m is a constant, D is the width of the absorbing buffer region and δ/D is the normalized distance measured from the beginning of the buffer zone. The ABC scheme creates an asymptotic transition towards a target flow defined by the target distribution function f^T , which reduces the amplitude of outgoing waves in the transition buffer and minimizes the reflected waves. The performance of the ABC scheme is influ-

enced by the value of both σ_m and D . Normally, a bigger D results in better absorption effects. The role of σ_m is more tricky, where $\sigma_m = 0.3$ is optimum but a higher value does not necessarily improve the results.

Compared to other options, the ABC scheme is robust, effective, easy to implement and provides second-order accuracy. It can also be used together with other non-reflective boundary conditions for a better performance. However, the ABC boundary does not perform as well for obliquely incident waves and suffers from wave reflections due to the difference between dispersion properties, because the governing equations of the absorbing zone do not match the interior lattice Boltzmann domain.

Due to its simplicity and efficiency, the ABC scheme has been chosen as the non-reflecting boundary of the LBGK models used in this thesis. An interesting bonus of the ABC scheme is that a source flow can be generated by simply assigning a non-zero target velocity. This method has been used to generate a mean flow or a pressure source in our simulations in the forthcoming chapters.

3.4 Numerical Procedure of LBGK model

The numerical procedure of the D2Q9 LBGK model, which is used exclusively in this study, consists of an initialization stage, an iterative process and a data probing process. During the initialization stage, the fluid variables and distribution functions are initialized according to the simulation parameters. Also, some intermediate boundary data is generated based on the geometries used in the simulation. The iterative process executes three key steps in a long *while-loop*, which include streaming, collision and the boundary treatments. Finally, a probing scheme is implemented at the end of the iterations to obtain the simulation results, which for a given simulation could be either the time histories or snapshots of the spacial distribution of the fluid variables. Once the iterative process is finished, the probed data is saved for further post-processing or visualizations.

Both the SRT and MRT collision schemes have been implemented in the LBGK model, namely the LBGK-SRT and LBGK-MRT models. The MRT model offers improved numerical stability in the situation involving a very low viscosity and / or a non-zero mean flow. When the numerical stability is not an issue, the SRT model can be used, which is about 20% faster than the MRT model.

3.4.1 Procedure of LBGK-SRT Model

```

1 Load simulation parameters;
2 Initialization of  $\rho, u, f, f^{eq}$ ;
3  $n = 0$ ;
4 while  $n \leq N_{sim}$  do
5   Streaming;
6   Boundary conditions;
7   Update  $\rho$  and  $u$  from  $f$ ;
8   Update  $f^{eq}$  from  $\rho$  and  $u$ ;
9   SRT Collision;
10  if  $n \% N_{pb} == 0$  then
11    | Save fluid variables;
12  end
13   $n = n + 1$ 
14 end

```

Procedure 1: LBGK-SRT model.

The LBGK-SRT model is described by the pseudo code in Procedure 1, where n is the index of iteration, N_{sim} is the total number of iterations and N_{pb} is the period of data probing.

In the beginning, the simulation parameters are loaded into the model, including the relaxation parameters, dimensions of the lattice, geometry parameters, etc.

The initial states of the space-dependent fluid properties (density ρ and velocity \mathbf{u}) are normally known. The value of the equilibrium distribution function \mathbf{f}^{eq} in each direction is calculated by Eq. 3.22, or more specifically Eq. 3.23 for the D2Q9 model. In the simplest case, i.e., a system with steady or quasi-steady flow and no specific initial excitation, the initial states of the distribution function \mathbf{f} can be approximated by its equilibrium states, i.e., $\mathbf{f}(t = 0) = \mathbf{f}^{eq}(t = 0)$.

The iterations start right after the initialization stage. The index of iterations n is set to zero at the beginning. In the streaming step, \mathbf{f} at every site propagates to all of the neighboring sites in a unity time step. The streaming process is formulated by

$$\mathbf{f}_i(\mathbf{x} + \mathbf{e}_i \Delta t, t + \Delta t) = \mathbf{f}_i(\mathbf{x}, t). \quad (3.35)$$

During the streaming process, the traveling particles may encounter various bound-

aries, such as solid walls, slippery walls, axis-symmetric boundaries and open boundaries, etc. In the boundary treatment stage, all the sites that contain particles crossing boundaries in any of the 8 directions are identified as *contaminated sites*. For static boundaries, the contaminated sites are identified only once at the initialization stage. For moving boundaries, the contaminated sites must be identified at each iteration. All of the contaminated distribution functions in the identified sites are recovered by boundary algorithms based on specific boundary conditions.

After the boundary treatment, the density and velocity fields are recovered from the local distribution functions on each site, according to Eqs. 3.5 and 3.6. The equilibrium distribution function f^{eq} on each site is updated by Eq. 3.23.

The SRT collision operator is derived from the BGK evolution equation (Eq. 3.20 or 3.7), which is written as:

$$\mathbf{f}(\mathbf{x}, t)_{post} = \mathbf{f}(\mathbf{x}, t)_{pre} - \frac{1}{\tau}(\mathbf{f}(\mathbf{x}, t)_{pre} - \mathbf{f}(\mathbf{x}, t)^{eq}), \quad (3.36)$$

where \mathbf{f}_{pre} and \mathbf{f}_{post} are distribution functions before and after the collision operator, respectively.

The fluid variables are probed and saved at the interval of N_{pb} after the collision stage. The post-collision distribution functions $\mathbf{f}(\mathbf{x}, t)_{post}$ are fed into the next streaming operator and the iteration continues.

3.4.2 Procedure of LBGK-MRT Model

The pseudo code in Procedure 2 describes the LBGK-MRT model, which is different from the LBGK-SRT model only in two aspects. First, a number of variables in the moment space are initialized before the iterative loop, including the transformation matrix \mathbf{M} and \mathbf{M}^{-1} , diagonal matrix \mathbf{S} as well as zero-filled containers of distribution functions \mathbf{m} and \mathbf{m}^{eq} . Second, during the iteration process, the collision operator is performed in the moment space, so the distribution functions f and f^{eq} are transformed into the moment space before the collision and transformed back to the velocity space afterwards. Apart from that, both models share the same code for the remaining parts.

```

1 Load simulation parameters;
2 Initialization of  $\rho, u, f, f^{eq}$ ;
3 if Using MRT then
4   | Initialization of  $M, M^{-1}, S, m, m^{eq}$ ;
5 end
6  $n = 0$ ;
7 while  $n \leq N_{sim}$  do
8   | Streaming;
9   | Boundary treatments.;
10  | Update  $\rho$  and  $u$  from  $f$ ;
11  | Update  $f^{eq}$  from  $\rho$  and  $u$ ;
12  | if Using MRT then
13    | Transform  $f$  to  $m$ ;
14    | Transform  $f^{eq}$  to  $m^{eq}$ ;
15    | Collision in moment space;
16    | Transform  $m$  to  $f$ ;
17  | end
18  | if  $n \% N_{pb} == 0$  then
19    | Save fluid variables;
20  | end
21  |  $n = n + 1$ 
22 end

```

Procedure 2: LBGK-MRT model.

3.4.3 Software Implementation

At the prototype stage, both the SRT and MRT models were implemented on a desktop computer CPU using the open-source *Python/NumPy* software package, which provides functionalities and an interactive computing shell comparable with common commercial software like *MatLab*. The data probed from the simulation was saved in NumPy's N-dimensional array class called *ndarray*. The post-processing code was also developed in the Python/NumPy environment, and the visualizations were produced using the *matplotlib* module.

At the workhorse stage, the SRT model and the MRT model were re-implemented using a GPU-accelerated parallel computation technique, which will be discussed in the next section.

3.5 Parallel LBGK Model on GPU

The LBM is expensive in terms of both computational cycles and memory consumption. Fortunately, the LBM is well suited for parallel implementation due to its simple and explicit algorithm and the feature that information coupling only occurs among the nearest neighbor cells.

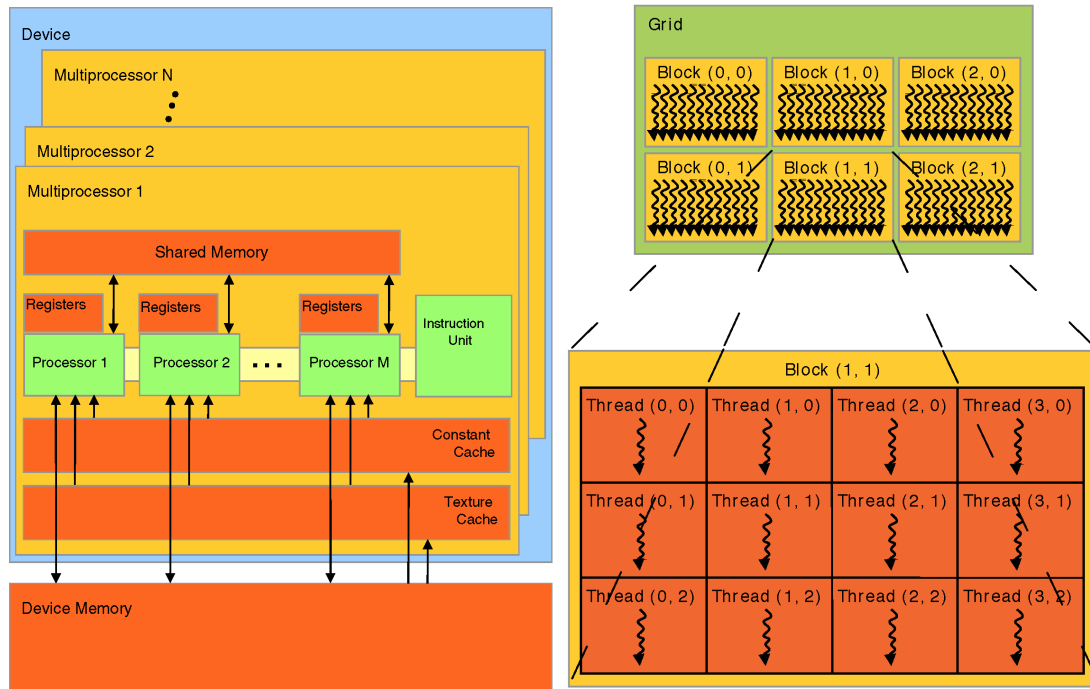
The Graphics Processing Unit (GPU) is a dedicated computational component that was originally designed to rapidly manipulate computer graphics and process image signals. Over the last decade, GPUs have been also used as general-purpose highly parallel processors for high-performance scientific computations.

There are some drawbacks of GPU accelerated computations. Some complex data structures are difficult for the GPU due to the lack of pointers. GPU computation may be inefficient for algorithms with complex control flows. In addition, GPU computation is restricted by the relatively small on-board memory. Fortunately, the data structures and the program control flow of a LBGK model are usually simple, and the on-board memory of a modern GPU is large enough for a reasonable lattice size of a LBGK model.

3.5.1 Previous Work

Li et al. (2003) accelerated the computation of a LBGK model with the grid size of 128^3 on a single nVidia GeForce4 GPU. In the next year, the same group (Fan et al., 2004) scaled a bigger 3D LBGK model onto a GPU cluster equipped with 32 nodes by decomposing the LBM lattice space into sub-domains, each of which is a 3D block, and each GPU node computes one sub-domain. Their model consisted of a $640 \times 320 \times 80$ lattice simulating the transport of airborne contaminants in a small city area. Their simulation speed was 0.317 seconds per iteration, which is a speed-up of about 4.6 times compared to a CPU cluster running the same model. Since then, as the newer, faster and cheaper GPUs have become available, many researchers have successfully used the combination of GPU and parallel LBM as a valid tool for simulating fluids and developed various optimization methods (Ryoo et al., 2008; Tölke, 2010; Kuznik et al., 2010; Obrecht et al., 2011; Rinaldi et al., 2012; Habich et al., 2013).

In the present study, both the SRT and MRT models discussed in Sec. 3.4 were re-implemented and parallelized on a single nVidia GeForce GTX 670 GPU using the PyCUDA language (Klößner et al., 2012). These models were used in various simulations



(a) nVidia CUDA hardware architecture.

(b) CUDA programming model.

Figure 3.7 nVidia CUDA programming model. (source nVidia).

presented in Chpts. 4 and 5.

3.5.2 GPU Programming Model

Number of SMs	7
Number of SPs per SM	192
Total number of SPs	1344
Registers per SM	65536
Maximum number of threads per SM	2048
Maximum number of threads per block	1024
Shared memory per block	49152 bytes
Global memory	4096 MBytes
Processing Power (GFLOPS)	2459.52 (32-bits), 102.48 (64-bits)

Table 3.2 Features of the nVidia GeForce GTX 670.

We now briefly present the hardware architecture and the parallel programming

model used to accelerate the LBGK models. CUDA, or Compute Unified Device Architecture, is a parallel GPU computing specification and programming model first released by nVidia in early 2007. Figure 3.7(a) shows the main aspects of a CUDA-compatible GPU. A GPU consists of a scalable array of multithreaded Streaming Multiprocessors (SMs). Each SM contains an array of Stream Processor (SP) cores and a shared memory which is accessible to SPs on the same SM. Each SP contains a fully pipelined integer arithmetic logic unit (ALU) and a floating-point unit (FPU) that executes one integer or floating-point instruction per clock cycle. A device memory, usually named the global memory, is accessible by all SPs on the device (the GPU) and the host (the CPU). Figure 3.7(b) shows the CUDA programming model. A GPU is designed to execute hundreds or thousands of lightweight threads concurrently. A thread executes a function called the kernel that contains the instructions to be run in parallel on the GPU. Threads are grouped into blocks and grids, and are indexed by two structures, `blockIdx` and `threadIdx`, each containing the three fields `x`, `y` and `z`. When a kernel is invoked by the CUDA program on the host CPU, a large amount of threads are automatically distributed to multiprocessors with available execution capacity. This process is automatically managed by an architecture called SIMT (Single-Instruction, Multiple-Thread), such that a compiled CUDA program can execute on any CUDA-enabled GPU with any number of multiprocessors.

Table 3.2 gives some of the features of the nVidia GeForce GTX 670 processor used in this study. The overall processing power of a GPU is evaluated by its GFLOPS, or 10^9 floating-point operations per second. The GTX 670 GPU performs around 102.48 GFLOPS in double precision (64-bit) calculations, which is 24 times lower than the performance in single precision (32-bit) calculations. Another issue is that a double precision number occupies double size in the memory compared to a single precision number. Because of this, we decided to use single precision calculations exclusively in the GPU parallel model for much better performance (simulation time) and half the memory consumption (maximum lattice cells allowed in the LBGK model). The accuracy of the GPU model using single precision floating-point numbers will be validated in Chpt. 4 as well as in Appendix A.

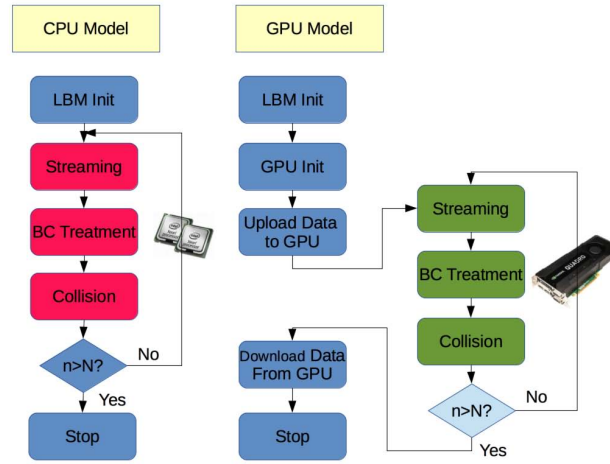


Figure 3.8 Flowcharts of CPU model and GPU model.

```

1 Load simulation parameters;
2 Initialization of  $\rho, u, f, f^{eq}$ ;
3 if Using MRT then
4 | Initialization of  $M, M^{-1}, S, m, m^{eq}$ ;
5 end
6 Upload data to GPU;
7  $n = 0$ ;
8 while  $n \leq N_{sim}$  do
9 | LoopOnGPU();
10 | if  $n \% N_{pb} == 0$  then
11 | | Download data (fluid variables) from GPU ;
12 | end
13 |  $n = n + 1$ 
14 end

```

Procedure 3: Parallel LBGK model: procedure on CPU. In the initialization stage, data is uploaded from CPU to GPU. For each iteration in the loop stage, the computationally intensive GPU function is invoked by a PyCUDA command on CPU and data is exchanged between CPU and GPU using a set of PyCUDA commands on CPU.

```

1 Def LoopOnGPU():
2 Streaming;
3 Boundary treatments.;
4 Update  $\rho$  and  $u$  from  $f$ ;
5 Update  $f^{eq}$  from  $\rho$  and  $u$ ;
6 if Using MRT then
7   | Transform  $f$  to  $m$ ;
8   | Transform  $f^{eq}$  to  $m^{eq}$ ;
9   | Collision in moment space;
10  | Transform  $m$  to  $f$ ;
11 else
12  | SRT Collision;
13 end

```

Procedure 4: Parallel LBGK model: procedure on GPU.

3.5.3 Software Implementation

In the CUDA Toolkit provided by nVidia, the underlying programming language is CUDA C, which consists of extensions to the standard C language and a runtime library, which allows the developer to define a kernel as a C function and specify the grid and block dimension each time the function is called. Many other language bindings have been developed by third parties, which generally provide easy accesses to nVidia's CUDA API.

Because our LBGK models were completely programmed in Python, we selected one of the open-source Python bindings of CUDA, PyCUDA (Klöckner et al., 2012), as the development tool to implement the parallel LBGK models on the GPU. Some PyCUDA features that particularly suit our needs include the GPU run-time code generation (RTCG), a complete access to the CUDA API and a NumPy-like array class called *gpuarray*. All functions in our CPU LBGK models written in Python can be seamlessly re-used in the GPU model, and the *ndarray* data objects on CPU can be switched with the *gpuarray* objects on GPU.

The GPU LBGK model is largely derived from the CPU LBGK model. Thanks to the object-oriented paradigm of Python, a large part of the code in the CPU model can be re-used in the GPU model. Figure 3.8 depicts the bare-bones flow chart of the CPU Model alongside the GPU Model. We parallelized the most computationally intensive

operators on the GPU, including streaming, boundary treatment and collision (SRT and MRT), and added the necessary code for GPU initialization and data transfer between CPU and GPU, where almost all of the LBM initialization code are reused. The procedures on the CPU and the GPU are described by the pseudo code in Procedure 3 and 4, respectively. The procedures in the *while-loop* of the CPU model are replaced by a single function *LoopOnGPU()*, which consists of a series of kernel functions performing the parallelized computations of streaming, boundary treatments, updating distribution functions and collisions on the GPU.

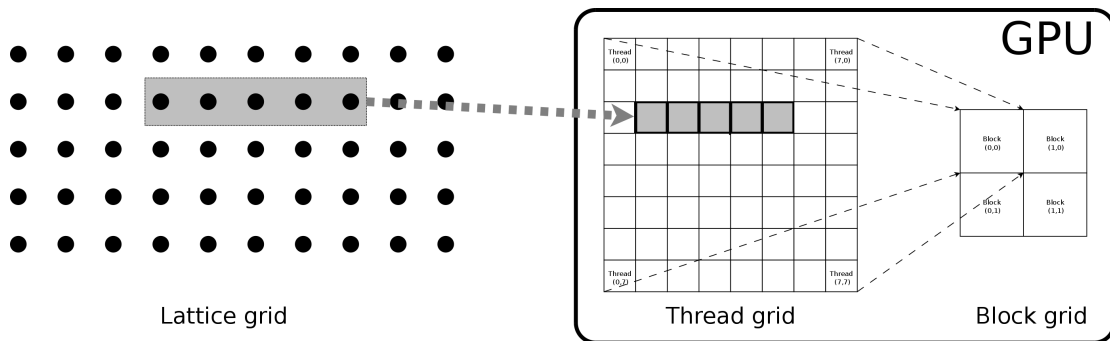


Figure 3.9 Mapping lattice grid to thread grid on the GPU.

Figure 3.9 depicts how the lattice grid is mapped to the thread grid on the GPU. Each node of the lattice is linked to one thread on the multiprocessor, which executes the same kernel functions implementing the LBGK operators during the main *while-loop*. The number of threads per block is set in order to obtain the maximal number of concurrent threads running on each multiprocessor.

We use a rather simple approach that all of the fluid variables (distribution functions, density and velocities) are saved in the global memory, which is big and slow, while the simulation parameters and coefficients (such as the relaxation parameter, the velocity weights, etc) are saved in shared memory, which is small but fast. In the case of the collision operator, the parallelization is straightforward because all computations occur locally and there is no information exchange between nodes. In the case of the streaming operator, there is some information exchange between neighboring cells, so a certain number of access to the global memory in the kernel function is unavoidable. The computation of the boundary treatment of the static curved walls requires a lot more overhead since a node is influenced by several neighboring nodes. That said, the

kernel function is optimized to some extent because the boundary data (i.e., the contaminated nodes and the distances between nodes and walls on all 8 directions) has been pre-calculated in the initialization stage in the CPU and copied to the global memory of the GPU. The parallelization of the moving curved wall and the distributed reed model used in Chpt. 5 requires further attention because the boundary data and the reed's status need to be updated on the fly at every iteration.

	Time per iteration	Time per 100000 iterations
CPU model	1.06 (seconds)	29.44 (hours)
GPU model	0.053 (seconds)	1.47 (hours)

Table 3.3 Performance of CPU model compared to GPU model (a D2Q9 LBGK model with a 1000×1000 lattice).

Table 3.3 compares the performances of a D2Q9 LBGK model with a 1000×1000 lattice running on a CPU and a GPU. A speedup ratio above 20 is achieved for the GPU model, which is an advantageous feature particularly useful for computationally intensive simulations of the hybrid clarinet model presented in Chpt. 5.

One of the major limiting factors of the GPU-accelerated computations in general is the high latency associated with the data transfer between the global memory on the device and the memory on the host. In order to minimize this negative impact in our GPU model, the data transfer between CPU and GPU during the main loop only occurs at the interval of N_{pb} times the execute period of the function *LoopOnGPU()*. The performance of the system might be further improved using optimization techniques, such as those presented in (Ryoo et al., 2008; Tölke, 2010; Kuznik et al., 2010; Obrecht et al., 2011; Rinaldi et al., 2012; Habich et al., 2013). However, such optimizations were beyond the desired scope of this thesis research and the achieved performance level of the GPU models was satisfactory for our needs.

Chapter 4

Numerical Modeling of Acoustic Systems with Static Boundaries

4.1 Overview

When compared to traditional numerical techniques, there has been less investigation on the use of the lattice Boltzmann method (LBM) to solve acoustic problems, though several interesting studies have been reported. For example, Buick et al. (1998, 2000) investigated sound waves in an unbound fluid using a two-dimensional lattice Boltzmann scheme with a Bhatnagar-Gross-Krook (BGK) approximation (Bhatnagar et al., 1954). Later on, Buick et al. (2011) investigated the jet formation at a pipe end. Viggen (2011) investigated the effects of viscosity on spatially damped acoustic waves using the BGK scheme. More recently, Viggen (2013) implemented acoustic multipole sources in an acoustic field with zero viscosity in the LBM scheme by including a source term and using a regularized collision operator. In aeroacoustic problems involving the interaction between the flow and the acoustic fields, Li et al. (2006) simulated wave propagations in the presence of compressible flow regimes. Kam et al. (2010) simulated the scattering of acoustic waves and Li and Shan (2011) proposed a LBM scheme for adiabatic acoustic phenomena. Lew et al. (2010) simulated the axisymmetric subsonic turbulent cold jet issuing from a pipe and its influence on sound radiation. Subsequently, Habibi et al. (2011) added a heat transfer model to the LBM scheme to study heated jets.

For the case of acoustic transmission and radiation of a static axisymmetric waveguide immersed in a stagnant fluid domain, da Silva (da Silva and Scavone, 2007; da Silva,

2008; da Silva et al., 2009) provide excellent results based on lattice Boltzmann technique, where the effect of the cold subsonic mean flow as well as the horn extension attached at the pipe end is also extensively investigated. The work of da Silva demonstrates that a BGK lattice Boltzmann model can be used to accurately predict the acoustic propagation of a radiating axisymmetric waveguide.

In Chpt. 3, we have discussed the lattice Boltzmann model and its CPU serial implementation on Python/NumPy platform as well as its GPU parallel implementation on a PyCUDA platform. Both the Python and the PyCUDA implementations have been programmed independently by the author from scratch, where the BGK-SRT LBM scheme is consistent with the Matlab implementation used by da Silva (2008). These LBM models are developed to address acoustic problems involving complex static boundaries or dynamic boundaries and carrying a quiescent or non-zero mean flow. In general, the GPU model is preferred because it is much faster than the CPU model. The running speed is especially important for problems involving a very long simulating time. However, the lattice size of the GPU model is limited by a rather small on-board memory and the accuracy might be slightly compromised by the 32-bit representation of floating-point numbers used on a GPU. The latter issue need to be scrutinized for computations involving weak acoustic signals usually found at distances far from an acoustic source.

The first objective of this chapter is to verify the LBM code developed in this study by simulating acoustic systems with static boundaries, i.e., to address the benchmark problem of sound transmission and radiation of unflanged pipes as well as horns, including the measurement of reflection coefficient R , the length correction l/a and the radiation directivity $G(\phi)$. The simulation conditions will be limited to the radiation of normal (planar) modes and low compressibility regimes. For this reason, the numerical scheme used in this paper is based on an isothermal model represented in a two-dimensional axisymmetric scheme. Furthermore, the reliability and applicability of the GPU LB model on acoustic systems with complicated curved boundaries in the presence of a relatively high speed fluid flow is verified. For this specific purpose, two whistles are modeled and their aeroacoustic behavior is investigated numerically. Moreover, the accuracy of the GPU LB model at various Reynolds numbers and grid resolution, which has been benchmarked against the analytical results of a 2D Poiseuille flow, is presented in Appendix A.

The second objective is to use the verified LB model to conduct further investigations

of phenomena for situations where the analytical solutions or experimental results are either unavailable yet or very difficult to obtain.

This chapter is structured as follows. Section 4.1 gives the general introduction. Section 4.2 discusses the numerical investigation of the acoustic transmission of unflanged thin-wall cylindrical pipes in terms of reflection coefficient and length correction. Section 4.3 investigates the external acoustic radiation field of the same system discussed in Sec. 4.2. The effect of the non-zero mean flow and the horn extension at the open end of the axisymmetric waveguide will be investigated as well. Section 4.4 investigates whistles comprising a complicated curved boundary measured from realistic objects, where the MRT technique is used to improve the stability of the numerical simulation in the condition of low viscosity and high jet speed, which is also commonly found in the numerical simulation of clarinet-like woodwind instruments. Section 4.5 provides a conclusion and suggestions for further investigations.

4.2 Acoustic Transmission in Pipes

4.2.1 Introduction

The cylindrical pipe is widely used in woodwind instruments. The propagation of plane acoustic waves in axisymmetric pipes and their reflection at open ends is a classical problem, and has been studied analytically and experimentally by many researchers. The sound wave propagating to the output end is partly transmitted into the external space and partly reflected back into the bore. The ratio of the magnitude of the reflected wave pressure p^- to the incident wave pressure p^+ measured at the output end ($x = L$) is defined as the *reflection coefficient*

$$R \triangleq \frac{p^-}{p^+}, \quad (4.1)$$

from which the *radiation impedance* can be derived as:

$$Z_r = Z_c \left(\frac{1 + R}{1 - R} \right), \quad (4.2)$$

where $Z_c = \rho c_s / S$ is the *characteristic acoustic impedance*, ρ is the density of air, c_s is the speed of sound and S is the cross-section area of the pipe.

The complex reflection coefficient can also be expressed as the product of its magnitude $|R|$ and a phase term:

$$R = -|R|e^{-2jkl(\omega)}, \quad (4.3)$$

where $k = \omega/c_s$ is the wavenumber and $\omega = 2\pi f$ is the angle frequency. The phase term $2kl(\omega)$ is related to the inertia of the acoustic flow when it interacts with the surrounding fluid at the open end, where the complex and frequency-dependent parameter l , known as the *length correction*, extends the equivalent length of the pipe and makes the resonance frequencies of the cylindrical pipe lower. The length correction plays a role in the intonation of woodwind instruments since even subtle variations of the resonant frequency, i.e. $\Delta f = O(-1)$, are perceptually obvious. For convenience, $l(\omega)$ is simply noted as l .

The reflection coefficient and the length correction are strongly influenced by the geometrical characteristics at the open end. They have become an interesting subject to many musical acoustics researchers since both the playability and the intonation of the woodwind instruments are influenced by the radiation impedance, which is just another expression of the reflection coefficient. The real part of Z_r is related to the dissipation of acoustic energy (resistive). In this case, the energy is lost through transmission. The imaginary part is related to the accumulation of energy either by kinetic or potential energy (reactive). In the case of an open end, the reactive phenomena is related to the inertia of air in the open end but also with the elastic property of the same mass of air at the open end.

The derivations of the analytical predictions of R at the open end of a cylindrical pipe are usually based on some simplified boundary conditions which are relatively easy to analyze. The theoretical radiation impedance Z_r at the end of a pipe of radius a with an infinite plane baffle are given as (Rayleigh and Strutt, 1896; Olson, 1957; Fletcher and Rossing, 1991):

$$Z_r = A + jB, \quad (4.4)$$

where the acoustic resistance A and acoustic reactance B in terms of the dimensionless quantity ka (also is called the *Helmholtz number*) are given by:

$$A = Z_0 \left[\frac{(ka)^2}{2} - \frac{(ka)^4}{2^2 \cdot 3} + \frac{(ka)^6}{2^2 \cdot 3^2 \cdot 4} - \dots \right] \quad (4.5)$$

and

$$B = \frac{Z_0}{\pi k^2 a^2} \left[\frac{(2ka)^3}{3} - \frac{(2ka)^5}{3^2 \cdot 5} + \frac{(2ka)^7}{3^2 \cdot 5^2 \cdot 7} - \dots \right]. \quad (4.6)$$

For the case of a flanged pipe in the absence of mean flow, Norris and Sheng (1989) give the approximation of the modulus $|R|$ and the dimensionless length correction l/a over the frequency range ($0 < ka < 3.8$) as:

$$|R| = \frac{1 + 0.323ka - 0.077(ka)^2}{1 + 0.323ka + 0.923(ka)^2} \quad (4.7)$$

and

$$l/a = \frac{0.82159 - 0.49(ka)^2}{1 - 0.46(ka)^3}, \quad (4.8)$$

respectively.

For the case of an unflanged thin wall pipe in the absence of mean flow, Levine and Schwinger (1948) give the first exact solution of the analytical sound propagation model in the form of an integral equation based on the Wiener-Hopf technique. For the case of a pipe with a finite wall thickness, Ando (1968, 1969) propose to use the outer radius of the pipe instead of the inner radius for the value of a . The following equations are the results given by Levine and Schwinger (1948) and corrected by Ando (1968).

The modulus of the reflectance at the open end is given by:

$$|R| = \exp \left\{ -\frac{2ka}{\pi} \int_0^{ka} \frac{\tan^{-1}(-J_1(x)/N_1(x))}{x[(ka)^2 - x^2]^{0.5}} dx \right\}. \quad (4.9)$$

The dimensionless length correction l/a is given by:

$$l/a = \frac{1}{\pi} \int_0^{ka} \frac{\log \pi J_1(x) [(J_1(x))^2 + (N_1(x))^2]^{1/2}}{x[(ka)^2 - x^2]^{1/2}} dx + \frac{1}{\pi} \int_0^\infty \frac{\log[1/(2I_1(x)K_1(x))]}{x[x^2 + (ka)^2]^{1/2}} dx. \quad (4.10)$$

Norris and Sheng (1989) provide a simple close-form expression of the modulus $|R|$ and length correction l of an unflanged pipe over the frequency range $0 < ka < 3.8$, which is an approximation of Levine and Schwinger's rather complicated solution:

$$|R| = \frac{1 + 0.2ka - 0.084(ka)^2}{1 + 0.2ka + 0.416(ka)^2} \quad (4.11)$$

and

$$l/a = \frac{0.6133 + 0.027(ka)^2}{1 + 0.19(ka)^2}. \quad (4.12)$$

In the low frequency limit, as $ka \rightarrow 0$, the reflection coefficient $|R| = 1$, and the dimensionless length correction l/a is 0.82159 for a flanged pipe and 0.6133 for an unflanged pipe, respectively. The relation of the length correction l and the resonance frequencies of a closed-open pipe, which influences the intonation of a woodwind instrument, is given by

$$f_n = \frac{(2n + 1)c_s}{4(L + l)}, \quad (4.13)$$

where $n = 1, 2, 3, \dots$.

Because of the thermoviscous losses at the pipe walls, the propagation of sound waves in a pipe is dissipative. Kirchhoff (1868) shows that, for a homogenous medium in the absence of a mean flow, the effect of losses can be taken account by using a complex wavenumber

$$K = \frac{\omega}{c_s} \left[1 + \frac{1-j}{\sqrt{2}s} \left(1 + \frac{\gamma-1}{\xi} \right) - \frac{j}{s^2} \left(1 + \frac{\gamma-1}{\xi} - \frac{\gamma(\gamma-1)}{2\xi^2} \right) \right], \quad (4.14)$$

where γ is the specific heat ratio, $\xi^2 = \mu C_p / \kappa_{th}$ is the Prandtl number, μ is the dynamic viscosity, C_p is the specific heat coefficient, κ_{th} is the thermal conductivity, $s = a\sqrt{\rho_0\omega/\mu}$ is the shear wavenumber and a is the pipe radius. The negative imaginary part of the complex wavenumber represents the contribution of the damping effect. Equation 4.14 indicates that the thermoviscous losses becomes large for a pipe with a very small radius a that at the same order of magnitude as the acoustic viscous shear layer. That happens in very narrow capillar tubes or very low frequencies. Inside the bore of a woodwind instrument, where the radius is much larger compared to a capillary tube, the thermoviscous losses are not particularly significant.

For a pipe carrying a non-zero subsonic mean flow, the reflection coefficient and the length correction at the open end are strongly influenced by the flow speed, (Munt, 1990; Peters et al., 1993), which is measured by the *Mach number* $M = U_0/c_s$, where U_0 is the mean volume flow divided by the pipe cross-sectional area πa^2 . The problem involving the effects of mean flow is also commonly characterized by two other parameters: the *mean flow Strouhal number* $Sr_0 = \omega a / U_0 = ka / M$ and the *acoustic Strouhal number* $Sr_{ac} =$

$\omega a/u'$, where u' is the amplitude of the acoustic velocity at the open end of the pipe.

The early studies on the acoustic transmission through the open end of a cylindrical pipe carrying a mean flow include the work of Carrier (1956) and Lansing et al. (1970) on the uniform flow problem, that is the flow is the same both inside and outside the pipe, where a simple modification of Levine and Schwinger's technique on the pipe in the absence of a mean flow has been used. For the problem of the flow mismatch between the ambient fluid surrounding the open end and the jet issuing from the open end, the first investigations were made by Mani (1973) for a two-dimensional duct and by Savkar (1975) for a cylindrical duct, respectively. However, their solutions are not exact and the effect due to the instabilities of the jet shear layer is not taken into account.

The exact solution of the linear analytical model of the sound transmitting through the open end of a cylindrical pipe in the presence of a subsonic flow issuing into the ambient fluid is given by Munt (1977, 1990). His model assumes that a uniform flow is separated from the ambient fluid (stagnant or co-flowing) by an infinitely thin cylindrical shear layer, which is inherently unstable. The governing equations are built upon the velocity potential wave equation in cylindrical coordinates. The boundary conditions are based on several assumptions including a rigid pipe wall, continuous pressure across the vortex layer and continuity of particle displacement across the vortex layer. In addition, a full Kutta condition is imposed on the vortex layer near the edge of the pipe and the condition of causality is applied which implies that the sound field shall vanish for impulsive excitation before the source is switched on. Due to the acoustic perturbations, the shear layer oscillations grow exponentially as they are convected away from the edges of the pipe end. The instability plays an important role and the sound field generated by the instability is an inseparable part of the exact solution to the thin shear layer model. The full Kutta condition imposed at the trailing edge of the pipe implies a finite velocity and zero pressure fluctuations at the edges, and the acoustic disturbance in the jet can create a transfer of acoustic energy into kinetic energy in the jet vortex sheet. Also, the Kutta condition implies that the magnitude of the pressure reflection coefficient approaches a value of -1.0 for all Mach numbers if the Helmholtz number approaches zero. The full Kutta condition was discussed by Howe (1979) for the case of low Mach numbers and low frequency.

The mathematical solution of Munt's model is based on Fourier transform and Wiener-Hopf technique. By applying a Kutta condition and causality, a solution is presented

which possesses an instability wave term that dominates within a region of approximately 45 degrees to the downstream jet axis. A numerical evaluation of the far-field sound radiation pattern is given in (Munt, 1977), which is in good agreement with the experimental measurement by Pinker and Bryce (1976) for the case of a cold jet. In (Munt, 1990), the solution is extended to the inner sound field and the acoustic reflection coefficient at the open end of the jet pipe is given in the form of integral equations, where the numerical evaluation for the amplitude of the plane wave reflection coefficient $|R|$ as a function of ka at moderate to low jet Mach numbers ($0.01 \leq M \leq 0.6$) and low frequencies ($0 < ka < 1.5$) is given. Munt's prediction of $|R|$ is a significant improvement over the approximated theoretical prediction provided by Savkar (1975), and is in good agreement with many experimental results (Alfredson and Davies, 1970; Schlinker, 1977; Moore, 1977; Coelho, 1980; Allam and Åbom, 2006), where within a critical range of ka at low frequencies, the reflection coefficient $|R|$ reaches some peak values exceeding unity, which might be caused by the shear layer instability. As ka approaches zero, $|R|$ approaches unity for all values of M .

The model presented in (Munt, 1977) is expressed in terms of integral equations, which is rather complicated to solve. Rienstra (1983) and Cargill (1982a,b) provided a simple explicit formula approximating Munt's solution of far field patterns and reflection coefficient at the open end of the pipe for the case of small Strouhal numbers ($Str_0 = ka/M$) and low frequencies. Both of them discussed the two distinguish conditions that whether a full Kutta condition was imposed at the sharp edge of the pipe end or not. When the Kutta condition was imposed, a similar behavior for the magnitude of the reflection coefficient was found. But a significantly different behavior was found for the case of no Kutta condition, where the magnitude of the reflection coefficient in the low Strouhal number limit is equal to $|R| = (1 - M)/(1 + M)$, which means all of the acoustic energy at the pipe end is reflected back. In the low Mach number limit, Howe (1979) discussed the problem of sound radiations that depends on the imposition of a Kutta condition at the edge of the flat plate, which is an extension of (Munt, 1977). He found that when a Kutta condition is enforced, the vortices are convected with the mean flow and no sound is radiated. Cargill (1982b) predicted that $|R|$ exceeded unity at $Str_0 \approx \pi$, which was in accordance with the experimental results provided by Mechel et al. (1965) and Ronneberger (1967). More recently, Bierkens (2002) solved Munt's model numerically in terms of absolute amplitude of the reflection coef-

ficient for the plane wave case. Panhuis (2003) extended Bierkens' work and provided the numerical results of both the complex values of reflection coefficient and the phase of the reflection coefficient and the length correction for both the plane mode and higher modes, which cover different values of the Helmholtz number ka and Mach numbers ($0.01 \leq M \leq 0.6$).

Munt's theoretical prediction of the plane pressure reflection coefficient of a sharp-edged pipe carrying a subsonic mean flow has been verified experimentally by Peters et al. (1993) using a multi-microphone measurement technique for low frequencies ($ka < 0.3$) and low jet speeds ($M < 0.2$). He also confirmed the effect of the wall thickness (Ando, 1969), and the influence of vortex shedding due to high amplitude of the acoustic field (Disselhorst and van Wijngaarden, 1980). The first complete experimental validation of Munt's theoretical model is presented by Allam and Åbom (2006). Using a full plane wave decomposition procedure based on a multi-microphone arrangement and an overdetermination method in a nonlinear least-squares procedure, they accurately measured the values of the reflection coefficient, the length correction and the complex wavenumber associated with the damping of plane waves in the duct carrying a subsonic mean flow. The measured result of damping is in good agreement with the model by Dokumaci (1997) for $\delta_A^+ < 10$ and the model by Howe (1995) for $\delta_A^+ < 30$, respectively, where δ_A^+ is the normalized boundary layer thickness. They also found that the pressure reflection calculated using the maximum flow velocity instead of averaged flow velocity is in better agreement with Munt's prediction.

Numerical techniques have been successfully used to investigate sound transmission of pipes involving complex conditions for some decades. Compared to traditional analytical models and experimental approaches, numerical techniques shine on investigating objects featured by complicated geometries and variables that are difficult or even impossible to obtain from conventional experimental methods.

In the specific case of sound radiation from the open end of ducts, da Silva and Scavone (2007) investigated the sound radiation from an unflanged cylinder immersed in a stagnant fluid. Later, they investigated the influence of a subsonic mean flow on the sound transmission in ducts terminated by horns with different geometries (da Silva et al., 2009) and by a catenoidal horn resembling the end of a clarinet-like instrument (da Silva et al., 2010). The accuracy of da Silva's LBM model is demonstrated by the excellent agreements found between numerical and analytical results in terms of the

reflection coefficient and the length correction at the open end.

4.2.2 A Pipe Carrying a Quiescent Flow

The goal of this section is to verify the LB models by addressing the classical problem of the reflection of plane waves propagating in an unflanged cylindrical pipe immersed in a quiescent fluid. The results of both the CPU and GPU SRT models are compared with the established theoretical model provided by Levine and Schwinger (1948) in terms of pressure reflection coefficient R and the dimensionless length correction l/a .

4.2.2.1 LBM Scheme

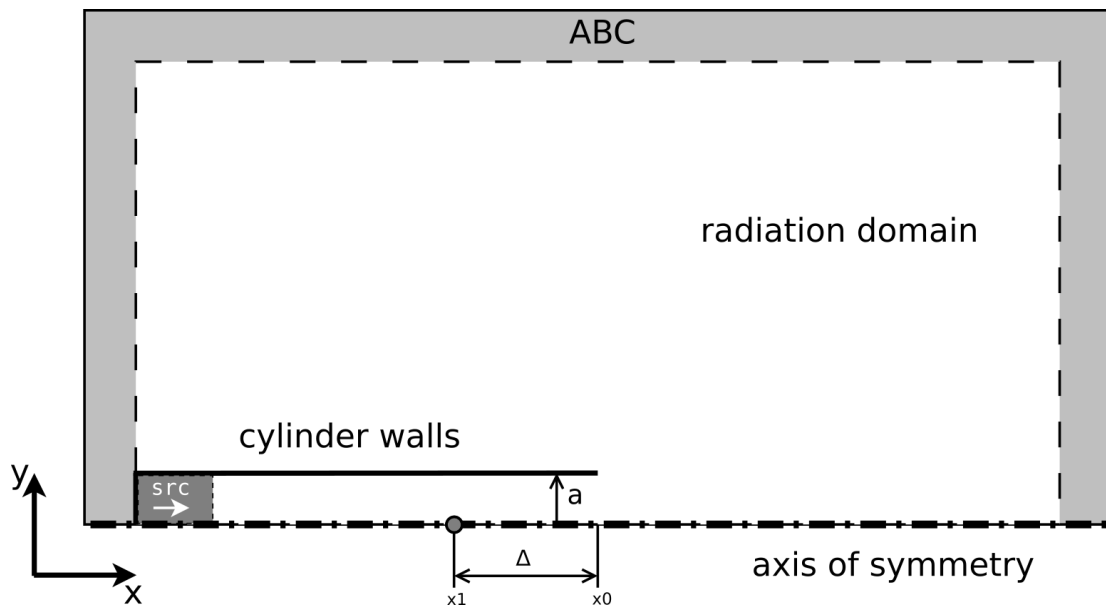


Figure 4.1 LB model of the axisymmetric pipe with a quiescent flow for the measurements of reflectance and length correction.

The numerical scheme is described by an axisymmetric cylindrical structure immersed in a fluid domain surrounded by open boundaries, as illustrated in Fig. 4.1. This scheme takes advantage of the axisymmetry such that the system can be fully represented by a half-plane without losing accuracy. The fluid domain defined by the half-plane is represented by a rectangular D2Q9 lattice consisting of 1000 by 500 cells.

The top, left and right side of the fluid domain are treated with an absorbing boundary condition (ABC) proposed by Kam et al. (2006), which is a transition buffer with

a target flow prescribed at the outlet. The non-reflecting condition is achieved by setting the distribution function of the target flow, f_i^T , to the equilibrium state, i.e., $\rho_t = \rho_0$ and $u_t = 0$, where ρ_0 is the undisturbed density of the fluid. For collisions inside the transition buffer, an extra damping term is added to the collision equation of the single relaxation time BGK lattice Boltzmann scheme:

$$f_i(\mathbf{x} + \mathbf{e}_i \Delta t, t + \Delta t) - f_i(\mathbf{x}, t) = -\frac{1}{\tau}(f_i - f_i^{eq}) - \sigma(f_i^{eq} - f_i^T), \quad (4.15)$$

where $\tau = 1/\Omega$ is the relaxation time, $\sigma = \sigma_m(\delta/D)^2$ is the damping coefficient, σ_m is a constant that normally equals to 0.3, δ is the distance measured from the beginning of the buffer zone and D is the thickness of the buffer. Inside the transition buffer, the amplitude of outgoing waves is attenuated asymptotically and the reflections from the outside boundary are minimized. The thickness of the ABC buffer used in the model is 15 cells, corresponding to a frequency-averaged pressure reflection coefficient of order of magnitude smaller than 10^{-3} for both perpendicular and oblique sound incidence. The lower boundary of the radiation domain representing the axis of symmetry of the system is treated with a free-slip condition.

The length and the radius of the cylindrical waveguide is $L = 500$ and $a = 20$ in lattice cells, respectively. The walls of the waveguide are represented by a solid boundary of zero thickness based on spatial interpolations (Bouzidi et al., 2001; Lallemand and Luo, 2003). The outer walls are treated by a simple bounce-back scheme (Succi, 2001) for which the viscous boundary phenomena are represented with second-order accuracy. Since the boundary layer plays a fundamental role on the radiation, the inner walls are treated using a free-slip scheme (Wolf-Gladrow, 2004) in order to reduce the inherent viscous boundary layer effects that result in a transfer of momentum by the tangential motion of particles along the walls.

The undisturbed dimensionless fluid density is set as $\rho_0 = 1.0$ for convenience. To ensure the numerical stability and to make the viscosity as small as possible, the relaxation parameter of the SRT model is set to $\Omega = 1.95$, which is equivalent to a relaxation time of $\tau = 0.5128$, or a dimensionless kinematic viscosity of $\nu = 4.27 \times 10^{-3}$.

In order to compare ν with the kinematic viscosity of air in standard conditions, which is $\nu_{air} = 1.51 \times 10^{-5} (m^2/s)$, the dimensionless value needs to be converted to physical units. Suppose that the numerical cylindrical waveguide represents the bore

of a clarinet that has an inner radius of $a_p = 8 \times 10^{-3}$ (m), the spatial resolution is $dx = a_p/a = 4 \times 10^{-4}$ (m) and the corresponding kinematic viscosity in physical units can be obtained by $\nu_p = 340 \times \sqrt{3} \times dx \times \nu = 10^{-3}$ (m²/s).

4.2.2.2 Representing a 3D Axisymmetric Flow in a 2D Model

The fluid/aeroacoustic system discussed in this study is characterized by a 3D axisymmetric flow in an unflanged cylindrical pipe. Although it is possible to simulate the 3D flow using a 3D LB model, this approach would require significant computational resources (CPU time, memory, etc.). Rather, an axisymmetric 2D LBGK scheme is chosen for its efficiency and simplicity. Halliday et al. (2001) first proposed an axisymmetric model for the steady 3D axisymmetric tube flow problems, where they inserted several spatial and velocity-dependent source terms into the RHS of the collision equation of a regular LBGK D2Q9 model, such that the Navier-Stokes equations in cylindrical polar coordinates can be recovered from the lattice Boltzmann equation by performing a Chapman-Enskog expansion. Later, Niu et al. (2003) derived an axisymmetric model for the Taylor-Couette flow problems. Lee et al. (2005) further proposed an axisymmetric scheme based on the incompressible LBGK D2Q9 model for simulations of 3D pulsatile flow.

Throughout this study, the axisymmetric incompressible LBGK D2Q9 model by Lee et al. (2005) is employed to simulate the 3D axisymmetric flow in a circular pipe. This scheme assumes that the flow is symmetric about the pipe's axis and thus can be expressed by the incompressible Navier-Stokes equations in cylindrical polar coordinates. Based on this assumption, the azimuthal component of velocity u_ϕ and the ϕ coordinate derivatives vanish. Consequently, the flow can be represented by the axial and radial coordinates, x and r , respectively, which can be written as a vector \mathbf{x} for convenience. The governing equation of the axisymmetric model is written as

$$f_i(\mathbf{x} + \mathbf{e}_i \Delta t, t + \Delta t) - f_i(\mathbf{x}, t) = -\frac{1}{\tau}(f_i - f_i^{eq}) + h_i^{(1)} + h_i^{(2)}, \quad (4.16)$$

which has the same form as the BGK lattice Boltzmann equation (Eq. 3.20) except that two source terms are introduced to the RHS. The equilibrium distribution function f^{eq} of the axisymmetric model is identical to that of the incompressible LBGK D2Q9 model

given by He and Luo (1997)¹, which is written as

$$f_i^{eq}(\mathbf{x}, t) = \omega_i \frac{(\rho_0 + \delta\rho)}{c_s^2} + \omega_i \rho_0 \left[\frac{\mathbf{e}_i \cdot \mathbf{u}}{c_s^2} + \frac{(\mathbf{e}_i \cdot \mathbf{u})^2}{2c_s^4} - \frac{\mathbf{u}^2}{2c_s^2} \right], \quad (4.17)$$

where \mathbf{e}_i is the discrete velocity connecting each site to its neighbor lattices, $\omega_0 = 4/9$, $\omega_1 = \omega_2 = \omega_3 = \omega_4 = 1/9$ and $\omega_5 = \omega_6 = \omega_7 = \omega_8 = 1/36$ and $c_s = 1/\sqrt{3}$ is the speed of sound in lattice units.

The source terms are given by

$$h_i^{(1)} = -\frac{\omega_i \rho_0 u_r}{r} \quad (4.18)$$

and

$$h_i^{(2)} = \omega_i \frac{3\nu}{r} [\partial_r p + \rho_0 \partial_x u_x u_r + \rho_0 \partial_r u_r u_r + \rho_0 (\partial_r u_x - \partial_x u_r) c_{ix}]. \quad (4.19)$$

The velocity derivation terms $\partial_r u_r$, $\partial_x u_x$ and $\partial_r u_x - \partial_x u_r$ in Eq. 4.19 can be solved using the technique proposed by Lee et al. (2005). Specifically, the terms $\partial_r u_r$, $\partial_x u_x$ and $\partial_r u_x + \partial_x u_r$ are explicitly calculated from the higher-order moments of f_i (Lee et al., 2005, Eq. (9)). The term $\partial_r u_x - \partial_x u_r$ is equal to $\partial_r u_x + \partial_x u_r - 2\partial_x u_r$, where the unknown term $\partial_x u_r$ at lattice node (i, j) can be calculated using the finite difference method provided in (Lee et al., 2005, Eq. (10)), that is, $(\partial_x u_r)_{i,j} = ((u_r)_{i+1,j} - (u_r)_{i-1,j})/2$.

According to previous experiments, the axisymmetric model derived by Lee et al. (2005) provides accurate results and offers a simpler numerical implementation. Generally speaking, an incompressible LBGK model is able to capture acoustic wave phenomena, provided that these are within the linear regimes characterized by low Mach numbers and low wave amplitudes. The highest Mach number used in this thesis is $M = 0.15$, which makes the flow slightly compressible. However, the incompressible model is still valid because the slightly unsteady compressible form of the Navier-Stokes equations can be fully recovered from the isothermal form of the Boltzmann equation by performing the Chapman-Enskog expansion (Qian et al., 1992; Wolf-Gladrow, 2004).

4.2.2.3 Source Signal

The exciting broadband signal is a customized swept-frequency signal running from a low frequency $ka_s = 0.01$ to a high frequency $ka_e = 3.8$ (less than the first evanescent

¹It is slightly different from Eq. 3.22 given by Qian et al. (1992).

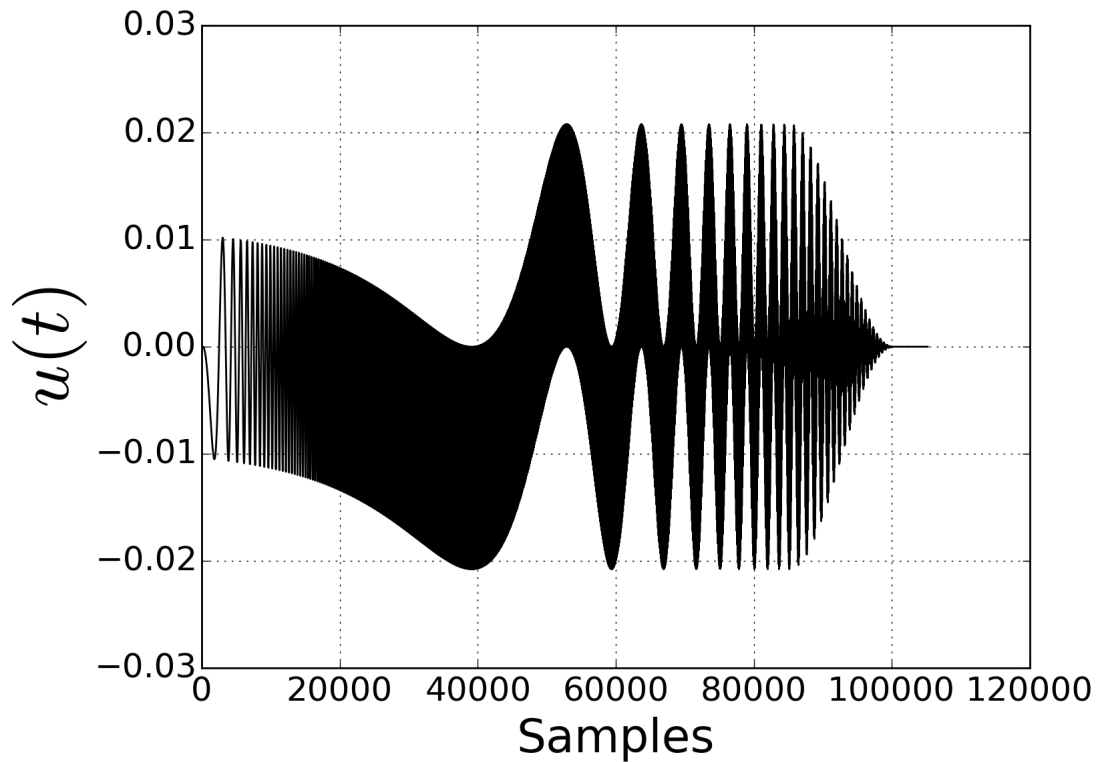


Figure 4.2 Source signal.

mode of the pipe), where ka is the dimensionless wavenumber, the subscript s and e indicate the starting and the ending, respectively. In order to provide a relatively high frequency resolution in both low frequency and high frequency bands within a relatively short time duration, the exciting signal u_t is made up of a linear combination of a linear chirp signal u_{t1} and a logarithmic chirp signal u_{t2} . The excitation is implemented by a source buffer with a length of 60 cells at the left end of the pipe using the same technique as an absorbing boundary condition but prescribed by a non-zero target velocity given by

$$\begin{aligned}
u_t &= H(n - N_t) \cdot u'_0 \cdot (u_{t1} + u_{t2})/2, \\
u_{t1} &= \sin \left[\frac{c_s}{a} \left(ka_s + ka_e \frac{(n - N_t)\Delta t}{N - N_t} \right) \right], \\
u_{t2} &= \sin \left[\frac{c_s}{a} \left(ka_s \left(\frac{ka_e}{ka_s} \right)^{\frac{(n - N_t)\Delta t}{N - N_t}} \right) \right],
\end{aligned} \tag{4.20}$$

where n is the time step, N is the total number of iterations in the simulations, N_t is a short initialization iterations, u'_0 is the amplitude of the acoustic particle velocity along the axial direction and $\Delta t = 1$ is the time increment of the numerical scheme. $H(n)$ is the Heaviside step function given by

$$H(n) = \begin{cases} 0, & n < 0, \\ 1, & n \geq 0. \end{cases} \tag{4.21}$$

The source signal used in the simulation is illustrated in Fig. 4.2, where 15 percent of the total duration of the envelope of the signal has been ramped by a Hanning window at the head and the end to prevent unwanted higher modes from being excited.

The suitable grid resolution of the simulation is relative to the ratio of the lattice cells per unit length of the model, or CPW, which depends on the maximum frequency analyzed in the problem. Wilde (2006) proposed that a minimum value of 12 cells per wavelength is required such that the phase speed error is reduced to less than 1 percent. In this simulation, the maximum dimensionless frequency of analysis ($ka = 3.8$, which corresponds to a wavelength of $\lambda = 2\pi/k = 2\pi a/ka \approx 33$ in lattice cells) can be well represented in the simulation. Moreover, the grid resolution determined by the lattice cells of the radius, which is $a = 20$, are suitable for simulating acoustic waves with high frequency components up to $ka = 10.47$ based on the criterion defined by Wilde.

4.2.2.4 Signal Probing and Post-Processing

The purpose is to obtain the acoustic pressure reflection coefficient $R(x = x_0)$ at the open end of the pipe, which will be written as R for the matter of convenience. Since the wavefront is not plane at the open end, and the travelling wave in two opposite

directions can not be measured directly, we can not simply calculate R by its theoretical definition, i.e. the ratio of the reflected pressure wave $p^-(x = x_0)$ and the incident pressure wave $p^+(x = x_0)$.

In this study, the reflection coefficient R is calculated from the radiation impedance Z_r at the open end by the relation

$$R = (Z_r - Z_c)/(Z_r + Z_c), \quad (4.22)$$

where $Z_c \approx \rho c_s/S$ is the characteristic impedance of the pipe, ρ is the density of air, c_s is the speed of sound and S is the cross-section of the pipe. The technique proposed by Dalmont et al. (2001) has been used to obtain the radiation impedance, which is briefly described here.

The time history of the acoustic pressure $p(t)$ and the volume velocity $u(t)$ at $x = x_1$, which is a distance of Δ from the open end ($x = x_0$), is measured. To ensure a plane wavefront under the first cut-off frequency, the distance Δ should be larger than $4a$. The input impedance being looked from $x = x_1$ can be calculated by

$$Z_1 = \frac{P(x = x_1)}{U(x = x_1)}, \quad (4.23)$$

where P and U is the Fourier transformed version of p and u in frequency domain. The radiation impedance Z_r can then be calculated from Z_1 by

$$Z_r = jZ_c \tan \left[\arctan \left(\frac{Z_1}{jZ_c} \right) - k\Delta \right]. \quad (4.24)$$

The complex reflection coefficient R can be obtained from the radiation impedance by Eq. 4.22. The length correction l can be derived from its relation with R and its modulus:

$$l = \frac{j}{2k} \log \left(\frac{R}{-|R|} \right). \quad (4.25)$$

4.2.2.5 Results

The results of the magnitude of the reflection coefficient $|R|$ and the dimensionless length correction l/a obtained from the CPU SRT model are presented in Fig. 4.3 along with the theoretical predictions by Levine and Schwinger (1948). Overall, the numerical

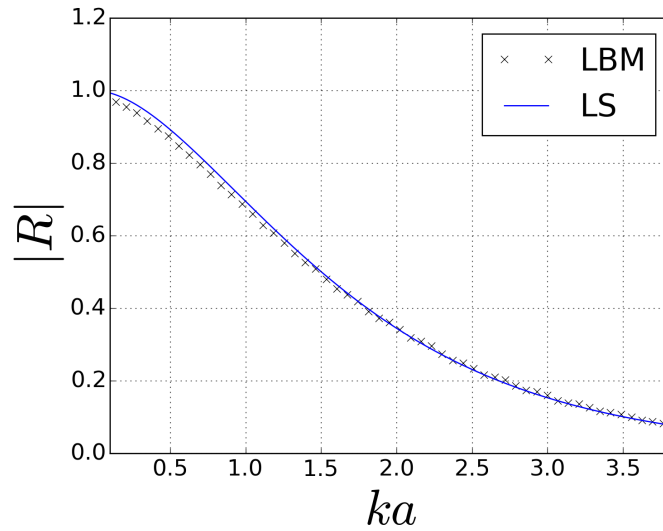
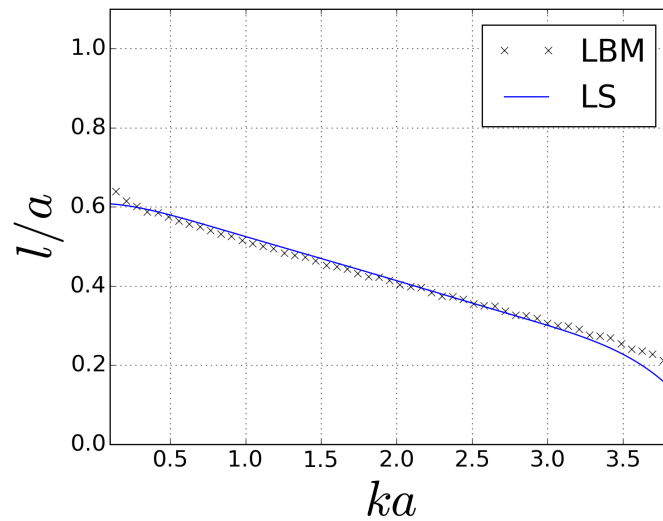
(a) Magnitude of reflection coefficient $|R|$.(b) Dimensionless length correction l/a .

Figure 4.3 CPU SRT model, comparison between numerical results (solid) and analytical predictions (- - -) of the reflection coefficient and length correction of an unflanged cylindrical pipe in the absence of a mean flow ($M = 0$).

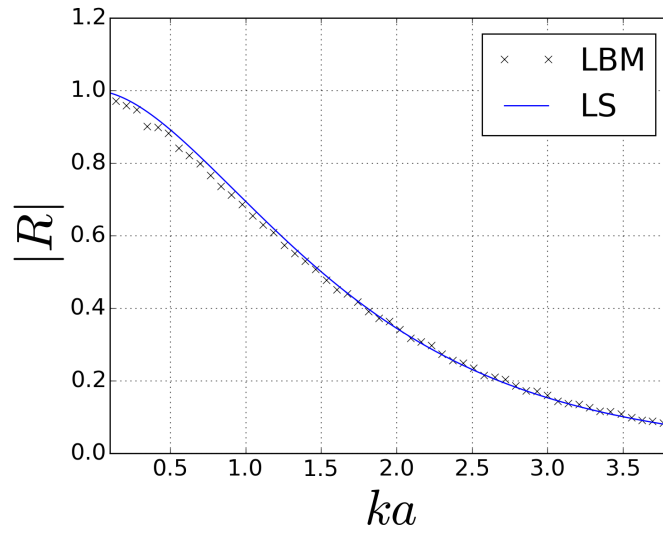
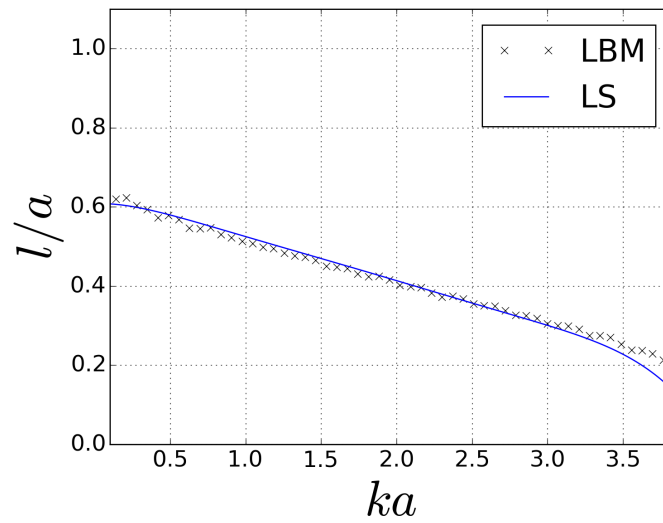
(a) Magnitude of reflection coefficient $|R|$.(b) Dimensionless length correction l/a .

Figure 4.4 GPU SRT model, comparison between numerical (solid) and analytical predictions (---) of the reflectance and length correction of an unflanged cylindrical pipe in the absence of a mean flow ($M = 0$).

result of the magnitude of the reflection coefficient $|R|$ is in good agreement with the theoretical prediction. For the region of $ka < 1.5$, the numerical result of $|R|$ is slightly lower than that predicted by the theory, though for the region of $1.5 < ka < 3.8$, the numerical result is almost perfectly overlapped on the theoretical prediction. Interestingly, the numerical result of $|R|$ obtained from a previous LBM simulation by da Silva (2008) shows a slightly higher amplitude than the theoretical predictions, and the discrepancies are attributed by the author to the effect of energy leakage caused by the truncation of the time history of the probed signal, which is the response of a Hanning-shaped impulse signal.

The dimensionless length correction l/a obtained from the numerical simulation has been compared to the theoretical predictions, as depicted in Fig. 4.3(b). A disagreement of about 4% is found in both the low frequency region ($ka < 0.1$) and the high frequency region ($ka > 3.25$). Similar patterns of disagreements have been reported by da Silva (2008) who attributes the energy leakage to the truncation effect of the probed signal in time domain.

We notice that although the exciting signal used in the present simulation is much longer than the Hanning-shaped impulse signal used by da Silva (2008), the discrepancies do not vanish but show a different characteristic. Besides the possible effect of energy leakage, the discrepancies might be also attributed to the accuracy of the numerical system, which is related to various factors including the time resolution, spatial resolution, radiation domain size and numerical precision representing floating-point numbers.

The results of $|R|$ and l/a obtained from the GPU SRT model are presented in Fig. 4.4. They are very close to the results obtained from the CPU SRT model. In general, the differences between the results of the GPU SRT model and the CPU SRT model are barely noticeable. A minor difference can be found in $|R|$ at $ka \approx 0.3$, where the GPU result shows a slightly bigger disagreement to the theoretical prediction than that of the CPU result, which might be caused by the lower digital precision (32-bit) offered by the GPU computation platform. Overall, both the CPU SRT model and the GPU SRT model show good results compared to either the theoretical predictions or the previous LBM predictions presented in (da Silva, 2008).

4.2.3 A Pipe Carrying a Mean Flow

This section simulates the transmission of acoustic waves out of a cylindrical pipe carrying a subsonic laminar cold mean flow. The GPU SRT model, which has been verified in Sec. 4.2.2 for the case of a cylindrical pipe carrying a zero flow, is exclusively used in this section.

4.2.3.1 LBM Scheme

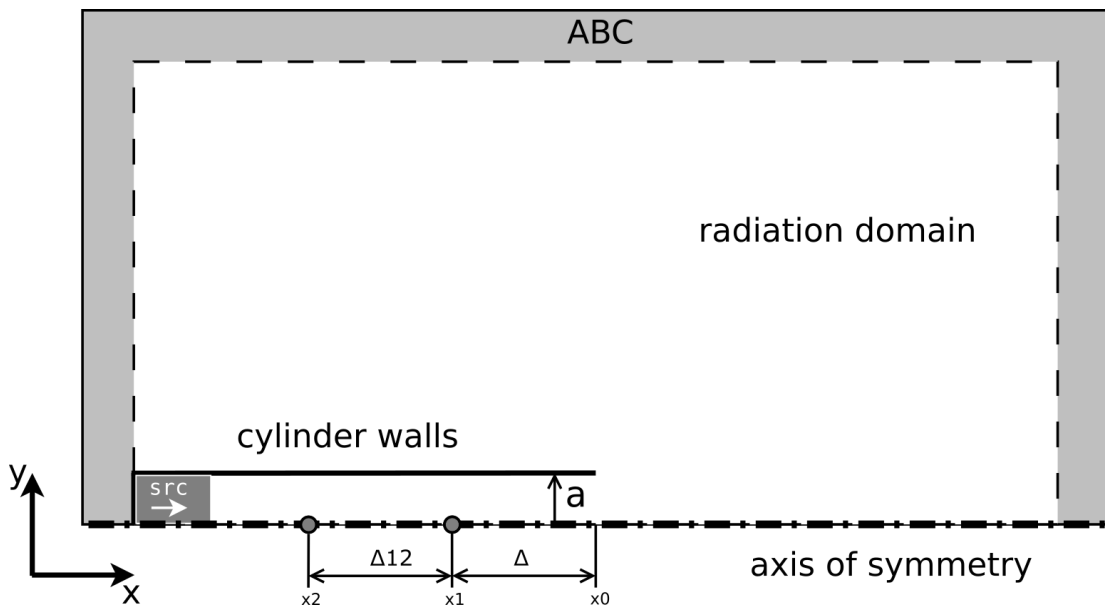


Figure 4.5 LB model of an axisymmetric pipe carrying a subsonic mean flow for the measurement of reflection coefficient and length correction at the open end.

Figure 4.5 depicts the numerical scheme representing a cylindrical pipe carrying a subsonic mean flow, which is almost the same as the system used in Sec. 4.2.2 except that one new probing point is added at x_2 .

In order to ensure the numerical stability in the situation of a non-zero mean flow and to make the viscosity as small as possible, the heuristic relaxation parameter Ω of the SRT model is chosen based on Mach number, as presented in Tab. 4.1

M	Ω
0.05	1.9
0.1	1.88
0.15	1.83

Table 4.1 Relaxation parameter Ω for different Mach numbers.

4.2.3.2 Source Signal

The system is excited by a source signal generated from a source buffer, which was described in Sec. 4.2.2. The source signal u_t consists of a customized swept-frequency signal running from a low frequency $ka_s = 0.01$ to a high frequency $ka_e = 1.5$, which is the highest Helmholtz numbers predicted by Munt (1990), superimposed on a DC offset representing the non-zero mean flow. The formula of u_t is expressed as

$$\begin{aligned}
 u_t &= u_0 + H(n - N_t) \cdot u'_0 \cdot (u_{t1} + u_{t2})/2, \\
 u_{t1} &= \sin \left[\frac{c_s}{a} \left(ka_s + ka_e \frac{(n - N_t)\Delta t}{N - N_t} \right) \right], \\
 u_{t2} &= \sin \left[\frac{c_s}{a} \left(ka_s \left(\frac{ka_e}{ka_s} \right)^{\frac{(n - N_t)\Delta t}{N - N_t}} \right) \right],
 \end{aligned} \tag{4.26}$$

where n is the time step, N is the total number of iterations in the simulation, N_t is a short initialization iterations, u_0 is the velocity of the non-zero mean flow, u'_0 is the amplitude of the acoustic particle velocity along the axial direction, $\Delta t = 1$ is the time increment of the numerical scheme and $H(n)$ is the Heaviside step function. To fulfill the condition of low acoustic amplitude specified in (Munt, 1990), the ratio of $u'_0/u_0 \sim 0.1$ is used.

Before the acoustic source is superimposed, there should be enough initialization time to allow the fluid in the pipe to accelerate from stagnation to a steady state. The initialization time can be determined by

$$N_t \geq N_{t0} + L_x/(M c_s), \tag{4.27}$$

where $N_{t0} \simeq 4000$ is the acceleration time for a source buffer with a thickness equivalent to 60 cells (da Silva et al., 2009), M is the Mach number of the non-zero mean flow and $L_x = 1000$ is the maximum traveling distance of the plane sound wave in the axial

direction in the radiation domain. For example, the minimum initialization time corresponding to $M = 0.036$ is $N_t = 5.21 \times 10^4$. For the jet speeds ($M = 0.05, 0.1, 0.15$) tested in this study, N_t is assigned to a safe constant value of 80000.

4.2.3.3 Signal Probing and Post-Processing

The wavenumber of the propagating acoustic waves are involved in the calculation of both the reflection coefficient and the length correction. For the case of thermoviscous acoustic wave motions in pipes with flow, the wavenumber is complex and is influenced by both the effect of viscous damping and the effect of convection due to the non-zero mean flow. Typically, the complex wavenumber can be decomposed to two components, $K = K^+ + K^-$, where K^- and K^+ are the components related to the left- and right-traveling waves, respectively. A number of theoretical models and experimental measurements of the complex wavenumber including the mean flow effect have been reported in literature (Davies et al., 1980; Dokumaci, 1997; Allam and Åbom, 2006). However, none of these results can be directly used in the post-processing of the present LB simulations, not only because of the differences between the data obtained from different sources, but also due to two inherent issues of the LB models. Firstly, the artificial viscosity being used in the current LB model is higher than that used in those theoretical models and experimental measurements. Secondly, although the boundary layer effect in the LB simulations is roughly approximated by the no-slip boundary conditions imposed on the pipe walls, it is still not an accurate reproduction of the real physical phenomenon.

In the present study, the complex wavenumbers as well as the reflection coefficient and length correction are calculated together from the signals of pressure and volume velocity probed at two different positions using the modified *two-microphone method* (TMM) proposed by da Silva (2008), which is based on the established multi-microphone method used by Peters et al. (1993) and Allam and Åbom (2006). The procedure is based on the linear theory of plane acoustic wave propagation in pipes and is described here, where all variables are in the frequency domain.

The four known signals of pressure and volume velocity probed at two different positions $x = x_1$ and $x = x_2$ (depicted in Fig. 4.5), namely p_1, p_2, u_1 and u_2 , can be

decomposed to left- and right-travelling signals:

$$\begin{aligned}
 p_1 &= p_1^+ + p_1^-, \\
 p_2 &= p_2^+ + p_2^- = p_1^+ e^{-jk^+ \Delta_{12}} + p_1^- e^{jk^- \Delta_{12}}, \\
 u_1 &= \frac{1}{\rho c_s} (p_1^+ - p_1^-), \\
 u_2 &= \frac{1}{\rho c_s} (p_2^+ - p_2^-) = \frac{1}{\rho c_s} (p_1^+ e^{-jk^+ \Delta_{12}} - p_1^- e^{jk^- \Delta_{12}}),
 \end{aligned} \tag{4.28}$$

where Δ_{12} is the distance between the two probing positions x_1 and x_2 , the superscripts + and - indicate the right- and left-traveling directions, respectively. In this study, the distance between the two virtual microphones is chosen as $\Delta_{12} = 1.5a$.

Equation 4.28 can be expressed in the form of matrix,

$$\begin{bmatrix} p_1^+ \\ p_1^- \\ p_2^+ \\ p_2^- \end{bmatrix} = \begin{bmatrix} 1 & 1 & 0 & 0 \\ 0 & 0 & 1 & 1 \\ 1/\rho c_s & -1/\rho c_s & 0 & 0 \\ 0 & 0 & 1/\rho c_s & -1/\rho c_s \end{bmatrix}^{-1} \begin{bmatrix} p_1 \\ p_2 \\ u_1 \\ u_2 \end{bmatrix}, \tag{4.29}$$

from which the four unknowns, p_1^+ , p_1^- , p_2^+ and p_2^- can be solved. The complex wavenumbers associated with the left- and right-traveling waves can then be solved as:

$$\begin{aligned}
 k^+ &= \frac{j}{\Delta_{12}} \log \left(\frac{p_2^+}{p_1^+} \right), \\
 k^- &= \frac{-j}{\Delta_{12}} \log \left(\frac{p_2^-}{p_1^-} \right).
 \end{aligned} \tag{4.30}$$

Finally, we can obtain the reflection coefficient and length correction as

$$R = \left(\frac{p_1^-}{p_1^+} \right) e^{j(k^+ + k^-) \Delta} \tag{4.31}$$

and

$$l = \frac{j}{(k^+ + k^-)} \log \left(\frac{R}{-|R|} \right), \tag{4.32}$$

where Δ is the distance between x_1 and x_0 (see Fig. 4.5).

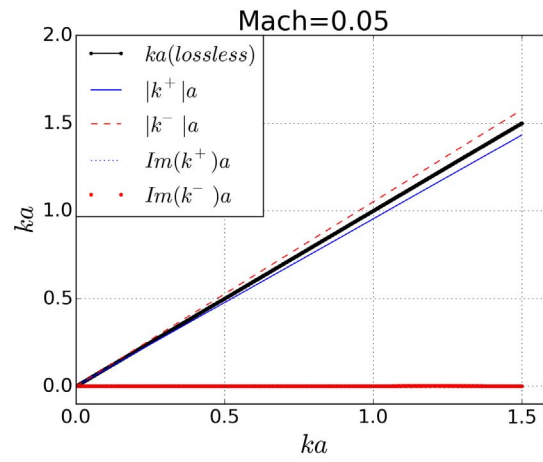
4.2.3.4 Results

Figure 4.6 depicts the Helmholtz numbers associated to the left- and right-traveling components of complex wavenumbers, k^+a and k^-a , for viscous flow with three different jet speeds ($M=0.05, 0.1, 0.15$). For convenience, the lossless ka for the case of inviscid quiescent fluid is plotted alongside the lossy one as a reference. In general, the amplitudes of both k^+a and k^-a are strongly influenced by the jet speeds (measured by Mach numbers), where a higher jet speed results in a larger deviation from the reference of the lossless ka . The imaginary part of the complex Helmholtz numbers are also depicted, which seems very small and contributes little to the calculations of the reflection coefficient and the length correction.

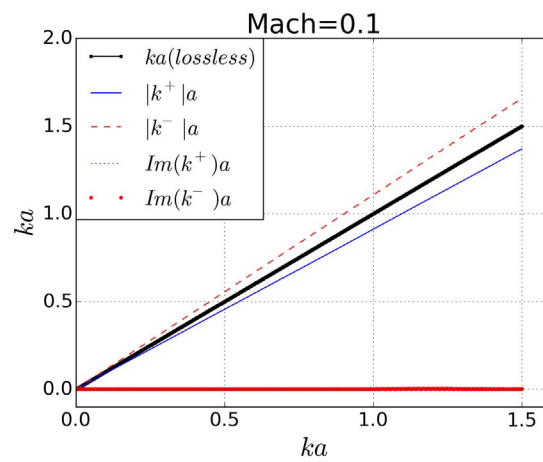
Figure 4.7 depict the results of the reflection coefficient at the open end obtained from the GPU SRT model plotted as both a function of the Helmholtz number ka (left) and a function of the Strouhal number $Sr_0 = ka/M$ (right). The theoretical predictions provided by Munt (1990) as well as the experimental data provided by Allam and Åbom (2006) are plotted alongside the numerical results. For cases of all three Mach numbers, overall, very good agreements between the numerical results, the theoretical predictions and the experimental results are observed throughout the frequency range $0 \leq ka \leq 1.5$. The agreement for the two lower Mach numbers ($M = 0.05, 0.1$) is better than that for the largest Mach number ($M = 0.15$), where the highest deviation (3%) from the theory is found at $ka \approx 0.3$. The slightly poor performance of the model in the highest Mach number can be explained by the fact that a Mach number of $M = 0.15$ is at the upper limit of the flow velocity allowed ($M \leq 0.15$) by the axisymmetric lattice Boltzmann scheme for simulations of low compressible fluid.

Interestingly, the performance of the present simulation in the high frequencies is as good as that in the low frequencies, where in a similar LB simulation, da Silva (2008) reported a much higher discrepancy for the results in the high frequency areas for all flow velocities. The better performance of the present simulation may be attributed to either a higher spatial resolution, i.e., a doubled lattice size (1000×500) is used in this study instead of the smaller one (500×250) used by da Silva (2008), or the mixed swept-frequency exciting signal which provides a better balance of components over the whole frequency range than that provided by a conventional single linear or logarithmic chirp signal of the same duration.

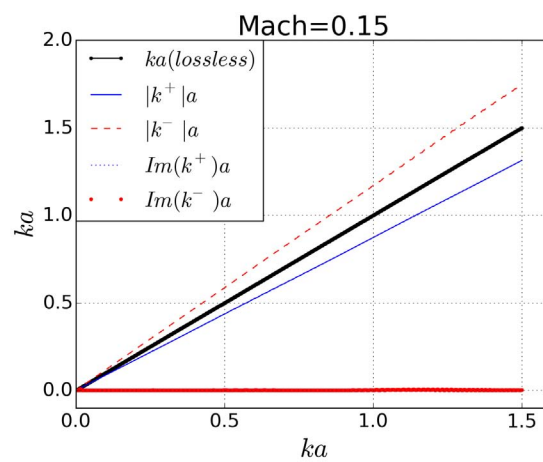
It can be noted that all curves in Fig. 4.7 have a value of 1 for $ka \rightarrow 0$ and have a



(a)



(b)



(c)

Figure 4.6 GPU SRT model, comparison between complex wavenumbers calculated from the simulations of an unflanged cylindrical pipe in the presence of a mean flow: (a) Mach=0.05, (b) Mach=0.1, (c) Mach=0.15.

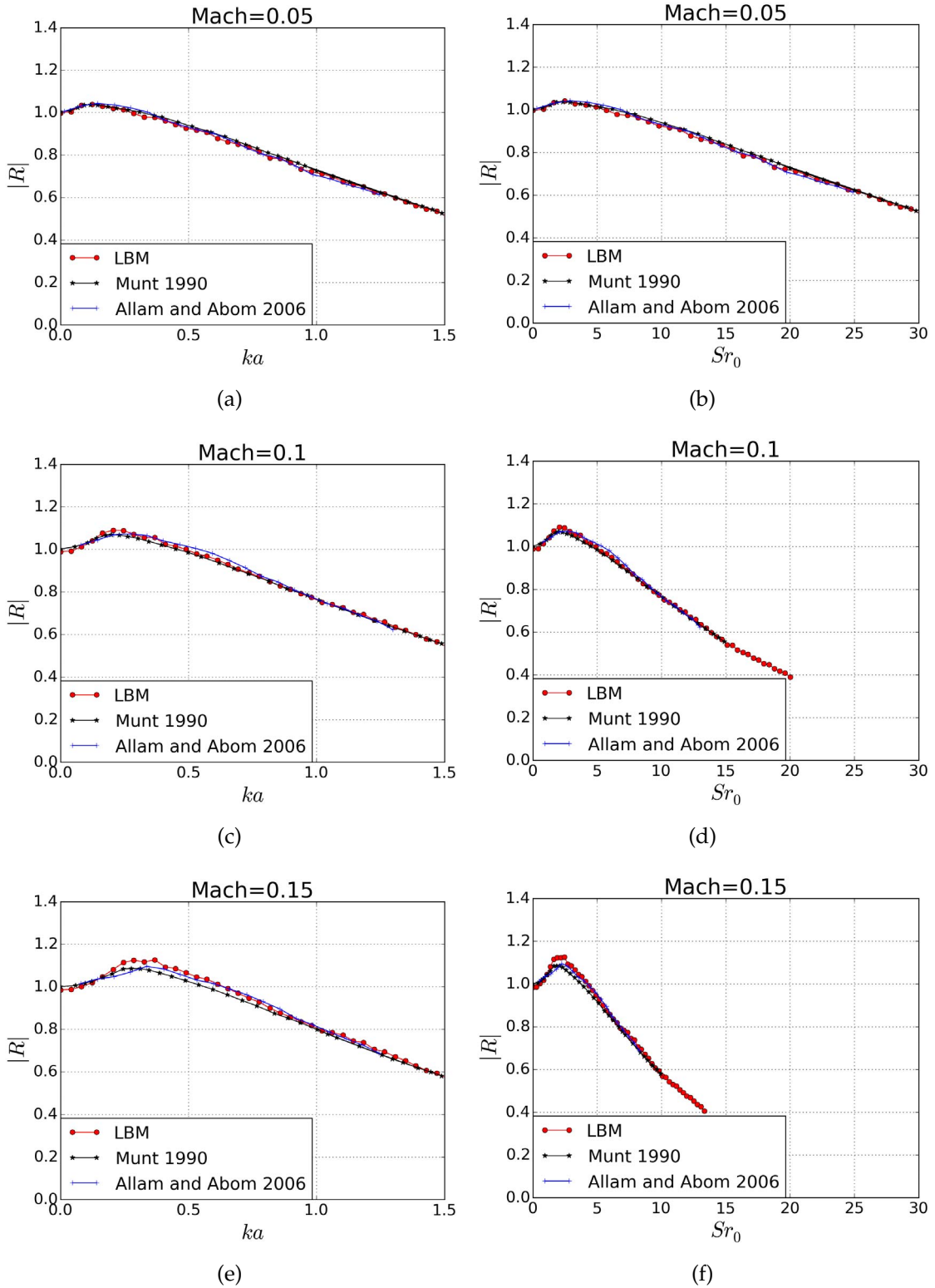


Figure 4.7 GPU SRT model, comparison between numerical results, analytical predictions and experimental measurements of the magnitude of the reflectance at the open end of an unflanged cylindrical pipe in the presence of a mean flow: (a) (b) Mach=0.05, (c) (d) Mach=0.1, (e) (f) Mach=0.15.

maxima higher than unity in the low frequency region. More specifically, all peaks are found at almost the same Strouhal number $Str_0 \sim \pi/2$. This phenomenon is exactly the same as that predicted by Munt (1990), i.e., for a jet pipe issuing a non-zero subsonic mean flow, the pressure reflection coefficient initially increases with frequency, reaching a maximum value at a nearly constant Strouhal number and thereafter decreasing, but still remaining higher than the value it had in the pipe without flow (Levine and Schwinger, 1948). The conservation of energy is not violated since $|R|$ is always less than $(1 + M)/(1 - M)$. According to the theory of Munt (1990), the peak region is due to the coupling between the acoustic source and the wave of vortical instabilities at the vortex sheet of the jet in a stagnant fluid, i.e., the acoustic reflection is reinforced by the transfer of kinetic energy from the flow to the acoustic field due to the interaction of the unstable vortex sheet with the lip of the pipe, and the instability of the vortex sheet is reinforced by the acoustic energy transmitted from the pipe end. This phenomenon is well visualized by da Silva et al. (2009).

The numerical results of the dimensionless length correction as a function of the Helmholtz number and of the Strouhal number are compared with the theoretical predictions (Munt, 1990) and the experimental results (Allam and Åbom, 2006) in Fig. 4.8. In general, the numerical results are in excellent agreements with the theoretical data in the high frequency region ($ka > 0.5$). In the low frequency region ($ka < 0.5$), all curves show that the values of the length correction are greatly reduced due to the influence of the mean flow. According to Rienstra (1984), the dimensionless length correction l/a is reduced to $0.2554\sqrt{1 - M^2}$ as $ka \rightarrow 0$ due to the mean flow effect, which is much shorter than that in the case of pipes without flow (Levine and Schwinger, 1948). However, the numerical results show a much shorter length correction for $ka < 0.2$, and the deviation becomes bigger for a higher Mach number. The discrepancy might be explained by two facts. The first fact lies in the low compressibility limit ($M \leq 0.15$) of the LB model, where the accuracy of a simulation involving a flow at the upper limit is likely degraded to some extent. Another fact is related to the inherent limitation of the two-microphone method. As Åbom and Bodén (1988) suggested, to avoid a large sensitivity to errors in the input data, the two-microphone method should be restricted to a frequency range which is related to the Mach number and the distance between the two microphones Δ_{12} , which is given by:

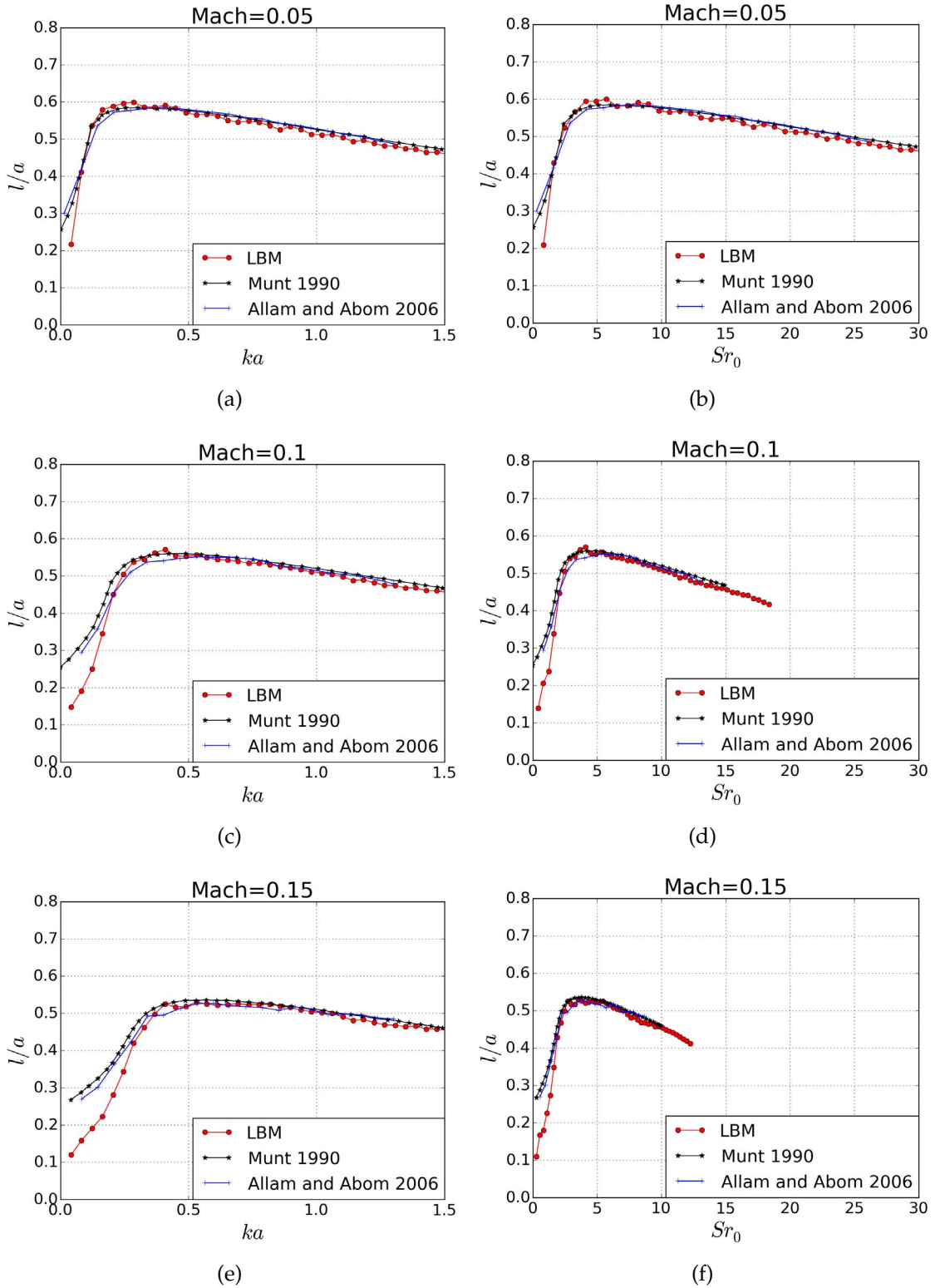


Figure 4.8 GPU SRT model, comparison between numerical results, analytical predictions and experimental measurements of the length correction at the open end of an unflanged cylindrical pipe in the presence of a mean flow: (a) (b) Mach=0.05, (c) (d) Mach=0.1, (e) (f) Mach=0.15.

$$0.1\pi(1 - M^2) < k\Delta_{12} < 0.8\pi(1 - M^2). \quad (4.33)$$

For the value used in this study, i.e., $\Delta_{12} = 1.5a$, the valid frequency ranges for different Mach numbers are given in Table 4.2, which suggests that the results in the low frequency region $ka < 0.2$ are more sensitive to errors of the input data.

M	ka (min)	ka (max)
0.05	0.2089	1.6713
0.1	0.2073	1.6588
0.15	0.2047	1.6378

Table 4.2 Valid ka range of the two-microphone method for $\Delta_{12} = 1.5a$.

4.2.4 Pipes with Horn Extension

One of the advantages of the LB model is its capability of handling boundaries involving complicated curved geometries. For example, we can easily change the open end of the acoustic waveguide to an arbitrary shaped termination. At this stage, we are interested in simulating the acoustic system of an unflanged pipe with a circular horn attached to the open end, which is normally found in the family of woodwind instruments. To the best knowledge of the author, the exact analytical model for a pipe terminated by a circular horn is not available yet. Peters et al. (1993) experimentally investigated the reflection coefficient and length correction of a pipe terminated by a horn with a radius of curvature four times of the pipe radius ($r = 4a$). For the case of zero mean flow, Selamet et al. (2001) obtained the reflection coefficients and length corrections of pipes terminated by curved interface surfaces of various radius and for a wide range of the Helmholtz number ($0 < ka \leq 3.0$) using the boundary element method (BEM), where the results are in good agreement with the experimental results provided by Peters et al. (1993). For the case of non-zero subsonic mean flow, Hirschberg et al. (1989) observed that a horn at the pipe end can increase the transfer of kinetic energy from the flow to the acoustic field at the open end, which was confirmed by an experiment conducted by Peters et al. (1993) where a peak region greater than unity was found in the low

frequency region of the energy reflection coefficient, which is defined as

$$|R_E| = |R|^2 \left(\frac{1 - M}{1 + M} \right)^2. \quad (4.34)$$

The LB simulation of the acoustic system of a cylindrical pipe terminated by a circular horn was first presented by da Silva (2008). He obtained the reflection coefficients and the length corrections of horns of two different radius of the curvature ($r = 2a$ and $r = 4a$), which were in good agreements with results obtained by BEM for the case of zero mean flow.

In this section, we continue to verify the new GPU LB model by simulating a pipe terminated with a horn using the same parameters of geometry and flow in accordance with (da Silva, 2008). The acoustic properties inside the pipe in terms of $|R|$ and l/a will be investigated in the current section. Further, the radiation directivity of a pipe terminated with a horn issuing a mean flow of various Mach numbers will be investigated in the next section.

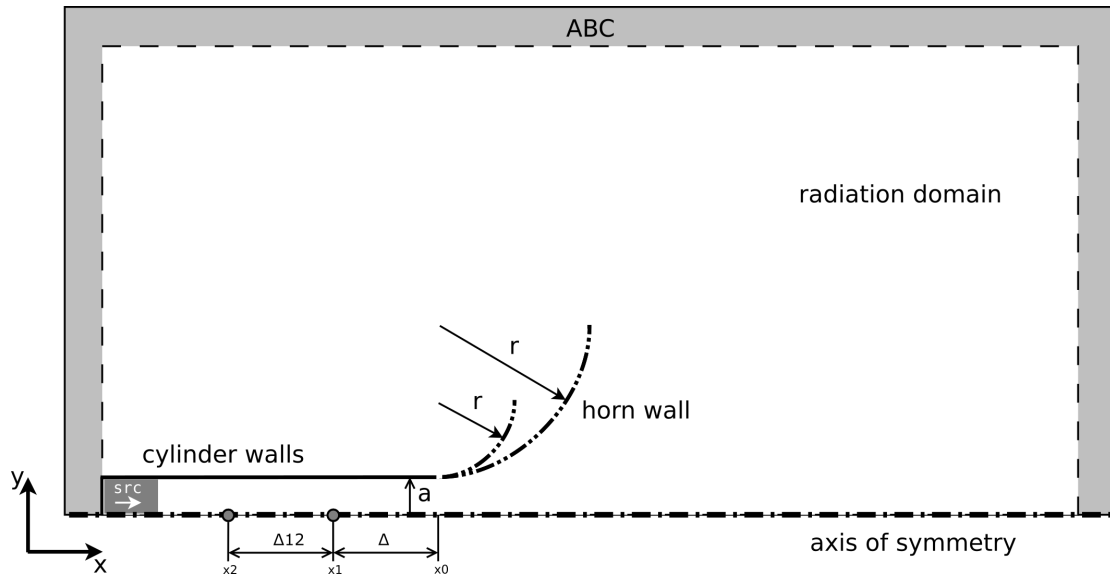


Figure 4.9 LB model of the axisymmetric pipe terminated by a horn for the measurements of reflectance and length correction.

Figure 4.9 depicts the LB scheme of the axisymmetric pipe terminated by a horn for the measurements of reflection coefficient and length correction, which has the same lattice parameters as the one illustrated in Fig. 4.5. The new solid boundary is constructed

by attaching a quarter circle wall to the end of a straight unflanged cylinder. The horn wall is implemented by the curved boundary condition discussed previously in Chpt. 3. Two different cylindrical horns with different curvature radii, namely $r = 2a$ and $r = 4a$, have been investigated.

4.2.4.1 Horns with a Quiescent Flow

Figure 4.10 depicts the magnitude of the reflection coefficient R obtained from the GPU LB model for an unflanged pipe extended by horns with two different curvature radii r . The reflection coefficient is measured at the end of the straight section of the pipe, which is consistent with Peters et al. (1993), Selamet et al. (2001) and da Silva (2008). Since there is no analytical model available for horns, the GPU LBM results are compared with the BEM results provided by da Silva (2008), which are obtained from the software package Sysnoise using the same geometry parameters and are in good agreements with results provided by Selamet et al. (2001). In addition, the theoretical prediction (Levine and Schwinger, 1948) for the $|R|$ of the unflanged pipe without a horn extension is plotted alongside for comparison.

In general, the R obtained from the GPU model is never greater than unity, and its overall shape is in good agreement with the BEM results. Compared with the analytical results of the cylindrical pipe, the influence of the horn extension is almost negligible for the low frequency limit ($ka < 0.2$), but becomes significant for the high frequency limit. The differences between the results of the horns with two different curvature radii are obvious in the high frequency region, where the large curvature radius corresponds to the bigger amount of reflected acoustic wave.

Figure 4.10 depicts the dimensionless length correction l/a in comparison with the BEM results. A general good agreement between the LBM results and the BEM results has been found for horns with both curvature radii. For the low frequency limit $ka < 0.1$, the LBM results are slightly higher than the BEM results, this discrepancy is also found in the previous LBM results provided by da Silva (2008). Compared to the case of $|R|$, the influence of different curvature radii on the length correction l/a is mainly found in the low frequency region. It is interesting that the length correction of the pipe with a horn extension is much higher than that of a straight unflanged pipe, this is because the length corrections presented in Fig. 4.10 comprise the effects of not only the inertial effect of the fluid load surrounding the open end but also the effect due to the extra

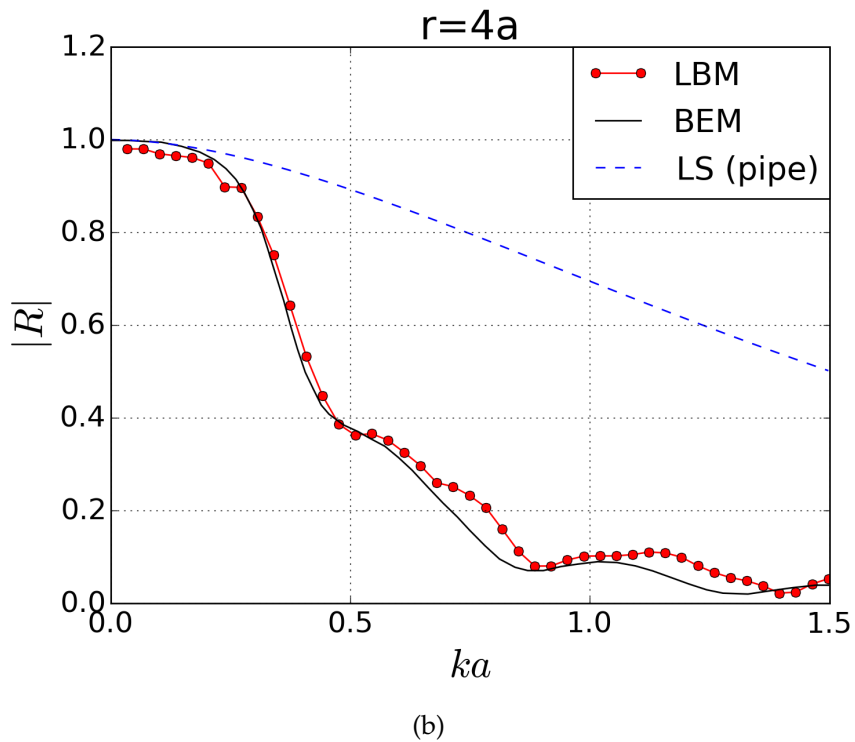
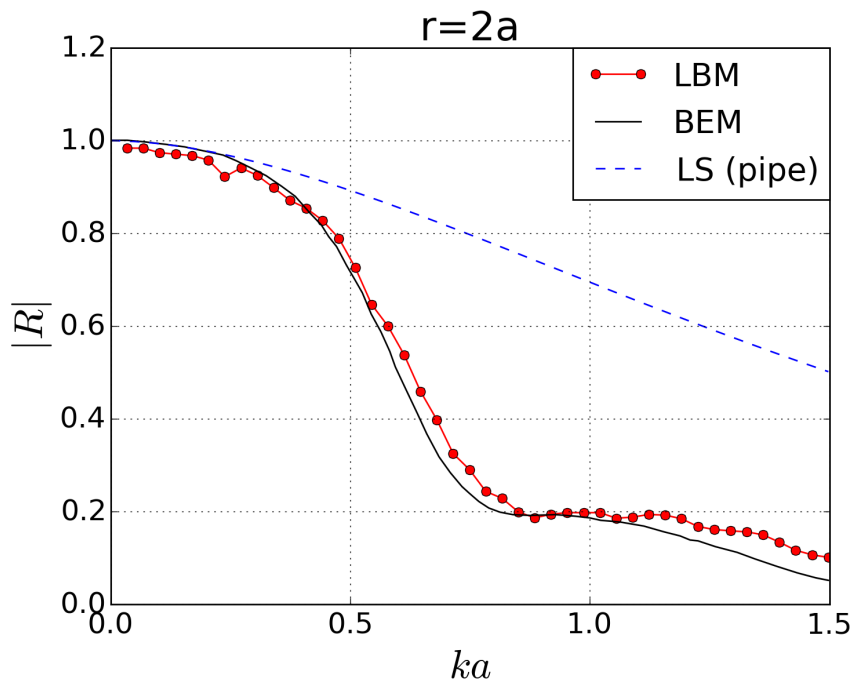
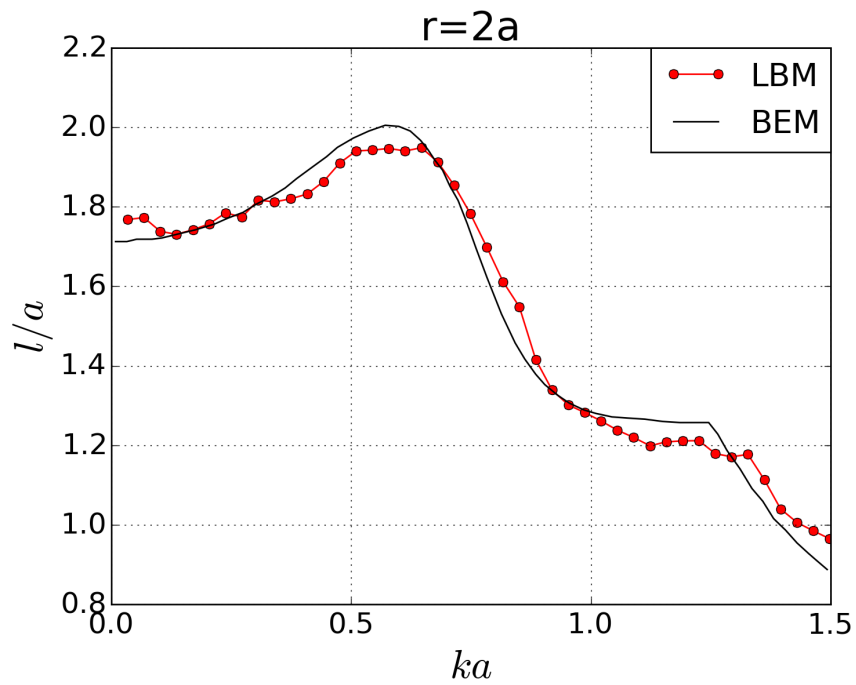
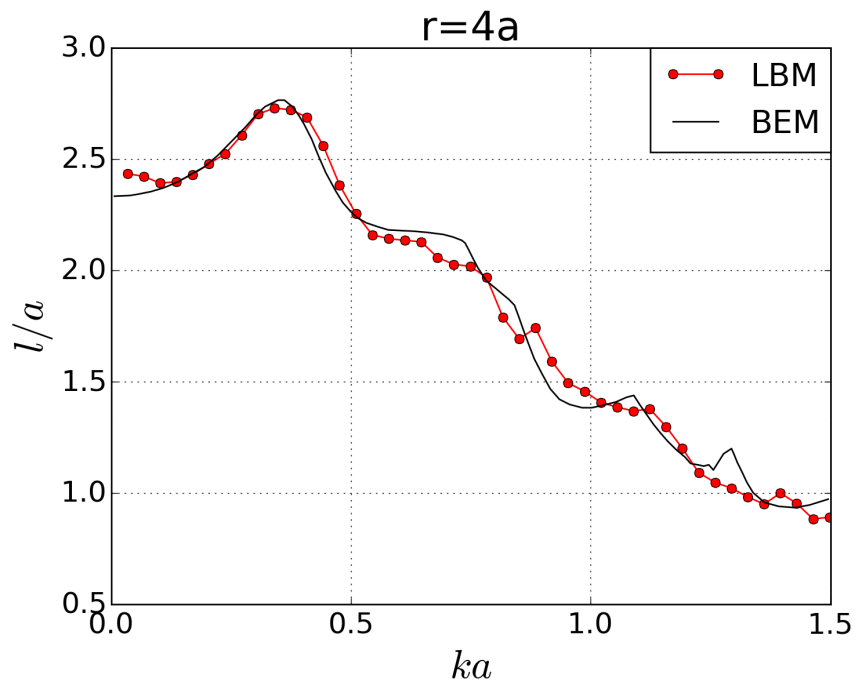


Figure 4.10 GPU SRT model, comparison between LBM and BEM results (da Silva, 2008) of the magnitude of the reflectance $|R|$ as a function of ka for horns with different curvature radii in the absence of a mean flow ($M = 0$): (a) $r = 2a$, (b) $r = 4a$. The $|R|$ of the unflanged pipe without a horn extension (Levine and Schwinger, 1948) is plotted for comparison.



(a)



(b)

Figure 4.11 GPU SRT model, comparison between LBM and BEM results (da Silva, 2008) of the length correction l/a as a function of ka for horns with different curvatures in the absence of a mean flow ($M = 0$): (a) $r = 2a$, (b) $r = 4a$.

length of the horn extension.

4.2.4.2 Horns Carrying a Mean Flow

The LBM results of the acoustic transmission in a cylindrical pipe with horn extensions in the presence of a non-zero mean flow is briefly presented here. Since the purpose is to verify the new GPU LB model on problems involving curved boundaries and a non-zero mean flow, the geometric configurations and flow parameters have been chosen exactly the same as that used by da Silva (2008), i.e., the curvature radii of horn are $r = 2a, 4a$, and the Mach numbers are $M = 0.05, 0.1, 0.15$, respectively.

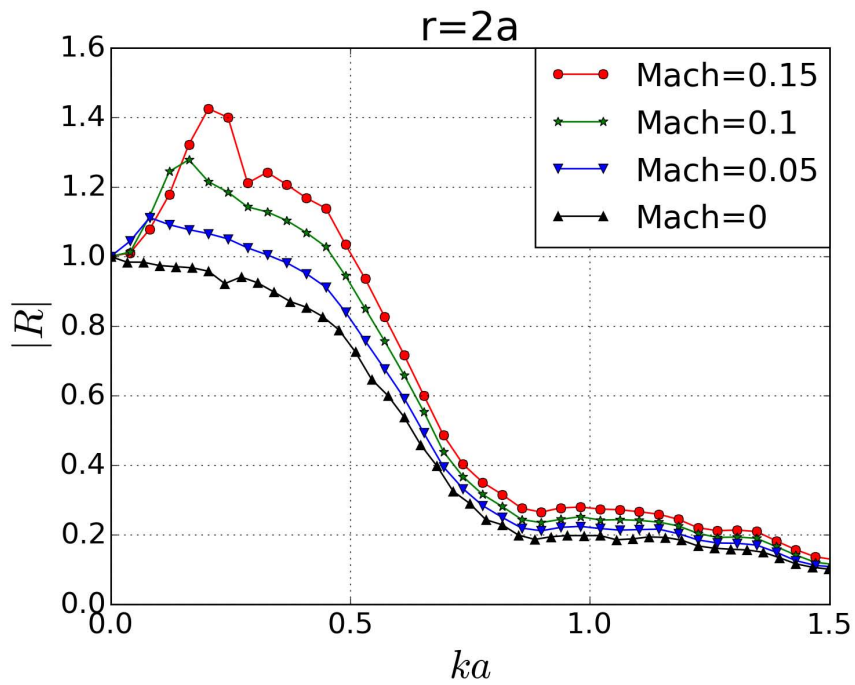
Figure 4.12 depicts the effect of the mean flow and the curvature radii of the horn extension on the behavior of the reflection coefficient $|R|$. In general, the present results are in good agreement with the results obtained from a previous LBM model developed in Matlab by da Silva (2008). For the low frequency limit $0 < ka < 0.5$, the effect of the mean flow on $|R|$ is significant where a peak of $|R|$ much higher than unity is found for both curvature radii, which is similar to the case of the unflanged pipe carrying a mean flow. The magnitude of the peak of $|R|$ seems not to be influenced by the curvature radii. As $ka \rightarrow 0$, the magnitude of R converges to 1 for all Mach numbers and curvature radii of the horns.

For the case of the effect of mean flow on length correction, the results are depicted in Fig. 4.13, which are also in very good agreement to the results reported by da Silva (2008). The effect of a mean flow is only obvious for the low frequency limit $ka < \pi a/2r$, where the length correction drops dramatically as the Mach number increases. The magnitude of the peak of the length correction is not influenced by the mean flow, but is influenced by the curvature radius of the horn.

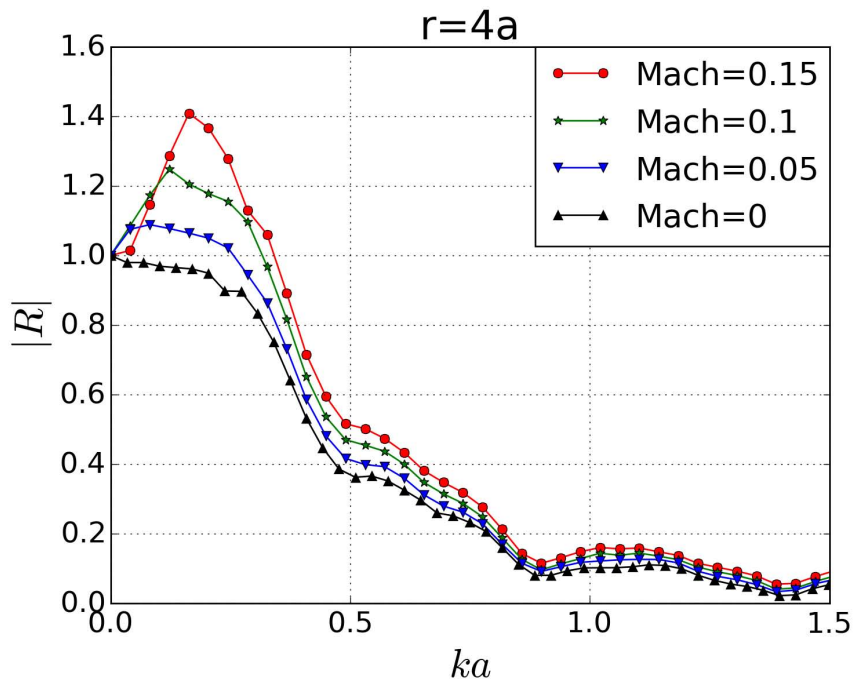
4.2.5 Summary

This section addresses the classical problem of the acoustic transmission in an unflanged cylindrical pipe immersed in a quiescent fluid by using an axisymmetric two-dimensional lattice Boltzmann scheme.

For the case of the cylindrical pipe carrying a zero mean flow, the results of both the CPU SRT model and the GPU SRT model, in terms of pressure reflection coefficient $|R|$ and length correction l/a , have been compared with the established theoretical pre-



(a)



(b)

Figure 4.12 GPU SRT model, comparison of the magnitude of the reflectance $|R|$ as a function of ka for horns with different curvatures in the presence of a mean flow with different Mach numbers: (a) $r = 2a$, (b) $r = 4a$.

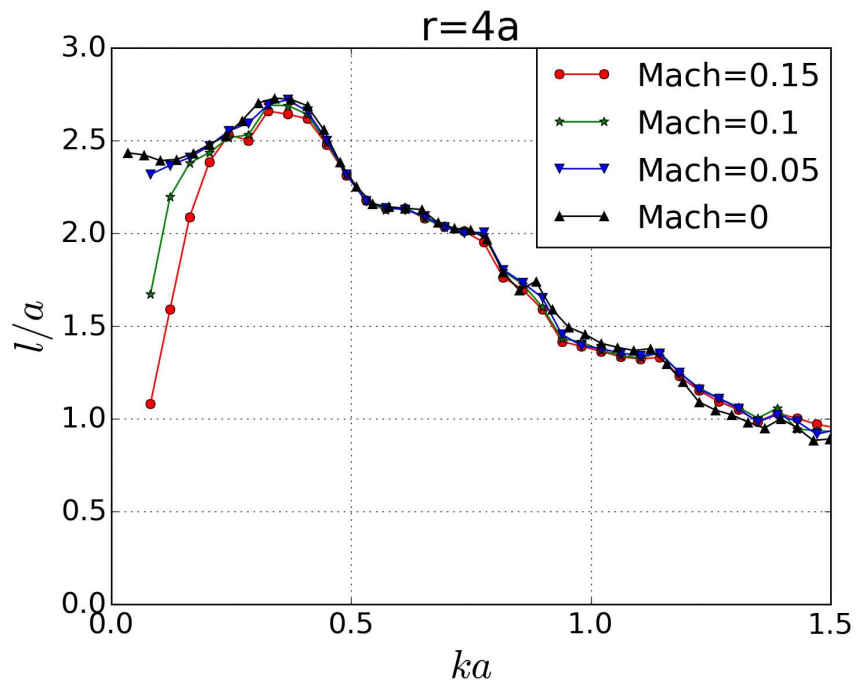
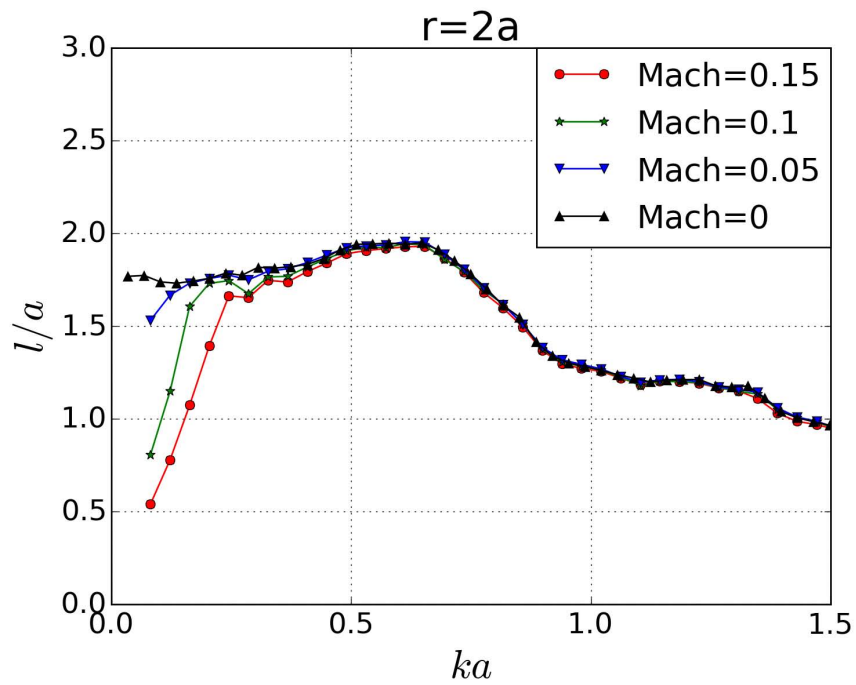


Figure 4.13 GPU SRT model, comparison of the length correction l/a as a function of ka for horns with different curvatures in the presence of a mean flow with different Mach numbers: (a) $r = 2a$, (b) $r = 4a$.

dictions provided by Levine and Schwinger (1948) and excellent agreements have been found. In general, the difference between the CPU SRT model and the GPU SRT model is negligible.

For the case of the cylindrical pipe carrying a non-zero subsonic mean flow, the GPU SRT model has been exclusively used for the numerical simulation. A two-microphone method is used to calculate the complex wavenumbers where the influence of both the thermoviscosity and the convection have been taken into account. The results of pressure reflection coefficient $|R|$ and length correction l/a have been compared with established theoretical predictions provided by Munt (1990) and the experimental data provided by Allam and Åbom (2006). In general, good agreements between the numerical results, the analytical results and the experimental data have been found. However, the numerical results show a shorter length correction for the low frequency limit $ka < 0.2$, and the deviation from the theoretical prediction is larger for a higher Mach number. The discrepancy might be due to two facts. One is that the accuracy of the low compressible LBM model is degraded in the upper limit of the flow velocity $M = 0.15$, another one is that the accuracy of the two-microphone method is degraded in the low frequency limit $ka < 0.2$. Further investigations are needed to address this problem.

The effect of the horn extension attached to the end of a cylindrical pipe has been investigated for different Mach numbers by using the GPU SRT model, where two different curvature radii of the horn have been studied, namely $r = 2a$ and $r = 4a$. For the case of a horn carrying a zero mean flow, the results of $|R|$ and l/a obtained from the GPU SRT model is in excellent agreement with the results obtained from a BEM modeling of the same acoustic system. For the case of a horn carrying a non-zero mean flow, the presented numerical results well agree to the results obtained from a previous LBM model developed in Matlab by da Silva (2008).

Specifically, the reliability and the accuracy of the GPU SRT model is successfully verified by the numerical results presented in this section, where three different conditions have been considered, including 1) the acoustic transmission inside an axisymmetric thin wall cylindrical pipe, 2) the effect of a non-zero subsonic mean flow, and 3) the effect of a curved horn extension attached at the end of pipe. In the next section, the same model will be used to investigate the sound radiation in the far field out of the open end of an axisymmetric waveguide.

4.3 Acoustic Radiation Out of Pipes

4.3.1 Introduction

The mechanisms of sound radiation from the open end of ducts have been investigated by many researchers over the last century and remains an important problem in acoustics. Among all the sound radiation parameters, the acoustic directivity, which is a measure of the angular distribution of acoustic energy around the sound source, is paramount to defining strategies for noise control in systems such as exhaust pipes, jet engines, ventilation systems and so on.

Nevertheless, exact analytical solutions for the directivity problem are only available for very simple geometries (cylindrical and annular pipes) and low compressibility regimes. In situations involving realistic outlet systems, the geometrical characteristics and flow conditions differ considerably from the conditions imposed by available analytical models. For such cases, numerical techniques provide essential tools for addressing the problem.

The first exact analytical model for the sound directivity from cylindrical pipes was proposed by Levine and Schwinger (1948), which was based on the Wiener-Hopf technique. The solution is limited to normal mode propagation (plane waves) and assumes a stagnant mean flow. Munt (1977) extended this model by considering the presence of a low-Mach number mean flow. In his solution, a full Kutta condition is imposed at the edges of the pipe, the mean flow is assumed to be uniform (plug) and the vortex sheet separating the jet and the outer fluid is considered infinitely thin. The solution is exact, provided that the Helmholtz number $ka < 1.5$ and the Mach number $M < 0.3$. Rienstra (1984) improved Munt's solution by introducing a complex parameter to take into account the effects of unsteady vortex shedding in the vicinity of the trailing edge, with particular attention to the energy balance between the sound and the fluid fields. Based on the work of both Munt and Rienstra, Gabard and Astley (2006) presented an extended model that includes a center body for the cases of annular pipe and proposed an explicit numerical procedure for evaluating the solutions for higher frequencies and higher compressibility regimes ($0 < ka < 60$ and $0 < M < 0.8$).

Numerical techniques have also been used to tackle problems of sound radiation directivity of ducts involving more complex conditions. For example, Rumsey et al. (1998) analyzed the generation and propagation of unsteady duct acoustic modes resulting

from a rotor-stator interaction in a 3D configuration by using a Navier-Stokes numerical simulation. Zhang et al. (2004) modeled the sound radiation from an unflanged duct of aircraft engines through linearized Euler equation (LEE) solutions. Özyörük et al. (2004) predicted the sound fields of ducted fans carrying an axisymmetric non-uniform background flow by solving the LEE. Chen et al. (2004) analyzed the planar wave radiation from an unflanged duct by solving the LEE. More recently, Hornikx et al. (2010) presented a numerical solution for calculating the sound field radiated from an automotive exhaust pipe situated over a rigid surface. The mean flow was represented by Reynolds averaged Navier-Stokes equations (RANS) and the sound field represented by the linearized Euler equations, which were resolved with the Fourier pseudo-spectral time domain technique (PSTD). The first work investigating the sound radiation directivity from an unflanged cylindrical pipe was presented by da Silva and Scavone (2007). Their results are in good agreement with the theoretical prediction provided by Levine and Schwinger (1948), but the influence of mean flow over the directivity pattern as well as the comparison with experimental results are not provided. Also, the effect of a geometrical expansion at the pipe end, such as the horn ending or the flare bell normally found in the woodwind instrument family, are not included in their investigation.

The objective of this section is to extend the GPU parallel LB model discussed in the previous section to the problem of the radiation directivity of an unflanged thin pipe carrying either a quiescent flow ($M = 0$) or a subsonic mean flow ($0 < M \leq 0.15$). The conditions will be limited to the radiation of normal (planar) modes and low compressibility regimes. For this reason, the numerical scheme used in this section is based on an isothermal model represented in a two-dimensional axisymmetric scheme. The simulation results for an unflanged thin-wall pipe will be compared to the analytical model provided by Levine and Schwinger (1948) and the experimental data provided by Gorazd et al. (2012), for the case of a zero flow. The directivity results obtained when considering a subsonic mean flow will be compared with the analytical results from Gabard and Astley (2006) and with the experimental results by Gorazd et al. (2012). The phenomenon associated with the *zone of relative silence* observed in the simulations will be discussed. Moreover, the same GPU LB model will be used to investigate the influence of a horn extension attached at the end of the unflanged thin pipe on the radiation directivity. The influence of the numerical precision representing the floating-point numbers will be investigated. Finally, a summary of the results and suggestions for

further investigations will be provided.

4.3.2 Numerical Scheme

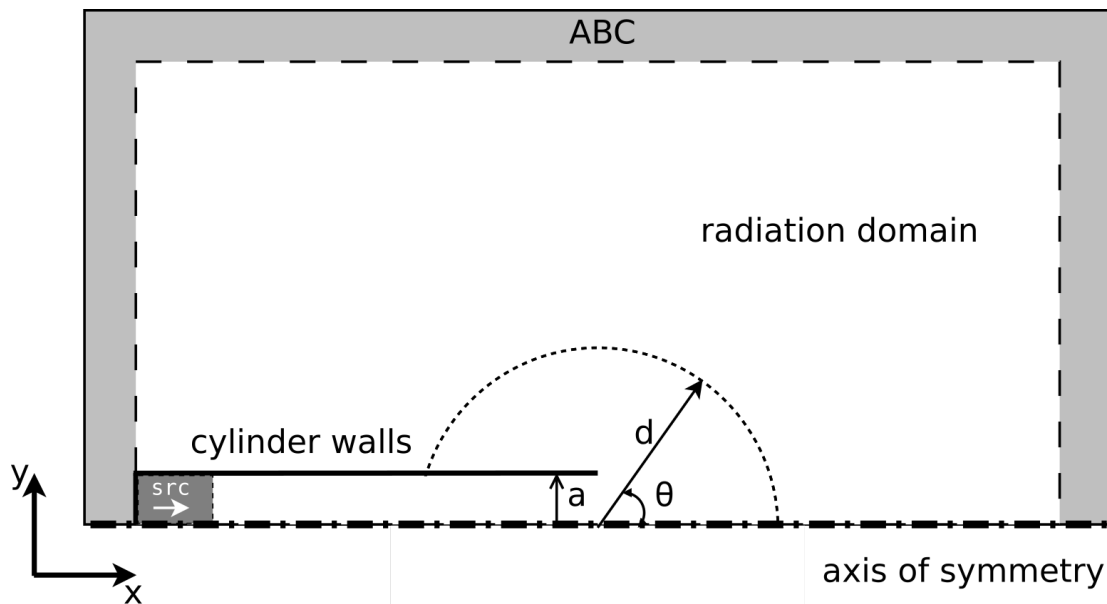


Figure 4.14 LB model of the axisymmetric pipe for the measurements of radiation directivity.

The numerical scheme representing a cylindrical pipe immersed in a rectangular fluid area depicted in Fig. 4.14 is similar to the one presented in Sec. 4.2. Here the purpose is to analyse the external acoustic field in terms of sound radiation directivity, which is the distribution of acoustic energy as a function of the angle measured about the pipe's main axis for plane wave radiation.

The length and the radius of the cylindrical waveguide is $L = 469.5$ and $a = 10$ in lattice cells, respectively. The walls of the waveguide are represented by a solid boundary of zero thickness based on spatial interpolations (Bouzidi et al., 2001; Lallemand and Luo, 2003). The outer walls are treated by a simple bounce-back scheme, the inner walls are treated using a free-slip scheme. The relaxation parameter of the SRT model is set to $\Omega = 1.75$ for all Mach numbers, which is equivalent to a dimensionless viscosity of $\nu = 0.0238$. In fact, due to the BGK limitations, the viscosity asserted is one order of magnitude higher than that of air in normal conditions. A higher viscosity could result in two significant effects: 1). Accentuated wave dissipation, particularly at higher

frequency components, and 2). Spurious directivity artifact caused by the interaction between the viscous boundary layer and the rim of the pipe. In fact, if the viscosity is relatively high, the pipe can be seen as a capillary tube, where the radiation directivity is dominated by viscous phenomena. These effects are significantly minimized by measuring sound pressures at positions sufficiently close to the sound source (open end) and imposing a free-slip condition at the pipe wall. This last boundary condition is in accordance with the exact model from Munt (1977), which is inviscid and the singularity at the sharp edge of the pipe is treated with a full Kutta condition.

The system is excited by the swept-frequency broadband signal described in Eq. 4.26, running from $ka = 0.1$ to $ka = 3.8$ (less than the first evanescent mode of the pipe). For the case of a non-zero mean flow, the source signal is superimposed on a DC offset. The excitation is implemented by a source buffer with a length of 60 cells at the left end of the pipe using the same technique as an absorbing boundary condition but prescribed by a non-zero target velocity, which is obtained from the source signal buffer on each iteration. An initialization time is set to $N_t = 800,000$ to allow the fluid in the whole domain to accelerate from stagnation to a steady state.

The time histories of fluid density are probed at 75 points evenly distributed around the semi-circle (corresponding to angle increments of 2°), with the center point at the outlet of the duct in the range of $\theta = 0^\circ$ to $\theta = 150^\circ$. The measuring points are rounded to the nearest lattice nodes. The measuring distance is $d = 250$ cells from the outlet. The acoustic pressure p' is calculated by

$$p'(\theta, t) = (\rho(\theta, t) - \rho_0)c_s^2, \quad (4.35)$$

where $\rho(\theta, t)$ is the spontaneous fluid density and ρ_0 is the equilibrium density. For the case of zero mean flow, ρ_0 is nearly a constant and usually has the value of 1. For non-zero mean flow, however, ρ_0 in the vicinity of the probing points fluctuates over time and the fluctuating density cannot be calculated by simply subtracting the stagnant field density (a value of 1) from the spontaneous fluid density. For such a case, a DC-blocking filter specified by the transfer function $H(z) = (1 - z^{-1})/(1 - \alpha z^{-1})$ can be used to remove the offset caused by the flow, where the value of α is usually given by 0.995 and z is the Laplace Transform variable. A smaller α allows faster tracking of fluctuation of DC levels but at the cost of greater low-frequency attenuation.

Once the time history of acoustic pressures has been obtained, the pressure directivity as a function of angle θ and frequency f can be calculated by

$$G(\theta, f) = \frac{P(\theta, f)}{P_h}, \quad (4.36)$$

where $P(\theta, f)$ is obtained through performing a Fourier transform on the time history of sound pressure $p'(\theta, t)$ measured at the same distance d and $P_h = \sqrt{\sum P^2(\theta)/N}$ is the square root of the averaged value of $P^2(\theta, f)$ over all measured angles.

4.3.3 A Pipe Carrying a Quiescent Flow

The LBM scheme in the absence of mean flow is first validated by comparing its results with the established analytical model proposed by Levine and Schwinger (1948) in the form of relative pressure directivity. For six different frequencies expressed in terms of the Helmholtz number ($ka = 0.48, 1, 2, 2.5, 3, 3.5$) that are below the cut-on frequencies of higher-order modes, the numerical simulations of both CPU SRT model and GPU SRT model are in good agreement with the analytical results, as shown in Fig. 4.15 and Fig. 4.16, respectively. The tiny ripples found for $ka = 0.48$ and $ka = 1$ in the numerical results can be explained by the fact that $G(\theta)$ should be measured in the far-field condition, which is not fully satisfied for low frequencies given the size of the lattice (1000×500 cells) and the measuring radius (250 cells) used in this study (due to computation time limits). Not surprisingly, the results for higher frequencies ($ka \geq 2$) are smooth and the ripples are barely observed.

There are small discrepancies between the results of CPU model and GPU model. For example, for angles less than about 15° and $ka = 2.5, 3.0, 3.5$, there are about 2 dB drops in the results of GPU model compared to that of the CPU model. This is likely due to the effect of the 32-bit precision of the floating-point numbers used on the GPU platform, which is not a salient issue for acoustic signals inside the pipe, but has a more prominent influence over the acoustic signals probed in the far field carrying a relatively lower energy.

To evaluate the far-field condition in this simulation, we measured the acoustic impedance $Z = P/U$ as a function of ka at a distance $d = 250$ and angle $\phi = 0$ from the outlet of the pipe, where P and U are obtained by performing a Fourier transform on the time history of acoustic pressure p and particle velocity u , respectively. As depicted in Fig.

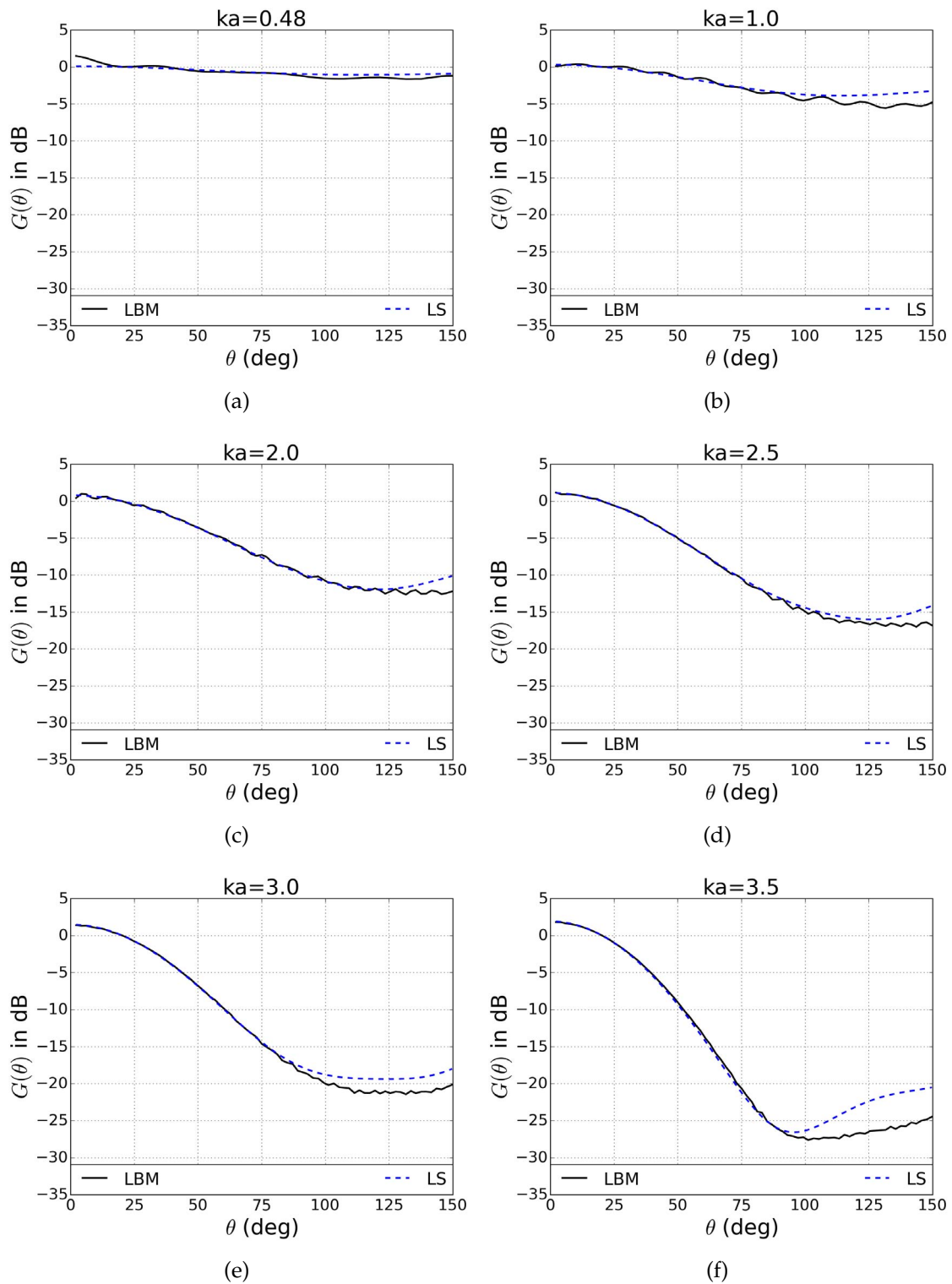


Figure 4.15 CPU SRT 64-bit model, comparison between numerical (solid) and analytical predictions Levine and Schwinger (1948) (---) of the acoustic pressure directivity as a function of the angle in the absence of a mean flow: (a) $ka = 0.48$, (b) $ka = 1$, (c) $ka = 2$, (d) $ka = 2.5$, (e) $ka = 3$, (f) $ka = 3.5$.

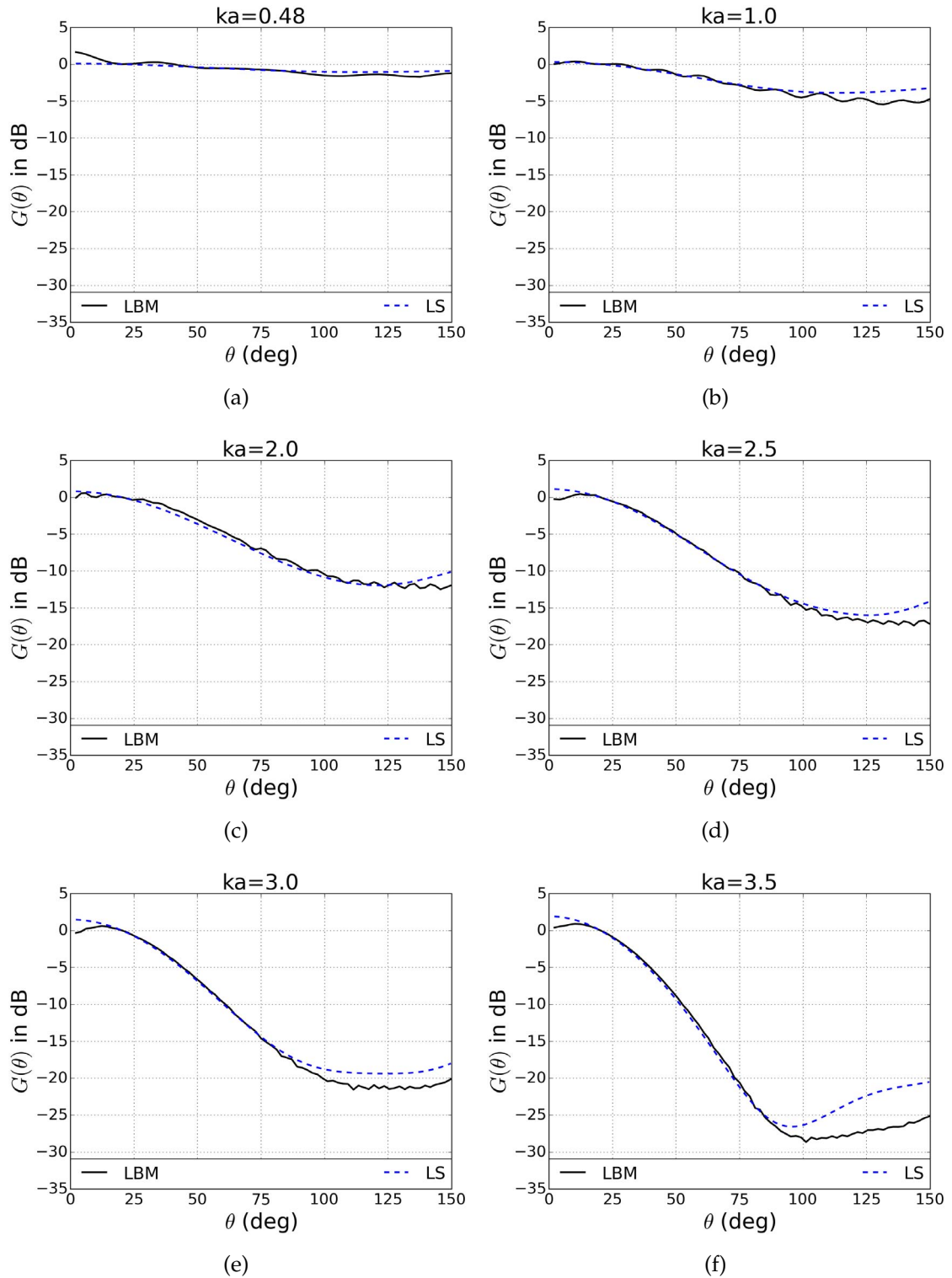
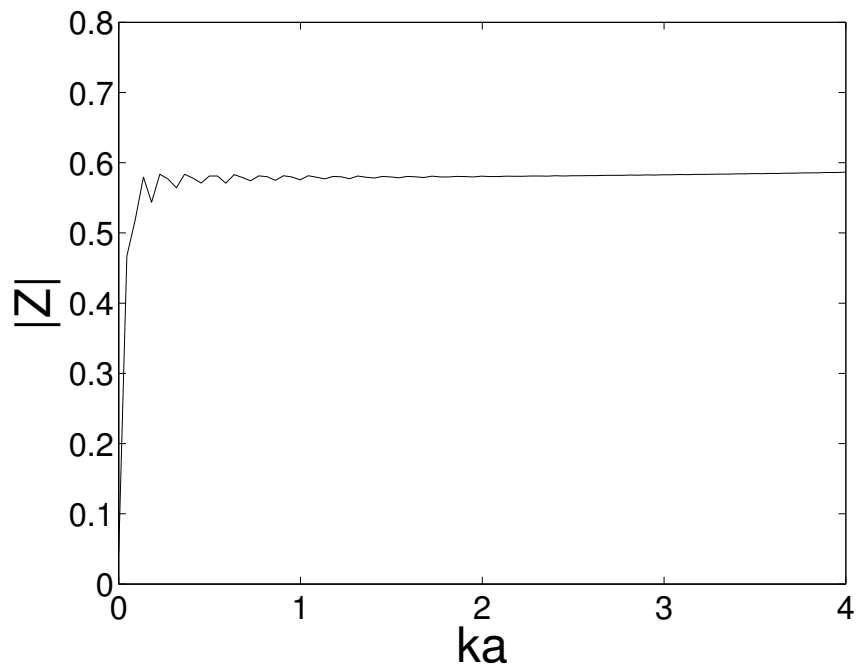
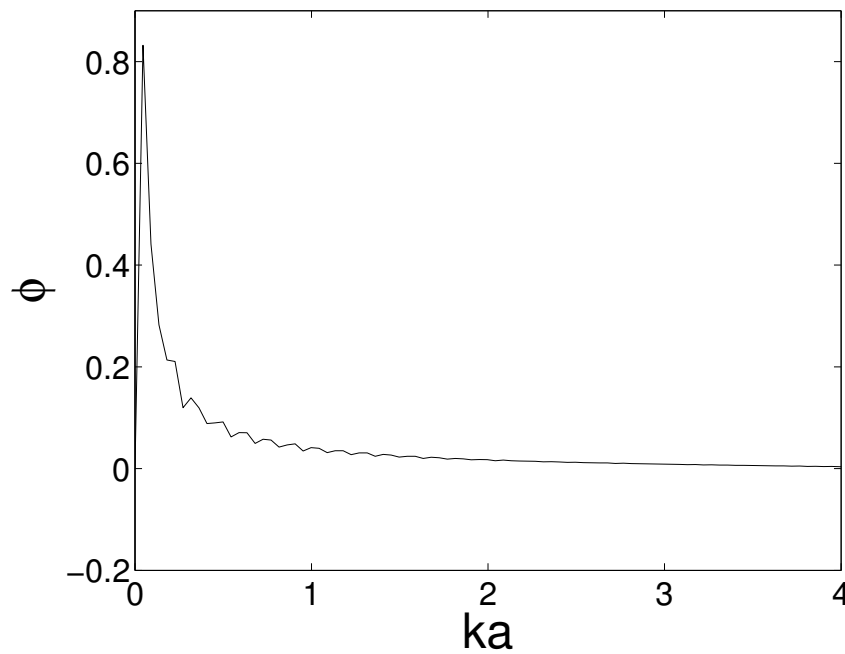


Figure 4.16 GPU SRT 32-bit model, comparison between numerical (solid) and analytical predictions Levine and Schwinger (1948) (---) of the acoustic pressure directivity as a function of the angle in the absence of a mean flow: (a) $ka = 0.48$, (b) $ka = 1$, (c) $ka = 2$, (d) $ka = 2.5$, (e) $ka = 3$, (f) $ka = 3.5$.



(a)



(b)

Figure 4.17 Evaluation of the far-field condition in terms of acoustic impedance in the radiation domain: (a) amplitude of acoustic impedance, (b) phase of acoustic impedance. The measuring distance is $d = 250$ cells from the outlet.

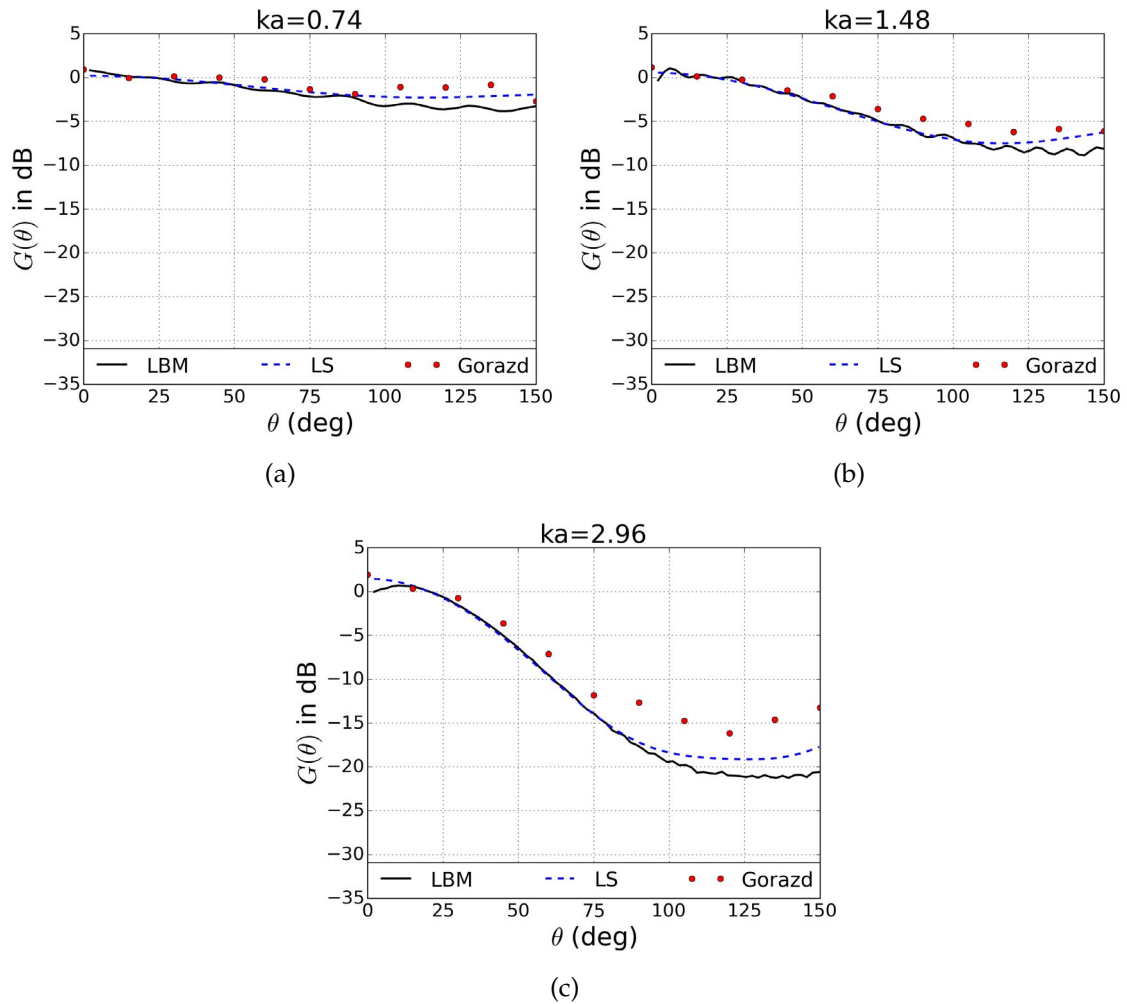


Figure 4.18 GPU SRT model, comparison between numerical (solid), analytical predictions (---) and experimental measurements (red dot) of the acoustic pressure directivity as a function of the angle in the absence of a mean flow ($M = 0$): (a) $ka = 0.74$, (b) $ka = 1.48$, (c) $ka = 2.96$.

4.17(a), the amplitude of the impedance Z quickly approaches the characteristic impedance of the medium, $Z_c = \rho_0 c_s$, for values of $ka \geq 1$. A similar phenomenon can be found for the phase between the acoustic pressure and particle velocity, ϕ , which gradually approaches zero for $ka \geq 2$, as depicted in Fig. 4.17(b). It is worth mentioning that the phase and the characteristic impedance will never converge completely to zero and ρc , respectively, due to the viscous nature of the fluid (Viggen, 2011). The results suggest that the far-field condition is not fully satisfied for $ka < 1$, while for $ka \geq 1$, the acoustic impedance Z of the spherical wave propagating into the radiation domain approximates that of a plane wave.

The results of both Fig. 4.15 and Fig. 4.16 show discrepancies at high angles (more obvious for $\theta > 100^\circ$). We believe that the high viscosity may change the characteristics of sound dispersion in the simulation, which consequently influences the radiation directivity and results in errors.

From Fig. 4.15(f) and Fig. 4.16(f), we can observe smoothing of directivity characteristics of numerical results in the vicinity of $\theta = 100^\circ$ compared to that of the analytical results for the high frequency $ka = 3.5$. That might be attributed to the issue that, in the numerical simulation, there may be some transfer of energy from the exciting broadband signal to higher-order modes, while for the case of the analytical model, no higher modes are involved and the energies are exclusively coming from the dominant plane mode. More specifically, the exact analytical model derived by Levine and Schwinger only takes into account the directivity due to plane mode propagation up to $ka = 3.82$. While the source in this study acts like a piston, it is possible that energy might be transferred to higher-order modes (via mode-coupling) near structural discontinuities, either in the form of evanescent or perhaps even propagating waves. Due to the shortness of the pipe, some of the energy associated with these higher modes may find its way out of the pipe. A similar phenomenon was reported in a recent experimental measurement conducted by Gorazd et al. (2012), where the curves presenting the directivity characteristics of the experimental results (excited by broadband noise) around $\theta = 100^\circ$ and for higher frequencies ($ka \geq 2.96$) are smoothed compared to those analytical results obtained for a single-frequency exciting signal.

In the next step, the numerical (GPU SRT model) and analytical results are compared with the experimental results by Gorazd et al. (2012) in the form of relative pressure directivity. All three results (numerical, analytical and experimental) have been nor-

malized to the same dB level, as depicted in Fig. 4.18. For the two lower frequencies of $ka = 0.74$ and 1.48 and for angles within the range of $0^\circ < \theta < 90^\circ$, the three results are in good agreement with each other, despite the fact that the measurements are carried out using 1/3 octave broadband noise and the calculation of numerical and analytical results are based on a single frequency. As the angle increases, the measurements are still in good agreement with the analytical results, though the numerical results have discrepancies less than $3 dB$ compared to the analytical results. For the higher frequency of $ka = 2.96$, the numerical results are in good agreement with both the analytical results and the measurements for angles within the range of $0^\circ < \theta < 75^\circ$. As the angle increases from 75° to 150° , both the measurements and the numerical results deviate from the analytical results, but in opposite ways. Compared to the analytical results, the highest discrepancies are found at the largest angle of $\theta = 150^\circ$, which is $+3.8 dB$ for the measurements and $-2.6 dB$ for the numerical results, respectively.

4.3.4 A Pipe Carrying a Mean Flow

For the case of a cold mean flow (i.e., the temperature gradient between the jet and the outer stagnant flow is zero) with a low Mach number ($M = 0.036$), the numerical results of the GPU model are compared with the theoretical prediction given by Gabard and Astley (2006) as well as the recent experimental results obtained by Gorazd et al. (2012) in the form of normalized pressure directivity, as depicted in Fig. 4.19. All three results (numerical, analytical and experimental) have been represented in the form of pressure directivity and normalized to the same dB level.

In general, the results are in good agreement for angles in the range $0^\circ < \theta < 60^\circ$. Discrepancies between the numerical and analytical results become more obvious as the angle increases and the maximum differences are found to be at $\theta = 150^\circ$, i.e., $-3.11 dB$ for $ka = 0.74$, $-2.22 dB$ for $ka = 1.48$ and $-2.3 dB$ for $ka = 2.96$, respectively. For all three frequencies and for most angles, the analytical solution is located between the numerical and the experimental results.

For the case of a cold mean flow with a higher Mach number ($M = 0.15$), the numerical results of the GPU model are compared with the theoretical prediction only, since no experimental results are available from (Gorazd et al., 2012) for $M = 0.15$. The comparisons are depicted in Fig. 4.20. In general, good agreement is found for angles in the range $30^\circ < \theta < 150^\circ$. For most angles, the discrepancy from the theory is less than 3

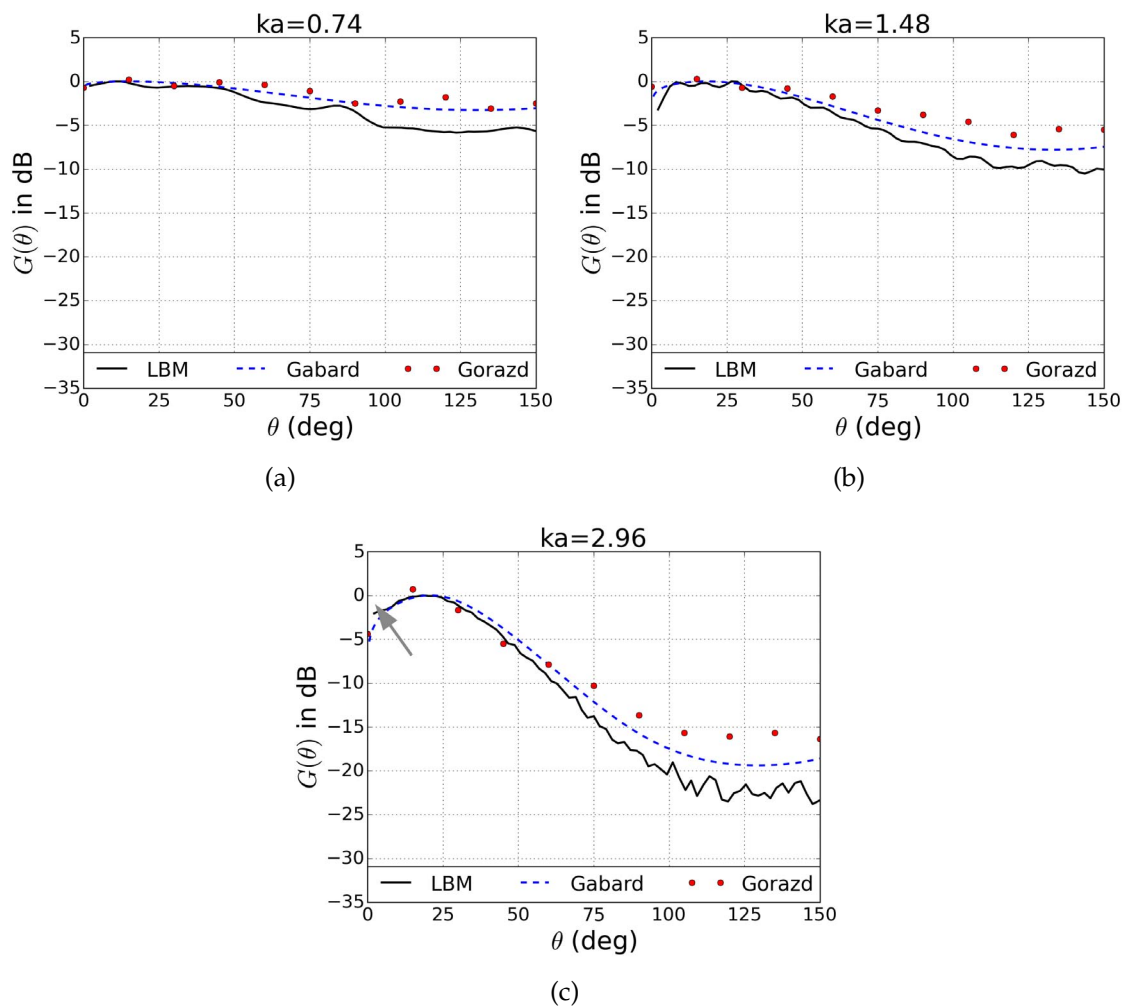


Figure 4.19 GPU SRT model, comparison between numerical (solid), analytical predictions (---) and experimental measurements (red dot) of the acoustic pressure directivity as a function of the angle in the presence of a mean flow at $M = 0.036$: (a) $ka = 0.74$, (b) $ka = 1.48$, (c) $ka = 2.96$. The zone of relative silence is indicated by a grey arrow.

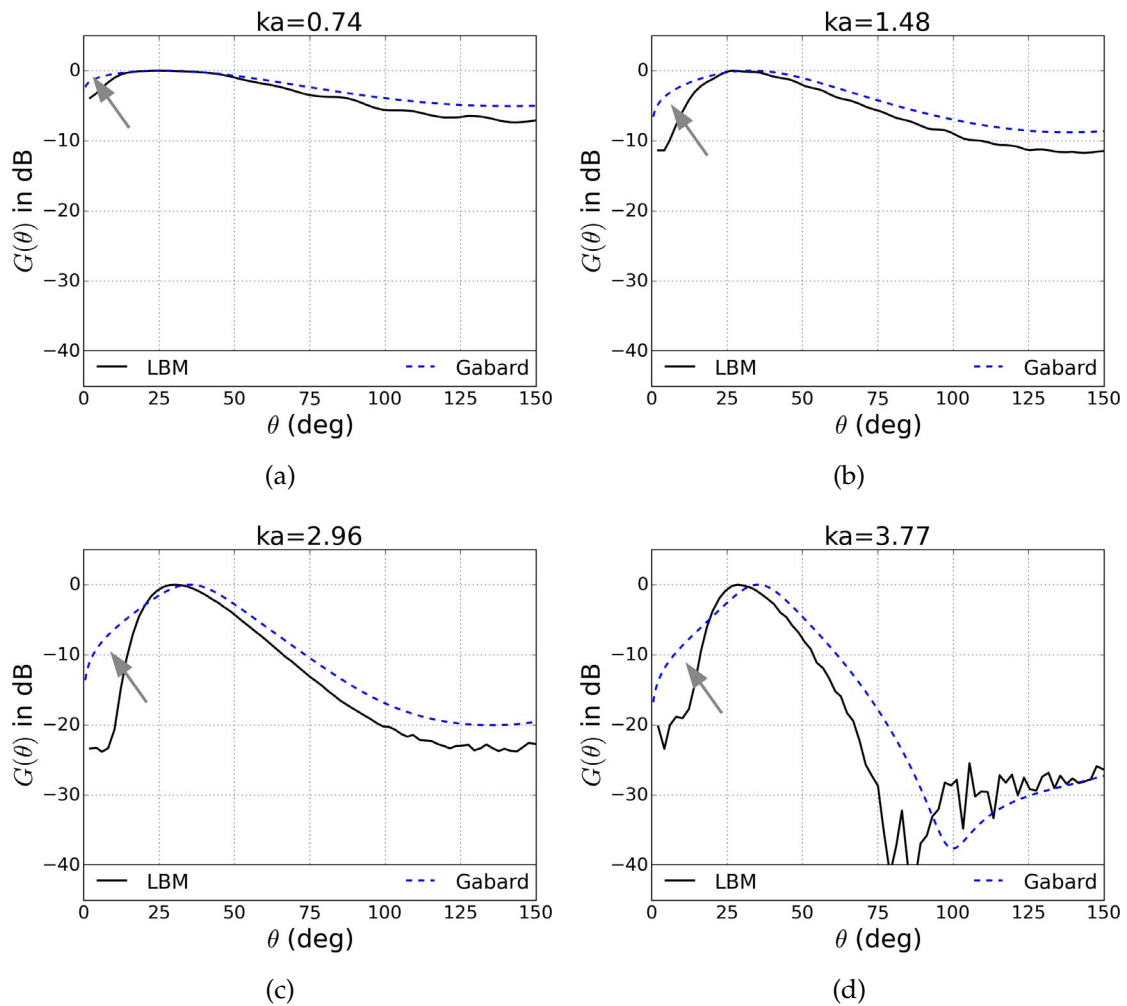


Figure 4.20 GPU SRT model, comparison between numerical (solid), analytical predictions (---) of the acoustic pressure directivity as a function of the angle in the presence of a mean flow at $M = 0.15$: (a) $ka = 0.74$, (b) $ka = 1.48$, (c) $ka = 2.96$, (d) $ka = 3.77$. The zone of relative silence is indicated by a grey arrow.

dB. The deviation of the simulation from the theoretical results is mainly found in the region of angles less than 30° . Interestingly, the trough at $\theta = 100^\circ$ found in the analytical results for $ka = 3.77$ is actually observed in the numerical curve but at a lower angle and with some fluctuations. This is in contrast to the result obtained from a previous 64-bit LB model excited by a single chirp signal (Shi et al., 2013), where the trough is totally missed in the previous numerical results. The improvement in the current numerical result might be owing to the new exciting signal comprising both a linear and a logarithmic chirp component used in the current LB model, which has a better balanced energy in the high frequency region.

An important feature of the directivity characteristics in the presence of a non-zero mean flow concerns the so-called *zone of relative silence*, where the sound wave in the vicinity of the axis is subject to additional attenuation. The result from the theoretical analysis of Savkar (1975) and Munt (1977) suggests that, for high frequencies and large Mach numbers, the zone of relative silence is so obvious that a cusp can be observed at $\theta = \theta_s$ in the directivity pattern. Assuming that the medium outside the duct is stagnant and the speed of sound remains constant, the zone of relative silence is defined by its characteristic angle (Savkar, 1975)

$$\theta_s = \cos^{-1} \left(\frac{1}{1 + M} \right), \quad (4.37)$$

where M is the Mach number inside the duct.

Even for the case of a low Mach number ($M = 0.036$), the zone of relative silence ($\theta_s = 15.15^\circ$) can be observed in both the experiments and the numerical results for $ka = 2.96$, as depicted in Fig. 4.19(c). For the case of a higher Mach number ($M = 0.15$), the zone of relative silence ($\theta_s = 29.59^\circ$) are more obviously observed in the numerical results for all four frequencies ($ka = 0.74, 1.48, 2.96$ and 3.77).

However, we also observed that the numerical results demonstrate significant discrepancies compared to Gabard's model for the region of angles less than 30° . This might be either due to the effect of high viscosity of the LBM scheme or some unknown effects associated with the 2D axisymmetric LBM scheme, where the higher modes can not be captured, and some spurious 2D transversal modes might be generated per se. The modes below the cut off frequency die out exponentially as they propagate downstream and their contribution on the directivity is negligible, although some acoustic energy

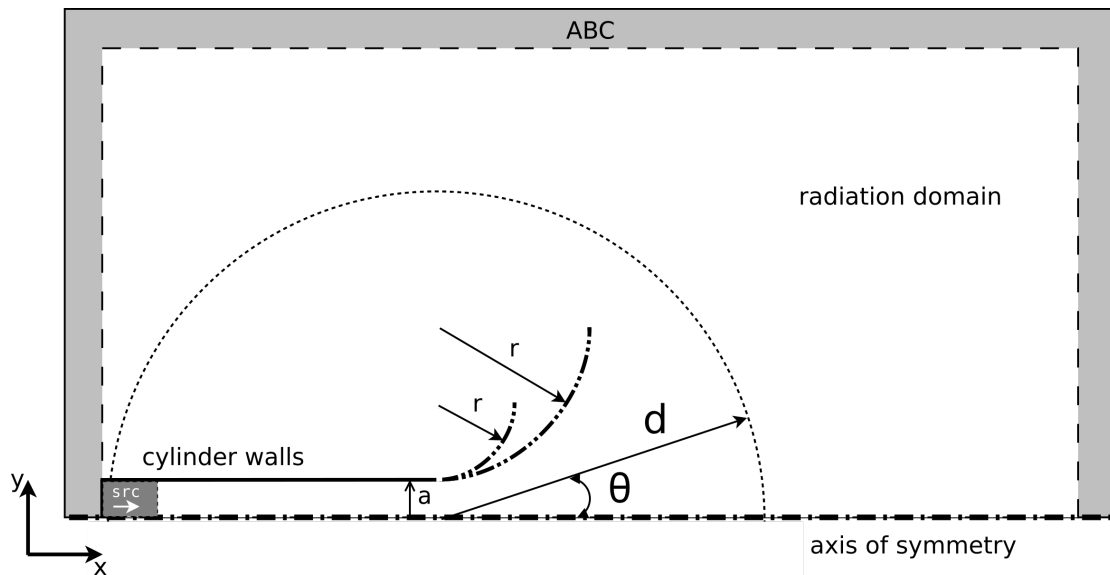


Figure 4.21 LB model of the axisymmetric pipe terminated by a horn for the measurements of radiation directivity.

associated with these modes may find its way out of the pipe due to its reduced length. However, at values of ka above the first cut off frequency for plane modes ($ka > 1.8$), the energy associated with transversal modes will propagate downstream and provide a significant contribution on the directivity pattern. This is evidenced in Fig. 4.20(c) ($ka = 2.96$) and 4.20(d) ($ka = 3.77$), where the highest deviation from Gabard's model for the region of angles less than 30° is more than 10 dB .

4.3.5 Pipes with Horn Extension

In Sec. 4.2.4, we have presented the reflection coefficient and length correction of a pipe terminated by a horn with two different curvature radii obtained from the GPU LB model. The effect of mean flow has also been investigated. Using the same GPU LB model, we are able to investigate the effect of the horn extension on acoustic radiation directivity in the far field of the same system.

Figure 4.21 depicts the LB scheme of the axisymmetric pipe terminated by a horn for the measurements of radiation directivity. The system has the same geometry parameters as the one illustrated in Fig. 4.9 for the measurement of reflection coefficient and length correction. Two cylindrical horn profiles have been investigated, namely

$r = 2a$ and $r = 4a$, where r is the curvature radius of the horn. The horn wall is implemented by the curved boundary condition discussed previously. The lattice parameters of the LB model and the flow parameters are identical to that used in the model depicted in Fig. 4.14. The simulation is carried out for three different Mach numbers, i.e., $M = 0, 0.036, 0.1, 0.15$.

The procedure of signal probing and processing follows the same steps described in Sec. 4.3.2. The time histories of the acoustic pressure $p'(\theta, t)$ are probed at 75 points evenly distributed around the semi-circle (corresponding to an angle increments of 2°), with the center point at the intersection of the straight pipe and the horn extension in the range of $\theta = 0^\circ$ to $\theta = 150^\circ$. The measuring distance is $d = 250$ cells from the center point (which is actually much larger than it appears in Fig. 4.21). The pressure directivity $G(\theta, f)$ is calculated from the acoustic pressure distribution in far field by Eq. 4.36.

The radiation directivity pattern as a function of ka and Mach numbers obtained from the far field of the end of pipe with horn extensions are presented in Fig. 4.22, for the horn profile of $r = 2a$, and Fig. 4.23, for the horn profile of $r = 4a$, respectively. Since there is no analytical prediction and experimental results of radiation directivity available for horn carrying mean flow, the numerical results are compared with the theoretical directivity shape of the unflanged pipe in the absence of mean flow provided by Levine and Schwinger (1948). In the following discussion, for convenience, the numerical model of the pipe with a horn extension will be called *LBM horn* and the analytical model of the cylindrical unflanged pipe without a horn extension will be called *LS pipe*, respectively.

In general, both the geometry parameter (the horn profile) and the flow parameter (Mach number) play important roles in the directivity pattern. The influence of the geometry parameter can be evaluated by comparing the curves of the LBM horn and the LS pipe for the case of zero mean flow ($M = 0$). If we divide the whole region into a low angle region and a high angle region by $\theta \approx 20^\circ$, which is close to the characteristic angle θ_s discussed in Eq. 4.37, we can observe that the value of $G(\theta)$ of the LBM horn is much lower than that of the LS pipe for the cases of $ka \leq 2.5$ in the high angle region. This trend can be found for cases of both $r = 2a$ and $r = 4a$, which suggests that the horn extension strongly influences the directivity characteristic of the pipe.

The phenomenon of zone of relative silence has been discussed previously in Sec.

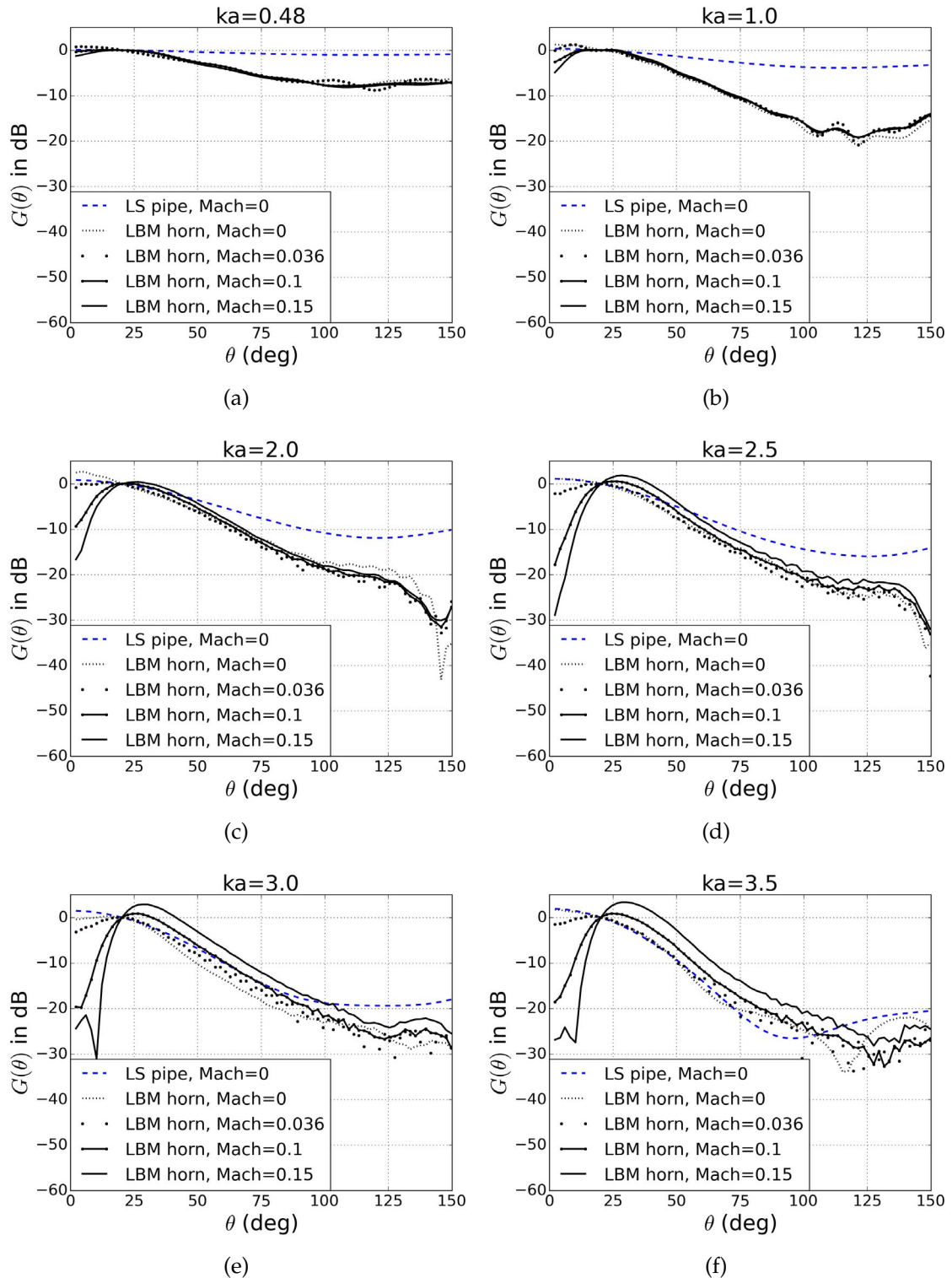


Figure 4.22 GPU SRT 32-bit model, comparison between analytical predictions Levine and Schwinger (1948) (unflanged pipe, - - -) and numerical (horn radius= $2a$) of the acoustic pressure directivity as a function of the angle in various mean flow: (a) $ka = 0.48$, (b) $ka = 1$, (c) $ka = 2$, (d) $ka = 2.5$, (e) $ka = 3$, (f) $ka = 3.5$.

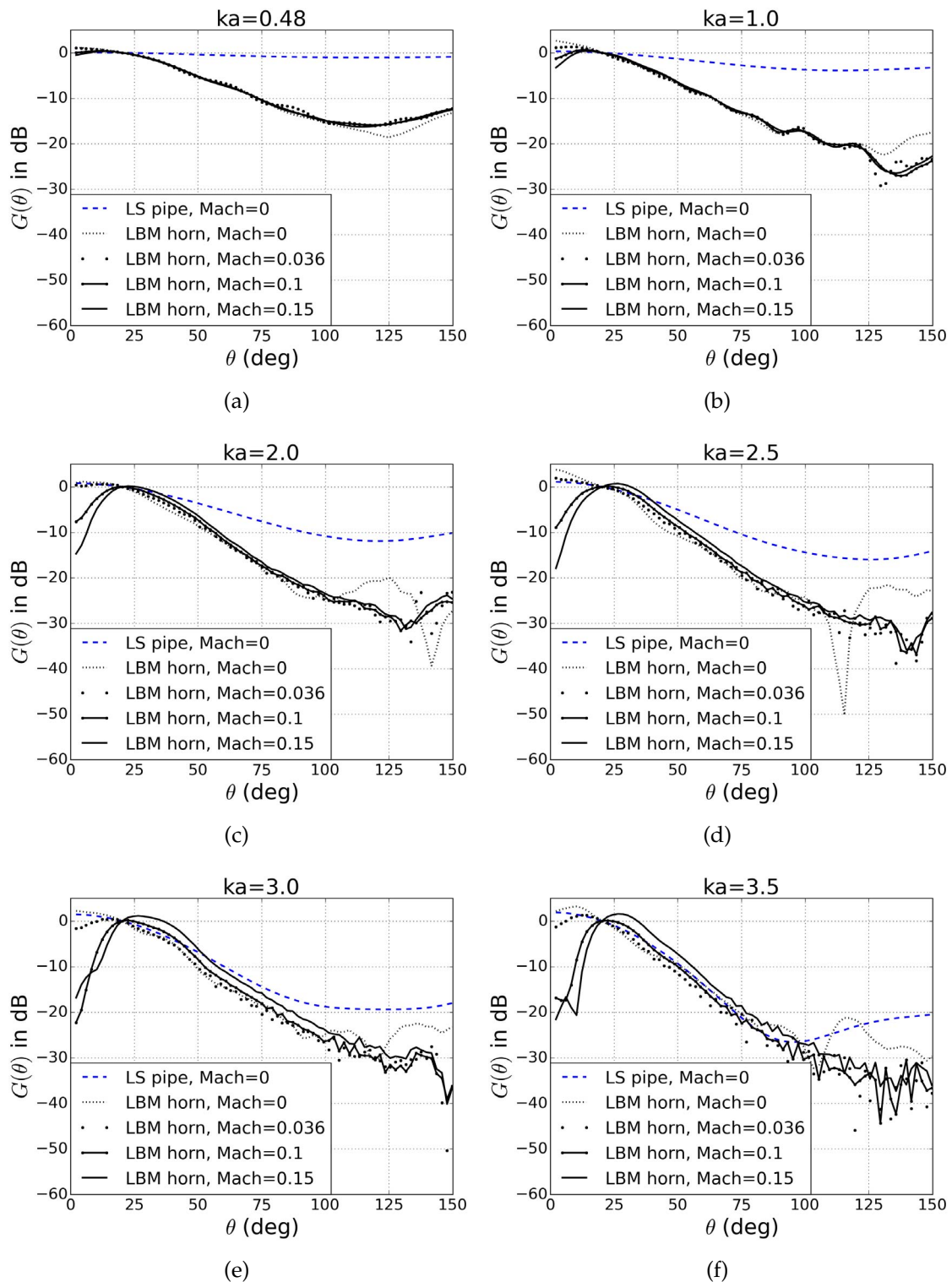


Figure 4.23 GPU SRT 32-bit model, comparison between analytical predictions Levine and Schwinger (1948) (unflanged pipe, - - -) and numerical (horn radius= $4a$) of the acoustic pressure directivity as a function of the angle in various mean flow: (a) $ka = 0.48$, (b) $ka = 1$, (c) $ka = 2$, (d) $ka = 2.5$, (e) $ka = 3$, (f) $ka = 3.5$.

4.3.4. For the case of non-zero mean flow ($M > 0$), the same phenomenon also can be observed in the directivity patterns of the LBM horn, where a peak at the characteristic angle θ_s (Eq. 4.37) can also be found. In fact, the directivity characteristic is strengthened by the horn extension in the presence of a mean flow. For example, for the case of the highest jet velocity ($M = 0.15$) and the highest frequency ($ka = 3.5, 3.77$), the difference of the value of $G(\theta)$ at $\theta = 0$ and its peak value at θ_s in the curve of the LBM horn is about 8 dB bigger than that found in the LS pipe. This phenomenon of *stronger directivity* is also observed in the high angle region of the curve of the LBM horn. For example, for the case of the highest mean flow speed $M = 0.15$, the difference of $G(\theta_s)$ and $G(\theta = 150^\circ)$ for the LBM horn is about 27 dB at the frequency of $ka = 3.0$ and 26 dB at $ka = 3.5$, where the corresponding difference for the LS pipe is about 22 dB at $ka = 2.96$ and 24 dB at $ka = 3.77$. The phenomenon of zone of relative silence is reinforced by the flow speed for the LBM horn and the characteristic angle θ_s is influenced by the Mach number, which is also found for the case of unflanged pipe.

The influence of the curvature radius of the horn extension on the directivity pattern can be observed by comparing Fig. 4.22 ($r = 2a$) and Fig. 4.23 ($r = 4a$). In the low angle region (inside the zone of relative silence), the $G(\theta)$ is influenced by the effect of mean flow to a lesser extent for the case of $r = 4a$ than that for the case of $r = 2a$. In the high angle region ($\theta > \theta_s$), the value of $G(\theta)$ of the LBM horn with the bigger curvature radius ($r = 4a$) for all Mach numbers is much lower than that for the case of the smaller curvature radius ($r = 2a$). In other words, a bigger curvature radius of the horn extension results in a stronger directivity pattern, i.e., a larger deviation from the LS model in general. Interestingly, for the case of $r = 4a$, the variation of the value of θ_s associated with the Mach number is less than that for the case of $r = 2a$.

4.3.6 Influence of Bit Depth

In order to investigate the influence of the bit depth representing the floating-point numbers used in the CPU and GPU model, especially its influence on the relatively weak signal obtained in the far field, the simulation of the acoustic radiation directivity from an unflanged pipe carrying a zero mean flow is performed on the same LB SRT model implemented on three different platforms: the CPU SRT 64-bit model, the CPU SRT 32-bit model and the GPU SRT 32-bit model. The CPU 64-bit model and the CPU 32-bit model are implemented on the Python/NumPy platform by specifying the data type of

NumPy array to float64 and float32, respectively, where the float32 represents a single precision (32 bits in total, including a sign bit, 8 bits exponent and 23 bits mantissa) and the float64 represents a double precision (64 bits in total, including a sign bit, 11 bits exponent, 52 bits mantissa). The GPU 32-bit model is implemented on the PyCUDA platform by using the class of *pycuda.gpuarray.GPUArray*, which supports a NumPy-like array with 32-bit precision by default.

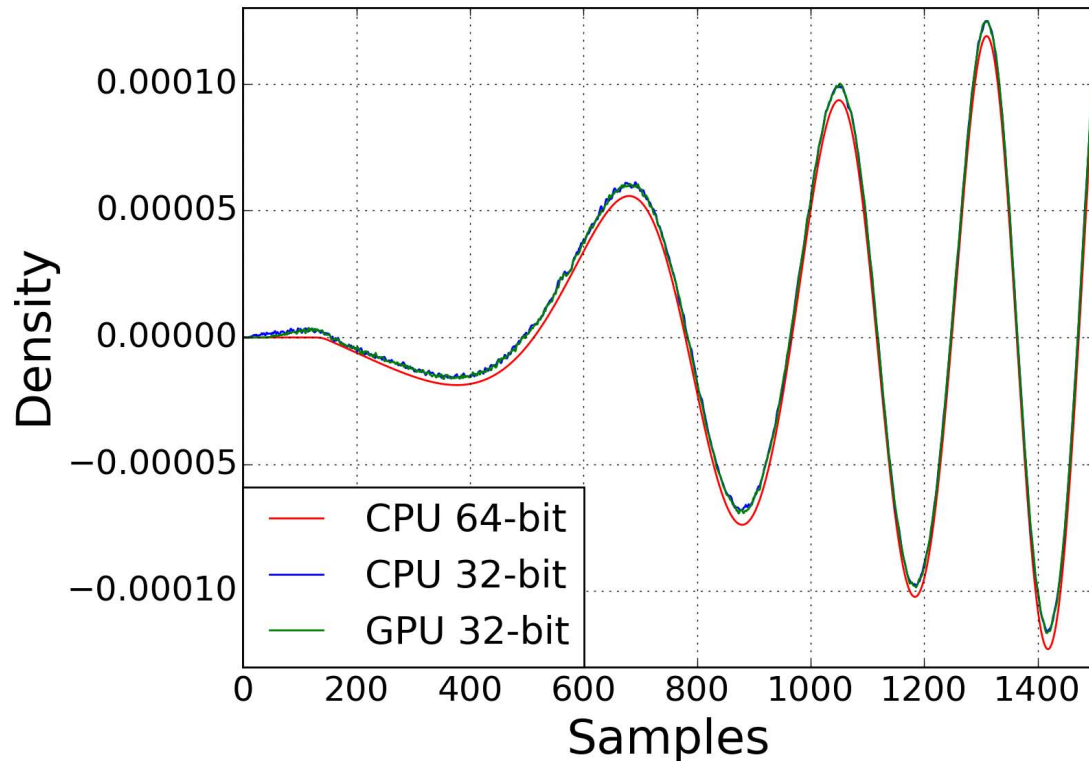


Figure 4.24 Comparison the results of three LBM-SRT models (CPU SRT 64-bit, CPU SRT 32-bit and GPU SRT 32-bit), Acoustic density signals are probed at a distance of 250 cells and angle of 32 degree from the open end.

Figure 4.24 depicts the first 1500 samples of the acoustic density signals probed at a distance of 250 cells and angle of 32° from the open end of a cylindrical pipe in the three different LB-SRT models. Some small irregularities can be observed on the signal probed from both the CPU 32-bit model and the GPU 32-bit model, where the signal probed from the CPU 64-bit model is smooth. The waveform of the signal obtained from both the CPU 32-bit model and the GPU 32-bit model slightly deviated from that obtained from the CPU 64-bit model. It can also be observed that the difference between the signal

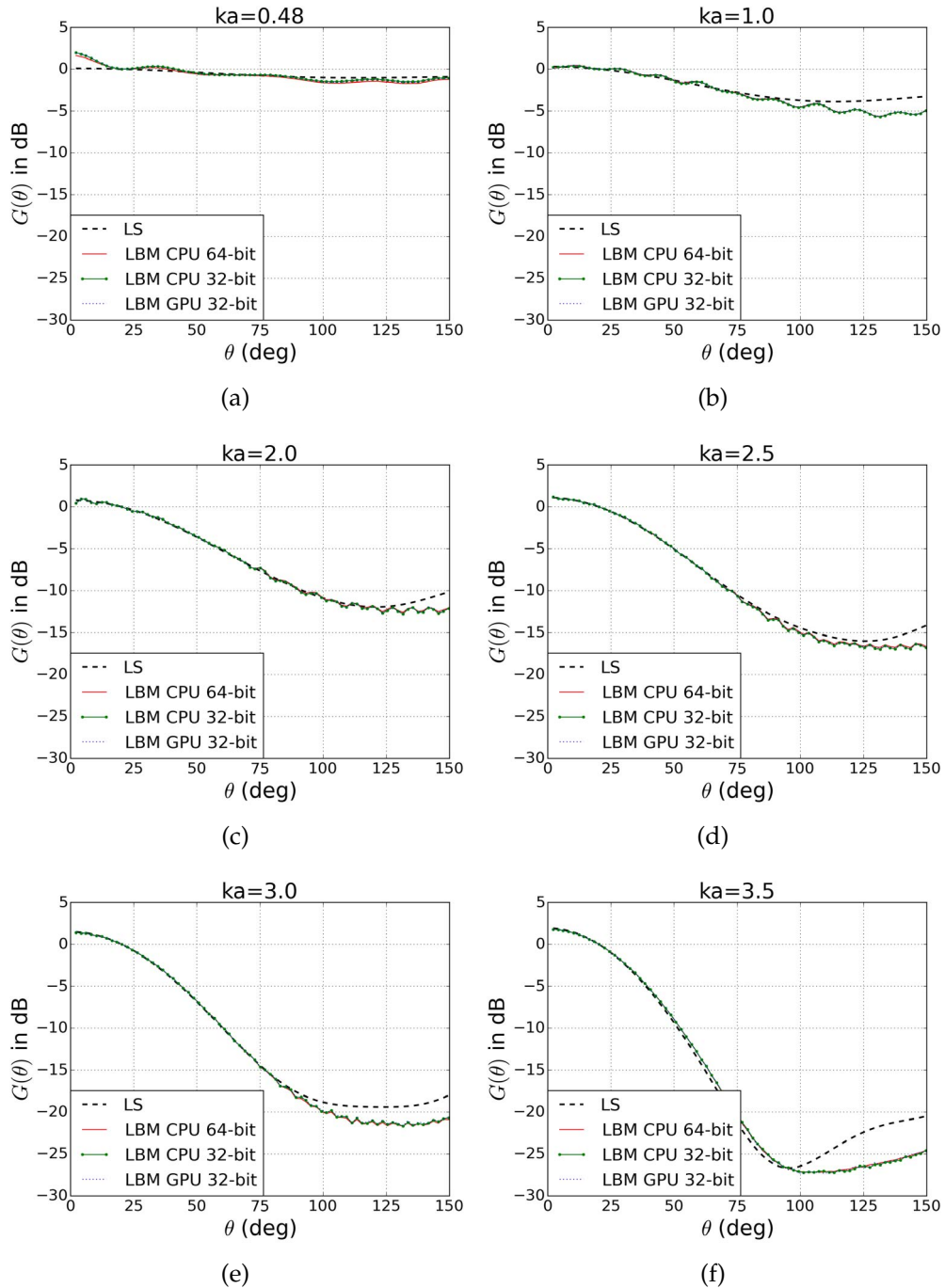


Figure 4.25 Comparison of numerical results between three LBM-SRT models (CPU 64-bit, CPU 32-bit, GPU 32-bit) and analytical predictions Levine and Schwinger (1948) (---) of the acoustic pressure directivity as a function of the angle in the absence of a mean flow: (a) $ka = 0.48$, (b) $ka = 1$, (c) $ka = 2$, (d) $ka = 2.5$, (e) $ka = 3$, (f) $ka = 3.5$.

probed from the CPU 32-bit model and the GPU 32-bit model is almost negligible.

Figure 4.25 depicts the radiation directivity pattern obtained from the CPU 64-bit model, the CPU 32-bit model and the GPU 32-bit model, alongside the theoretical prediction provided by Levine and Schwinger (1948). Despite the tiny difference found in the time history of the probed signals from the three models, in general the discrepancies between the directivity patterns of the three LB models is barely noticeable, though there is a tiny difference between the numerical results obtained from the 32-bit models (CPU and GPU) and the CPU 64-bit model.

4.3.7 Summary

This section presents a numerical investigation of the sound radiation pattern at the open end of axisymmetric cylindrical waveguides using an axisymmetric two-dimensional LBM SRT scheme implemented on both CPU and GPU platforms.

The CPU SRT model and the GPU SRT model were first validated by comparing the numerical results with the analytical prediction provided by Levine and Schwinger (1948) and the experimental results provided by Gorazd et al. (2012) for the case of an unflanged cylindrical pipe carrying a quiescent flow. Then for the case of an unflanged cylindrical pipe carrying a non-zero mean flow, the numerical results of the GPU SRT model were compared with the theoretical prediction provided by Gabard and Astley (2006) for Mach number $M = 0.036$ and $M = 0.15$ as well as experimental results obtained by Gorazd et al. (2012) for Mach number $M = 0.036$. Very good agreement was found between the theoretical and experimental results for the case of no flow and the lower Mach number of $M = 0.036$. For the relatively higher Mach number of $M = 0.15$, the numerical result agrees well with the theoretical prediction for angles greater than 30° , though significant discrepancies are observed for angles less than 30° . The effects of the so-called zone of relative silence are clearly observed in the results of non-zero mean flow even for a very low Mach number ($M = 0.036$). This is interesting for studies of musical acoustics involving woodwind instruments, which normally exhibit a very low Mach number flow.

The aforementioned discrepancies for the case of $\theta < 30^\circ$ and $M = 0.15$ are not well explained yet. For further investigations conducted by either experimental measurements or numerical simulations, some limitations should be considered. The theoretical model of the unflanged cylindrical pipe carrying a mean flow assumes an infinitely thin

vortex sheet separating the jet and the neighboring quiescent fluid, which is not true for far field situations. In addition, the present numerical simulation shows that the directivity pattern in directions close to the axis is very sensitive to the probing distance, which is probably due to the influence of the unstable vortex sheet with the lip of the pipe. Moreover, in order to better explain the aforementioned smoothing effects demonstrated in the LBM results (see Fig. 4.15(f) and Fig. 4.16(f)), we need more insight towards the axisymmetric D2Q9 model in terms of its capability of fully representing the higher radial modes, although the anti-axisymmetric circumferential modes are not supported for sure.

The effect of a horn extension at the open end of a thin wall cylindrical pipe on acoustic radiation directivity in far field is investigated using the GPU LB model. The results show that both the geometry parameter of the horn extension and the flow parameter play an important role in the directivity pattern. The influence of the horn profile is evaluated by comparing its directivity pattern to that of the unflanged cylindrical pipe for the case of zero mean flow. The result shows that the directivity effect is reinforced by the horn extension. For the case of non-zero flow, the phenomenon of zone of relative silence observed in the system of a cylindrical pipe attaching a horn extension presented in Sec. 4.3.4 is similar to that observed in the system of an unflanged cylindrical pipe presented in Sec. 4.3.5. The influence of the curvature radius of the horn extension is investigated, where it shows that a big curvature radius of the horn results in a stronger directivity effect.

Finally, the influence of the bit depth representing the floating-point numbers on different computation platforms is investigated for the relatively weak acoustic signal measured in the radiation field out of the cylindrical waveguide. The results show that the accuracy of the GPU LB model is almost the same as the CPU LB model in 32-bit mode and is in general good enough for the sound radiation problems, although the accuracy of the 64-bit model is slightly better than that of the 32-bit models.

4.4 Aeroacoustic Behavior of Whistles

4.4.1 Introduction

The objective of this section is to numerically investigate the aeroacoustic behavior of whistles using the GPU LB model. In this section, we continue to ascertain the reliabil-

ity, validity and the extension of applicability of the GPU LB model on acoustic systems, especially for those involving conditions of complicated curved boundary and relative high speed fluid volume flow in that they are typically found in wind instruments and remain a challenge to the numerical stability and accuracy of LBM models. Compared to the simple geometry of a cylindrical pipe or horn, a whistle has a complicated geometry and is very difficult, if not impossible, to investigate analytically. For this reason, the whistle is chosen as the target acoustic system to be investigated numerically. Besides, the numerical technique of simulating a whistle will be re-used in Chpt. 5 to simulate a clarinet, for which the numerical stability is also challenged by the complicated geometry and the relatively high speed fluid volume flow.

The sound production of aerodynamic whistles and air-reed instruments, or the phenomenon of flow-excited acoustic resonance in general, is subject to the interaction of two closely integrated systems: the aerodynamic generator, which includes an air jet impinging on a sharp edge (the labium) acting as an acoustic dipole, and the ancillary structure functioning as an acoustic resonator.

Depending on the sound generating mechanisms, Chanaud (1970) categorized aerodynamic whistles into three classes. Class I whistles only consist of purely hydrodynamic oscillations such as aeolian tones. Class II whistles involve direct acoustic feedback but without any ancillary structures. Examples of this type of whistle include edge tones, hole tones, ring tones and human whistling, etc. Class III whistles are those featured by a resonant or reflecting structure controlling the frequency of the tone.

The musical instruments of Class III include the ocarina, Chinese Xun, Japanese tsuchibue, etc., and the flute-like instruments, such as flute, organ pipe, recorder, etc. The ocarina-type instruments are distinguished by a Helmholtz resonator. On the other hand, the resonator of a flute-like instrument consists of a pipe-like air column. We consider the sport whistle as a special ocarina-type instruments characterized by a Helmholtz resonator excited by the edge tone.

The edge tone phenomenon, produced by blowing a jet of air that impinges on a sharp edge, has been investigated by a number of authors but its mechanics are still not completely understood. Since some decades ago, the theory and empirical formulas for edge tones have been presented by a number of authors (Brown, 1937a,b; Curle, 1953; Powell, 1961; Coltman, 1968, 1976). Brown (1937a) might be the pioneer who experimentally investigated the edge tone. In his apparatus, both the velocity of the air exiting

a brass slit and the distance of wedge-to-orifice can be adjusted. Using a setting of constant jet velocity, he found the threshold of distances for the onset and extinction of an edge tone. Then using a setting of constant distance, he demonstrated four stable stages of edge tone related to different velocities. The dependence of the frequency f of the edge tone on the distance h and the jet velocity U for a specific slit width of 1.0 mm is described by an empirical formula

$$f = 0.466k(U - 40.0)(1/h - 0.07), \quad (4.38)$$

where $k = 1, 2.3, 3.8$ and 5.4 are coefficients related to the four different stages corresponding to the fundamental frequency and other overtones. In the same stage, the frequency of oscillation is in proportion to the jet velocity U , but it jumps to another stage hysteretically if U exceeds a threshold value. In another paper, Brown (1938) provided valuable discussion regarding the interaction between edge tones and pipe tones.

4.4.2 Previous Works

In the last two decades, there has been growing interest in the use of computational fluid dynamic (CFD) tools or computational aeroacoustic (CAA) techniques based on the solution of the Navier-Stokes equations to investigate the aero-acoustic behaviors of edge tones and the more complicated phenomenon related to acoustical feedback from an ancillary resonator. However, the direct numerical simulation (DNS) of aero-acoustic problems are still expensive and limited to simple geometries and short time scales (typically 10 to 20 ms), which is due to the huge consumption of computing resources.

Dougherty et al. (1994) numerically replicated Brown's experiments of edge tone including all four stages by using a compressible full Navier-Stokes flow solver based on a finite-volume scheme and obtained excellent agreement on frequency results compared with Brown's data. The direct simulation of flute-like instruments can be found in more recent literature by Obikane and Kuwahara (2009), Obikane (2009, 2011) and Giordano (2013, 2014). Giordano simulated a recorder using a two-dimensional and then a three-dimensional Navier-Stokes solver based on a finite difference scheme and presented both qualitative results concerning dynamics of the density and air jet, and quantitative results for the sound spectrum and its dependence on blowing speed. On the other hand, the numerical simulation of ocarina-type instruments is less commonly found in

literature. Kobayashi et al. (2009) reproduced the sound vibration of an ocarina and investigated the relationship between the oscillation frequencies and the blowing speed using compressible large-eddy simulations (LES). Miyamoto et al. (2010) simulated a recorder-like instrument using the LES method and showed interesting results including spatial distributions of air density, flow velocity, vorticity and Lighthill's aeroacoustic source. They also compared the changes of frequencies with jet velocity to both edge tone and resonance frequencies of the pipe. Liu (2012) simulated a pea-less whistle using a hybrid CFD scheme and compared the frequencies with the experimentally measured results. But as Kobayashi et al. (2009) pointed out, the hybrid model consisting of separate stages of fluid mechanics and sound propagation is not well suited for simulating a Helmholtz resonance subjected to the elastic property of air.

The LBM modeling of flue instruments was pioneered by Skordos's work on recorders and organ pipes (Skordos, 1995). He simulated the interaction between fluid flow and the acoustic waves within the instruments at different blowing speeds based on a two-dimensional model. Kühnelt (2003, 2004, 2005, 2007) simulated several flute-like instruments including organ pipe and square flue pipe using three-dimensional LB models and obtained interesting results including the visualization of jet formation and vortex motion, the time history of fluctuating density and the steady state spectra at different jet speeds. Unfortunately, due to the restriction of computer resources, Kühnelt's models are based on rather simplified geometries with a large lattice spacing (in the range from $dx = 0.175$ to 0.3 mm). Also, he had to increase the viscosity by 10 times higher than air to maintain the numerical stability, and consequently increased the jet speed by the same factor to get an identical Reynolds number.

In this study, we carried out the simulation of pea-less sport whistles using the two-dimensional LBM. The relatively simple implementation of boundary conditions of the LBM allows us to handle the complicated curved boundary measured from a real whistle. Skordos (1995) and Kühnelt (2003, 2004, 2005, 2007) used unrealistic higher viscosities in their LBM scheme to maintain numerical stability. This was most likely due to the restriction of the single relaxation time (SRT) scheme, which is prone to be unstable in conditions of very low viscosities. In contrast, we used the multiple relaxation time (MRT) scheme to maintain the numerical stability and consequently we were able to use a more realistic, lower viscosity appropriate for air in our simulations. However, we should keep in mind that LBM is slightly compressible and valid for $M < 0.15$. Due to

this reason, the blowing speeds in our simulations are restricted to relatively low values.

4.4.3 Numerical Scheme

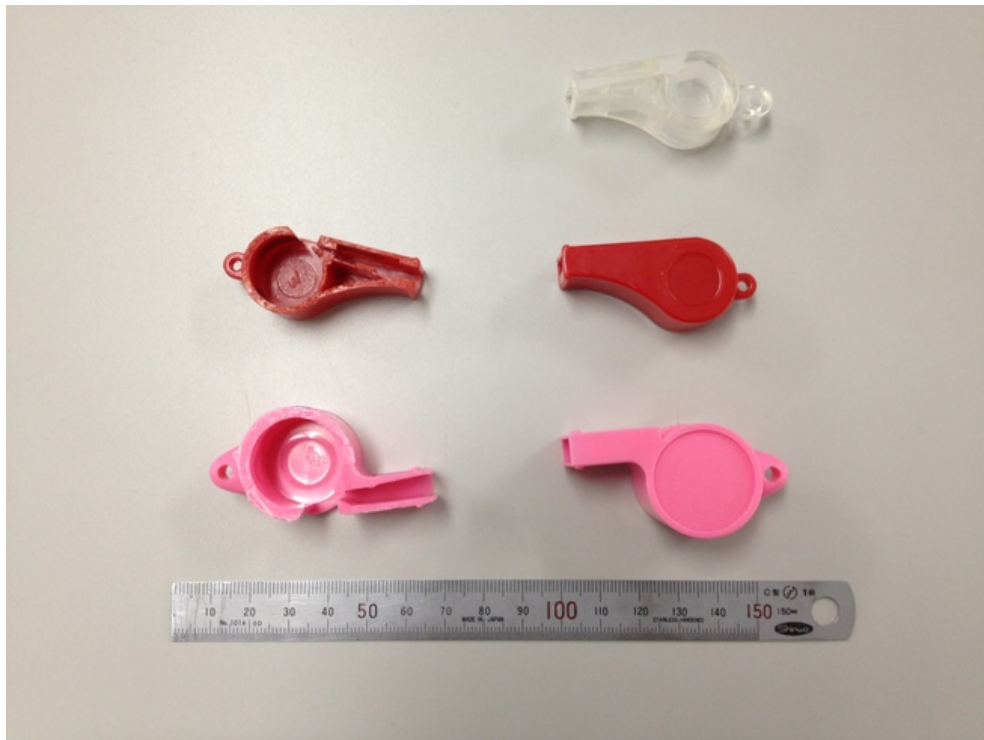


Figure 4.26 Whistles of different size.

Figure 4.26 shows pea-less whistles of different size and color which can be found at many convenient stores. The structure of a whistle consists of a narrow flue channel and a cavity resembling a Helmholtz resonator. The cross-sectional area of the opening at the end of the flue channel, or the flue exit, is smaller than the inlet, such that the jet flow is accelerated before it leaves the flue exit. It is known that the sound of a whistle combines both edge tone and Helmholtz resonance sounds (Chanaud, 1970). As the jet impinges upon the edge of aperture of the cavity, the force exerted by the edge on the flow acts as an acoustic dipole which creates sound oscillations. Part of the sound field propagates back towards the orifice where the flow is more sensitive to disturbances. In this way, the oscillation is reinforced and maintained and the feedback cycle is completed. This is how the edge tone is established. Meanwhile, the edge tone excites the Helmholtz

resonator such that sound energy is reinforced for the preferred resonance frequency.

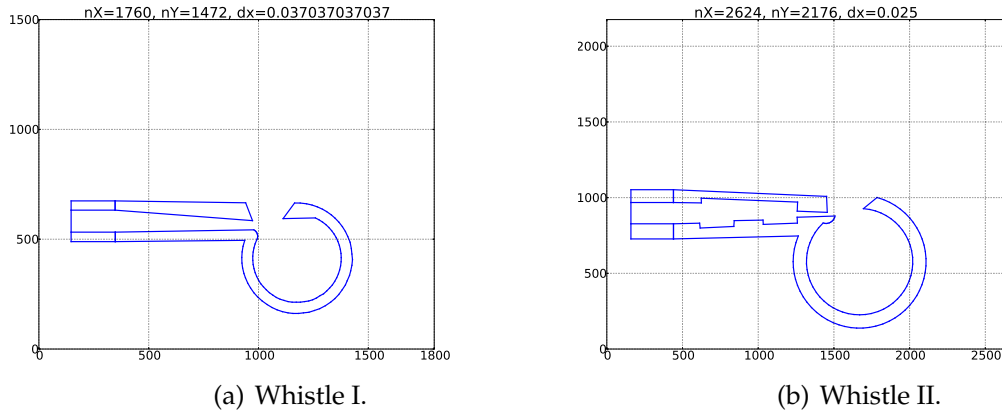


Figure 4.27 Boundaries of the whistles.

	H (mm)	W (mm)
Whistle I	1.245	12.7
Whistle II	0.45	13.15

Table 4.3 Height (H) and width (W) of the two whistles.

The LBM scheme is described by thin walls resembling the cross section of a whistle immersed in a fluid domain surrounded by open boundaries. The fluid domain is represented by a rectangular D2Q9 structure (Qian et al., 1992). The left, right, top and bottom boundaries of the radiation domain are implemented by absorbing boundary conditions prescribed with a zero velocity (Kam et al., 2006).

We generated 2D thin curved boundaries (Guo et al., 2002) based on the geometry profile measured from the clear whistle (Whistle I) and the red whistle (Whistle II) shown in Fig. 4.26. The curved boundaries were then imported into the 2D LB model by a custom Python script, as shown in Fig. 4.27. The height H and the width W of the open mouth of the resonance cavity of the two whistles are given in Table 4.3. Whistle I features a smaller ratio of W/H and a smooth wall inside the wind channel. For both whistles, the height of the channel is almost 10 times smaller than the depth. In such a situation, a 2D model would give reasonable results. The walls are treated by a simple bounce-back scheme (Succi, 2001), which creates a no-slip condition at the wall and simulates a viscous boundary layer.

	nX	nY	dx (mm)
Whistle I	1760	1472	0.037
Whistle II	2624	2176	0.025

Table 4.4 Size of the two LB models.

The size of the LB model representing the two whistles is given in Table 4.4, where nX and nY are the number of lattice cells along the x- and y-axis, respectively. The spatial resolution dx representing the unit length of one lattice cell is decided by both the available computing resources and the smallest geometrical length of the boundary, which is the height H measured at the exit of the flue channel for our specific case. The number of lattice cells representing the height H is 40 for Whistle I and 18 for Whistle II, respectively, which is sufficient in consideration of both stability and accuracy, according to our previous experiences.

The dimensionless kinematic viscosity ν can be calculated from the physical kinematic viscosity of air ν^* and the spatial resolution dx by the relation $\nu^* = \frac{\nu c_s^* dx}{c_s}$, where c_s^* is the physical speed of the sound and c_s is the speed of sound in lattice units. The undisturbed fluid density was set as $\rho_0 = 1.0$ (in lattice units) for convenience.

The source flow is implemented by a source buffer attached at the left end of the flue channel using absorbing boundary conditions with a non-zero target velocity prescribed by the source signal. The jet speed is measured at the center of the flue exit.

The time histories of fluid density are probed above the open mouth using a sampling rate of 80 kHz, where the coordinates of the probing point is $(x = 1000, y = 800)$ for Whistle I and $(x = 1400, y = 1100)$ for Whistle II. A DC-blocking filter must be used in the post-processing to remove the fluctuation caused by the fluid flow.

4.4.4 Results

4.4.4.1 Jet Formation and Oscillation

Figure 4.28 shows how the jet is formed at the start-up stage. The formation of the first vortex is demonstrated in Fig. 4.28(a) ~ 4.28(c). The vortex shedding above the flue exit are clearly visible in Fig. 4.28(c) ~ 4.28(f). Inside the resonator, the vortex shedding is far less strong but still observable.

Figure 4.29 shows the jet motion around the labium during the course of one cycle for

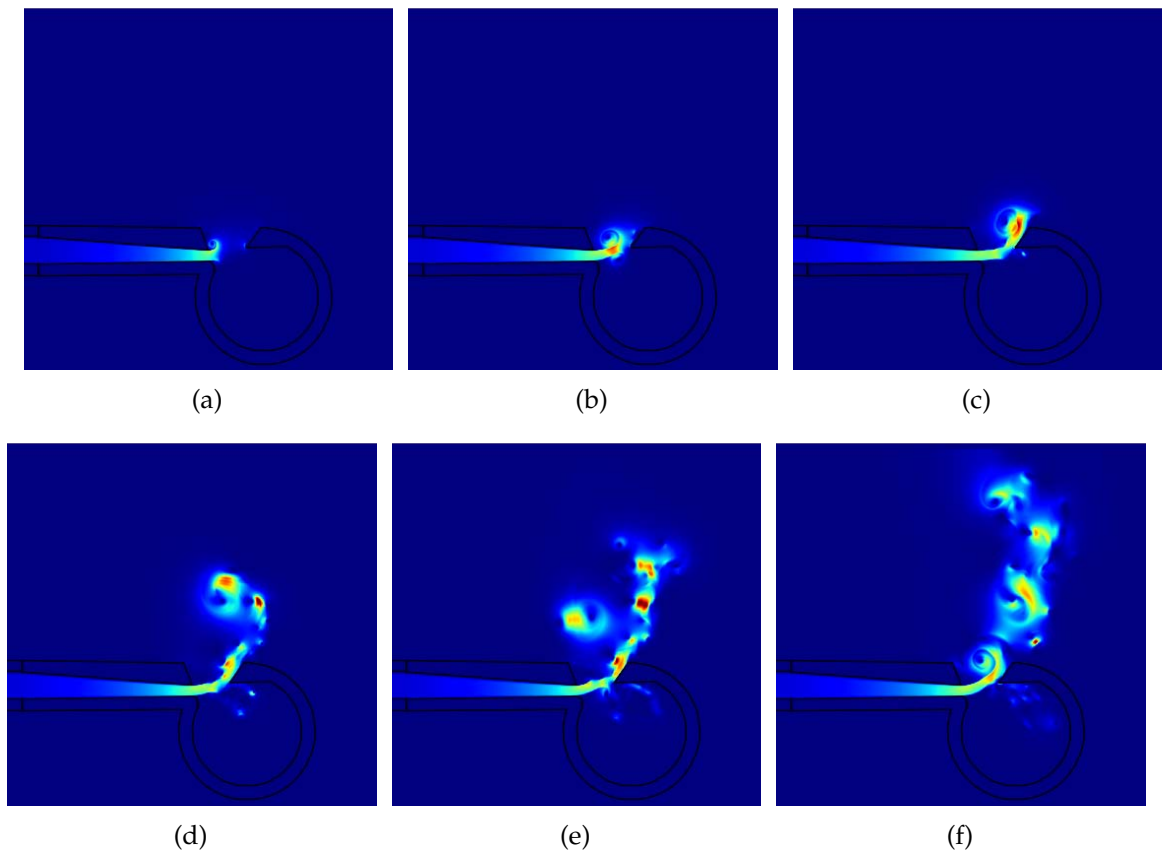


Figure 4.28 The formation of the jet during start-up. The colors represent the absolute value of velocity ($\sqrt{u_x^2 + u_y^2}$). The red color corresponds to the highest speed and the dark blue to the lowest speed. For the simulation the jet speed at the center of the flue exit is $U_{jet} = 30 \text{ m/s}$.

Whistle I at $U_{jet} = 30 \text{ m/s}$. The air jet oscillates mainly above the labium. This behavior is qualitatively similar to that found in a 2D DNS of a recorder by Giordano (2013), but different from that observed in a 3D DNS carried out by the same author (Giordano, 2014). According to Miyamoto et al. (2013), this phenomenon is due to differences in energy dissipation and vortex motion in two and three dimensions.

4.4.4.2 Sound Oscillation

The time histories of the acoustic density (in numerical units) measured above the open mouse for four different jet speeds ($U_{jet} = 10, 20, 30, 40 \text{ m/s}$) are shown in Fig. 4.30. The

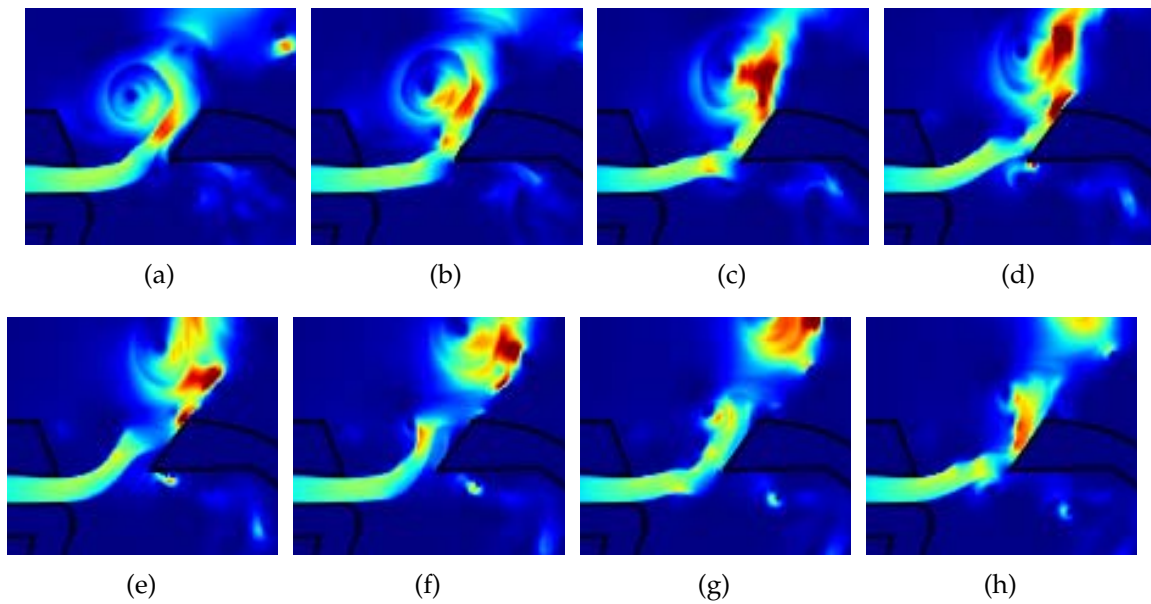


Figure 4.29 Images of the air speed near the flue channel exit and labium of Whistle I during one cycle. The colors represent the absolute value of velocity ($\sqrt{u_x^2 + u_y^2}$). The red color corresponds to the highest speed and the dark blue to the lowest speed. For the simulation the jet speed at the center of the flue channel is $U_{jet} = 30 \text{ m/s}$.

amplitude of the signal at the start-up stage is almost in linear proportion to the jet speed, as we will find later. The oscillation is not visible for $U_{jet} = 10 \text{ m/s}$, though it is visible for the other three higher jet speeds.

The normalized spectrum of the simulation for three different jet speeds are depicted in Fig. 4.31. For $U_{jet} = 20 \text{ m/s}$, there is almost no harmonics found in the result, suggesting the typical behavior of a Helmholtz resonance. For $U_{jet} = 30$ and 40 m/s , harmonics emerge in the results, though they are not necessarily relative to the high-frequency components in the case of $U_{jet} = 20 \text{ m/s}$. The simulation results show a relatively high level of noise compared to the peak frequency, which is probably due to the rather short simulation time which is insufficient for the build-up of a steady oscillation. Another reason could be due to the fact that the signals were measured in the near field, which includes lots of noise.

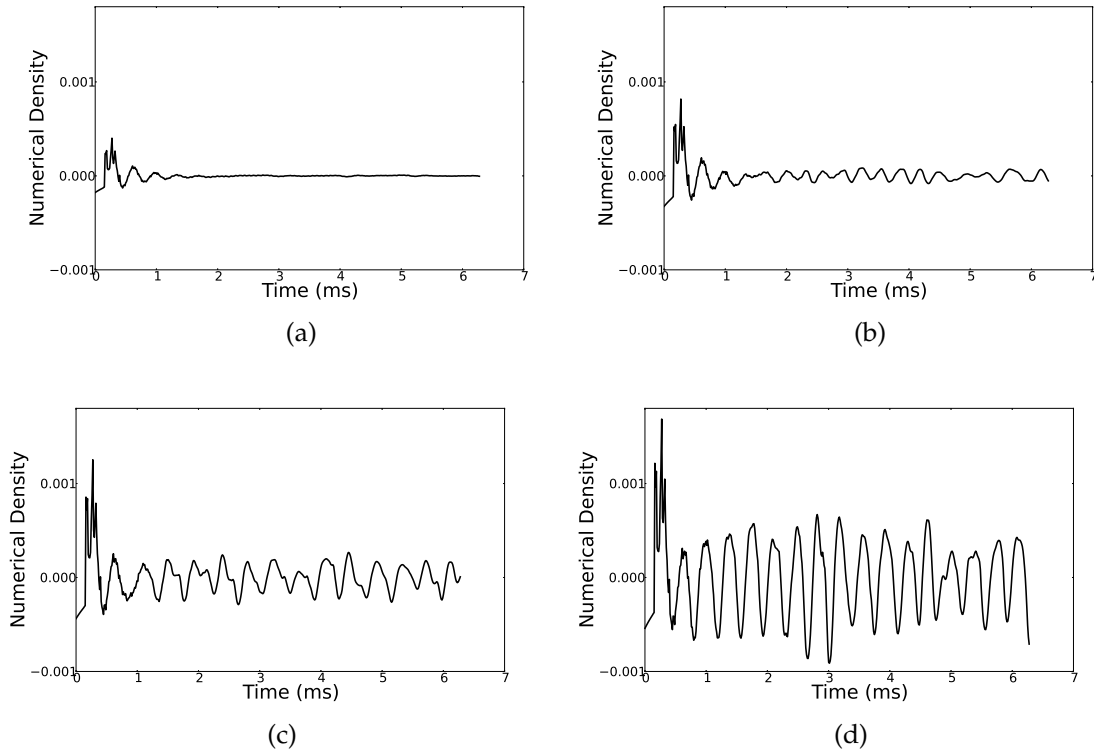


Figure 4.30 Numerical density of whistle I with various jet speed. Jet speed: (a), $U_{jet} = 10 \text{ m/s}$. (b), $U_{jet} = 20 \text{ m/s}$. (c), $U_{jet} = 30 \text{ m/s}$. (d), $U_{jet} = 40 \text{ m/s}$.

4.4.4.3 Change of Frequency and Amplitude with Jet Speed

Figure 4.32(a) shows the change of peak frequency with increase of jet speed U_{jet} in the simulation of Whistle I. The edge tone frequencies of the four stages given by Brown's empirical equation (Eq. 4.38) are also depicted (fb1, fb2, fb3 and fb4). No overtone is observed, which is typical for Helmholtz-type resonators. In the range of $13 \leq U_{jet} \leq 18$, the simulation results are close to the curve of fb4, the fourth stage of Brown's edge tone, but this might be only a coincidence, because the oscillation is not stable for low jet speeds. A transition is observed in the range of $20 < U_{jet} < 25$. For jet speeds beyond 25, the simulation results are very close to the edge tone curve.

The same comparison of the change of peak frequency with increase of jet speed is made for Whistle II, as depicted in Fig. 4.33(a). We notice fluctuations of the frequencies for jet speeds higher than 20 m/s , which is not surprising because the simulation is terminated before the steady acoustic oscillation can be developed.

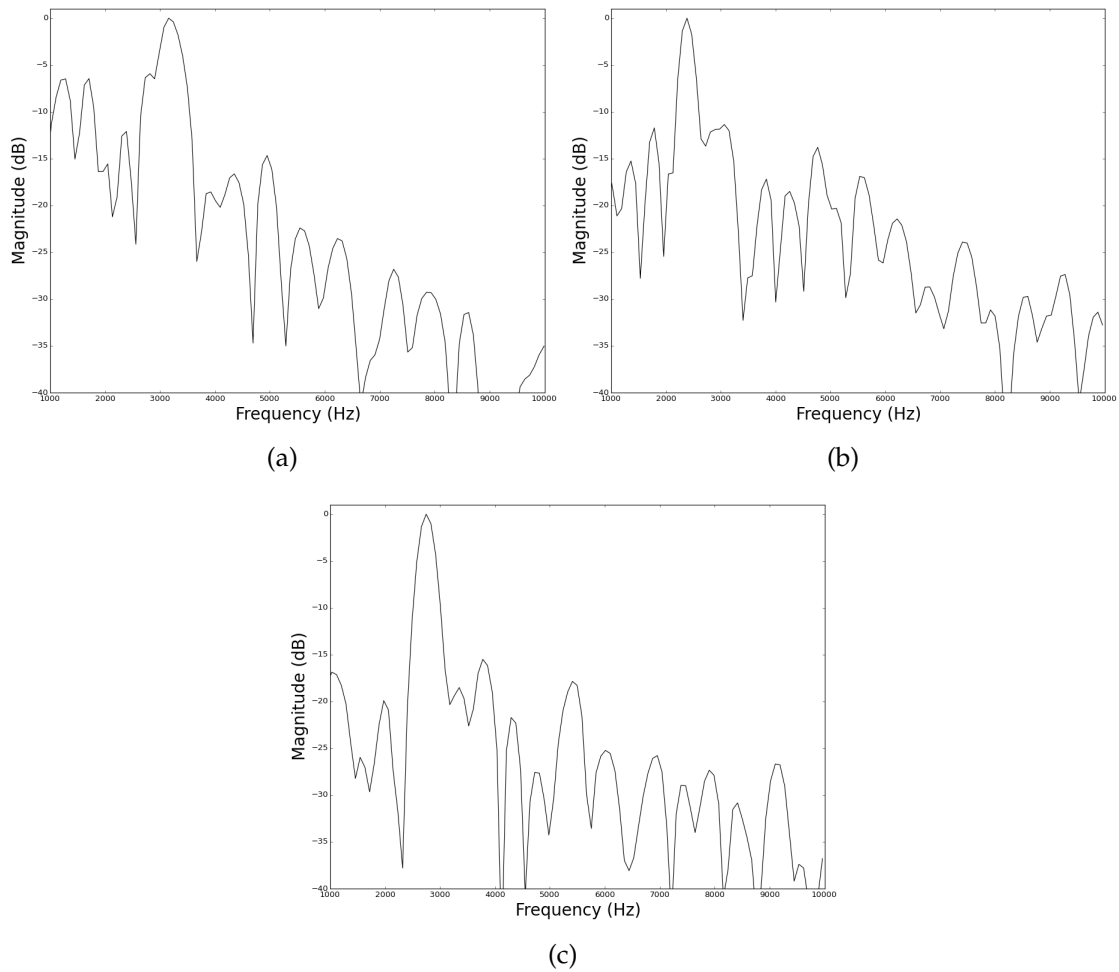
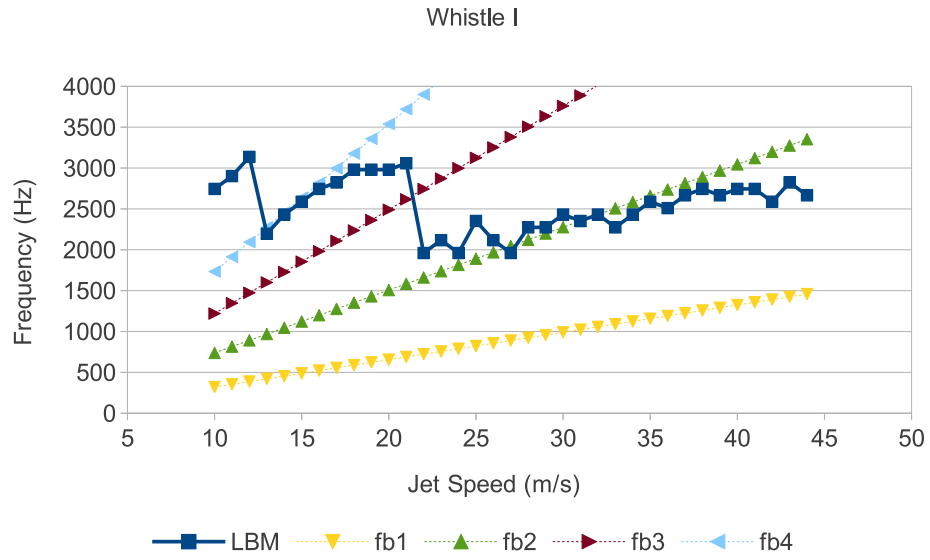


Figure 4.31 Normalized spectrum of whistle I with various jet speeds: (a), $U_{jet} = 20$ (m/s). (b), $U_{jet} = 30$ (m/s). (c), $U_{jet} = 40$ (m/s).



(a)



(b)

Figure 4.32 Peak frequency and normalized magnitude of whistle I for various jet speeds. 4.32(a): peak frequency and frequency of edge tone (fb1, fb2, fb3 and fb4, see Eq. 4.38), (b) normalized magnitude.

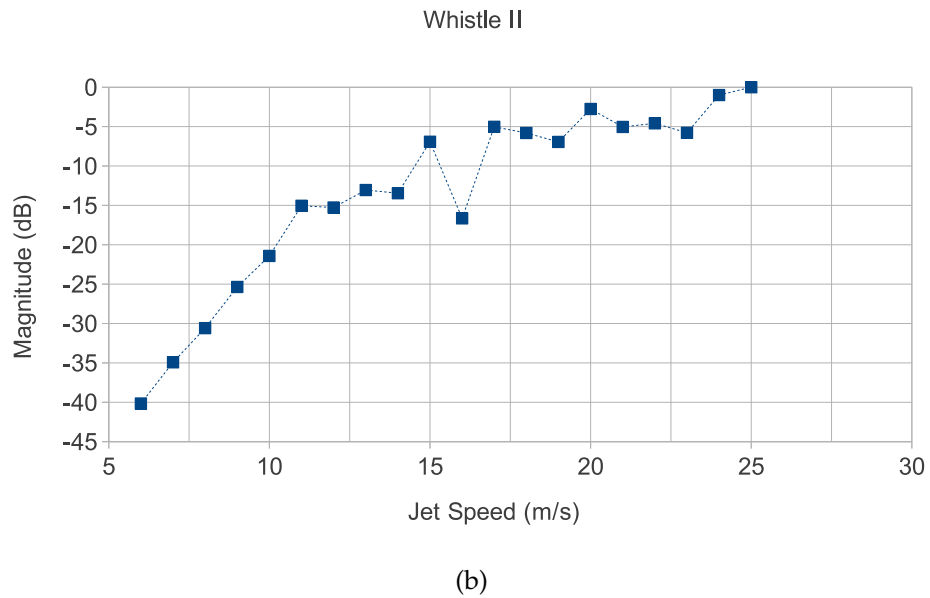
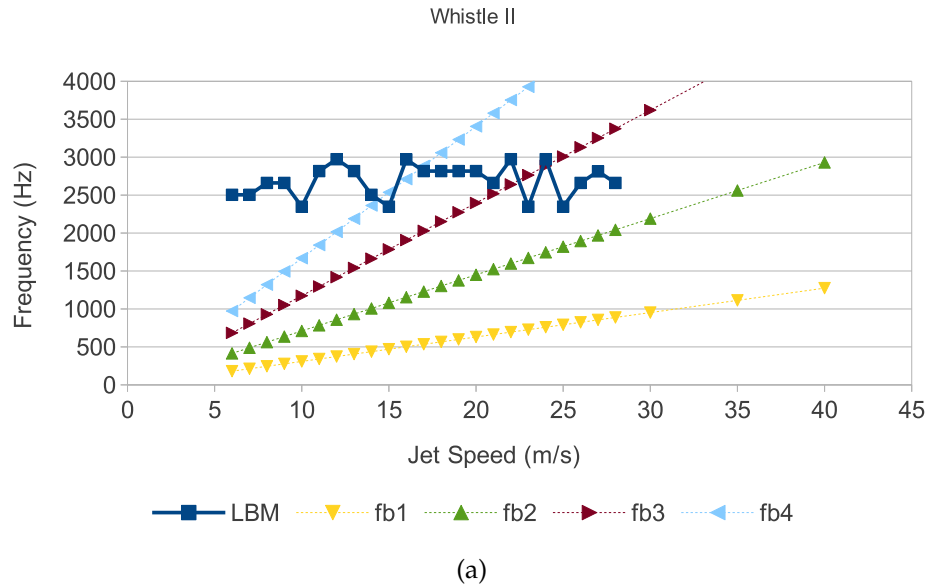


Figure 4.33 Peak frequency and normalized magnitude of whistle II for various jet speeds. (a): peak frequency and frequencies of edge tone (fb1, fb2, fb3 and fb4, see Eq. 4.38), (b) normalized magnitude.

The magnitudes of the peak frequency of simulation are depicted in Fig. 4.32(b) for Whistle I and Fig. 4.33(b) for Whistle II. The curve is normalized to 0 dB for jet speed at $U_{jet} = 36$ for Whistle I and $U_{jet} = 25$ for Whistle II. Overall, the amplitude increases almost linearly for jet speeds less than 10 m/s. We can observe some fluctuations and slight drops in the range of $20 < U_{jet} < 25$ for Whistle I and $15 < U_{jet} < 20$ and $20 < U_{jet} < 25$ for Whistle II.

The results reported above are in partial agreement with measured data known to the authors but not available for publication at this time. In particular, the peak frequencies in the spectrum of the simulation are close to those of the measured results, and similarities have been found in the change of frequency with the increasing jet speed. The measured results display a general increase of oscillation frequency with jet speed, except for a transition zone found in the mid-range of jet speeds ($20 < U_{jet} < 25$). The frequency curves of both simulations and measured results of Whistle I are close to the edge tone curve for higher jet speeds ($U_{jet} \geq 25$). On the other hand, the measured results show a dip in the magnitude of the peak frequencies in the mid-range of jet speeds (in the transition zone) that was not observed in the LBM results.

4.4.5 Summary

We have presented results from a two-dimensional LBM simulation of whistles, including 1) the qualitative visualization of the jet formation and vortex shedding, and 2) the quantitative results of the spectrum and the change of peak frequencies for various jet speeds. We are able to use a low viscosity thanks to the MRT technique. Also, the simulation speed is greatly improved by the parallel GPU computing, which makes it feasible for more simulations, longer simulation time, larger fluid domain and higher space resolutions.

However, the actual simulation time is still restricted by some factors. The fluid vortices is not well absorbed by the absorbing boundary conditions, which results in spurious reflections from the open boundaries after a certain amount of iterations. Even with the help of MRT, the numerical stability for conditions of relatively high jet speeds is not well maintained after a certain amount of iterations. The Mach number in LBM is limited to about 0.15, or even lower for low viscosity cases, so it is not capable of handling all possible jet speeds found in a typical whistle. Nonetheless, for flute-like instruments with relatively low jet speeds, such as the recorder and organ pipes, the

LBM can be a good simulation tool.

4.5 Conclusion

The essential objective of this chapter was to provide a reliable, accurate and efficient LBM model capable of representing the acoustic system comprising waveguides constructed by static solid boundaries. Another objective was to use the verified model to provide a deeper understanding of some phenomena that have not yet been addressed analytically.

Three benchmark problems, namely the acoustic transmission in pipes, acoustic radiation out of pipes and aeroacoustic behavior of whistles, were numerically investigated based on the customized two-dimensional isothermal LB models implemented on a GPU platform and / or a CPU platform.

Both the CPU SRT model and GPU SRT model demonstrate good accuracy on simulations of the wave propagation inside an axisymmetric waveguide immersed in a stagnant fluid field. The numerical results in terms of reflection coefficient and length correction are in excellent agreement with the established analytical predictions provided by Levine and Schwinger (1948). When the condition of a non-zero subsonic mean flow is introduced to the system, the numerical results are still in good agreement with the available analytical predictions provided by Munt (1990) and the experimental results provided by Allam and Åbom (2006). One drawback of the proposed LB model is its questionable results of the length correction for the low frequency limit $ka < 0.2$, which might be related to the degraded accuracy of the two-microphone method in the low frequency limit. For the case of a horn carrying a non-zero mean flow, the presented numerical results well agree to the results obtained from a previous LBM model developed in Matlab by da Silva (2008).

For the second benchmark problem on the radiation directivity pattern of an axisymmetric waveguide, the presented LB models also show good agreement with the analytical results provided by Levine and Schwinger (1948), for the case of an unflanged cylindrical pipe issuing a zero mean flow, and the analytical results provided by Gabard and Astley (2006) and the experimental results provided by Gorazd et al. (2012), for the case of an unflanged cylindrical pipe carrying a non-zero mean flow. The effects of the so-called zone of relative silence are well predicted by the LB model. The numerical

investigation on the influence of a horn extension shows that the directivity effect is reinforced by the presence of a horn extension, this is especially true for a horn profile with a bigger curvature radius. A quick numerical investigation shows that, although the bit depth (32-bit) representing the floating-point numbers on the GPU platform is only a half of that used by the Python/NumPy and Matlab LB model on a main stream CPU platform (64-bit), the GPU LB model is still good enough to address the sound radiation problems.

Finally, to examine the stability of the GPU LB model on acoustic systems involving a complicated geometry and a jet with relative high speed in a low viscosity fluid field during a long simulation time, two realistic whistles with slightly different geometries were simulated. Throughout the simulations, the numerical stability is well maintained mainly thanks to the curved boundary based on extrapolation algorithm (Guo et al., 2002) and the MRT scheme (d'Humieres, 1994; Guo and Shu, 2013).

Chapter 5

Numerical Modeling of Acoustic Systems with Moving Boundaries

5.1 Overview

In Chpt. 4, we have discussed the application of parallel GPU LB models on acoustic problems involving complex curved boundaries and non-zero mean flows. Our goals in this chapter is to extend the GPU LB model one step further: simulating a single-reed woodwind instrument which comprises a dynamic mouthpiece-reed structure and a fully coupled acoustic resonator. A clarinet-like system has been chosen as the target instrument, because it has been relatively thoroughly investigated previously such that we are able to compare some of the numerical results with prior literature. Since the LB model at our disposal is limited to 2D, we will focus on problems that can be reasonably represented in 2D. Any problems involving 3D behaviors, such as tone holes, will be excluded.

A clarinet can be roughly divided into a non-linear active component (the mouthpiece-reed system) and a linear passive component (the instrument's resonant bore). Previous studies on the resonator components have produced many useful discoveries and satisfactory models. As well, studies on the non-linear mouthpiece-reed system have produced some important results. Most previous models are restricted to quasi-stationary approximations that are over-simplified because they assume that the flow in a mouthpiece with an oscillating reed is the same as that in a mouthpiece with a fixed channel height at any given instant. The characteristic of the mouthpiece-reed system, defined

as the non-linear relationship of the volume flow and the pressure difference across the reed channel, is expressed as an explicit function if the effects of inertia, damping and acoustic coupling are neglected. Since the pioneering work of Backus (1963) on small amplitude vibrations, the non-linear function of single-reed woodwind instruments in the quasi-stationary condition has been investigated experimentally and theoretically by a number of authors (Nederveen, 1969; Worman, 1971; Wilson and Beavers, 1974; Saneyoshi et al., 1987; Fletcher, 1993; Kergomard, 1995; Kergomard et al., 2000; Ollivier et al., 2004, 2005; Dalmont et al., 2003; Almeida et al., 2007).

A more sophisticated model taking the viscous phenomena into account has been proposed by Hirschberg et al. (1990), which is based on results obtained from the numerical simulation of a steady viscous flow passing through a two-dimensional Borda tube. They found that for sufficiently high Reynolds number ($Re > 10$), the flow pattern is strongly influenced by the minor geometry difference measured by the ratio of L/h , where L and h are the length and the height of the reed channel, respectively. This model has been experimentally validated and improved by van Zon et al. (1990). The same flow behavior has been found by Dalmont et al. (2003) using a realistic mouthpiece in the stationary condition (with a static reed). However, the flow measured in a mouthpiece with a moving reed suggests that the quasi-stationary model is unrealistic in dynamic regimes (van Zon et al., 1990), where the reed's behavior is strongly influenced by the detachment / reattachment phenomenon caused by unsteady flow.

Previous attempts of investigating the behavior of unsteady flow in a dynamic regime involving a moving reed by experimental measurements are limited to qualitative results (van Zon et al., 1990; Lorenzoni and Ragni, 2012). Also, it is not a trivial task to simulate the unsteady flow in a dynamic regime using traditional computational fluid dynamic (CFD) approaches based on continuum theory. For such a task, da Silva (2008) showed that the particle-based lattice Boltzmann method is a promising tool. He simulated the flow in a clarinet mouthpiece of different geometries using a 2D LB model for cases of both static and free oscillating reed. In the quasi-stationary regime, da Silva's results agree well with van Zon's quasi-stationary model for both short and long reed channels. In the dynamic regime, however, the results obtained in a LBM simulation show some significant discrepancies compared to the results predicted by the quasi-stationary model. His LBM simulation also confirmed the hypothesis discussed by Hirschberg et al. (1994), which states that even in the absence of acoustic feedback,

a self-sustained oscillation can be developed from the aerodynamic forces acting on the reed due to the energy absorbed from the fluid field. Despite potential problems that might be introduced by simulating a 3D mechanic-acoustic system in a 2D scheme, da Silva's simulation was less realistic because of two other issues. The first issue is that his model was driven by a negative flow source located at the open end of the mouthpiece. This scheme is justifiable in the quasi-stationary regime or the dynamic regime when an acoustic feedback is not involved, but is different from the blowing scheme used by musicians. Another issue is the lack of an acoustic resonator in his bore-less system.

The present study aims to simulate a complete clarinet that comprises a dynamic mouthpiece-reed structure and a fully coupled acoustic resonator using a relatively realistic blowing scheme. The aero-dynamic aspects of the dynamic flow and its dependency on the reed channel geometry in both quasi-stationary regime and dynamic regime involving an acoustic coupling will be investigated.

To archive that, a hybrid clarinet model is developed, which includes a LBM-MRT scheme representing the fluid and acoustic domain and a finite difference (FD) scheme representing the motion of reed based on the distributed model proposed by Avanzini and van Walstijn (2004). The interaction of the moving reed and the fluid is solved by the extrapolated curved wall scheme proposed by Guo et al. (2002).

The computation cost of the present model is significantly higher than that of da Silva's model, mainly because of the prolonged duration of the acoustic oscillations and the extra lattice cells required by the acoustic resonator and a radiation domain. To solve this problem, both the LBM-MRT model and the FD reed model have been parallelized and implemented on a PyCUDA-GPU platform such that the total time required by one simulation is reduced to a reasonable time-frame, i.e., measured by hours or days rather than by weeks.

The player's lip force and the coupling of the player's vocal tract is not included in the present system. Also, only the soft playing condition is investigated, i.e., the reed tip does not collide with the lay during the stable stage of the oscillation. This is not due to any restriction of the model but rather an issue in limiting the length and scope of the thesis.

This chapter is organized as follows. Section 5.2 provides a review of the quasi-stationary flow model proposed by Hirschberg et al. (1990) and van Zon et al. (1990), and the previous experimental and numerical investigations with respect to the flow

behaviors in single-reed woodwind instruments. Section 5.3 introduces the numerical scheme used in this study. Section 5.4 provides the results and discussions in the quasi-stationary regime. Section 5.5 provides the results and discussions in the dynamic regime. Finally, Sec. 5.6 provides a conclusion and suggestions for further investigations.

5.2 Previous Flow Behaviour Studies

It is not trivial to measure the flow in the reed channel or mouthpiece chamber of a clarinet under normal playing conditions. As a result, the majority of previous studies are restricted to quasi-stationary conditions. As well, the flow is assumed to be steady, inviscid, incompressible and laminar.

The first result of experimentally measured characteristics of a single-reed instrument under steady flow and low blowing pressure conditions was given by Backus (1963). He fit his experimental results by a non-linear expression which relates the volume flow U , the pressure difference across the reed channel Δp and the opening h , given as $U = 37\Delta p^{2/3}h^{4/3}$. However, the validity of Backus' empirical formula was questioned by later researchers (Hirschberg et al., 1990; Hirschberg, 1995; Gilbert, 1991).

Assuming no pressure recovery from the reed channel to the air column input, most flow models describe the relationship between the volume flow and the pressure difference across the reed channel by means of the stationary Bernoulli equation (Wilson and Beavers, 1974; Saneyoshi et al., 1987; Fletcher, 1993), given as

$$U = S_j \sqrt{\frac{2|\Delta p|}{\rho}} \operatorname{sgn}(\Delta p), \quad (5.1)$$

where ρ is the density of the air, w is the effective width of the reed channel, h is the opening of the reed channel and $S_j = wh$ is the effective cross section of the jet.

Then assuming the opening is linearly related to the pressure difference by its stiffness, the volume flow U can be described by the elementary model:

$$U = \begin{cases} wh \left(1 - \frac{\Delta p}{P_M}\right) \sqrt{\frac{2|\Delta p|}{\rho}} \operatorname{sgn}(\Delta p), & \text{if } \Delta p \leq P_M \\ 0, & \text{if } \Delta p > P_M \end{cases}, \quad (5.2)$$

where P_M is the threshold of pressure closing the reed channel. Since the Bernoulli equation is only valid for inviscid and irrotational flow, the elementary model only holds for a range of Reynolds number in which inertial forces predominate over the viscous force but the flow regime is still laminar, which would be between 10 (as stated by Hirschberg et al. (1990)) and ~ 2000 . Here the Reynolds number is defined as $Re = U/w\nu$, where ν is the kinematic viscosity of the fluid.

Hirschberg et al. (1990) proposed a more complex flow model using numerical simulations which takes the effects of flow separation and friction into account. This model is improved and verified based on experimental results by van Zon et al. (1990). Depending on the geometry of the flow channel characterized by L/h , where L and h are the length and the height of the flow channel respectively, there are two types of flows.

For short channels ($L/h \leq 1$), the flow is estimated by a contracted uniform flow:

$$U = \alpha wh \sqrt{\frac{2|\Delta p|}{\rho}} \operatorname{sgn}(\Delta p), \quad (5.3)$$

where α is a dimensionless contraction parameter (also called the *vena contracta factor* or *vcf*), typically found in the range of $[0.5, 0.611]$ in van Zon's measurement.

For long channels ($L/h \geq 4$), the flow is given by

$$U = \Omega \left[1 - \sqrt{1 - \frac{h^4(24c - 1)\Delta p}{72\rho\nu^2(L - l_r)^2(1 - \delta^*)^2}} \right], \quad (5.4a)$$

$$\Omega = 12\nu w(L - l_r)(1 - \delta^*)^2/h(24c - 1), \quad (5.4b)$$

where ρ is the undisturbed density of the fluid, $l_r \simeq 2h$ is the distance from the entrance of reed channel to the reattachment point where the fully separated flow develops into a Poiseuille flow, $\delta^* = 0.2688$ is a generalization of the boundary layer thickness for an arbitrary h and $c = 0.0159$ is a constant.

Dalmont et al. (2003) measured the flow behavior using an artificial mouth-lip system and a real clarinet mouthpiece and found a flow behavior similar to that described by the quasi-stationary flow model. Interestingly, Almeida et al. (2007) measured double-reed woodwind instruments and found that the normalized pressure flow characteristics of a bassoon and an oboe are similar to that of a clarinet and can be well described by the

quasi-stationary model.

da Silva et al. (2007) simulated the flow into an anechoically terminated mouthpiece of clarinet with different geometries of reed channel using the two-dimensional lattice Boltzmann method for cases of both a static and an oscillating reed in the absence of acoustic coupling. For the case of a static reed, da Silva's results agree well with van Zon's model for both short and long reed channels in terms of vena contracta factor and volume flow. Nonetheless, the characteristic in the static regime provided in (da Silva et al., 2007) is not complete because only a discrete number of values of mouth pressure were tested.

The flow in the dynamic regime featured by a moving or oscillating reed is more difficult to measure. The vena contracta factor measured in the dynamic regime provided by da Silva et al. (2007) is constant for about 40% of the duty cycle, which is significantly different from van Zon's prediction in a quasi-stationary condition. Since the acoustic coupling is not included in the numerical model, the oscillation frequency and the corresponding Strouhal number in da Silva's results are an order of magnitude higher than under normal playing conditions. Also, the simulation was less realistic because the flow was generated by a negative pressure source at the outlet of the mouthpiece.

More recently, Lorenzoni and Ragni (2012) measured the flow velocity field inside the mouthpiece of a tenor saxophone driven by an artificial blowing machine using the particle image velocimetry (PIV) technique. The measured vena contracta factor is found to be a constant value around 0.6 for about 50% of the duty cycle, which is in good accordance with van Zon's steady experiments and suggests that a constant vena contracta factor is a reasonable first approximation for sufficiently large reed openings. Unfortunately, the phenomenon of flow detachment and reattachment is not provided in their results due to the low spatial resolution. In the next year, using the numerical clarinet model proposed in (da Silva et al., 2007), da Silva et al. (2013) prescribed artificial sinusoidal oscillations of different frequencies and amplitudes on the reed tip in the hope to simulate a more realistic playing condition. They found that for the case of a short reed channel, the averaged vena contracta factor is proportional to the playing dynamic. For the case of a long reed channel, an analysis based on the numerical results implies that the jet formed at the entrance does not reattach on the reed walls within the reed channel. This conclusion is in contrast with previous results provided by Hirschberg et al. (1990) and van Zon et al. (1990). The reattachment point may be verified in a vi-

sualization with a better spatial resolution, which was not available in (da Silva et al., 2013).

5.3 Numerical Scheme

The present study aims to investigate the aeroacoustic aspects in the mouthpiece-reed system of a clarinet using numerical modeling. The investigations are scheduled at two stages. At the preliminary stage, the objective is to obtain a complete characteristic of the reed in the quasi-stationary regime roughly and quickly. Subsequently, the objective is to investigate the flow behavior with some more details in a dynamic regime featured by a vibrating reed driven by aerodynamic forces and coupled with acoustic oscillations.

To archive this purpose, a hybrid clarinet model is developed. The full system is described by a clarinet immersed in a fluid domain surrounded by open boundaries. The dynamics of the fluid field are solved by a 2D rectangular LBM-MRT scheme. The clarinet comprises a static mouthpiece, a moving thin reed and an acoustic resonator. The mouthpiece, resembling the geometry of a realistic clarinet, is a 2D structure defined by static solid thin walls. The moving curved wall of the reed is associated with a 2D distributed reed model implemented by an implicit finite difference scheme (Avanzini and van Walstijn, 2004). The acoustic resonator is an axisymmetric cylindrical pipe with one end attached to the outlet of the mouthpiece and another end open in an axisymmetric acoustic radiation domain.

5.3.1 The Reed Model

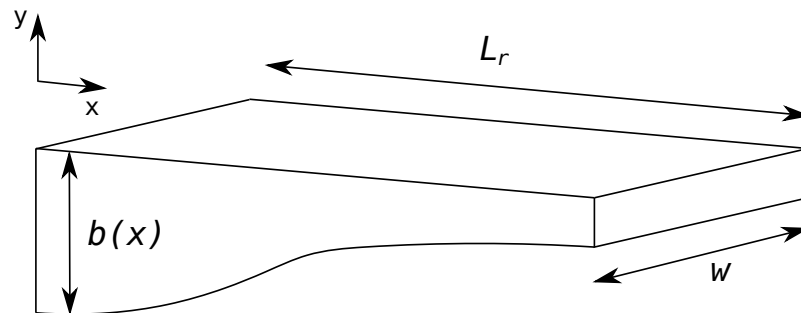


Figure 5.1 Geometry of the distributed reed model.

Following the approach proposed by Chaigne and Doutaut (1997) and Avanzini and van Walstijn (2004), the mechanical system of the vibrating reed is modeled as a clamped-free bar with length L_r , slowly varying non-uniform thickness $b(x)$ and a constant width w , shown in Fig. 5.1. The material is assumed homogeneous and isotropic, such that the density ρ_r and Young's modulus Y are constants. Neglecting the contributions of flexural waves on longitudinal and horizontal directions, the governing differential equation is represented by the relationship of the distributed driving force $F(x, t)$ and the vertical displacements $y(x, t)$, which is written as

$$F(x, t) = \rho_r A(x) \left[\frac{\partial^2 y}{\partial t^2}(x, t) + \gamma_B \frac{\partial y}{\partial t}(x, t) \right] + \frac{\partial^2}{\partial x^2} \left[Y I(x) \left(1 + \eta \frac{\partial}{\partial t} \right) \frac{\partial^2 y}{\partial x^2}(x, t) \right], \quad (5.5)$$

where t is time, $x \in [0, L_r]$ is the horizontal position, $A(x) = wb(x)$ is the cross-section area, $I(x) = A(x)B^2(x)/12$ is the moment of inertia about the longitudinal axis, η is the viscoelastic damping coefficient and γ_B is the fluid damping coefficient which represents the losses due to the surrounding fluid. In the case that the reed model is fully coupled with a LB fluid model, γ_B should be neglected.

The boundary conditions of the reed system are imposed by the geometrical constraints of the clamped-free structure and the combined external forces due to the pressure difference across both sides of the reed's surface and the interaction with the player's lip and the mouthpiece lay. Following the earlier work of da Silva et al. (2007), the lip force is neglected in the present model, and the interaction with the mouthpiece lay is simply modeled as an inelastic collision, which is somewhat unphysical but is acceptable because the influence on flow behavior is barely noticeable (da Silva et al., 2007).

Reed length	$L_r = 34.0 \times 10^{-3} (m)$
Reed width	$w = 13.0 \times 10^{-3} (m)$
Reed density	$\rho_r = 500 (Kg/m^3)$
Young's modulus	$Y = 5.6 \times 10^9 (N/m^2)$
Viscoelastic damping coefficient	$\eta = 6.0 \times 10^{-7} (s)$
Fluid damping coefficient	$\gamma_B = 100 (s^{-1})$

Table 5.1 Geometric and mechanic parameters of the reed.

Equation 5.5 can be discretised in both time and space and represented by an implicit finite difference scheme. The result in matricial form is given by Avanzini and van

the right side, the static walls of the mouthpiece are coupled with a dynamic reed. The entrance of the reed channel is situated inside a mouth cavity functioning as an air reservoir, which is enclosed by three flow sources (SRC). The SRC is a variation of the ABC scheme generating a positive source flow that can be prescribed based on a customized pressure profile.

The moving curved boundary associated with the moving reed is solved by an extrapolation scheme proposed by Guo et al. (2002). This technique represents the no-slip condition and the transfer of momentum from the reed to the flow with an accuracy of second order. The displacement and the velocity of the reed is updated by the reed model driven by the aerodynamic force imposed on the reed's surface in each iteration, and the curved boundary is updated accordingly.

Geometric parameters	Values (<i>mm</i>)
h	1.2 (quasi-stationary), 1.0 (dynamic)
D_1	20.0
D_2	16.0
D_3	4.0
L_1	15.2
L_2	64.8
L_3	0 (quasi-stationary), 64.0 (dynamic)

Table 5.2 Geometric parameters of the clarinet.

On the left side, an axisymmetric cylindrical pipe that functions as an acoustic resonator is immersed in a radiation domain. The right end of the pipe is connected to the outlet (the vertical dashed line) of the mouthpiece. The axisymmetric flow on the left side is implemented by adding an extra axisymmetric source term to the right hand side of the collision equation of LBM, as described by Eq. 4.16. The axisymmetric flow is then directly coupled to the upstream 2D flow coming from the outlet of the mouthpiece, for which the collision equation without an axisymmetric source term is used, as described by Eq. 3.20. Physically, this can be interpreted as a semi-infinite 2D channel coupled to a 3D cylindrical pipe. This hybrid scheme attempts to simulate the structure of a realistic clarinet, which can be described as an axisymmetric cylindrical pipe attached to a semi-2D mouthpiece chamber with a rectangular-like cross-section. The choice of a semi-3D axisymmetric pipe is justified by the reflection coefficients measured at its open end, which has a higher magnitude compared to the counterpart associated with a 2D

channel. A higher reflectance at the open end provides sufficient energy to compensate the losses, which is essential to maintain the acoustic standing wave in the pipe.

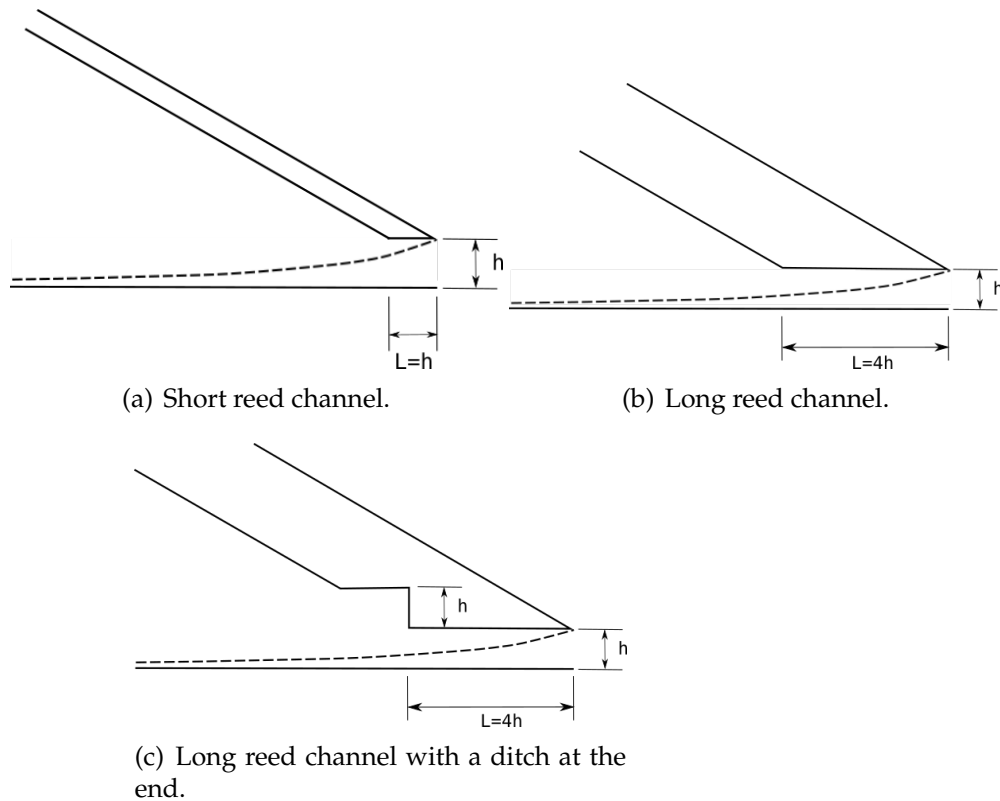


Figure 5.3 Three different lay geometries used in the simulations.

A number of fundamental geometry parameters of the clarinet are given in Table 5.2. These parameters are read by a Python script to generate the boundary data required by the numerical model. Other geometrical dimensions are derived from the fundamental parameters. The height of the reed channel entrance at rest is $h = 1.2$ (mm) for the quasi-stationary simulations and $h = 1.0$ (mm) for the dynamic simulations. Since a higher spatial resolution is used in the dynamic simulations, we use a smaller value of h to reduce the computation cost. Also, a smaller aperture can facilitate the acoustic oscillations.

In the dynamic simulations, the length of the acoustic pipe L_3 is set to 64.0 (mm), which is four times of the inner diameter D_2 . The size of the radiation domain on the left side is measured by $2D_2$ and $2(D_2 + D_3)$ in the x- and y-direction, respectively. For the quasi-stationary case, since acoustic resonances are not desired, the acoustic resonator

dx	h	nX	nY	$nX \times nY$
$8.5 \times 10^{-5}(m)$	12	2125	538	1,143,250
$4.25 \times 10^{-5}(m)$	24	4214	1008	4,247,712

Table 5.3 Number of cells corresponding to different spatial resolutions.

is removed by simply setting L_3 to zero.

The length of the reed channel L is either $4h$ or h , depending on which lay geometry is engaged. Figure 5.3 depicts the three different lay geometries used in this study. The short and long reed channel (Figs. 5.3(a) and 5.3(b)) will be investigated in all simulations. For the dynamic case, the effect of a ditch cut at the end of the long reed channel (Fig. 5.3(c)) will be investigated.

The total number of cells of the LB model is scalable and is related to the physical dimension and the spatial resolution dx , which is defined as the unit length of one lattice cell. A simulation using a very small dx provides more details of the flow behavior, but it also requires more cells which in turn costs more computation resources and demands a longer simulation time. At the preliminary stage of this study, a relatively rough spatial resolution, $dx = 8.5 \times 10^{-5} (m)$, has been chosen for the quasi-stationary simulations. At the later stage of dynamic simulations, a smaller value of $dx = 4.25 \times 10^{-5} (m)$ is chosen in order to capture more details of the flow behavior in the rather small space inside the reed channel. Table 5.3 compares the typical number of cells related to the two different spatial resolutions, where $h = 1.0 (mm)$ is the equilibrium tip opening of the reed channel, nX and nY are the lengths of the lattice in the x- and y-dimension and $nX \times nY$ is the total number of cells. A half value of dx requires about four times the total number of cells, corresponding to about four times the memory consumption and simulation time.

5.4 Investigations of the Quasi-stationary Regime

In this section, we investigate the nonlinear characteristics of the mouthpiece-reed system in order to cross-check the validity of the quasi-stationary flow model for cases of both a fixed reed and a freely moving reed. The simulations are carried out in the absence of aero-dynamic or acoustic oscillations. The investigation for the case of an oscillating reed in the presence of acoustic feedback will be presented in the next section.

5.4.1 Setup of Simulations

The setup of the numerical simulations is based on the hybrid clarinet model discussed in Sec. 5.3. To obtain the complete curve of the characteristics, the volume flow must be measured in a quasi-stationary condition, i.e., the air flow is free to pass through the reed channel under both fixed and slowly moving reed conditions. In such a case, the transfer of momentum between the fluid and the reed is neglected.

For a fixed reed, it is easy to fulfil the requirement of the quasi-stationary condition using a slowly varying profile of mouth pressure in the simulations. For the case of a freely moving reed, as the mouth pressure continuously increases from zero to a maximum value until the reed reaches the lay, the reed channel is changing from fully open to fully closed. In this process, a tiny initial disturbance of the reed might be reinforced by the acoustic feedback from the mouthpiece chamber as well as the resonator. Dalmont et al. (2003) used an orifice as a non-linear acoustic absorber to thwart possible acoustic oscillations in the experimental measurement. To serve a similar purpose in this study, the outlet in the left side of the mouthpiece is replaced by an absorbing boundary condition (ABC) which is used as a pressure-reducing element and a nonlinear absorber that suppresses possible standing waves in the mouthpiece.

The inside boundaries of the mouth cavity are equipped with SRC prescribed with non-zero pressure and velocity, functioning as both the flow source and an acoustical absorber. The pressure in the mouth cavity (pm) and in the mouthpiece chamber (pa), as well as the volume flow in the reed channel (U) are measured, averaged and saved during the simulation. The pressure difference dp is calculated as $dp = pm - pa$. Due to the viscoelasticity of the reed and the inertia and damping effects of the fluid, it is very possible to observe a hysteresis effect due to the change of the rest position of the reed when closing versus when opening. Thus, the measurement of the flow for both an increasing mouth pressure and a decreasing mouth pressure is required in order to obtain the full picture.

The spatial resolution is set at a relatively large value of $dx = 8.5 \times 10^{-5}$ (m), and the equilibrium tip opening of the reed channel is set as $h = 1.2 \times 10^{-3}$ (m), corresponding to about 14 cells. The time step is $dt = 1.44 \times 10^{-7}$ (s). To maintain the numerical stability in the moving reed configuration, the lattice relaxation parameter is chosen as $\Omega = 1.88$ and used in both static reed and moving reed cases, corresponding to a relatively high physical kinematic viscosity of 5.33×10^{-4} (m^2/s). The duration of such a simulation is

set to 68 ms , or 500,000 iterations. According to our previous experience, this duration is the minimum value required to prevent the oscillation from occurring in case the reed is not fixed.

Two different geometries of reed channel, namely the short channel ($L/h = 1$, Fig. 5.3(a)) and the long straight channel ($L/h = 4$, Fig. 5.3(b)) have been used in the quasi-stationary simulations for both a static reed and a moving reed, respectively. There are two main differences between the present study and the previous work conducted by da Silva et al. (2007). For the case of a static reed, the complete characteristic is measured continually for both increasing mouth pressure and decreasing mouth pressure. For the case of a moving reed, the disturbance of acoustic oscillations is minimized by using two approaches. One approach is to use a relatively slow change rate of the mouth pressure. Another approach is to use a higher fluid damping coefficient in Avanzini and van Walstijn's reed model, keeping key mechanical parameters such as Young's modulus of elasticity and viscoelastic damping coefficient unchanged such that the mechanical characteristic of the reed is not affected.

5.4.2 Results of Static Reed

The results of the stationary simulations for the cases of short channel and long channel are shown in Figs. 5.4 and 5.5, respectively.

Figures 5.4(a) and 5.5(a) depict the time history of the target pressure p_{mt} prescribed on the SRC in the mouth cavity, the measured mouth pressure p_m , the average pressure in the mouthpiece chamber p_a and the pressure difference across the reed channel $dp = p_m - p_a$. In a typical simulation, the target pressure p_{mt} increases linearly from zero to the highest value 9.5 kPa in a duration of about 28.87 ms (200,000 iterations, marked as Stage I) and holds for about 7.22 ms (50,000 iterations), then decreases linearly to zero in the duration of about 28.87 ms (marked as Stage II), and holds there for about 7.22 ms until the simulation is finished. The mouth pressure follows the pattern of p_{mt} though at a reduced level. Since the reed is fixed, the reed channel is fully open during the course of the simulation and the mouth pressure never reaches the prescribed pressure due to the non-zero flow passing through the mouthpiece.

The measured flow U is compared to the Bernoulli flow U_b and the theoretical flow U_z calculated from van Zon's model for both the short channel and the long channel, as shown in Figs. 5.4(b) and 5.5(b), respectively. Since the opening and the width of

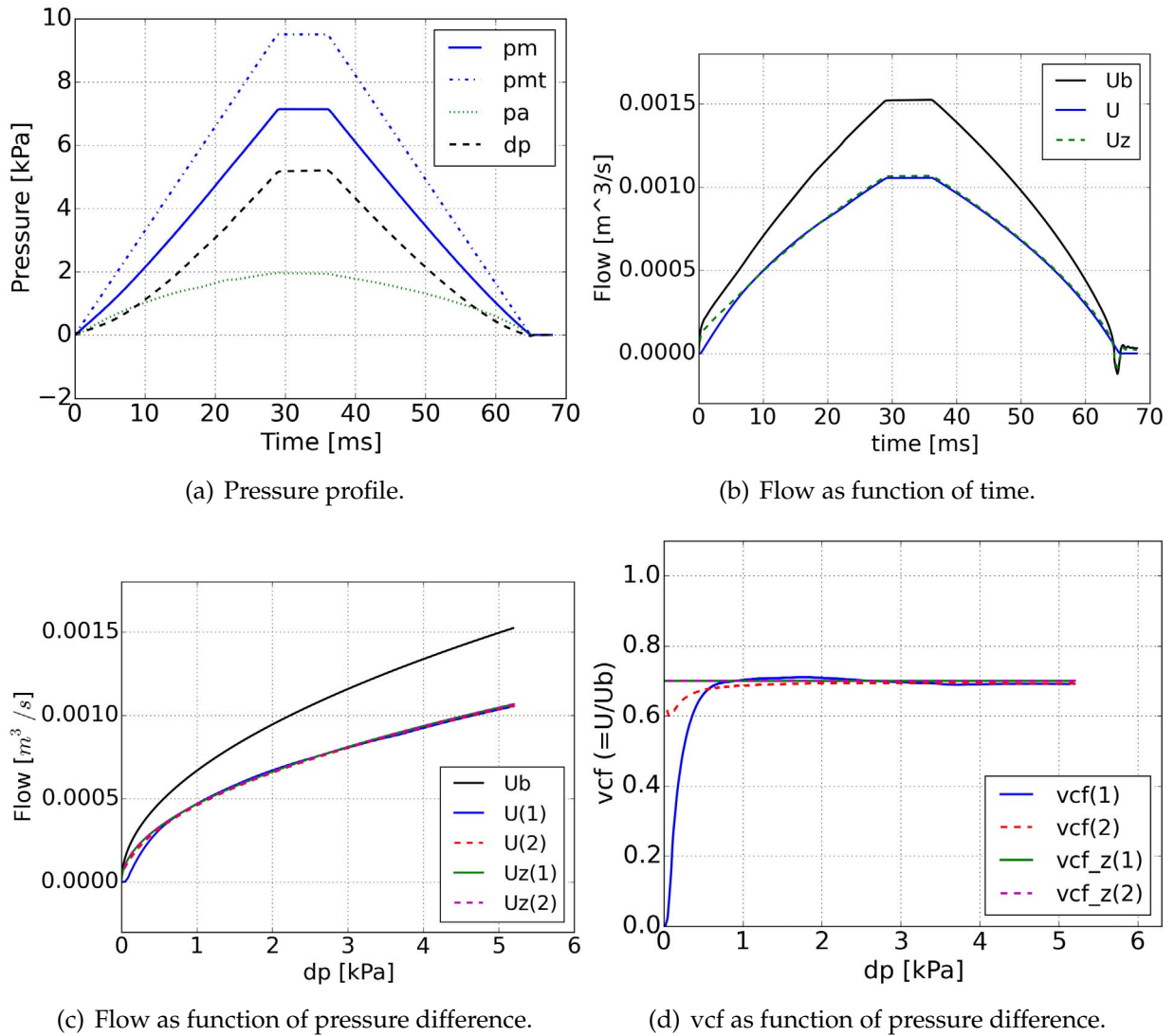


Figure 5.4 Results of static reed, short channel ($L/h = 1$).

the reed channel is fixed, the Bernoulli flow is only related to the measured pressure difference dp . Figures 5.4(c) and 5.5(c) represent the same flow data as a function of pressure difference, where $U(1)$ and $Uz(1)$ are the flows associated with Stage I, and $U(2)$, $Uz(2)$ are the flows associated with Stage II. The contraction parameter of van Zon's model for the short channel is 0.7. In general, the measured flow is lower than the Bernoulli flow due to the flow separation occurring at the entrance of the reed channel. For the short channel, the measured flow is in good agreement with van Zon's model for

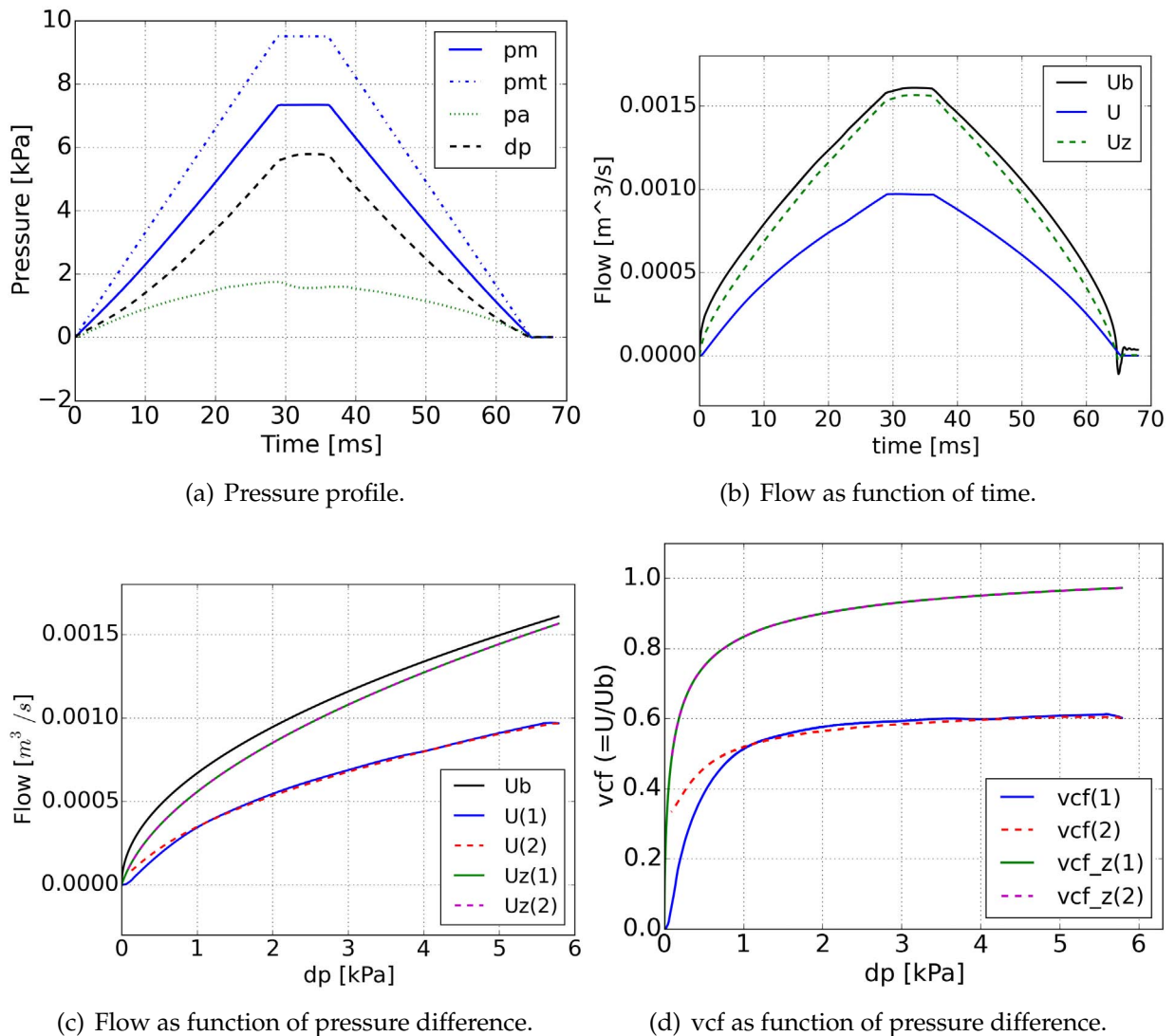


Figure 5.5 Results of static reed, long channel ($L/h = 4$).

most of the duration. However, for the long channel, the measured flow is significantly lower than the theoretical flow, which is only a little bit lower than the Bernoulli flow.

The phenomena of flow contraction, caused by the boundary layer effects on the walls of the lay and the reed and the flow separation at the entrance, can be quantitatively described by the vena contracta factors $vcf = U/U_b$, as depicted in Figs. 5.4(d) and 5.5(d), where $vcf(1)$ is associated to Stage I and $vcf(2)$ is associated to Stage II. The vena contracta factors of van Zon's model, noted as $vcf_z(1)$ and $vcf_z(2)$, corresponding

to Stage I and Stage II respectively, are depicted in parallel.

In the case of short channel, the measured vcf is in good agreement with theoretical vcf_z for most of the duration. In the case of long channel, the measured vcf is significantly lower than the theoretical vcf_z . Also, the vcf corresponding to the long channel is lower than that of the short channel, which might be explained by the relatively higher damping in the long channel that is caused by friction from the flow and the walls. In other words, the pressure drop due to viscous dissipation in the long channels is much more accentuated. The numerical volume flow in the long channel probably is underestimated due to the relatively low spatial resolution in the reed channel. We will improve this situation in the later dynamic simulations in Sec. 5.5 using a higher spatial resolution.

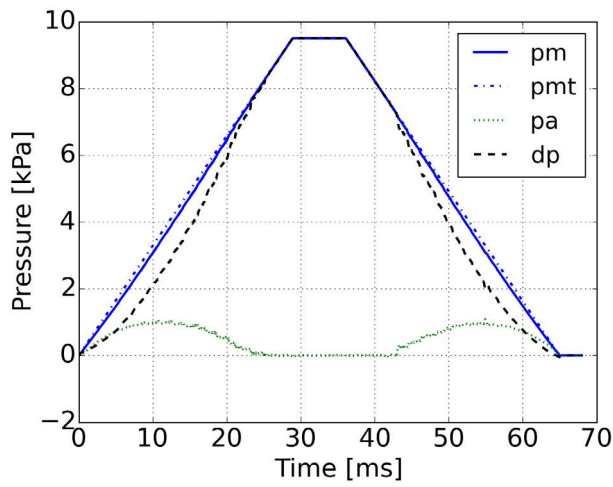
A slight hysteresis effect can be observed in the region of low pressure difference for both geometries, i.e., $dp < 0.5 \text{ kPa}$ for the short channel and $dp < 1 \text{ kPa}$ for the long channel. Since the reed is fixed, the hysteresis phenomena cannot be caused by the viscoelasticity of the reed, rather, it is more likely due to the inertia of the air flow. We notice the variation of vcf is very small in about 80% of the duration of the simulation for both geometries, which suggests that a constant vcf used in the quasi-stationary model is a reasonable approximation for the case of a fixed reed.

5.4.3 Results of Moving Reed

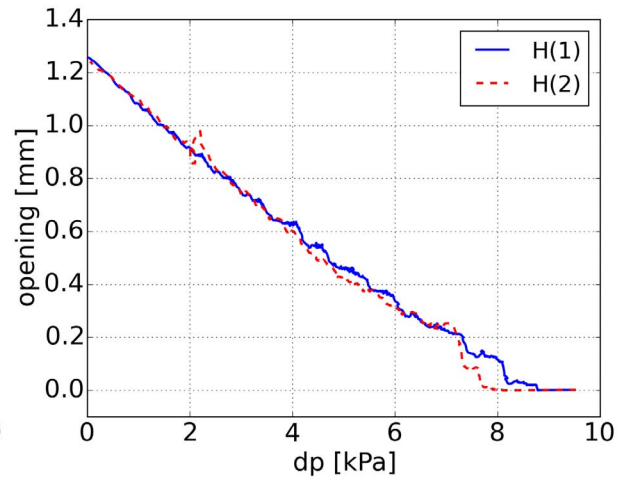
Throughout the dynamic simulations, the reed is moving as the pressure difference across the reed channel changes. The results corresponding to the short channel and the long channel are depicted in Figs. 5.6 and 5.7, respectively.

Figures 5.6(a) and 5.7(a) depict the time history of the target pressure p_{mt} prescribed on the absorbing boundary in the mouth cavity, the measured mouth pressure pm , the average pressure in the mouthpiece chamber pa and the pressure difference across the reed channel $dp = pm - pa$. The target pressure is prescribed in the same way as in the simulations of the fixed reed, i.e., p_{mt} increases linearly from zero to the highest value of 9.5 kPa , holds, and then decreases linearly and holds at zero until the simulation is finished.

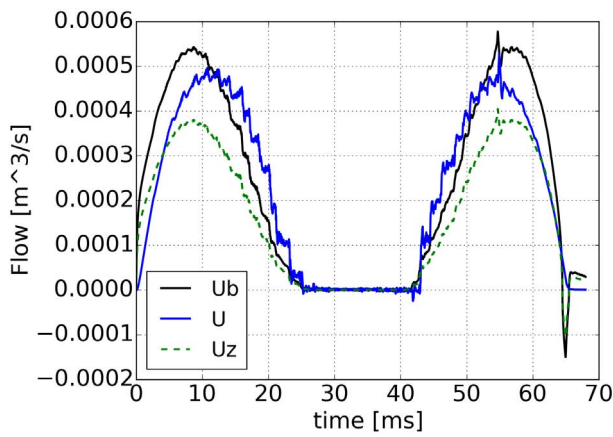
Before the reed closes in Stage I, the mouth pressure increases along with p_{mt} , though at a reduced level. The pressure in the mouthpiece pa increases and reaches a peak value in about 9 (short channel) to 12 ms (long channel), then decreases because the amount



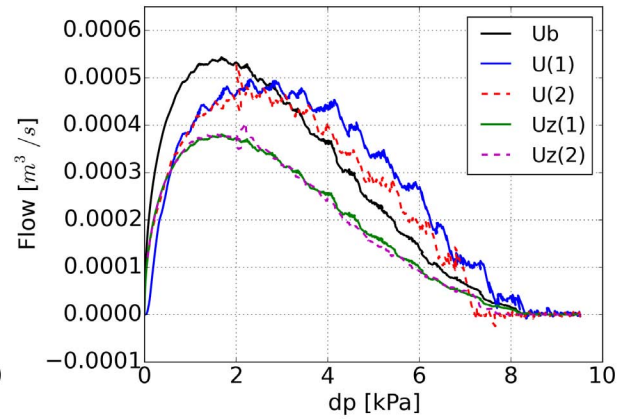
(a) Pressure profile.



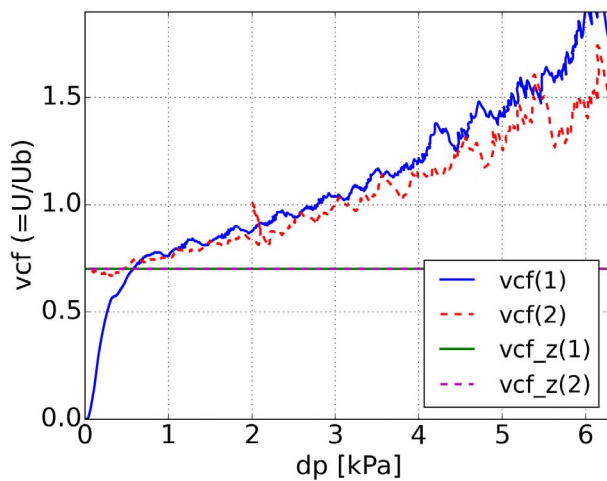
(b) Opening as function of pressure difference.



(c) Flow as function of time.

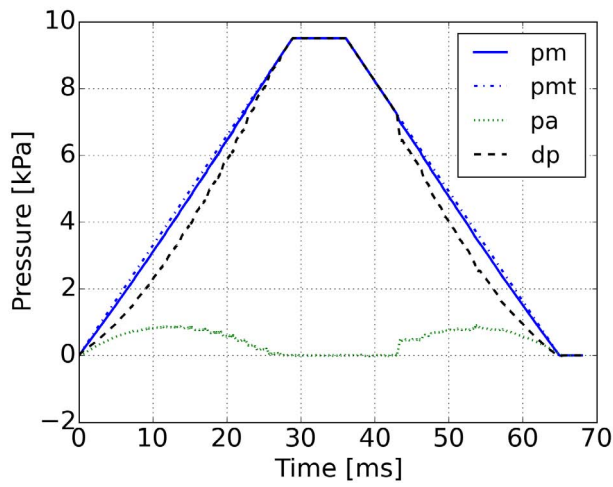


(d) Flow as function of pressure difference.

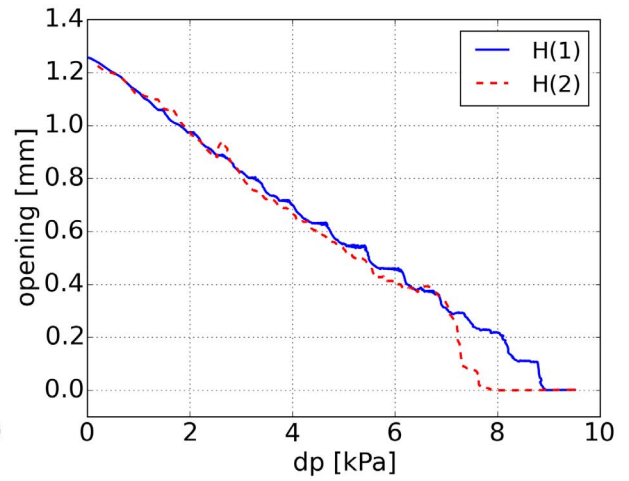


(e) vcf as function of pressure difference.

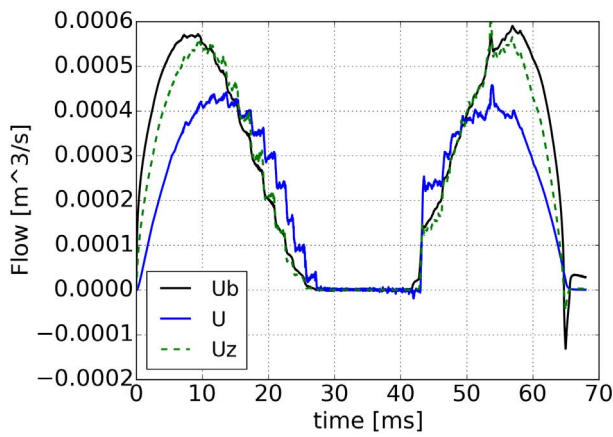
Figure 5.6 Results of moving reed, short channel ($L/h = 1$).



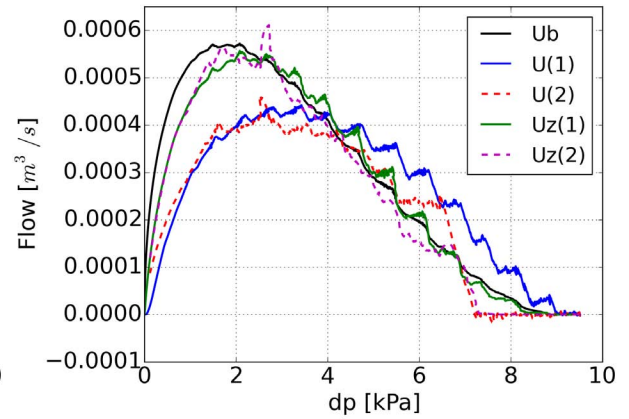
(a) Pressure profile.



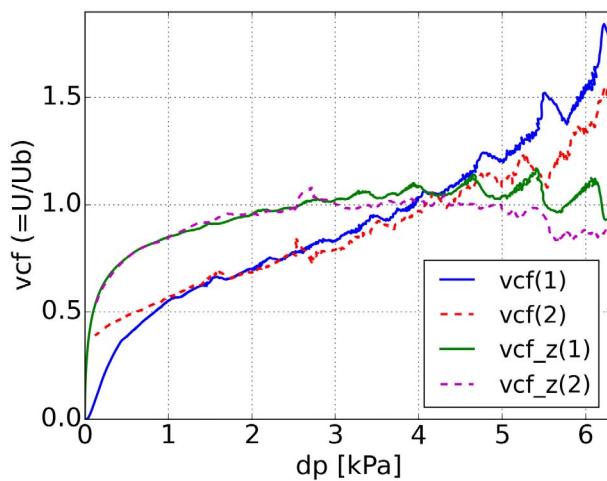
(b) Opening as function of pressure difference.



(c) Flow as function of time.



(d) Flow as function of pressure difference.



(e) vcf as function of pressure difference.

Figure 5.7 Results of moving reed, long channel ($L/h = 4$).

of flow entering into the mouthpiece chamber is reduced due to a smaller opening of the reed channel. When the reed is completely closed at the closing pressure, which is about $8783 Pa$ for the short channel and $8939 Pa$ for the long channel, there is almost no flow entering into the mouthpiece chamber, and pa drops to zero. In Stage II, pa starts to increase when the decreasing mouth pressure is lower than the closing threshold. The threshold of the closing pressure in Stage II is lower than that in Stage I. This phenomenon is explained by the bifurcation delay (Atig et al., 2004; Bergeot et al., 2014).

Figures 5.6(b) and 5.7(b) depict the reed channel opening as a function of dp for the case of short channel and long channel, respectively. For the most part, the opening is almost linearly related to dp . A hysteresis effect is found in the region of dp that is higher than about $7 kPa$. There is a sudden drop and increase of opening when the mouth pressure reaches the closing pressure in Stage I and Stage II, respectively.

Figures 5.6(c) and 5.7(c) depict the Bernoulli flow U_b , the measured flow U and the theoretical flow U_z calculated from van Zon's model as a function of time. Figures 5.6(c) and 5.7(c) represent the same flow data as a function of pressure difference, where $U(1)$, $U_z(1)$ and $U(2)$, $U_z(2)$ are the flow associated with Stage I and Stage II, respectively. The contraction parameter of van Zon's model for the short channel is 0.7.

The measured flow in the moving reed case shows some differences to the quasi-stationary model. The measured flow shows hysteresis for cases of both short channel and long channel. The quasi-stationary model, on the other hand, only shows hysteresis for the long channel because the displacement of reed is taken into account. For the short channel, the measured flow U is higher than the Bernoulli flow U_b and theoretical flow U_z of the quasi-stationary model in the region where dp is more than about $3 kPa$. Similarly, for the long channel, U is higher than U_b and U_z in the region where dp is more than about $4 kPa$. It can also be observed in Figs. 5.6(e) and 5.7(e) that the vena contracta factor shows a value larger than unity in the region of higher dp . This phenomenon might be explained by the discussion in Dalmont et al. (2003), where the quasi-stationary model assumes the reed channel with a fixed separation point and a uniform height, which is questionable in the case of a more realistic clarinet mouthpiece, in which the height across the reed channel varies and the separation point may change. The discrepancies might also be related to the flows of low Reynolds number that cannot be described by the Bernoulli's equation. The measured vcf associated with the region of $dp > 6.5 kPa$ is questionable and is discarded due to the dramatical change

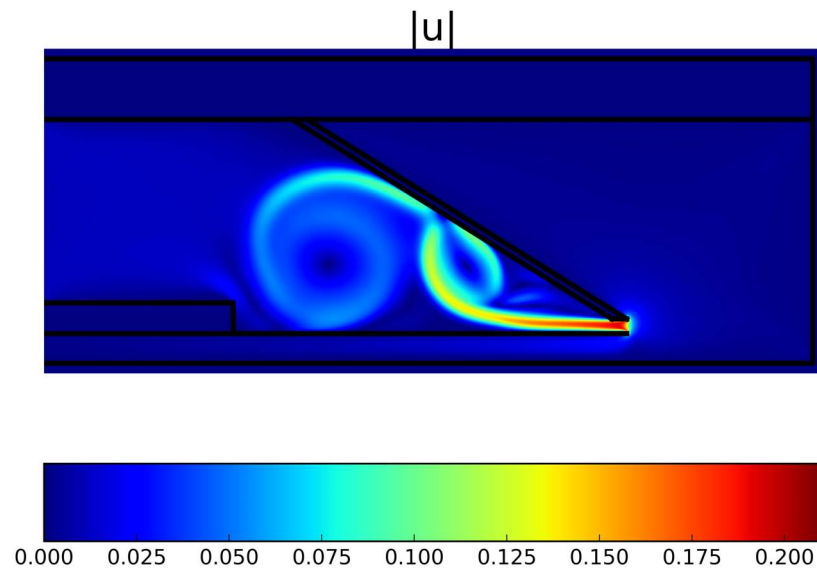
of both U and Ub , as depicted in the region around about 43 ms in Figs. 5.6(c) and 5.7(c).

5.4.4 Discussions

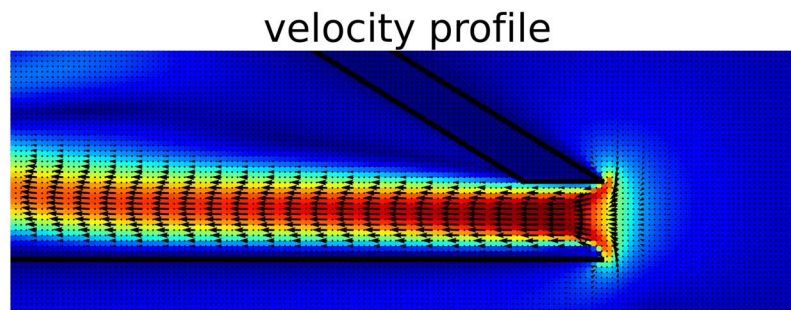
The staircase-like ripples found in the measured flow and opening for the cases of moving reed (Figs. 5.6 and 5.7) might be explained by the low spatial resolution. Even in the full opening, the tip height is represented by only 14 cells. When the reed channel is nearly closed, the cells are even fewer and insufficient to represent the flow crossing the reed channel and the boundary layer effect. When the reed tip is moving across a fluid cell, there is an abrupt change of the pressure difference across the surfaces of the reed which functions as a step exciting signal. The staircase-like ripples are probably resulted from the reed's motion driven by the step-like aerodynamic force. One may think that there might having some sort of acoustic reflections at the outlet of the mouthpiece, which might be driving the reed. To verify this hypothesis, we can calculate the fundamental oscillation frequency due to the acoustic resonance of the mouthpiece, which is approximated by $f_0 \simeq 340/(2 * L) = 2623 Hz$, where $L = 64.8 \times 10^{-3} (m)$ is the length of the mouthpiece chamber. On the other hand, there are about 6.5 ripples during the time span of 10 ms , which corresponds to a fundamental frequency of $\simeq 650 Hz$ that is much lower than the frequency of the hypothetic acoustic standing wave. Thus, the ripples are not driven by the acoustic reflections.

The measurements can be further improved by using a higher spatial resolution, as we will do in the next section for the case of an oscillating reed. However, this problem cannot be fully solved by simply using an extremely large lattice because of the limited computation and memory resources allowed by the GPU device, and the results are always dubious when the opening is very small. An adaptive grid refinement technique (Rohde et al., 2006) might be helpful but is not implemented in the current model yet. Nevertheless, a low-discretized lattice can still capture reasonable well global parameters such as the averaged volume flow.

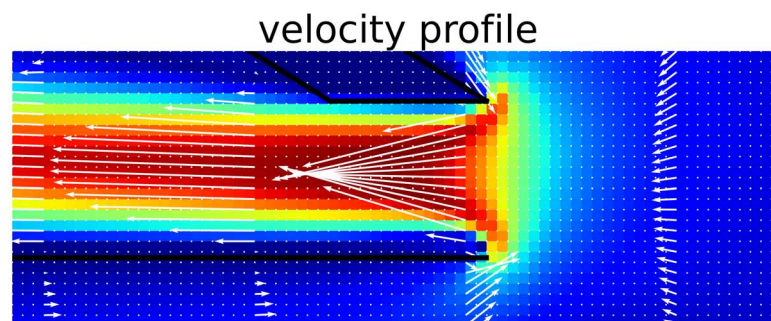
Due to the relatively higher numerical viscosity, the Reynolds number in the numerical simulation is lower than the realistic one. In the situation of the static reed, the highest Reynolds number is 140, which is much lower than the realistic Reynolds number 4762 (assuming the same volume velocity). Consequently, the measured flow is not exactly the same as the Bernoulli flow and the quasi-stationary model, which is based on the assumption of inviscid flow. A low numerical viscosity is not practical for the



(a) Absolute velocity.

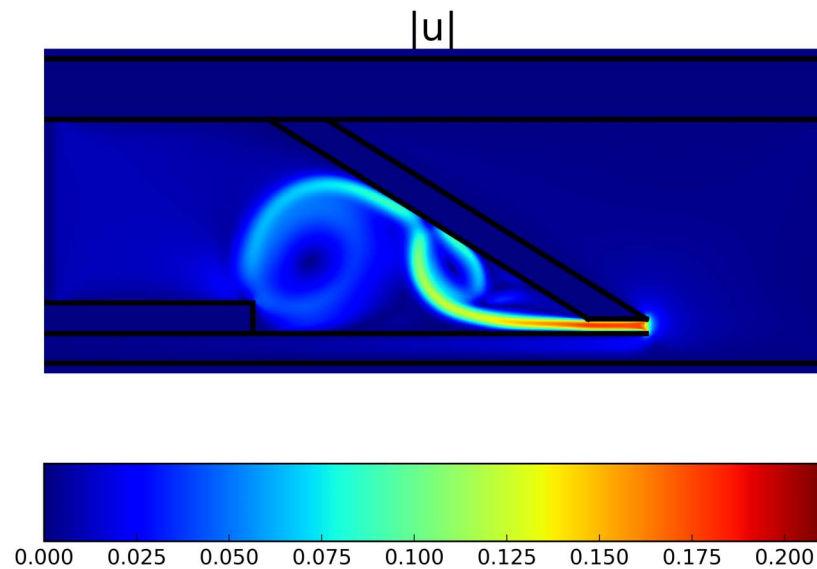


(b) Velocity profile of the jet passing through the reed channel.

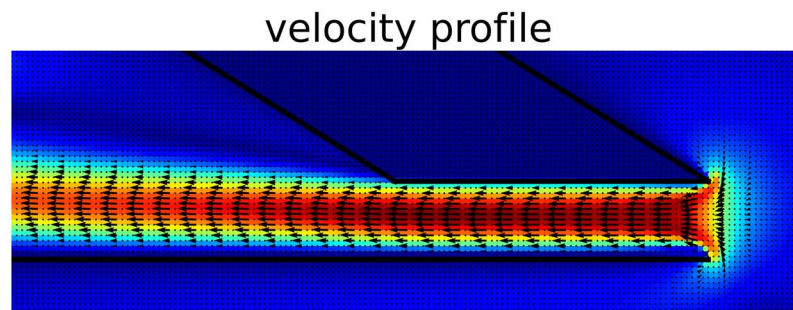


(c) Velocity profile depicted in a larger scale.

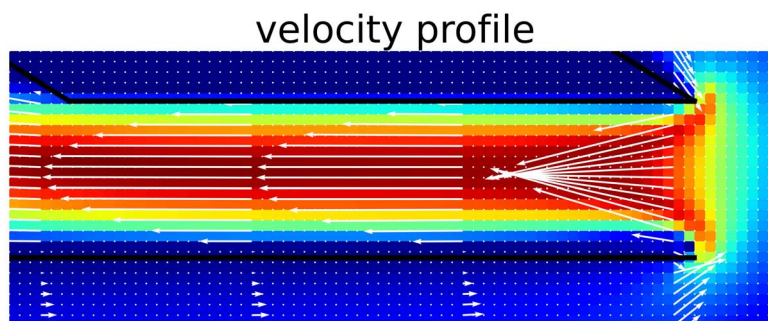
Figure 5.8 Visualization of the velocity field, short channel.



(a) Absolute velocity.



(b) Velocity profile of the jet passing through the reed channel.



(c) Velocity profile depicted in a larger scale.

Figure 5.9 Visualization of the velocity field, long channel.

dynamic reed case because, apart from the issue of numerical stability, there is the difficulty of eliminating the noise caused by acoustic oscillations when the viscosity is very low. Nevertheless, useful results can still be obtained from the current model.

As already noted in Fig. 5.5(b), the predicted volume flow rate deviates largely from van Zon's model for the long channel case. We attempted to investigate this discrepancy by estimating the boundary layer thickness from the spatial distribution and evolution of the jet. Figures 5.8(a) and 5.9(a) visualize the velocity field ($u = \sqrt{u_x^2 + u_y^2}$) for the cases of static short and long reed channels respectively, from which we can observe that the flow is passing through the reed channel and is dissipated in the mouthpiece chamber. Figures 5.8(b) and 5.9(b) depict the velocity profile of the jet passing through the short and long reed channel, respectively. In the short channel, a flow separation can be observed at the entrance and the total critical thickness of the boundary layers on both the top and bottom walls is about 7 cells, corresponding to an averaged dimensionless thickness of 0.2333 for one wall, which is slightly lower than the thickness of 0.2688 used in van Zon's model. For the case of long channel, a reattachment of the flow occurs after a distance on the order of the reed channel height, and a Poiseuille flow is developed after a transition zone. The averaged dimensionless thickness of the boundary layer is about 0.3 (9 cells in total). The lower volume flow for the long channel case might be caused by the boundary layer thickness which is slightly higher than that used in van Zon's model, But it could also be influenced by the flow pattern characterized by a low Reynolds number, because the boundary layer thickness estimated from the velocity profile is not very accurate due to the low-discretization. In a dynamic situation, though, the flow profile would certainly not match van Zon's assumption. The flow detachments at the reed tip can be better observed in Figs. 5.8(c) and 5.9(c), where the velocity profiles in the neighboring area of reed tip are depicted in a larger scale. The magnitude of the counter-flow at the reed wall is much lower than that of the maximum flow velocity but still can be observed.

5.5 Investigations of the Dynamic Regime

In this section, we investigate the characteristics of the mouthpiece-reed system of a clarinet with an acoustic resonator in the dynamic regime.

5.5.1 Setup of Simulations

The hybrid clarinet model discussed in Sec. 5.3 has produced reasonable good results in the quasi-stationary simulations presented in Sec. 5.4, though we have also found some of the results might be compromised by the rather low spatial resolution. With some refinement in this model, we are able to simulate the clarinet in the dynamic regime as well in a reasonably short time span, which is an aspect that must be taken into account when the system is fully coupled with aerodynamic and acoustic oscillations.

Firstly, to facilitate the acoustic oscillation, we set the aperture of the reed channel at rest to $h = 1$ (mm), which is slightly smaller than the one used in the quasi-stationary simulations. We also found that an acoustic oscillation is much easier to obtain when the reed is less rigid, so a smaller Young's modulus with a half value of that used in Sec. 5.4 is chosen here, i.e., $Y = 2.8 \times 10^9$ (N/m^2). The next refinement is using a higher spatial resolution, $dx = 4.25 \times 10^{-5}$ (m), which corresponds to about 24 cells covering the tip aperture at rest. Therefore we are able to capture more details of the flow behavior, which is essential to visualize the phenomenon of flow separation and reattachment in the reed channel. Last but not least, in order to provide a precise and stable pressure source in the mouth cavity in the presence of strong acoustic oscillations typically found in the dynamic simulations, we improved the SRC scheme previously used in the quasi-stationary simulations with an auto-feedback procedure (AFP), such that the target pressure and velocity of the SRC is not only read from the prescribed static profile but also compared and adjusted with the instantaneous pressure measured in the mouth cavity.

The lattice relaxation parameter is chosen as $\Omega = 1.88$, which is the same as the value used for quasi-stationary simulations, but the corresponding physical kinematic viscosity of the fluid changes to 2.66×10^{-4} (m^2/s) because of the new smaller dx . The time step is $dt = 7.22 \times 10^{-8}$ (s). The duration of each simulation is set to 500,000 iterations, or about 36 ms .

All three different geometries depicted in Fig. 5.3 are used in the dynamic simulations, namely a), short channel ($L/h = 1$), b), long channel ($L/h = 4$) and c), long channel with a ditch at the outlet.

The source signal has been generated by the three SRC buffers attached on top of the inner walls of the mouth cavity. In order to simulate the playing of a clarinet by a musician, the mouth pressure pm is prescribed by an "attack-drop-sustain" profile,

Geometries	pmt_0	pmt
Short channel	3000 (Pa)	700 (Pa)
Long channels	3000 (Pa)	1000 (Pa)

Table 5.4 Mouth pressures prescribed for different lay geometries.

i.e., pm increases from zero to an initial high target pressure pmt_0 in a very short time span (1 percent of the total simulation time, or about 0.36 ms), then drops quickly in 0.07 ms and remains a constant value pmt until the end of the simulation. In the present study, only the *soft playing condition* is investigated, i.e., the amplitude of the mechanical vibration is kept at a small level such that no beating happens during the stable stage. In such a case, the flow consists of a small oscillation component superimposed on a steady component, and the reed and air-column vibrations are nearly sinusoidal. Table 5.4 lists the playing parameters used in the simulations. The initial target pressure pmt_0 is close to the threshold of pressure closing the reed channel, which is lower than the one found in the quasi-stationary simulations using a harder reed. It takes some try and errors to find the appropriate pmt to maintain a soft oscillation without a beating reed during the whole simulation. A lower pmt is assigned for the short channel geometry because the reed is very prone to beating.

The analysis is performed on two steps. In the first step, the velocity field and the pressure field in the whole mouthpiece chamber are qualitatively visualized, which provide an overview of the distribution and evolution of the fluid flow and the pressure field. In the second step, the time histories of reed tip displacement, pressure difference across the reed channel and volume flow in one reed duty cycle are analyzed, and the numerical volume flow is compared to the results predicted by van Zon's quasi-stationary model.

Due to the huge amount of data generated in the simulations, it is not practical to save all the velocity and density fields at every single time step. For the qualitative visualization in the first step, 40 snapshots of velocity and density field in a rectangular area enclosing the baffle and the reed channel have been probed during the period of two acoustic cycles. The period of one acoustic cycle T_{ac} in a static clarinet with a closed reed channel can be approximated from the effective length of the system including the length correction by

$$T_{ac} \approx \frac{4(L_3 + L_2 + 0.61a)}{c_s} = 1.53 \text{ (ms)}, \quad (5.7)$$

where $c_s = 340$ (m/s) is the speed of sound, $L_3 = 64$ (mm) is the length of the bore, $L_2 = 64.8$ (mm) is the length of mouthpiece and $a = 8$ (mm) is the radius of the bore. The fundamental acoustic resonance frequency of the system under the static condition is obtained by $f_{ac} = 1/T_{ac} \approx 654$ (Hz). The actual fundamental operating frequency of the system under the dynamic condition must be lower due to the additional effective volume of the reed channel caused by the reed's motion. Nonetheless, we can obtain some 20 frames for one full reed duty cycle from the probed data of 40 frames.

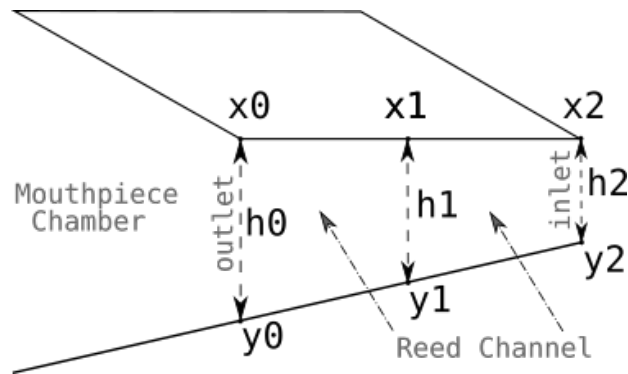
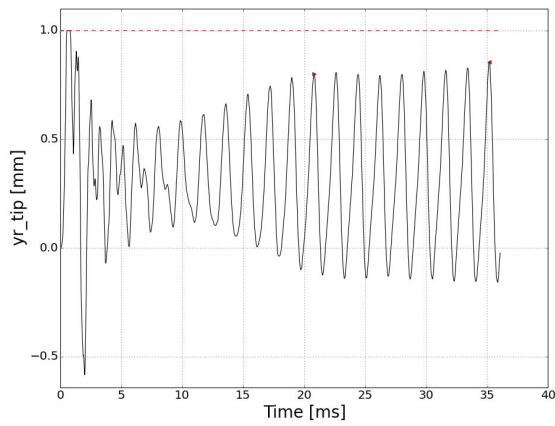


Figure 5.10 Three probing points in reed channel.

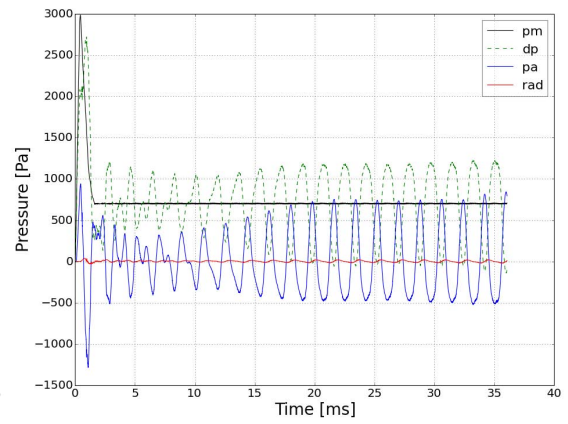
For the analysis in the second step, the time histories of pressure in the mouth cavity, the mouthpiece and the radiation domain out of the pipe are probed, namely pm , pa and rad , as depicted in Fig. 5.2. The velocity profiles and the reed displacements at the outlet x_0 , the middle (x_1) and the inlet (x_2) of the reed channel, as depicted in Fig. 5.10, are probed and used to calculate the corresponding volume flow (U_0 , U_1 and U_2) and openings (h_0 , h_1 and h_2). The corresponding sampling period is set to $10 \times dt$, which is more than enough for our analysis while the data size is reduced by 10 times.

5.5.2 Waveform and Spectrum

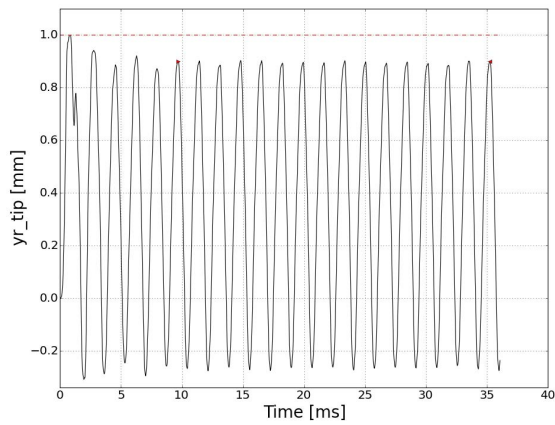
The time histories associated with the displacement of the reeds measured at their tips, y_{tip} , as well as pressures measured in the mouth (pm), in the middle of the mouthpiece (pa) and in the radiation domain (rad) and the pressure difference across the reed channel ($dp = pm - pa$) for different lay geometries are depicted in Fig. 5.11, respectively. The reed oscillation associated with the short channel presents a lower amplitude and a longer transient period before the oscillation becomes almost stable, this is likely due to



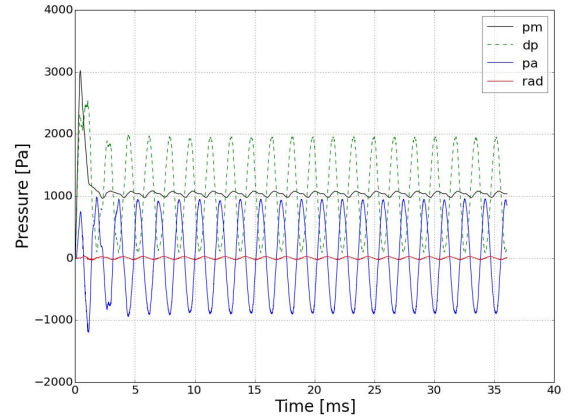
(a) Short channel.



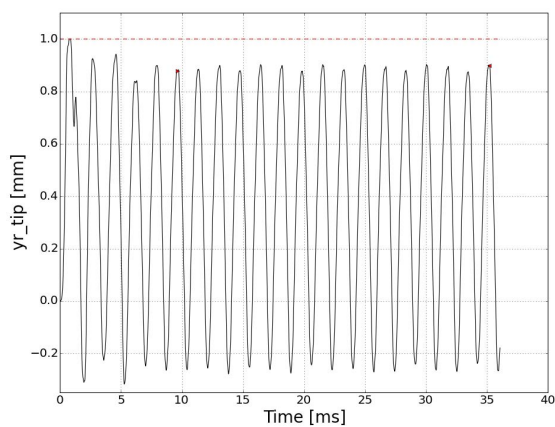
(d) Short channel.



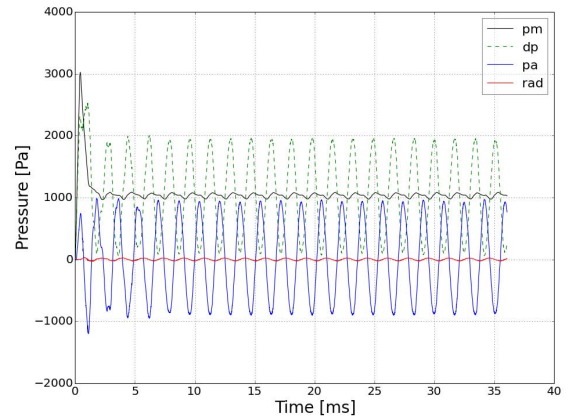
(b) Long channel.



(e) Long channel.



(c) Long channel with a ditch.



(f) Long channel with a ditch.

Figure 5.11 Time histories of displacements of reed tips (left) and pressures (right) for different geometries.

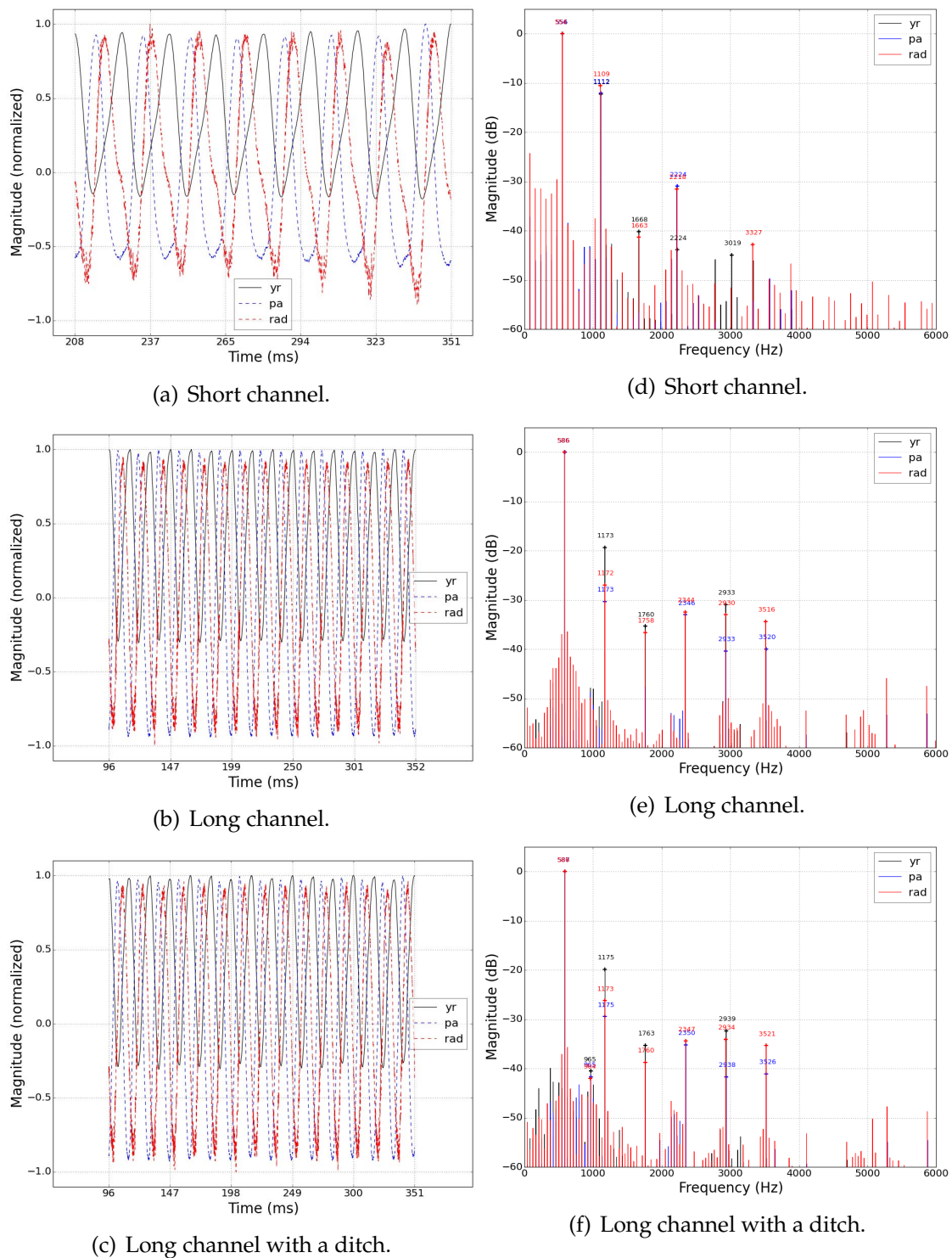


Figure 5.12 Normalized waveforms (left) and spectrum (right) of reed tips (*yr*) and acoustic pressures (*pa* in mouthpiece, *rad* in radiation domain) for different geometries.

the lower prescribed mouth pressure associated with the short channel ($pm = 700 Pa$) compared to the one associated with the long channels ($pm = 1000 Pa$). There is no beating except for the very first cycle when the systems are excited by a step-like initial pressure signal. Since the reed is relatively soft and there is no lip forces, the reed tip can move below the equilibrium point by $0.25 mm$. Due to the time required for the acoustic wave propagating back and forth in the pipe and in the radiation domain, there is a phase delay between the radiated pressure (rad) and the pressure measured in the mouthpiece (pa). As expected, the amplitude of rad is significantly lower than that of pa , because most acoustic energy is dissipated in the pipe due to the viscous losses and wall frictions. Having said that, the pressure rad captured in the radiation domain is a near-field representation. Therefore, it does not represent exactly what we hear.

Figure 5.12 compares the normalized waveform (left) of the reed tip oscillation (yr) and the acoustic pressures (pa, rad) extracted from the relatively stable part of the time histories and the corresponding power spectrum (right) for all three geometries, where the frequencies of the relatively strong modes (amplitudes greater than $-40 dB$) are annotated. First of all, the fundamental frequency f_0 associated with all three geometries is significantly lower than the theoretical fundamental frequency ($f_0^{(static)} = 654 Hz$) estimated from the effective length of the system in static condition. $f_0^{(s)} = 556 Hz$ associated with the short channel has a value lower by 15 percent, and $f_0^{(l)} = 586 Hz$ associated with the long channel is lower than $f_0^{(static)}$ by 10 percent. These phenomenon is explained by the additional length correction caused by the reed volume velocity (Nederveen, 1998, pp. 28-35). There are some differences between the spectrum of the short channel and the long channel. For example, the fundamental mode of the short channel is lower than that of the long channel by 5.5% ($556 Hz$ vs. $586 Hz$), which makes sense in that the effective length of the mouthpiece-bore system having a short channel is longer. Also, most higher modes of the mouthpiece-bore system with the long channels are stronger than that of the short channel case, excepts for the second mode. These differences are likely explained by the lower pm used for the short channel geometry. On the other hand, the ditch cut at the outlet of the long channel does not make a noticeable difference in the spectrum.

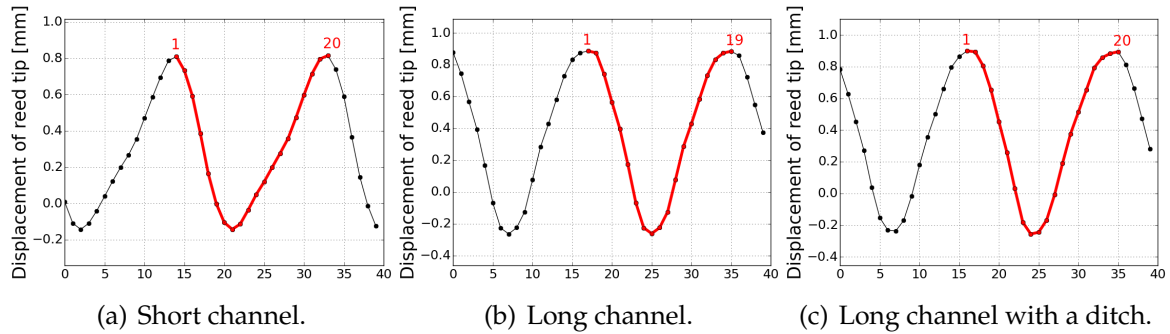


Figure 5.13 Instances selected for visualization in one duty cycle.

Geometry	Opening stage	Largest opening	Closing stage
Short channel (a)	n=1,2,3,4,5,6	n=8	n=10,13,15,17,19
Long channel (b&c)	n=1,3,4,5,6,7	n=9	n=11,13,15,17,19

Table 5.5 Instances selected for sequential field visualizations in one duty cycle.

5.5.3 Field Visualizations in One Duty Cycle

The velocity field and density field in the mouthpiece area has been captured and visualized in various manners. For the economic reason, only 40 snapshots roughly covering two acoustic cycles in the middle of the stable oscillations are saved for each simulation. Figure 5.13 depicts the motion of the reed tip in 40 instances for different lay geometries. The instances covering one duty cycle are depicted as red dots, where the indices of instances at the beginning and the end of the duty cycle are indicated. During one duty cycle, we select 12 instances for sequential field visualizations, i.e. 6 instances during the opening stage, 1 instance at the largest opening and 5 instances during the closing stage, as shown in Table 5.5. The redundant measurements outside of the duty cycle are discarded.

5.5.3.1 Pressure Field in Mouthpiece

Figures 5.14, 5.15 and 5.16 depict 12 instances of the sequential pressure fields in terms of normalized fluid density in the mouthpiece chamber as well as the reed channel and part of the mouth cavity. The reed is represented by a red thick curve and the walls of the

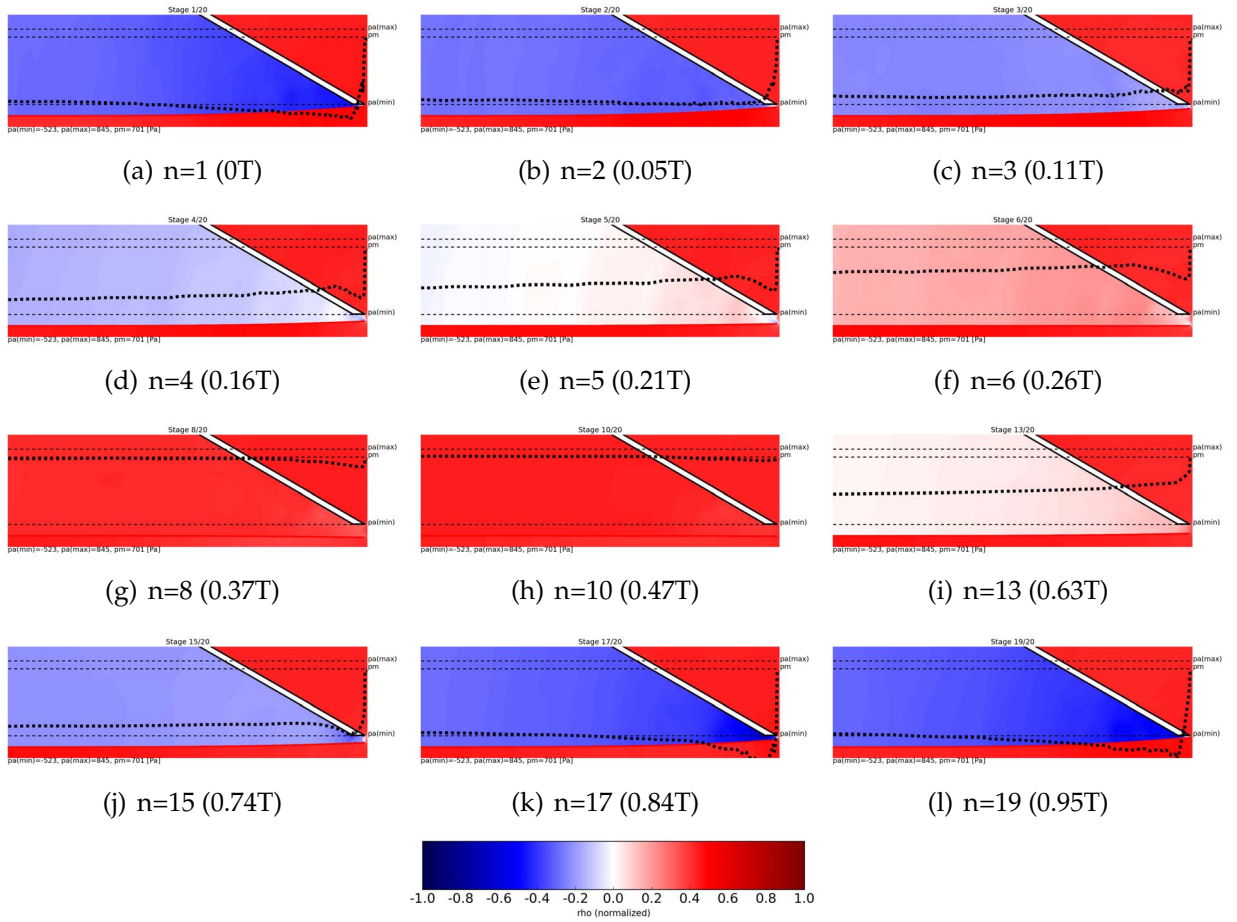


Figure 5.14 Short channel: pressure field (background) and profile of averaged pressure (thick black dashed line) in mouthpiece.

Geometry	pm (Pa)	dynamic range of pa (Pa)
Short channel	701	[-523, 845]
Long channel	1035	[-904, 955]
Long channel with a ditch	1034	[-902, 972]

Table 5.6 Mean value of pm and dynamic range of pa in one duty cycle for different lay geometries.

baffle by black lines. The color in the background is mapped to the normalized density field. The mean value of the mouth pressure and the minimum and maximum values of

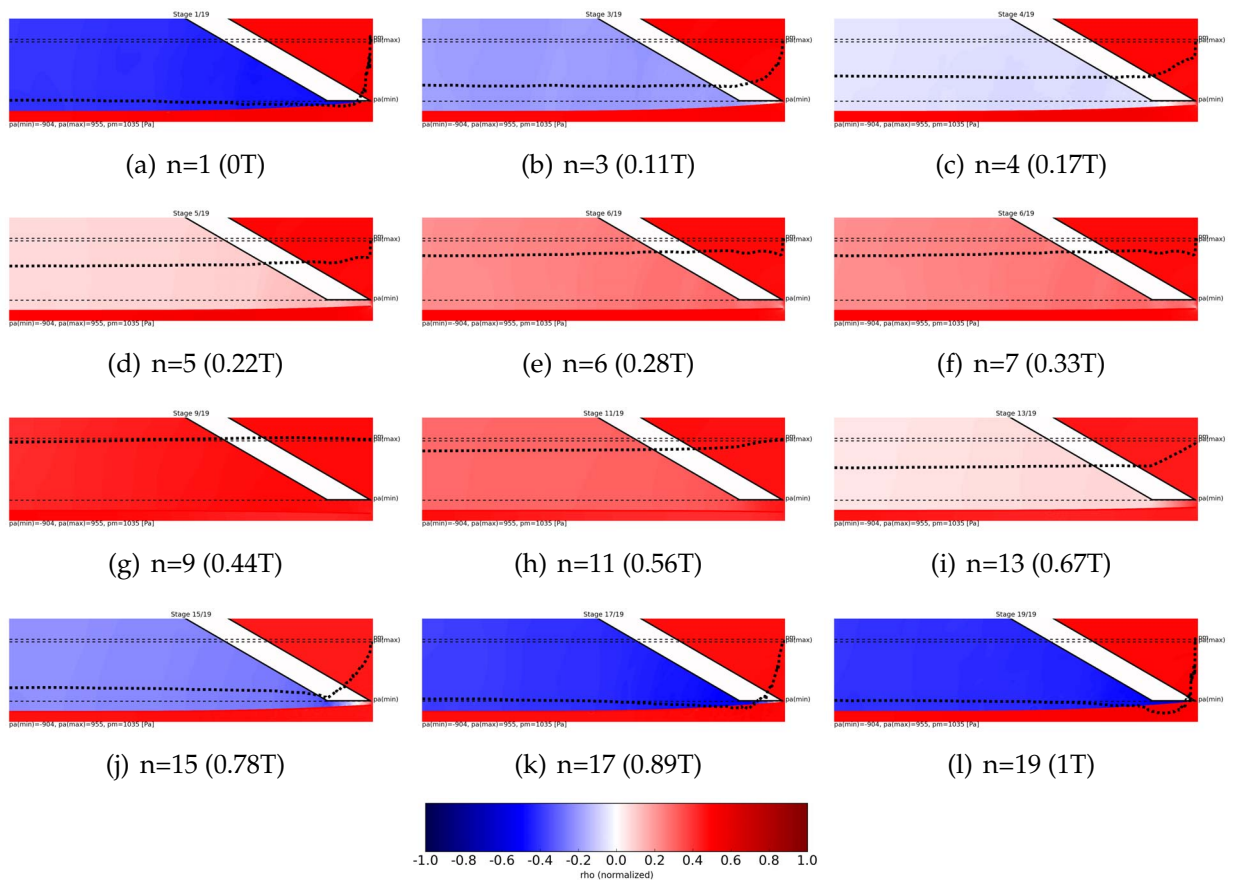


Figure 5.15 Long channel: pressure field (background) and profile of averaged pressure (thick black dashed line) in mouthpiece.

the pressure in one duty cycle in the mouthpiece have been mapped to three horizontal thin black dashed lines, respectively. These values for each geometry are listed in Table 5.6. The pressure variations in the mouthpiece chamber are visualized by the thick black dashed curve.

The pressure fields associated with the three geometries share some similarities. For all instances in the duty cycle, the pressure variation in the left part of the mouthpiece, i.e. far away from the outlet of reed channel, is negligible, that is partly in agreement with the assumption by van Zon et al. (1990) that the pressure in the mouthpiece is uniform and equal to the pressure at the end of the reed channel. The influence on the

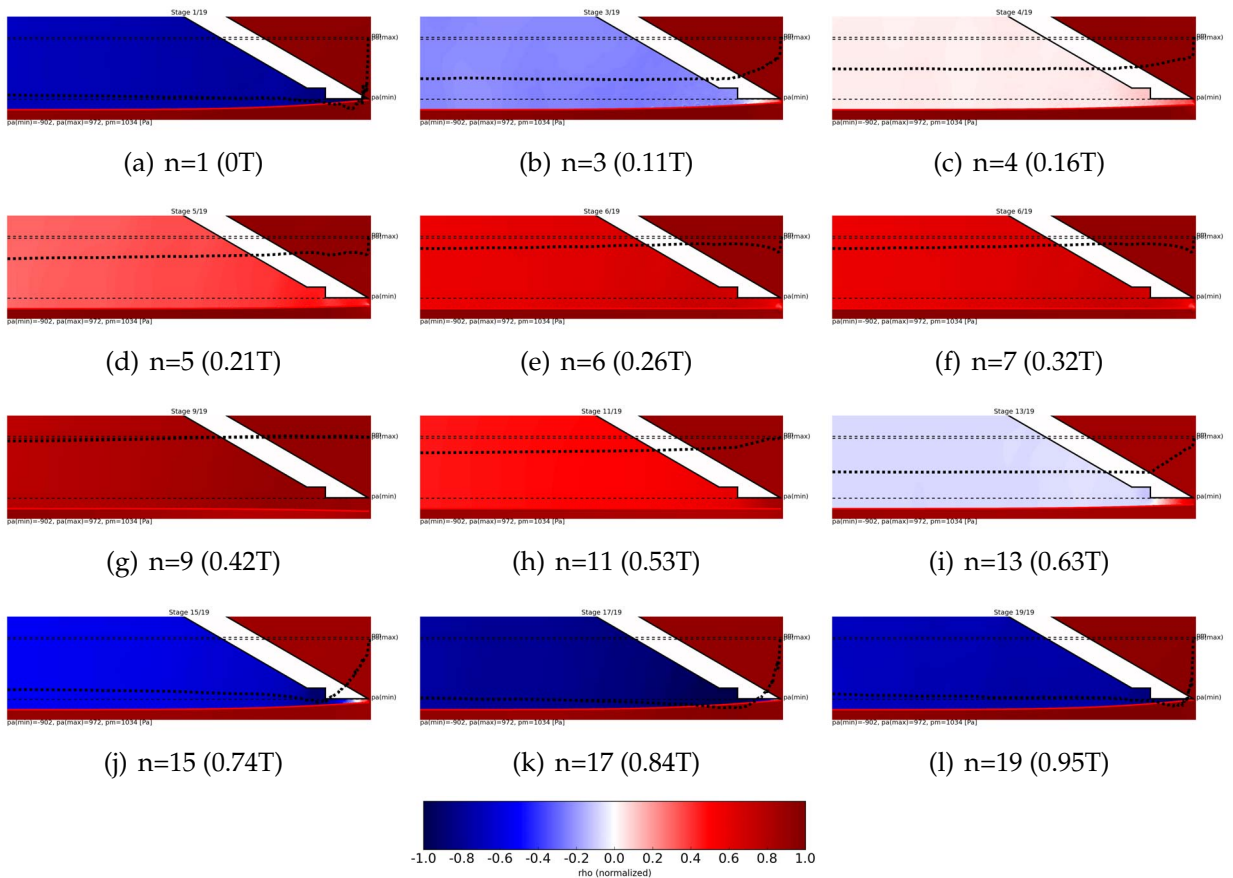


Figure 5.16 Long channel with a ditch: pressure field (background) and profile of averaged pressure (thick black dashed line) in mouthpiece.

pressure field due to the acoustic coupling is negligible because the dimension of the mouthpiece is much smaller than the wavelength of the low acoustic modes carrying higher energy. However, the pressure variations in the area near the outlet of the reed channel are not negligible, this is particularly true for the short channel geometry. Only at the very instant of the largest tip opening, the pressure in the whole mouthpiece is almost uniform and identical to the mouth pressure. In other words, the pressure difference is near zero when the reed channel is fully opened. In the intermediate stages between the fully opened and fully closed reed channels, the pressure difference is not a constant as assumed by quasi-stationary theory but is influenced by the channel open-

ing, i.e., the pressure difference in the downstream direction increases as the channel is closing, and vice versa. The prominent pressure variations found in the area close to the outlet and inside the reed channel should be attributed to the complex flow patterns in the mouthpiece and the reed channel, which will be discussed later.

5.5.3.2 Velocity Field in Mouthpiece

The velocity fields associated with the three geometries are visualized in two different zoom levels. Figures 5.17, 5.18 and 5.19 provide snapshots of the normalized absolute velocity field $u = \sqrt{u_x^2 + u_y^2}$ in the mouthpiece chamber, taken at 12 different instances within the same duty cycle. The direction and magnitude of the velocity vector associated with each cell is indicated by the white arrows and the raw image is kept as background. For the sake of clarity, the velocity vector is plotted sparsely at 24 cells intervals.

For all three lay geometries, the flow direction is from right to left. The maximum magnitude of velocity is 10.1 (m/s) for the short channel, 15.6 (m/s) for the long channel and 15.6 (m/s) for the long channel with a ditch, respectively. The region of highest velocity is mainly found along the upper surface of the mouthpiece, this phenomenon is also found in the numerical results by da Silva et al. (2007) for the case of a dynamic anechoically terminated mouthpiece of clarinet and experimental results by Lorenzoni and Ragni (2012) for the case of a saxophone under the normal playing condition, but is different from the quasi-stationary case shown in Figs. 5.8 and 5.9, where the jet of high velocities out of the reed channel is still close to the reed wall.

For the case of the short channel, the flow pattern during the opening stage is complex. In the lower part of the mouthpiece near the reed wall, there is a flow in the opposite direction due to the acoustic coupling. Along the upper surface of the mouthpiece, the fluid field is dominated by positive flow. In between, there are zero velocity regions in the middle of the mouthpiece chamber and vortices formed in the downstream direction due to the interaction of positive flow and negative flow.

For the case of the long channels (with and without a ditch), the negative flow and zero velocity region due to the influence of the acoustic wave are also found in the middle of the mouthpiece chamber during the opening stage, but there is no vortices because the positive flow is much stronger than the negative one due to a high pressure prescribed in the mouth. In the instances of the largest tip opening and during the

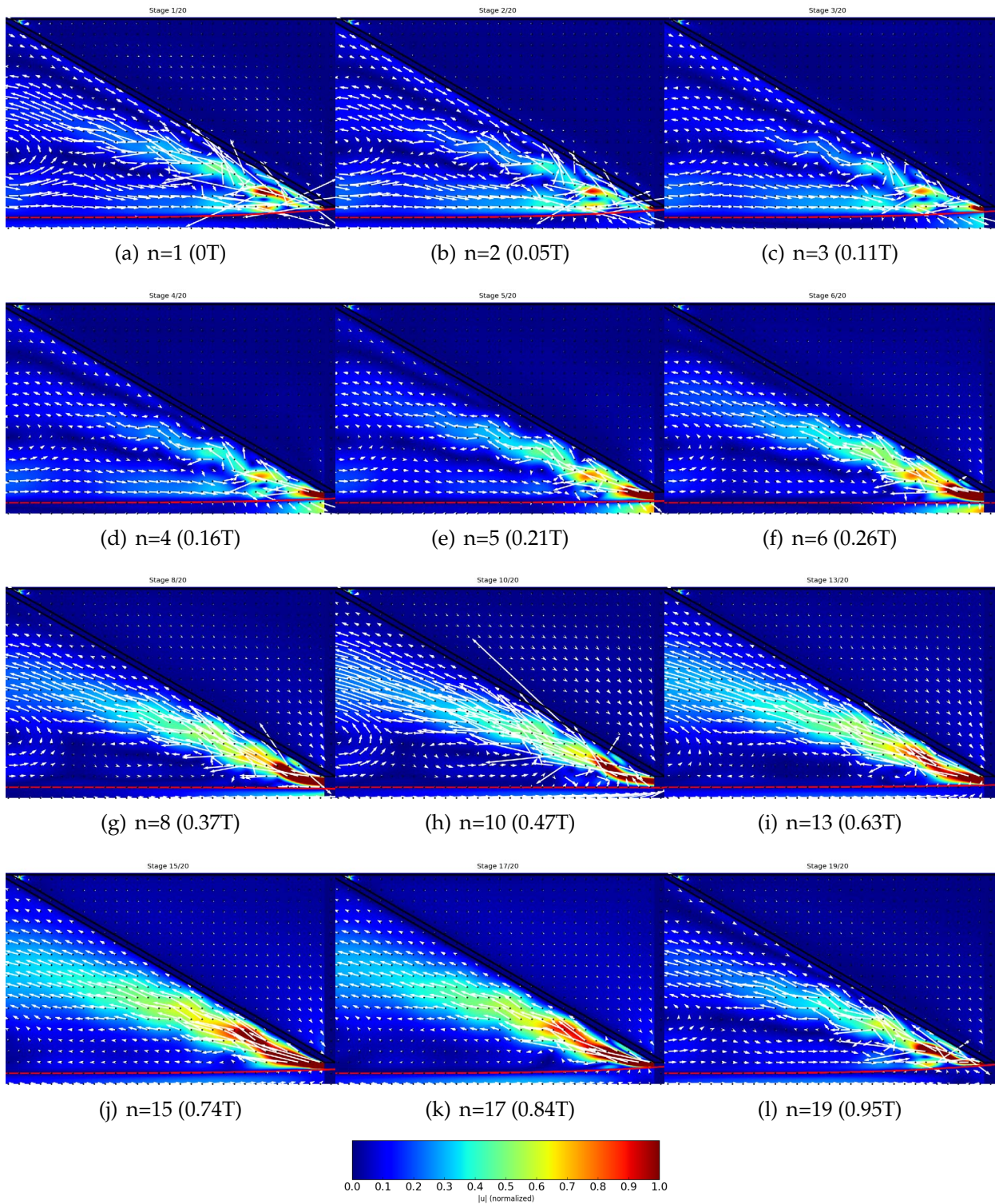


Figure 5.17 Short channel: absolute velocity field u (background) and velocity vectors (white arrows) in mouthpiece.

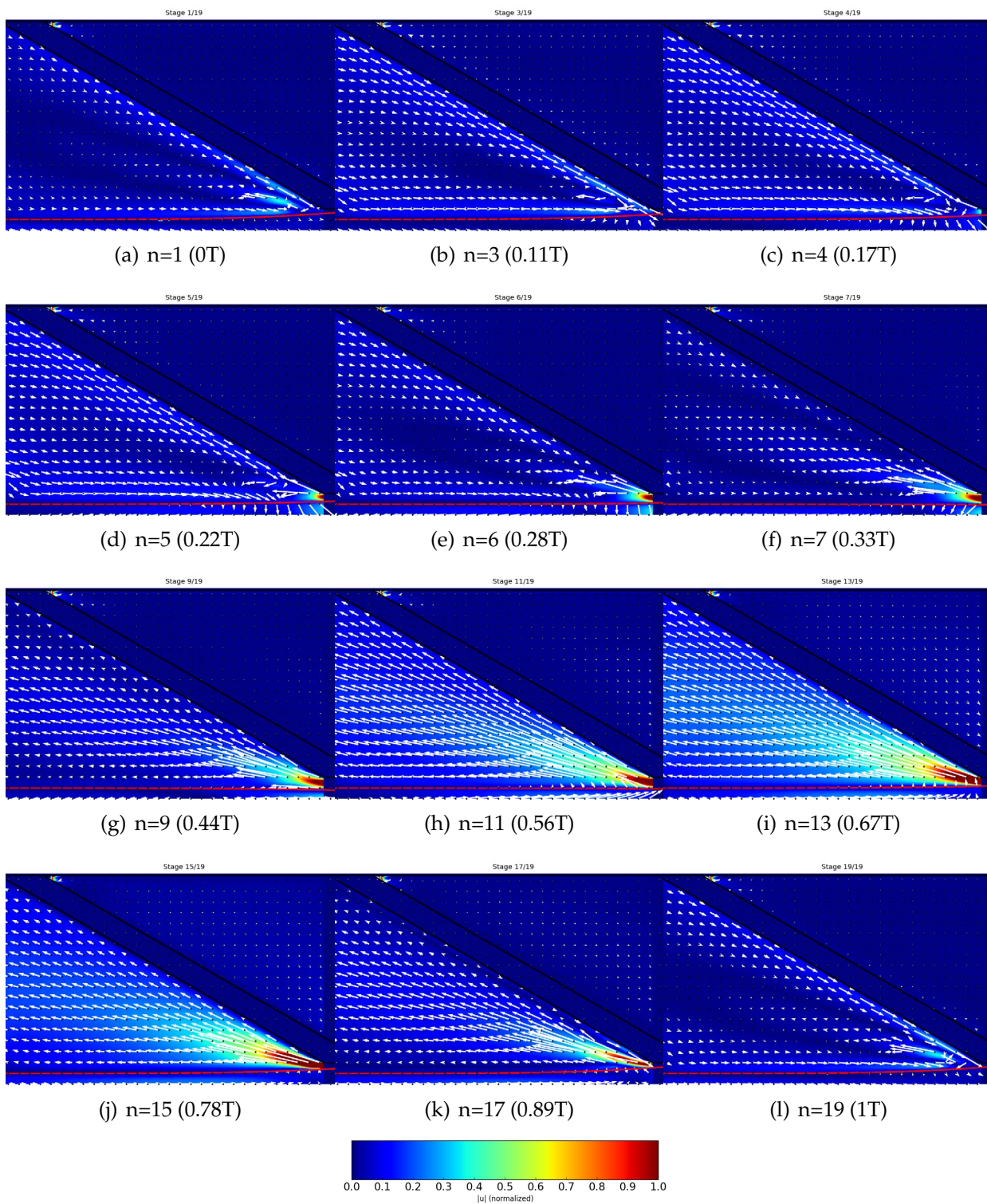


Figure 5.18 Long channel: absolute velocity field u (background) and velocity vectors (white arrows) in mouthpiece.

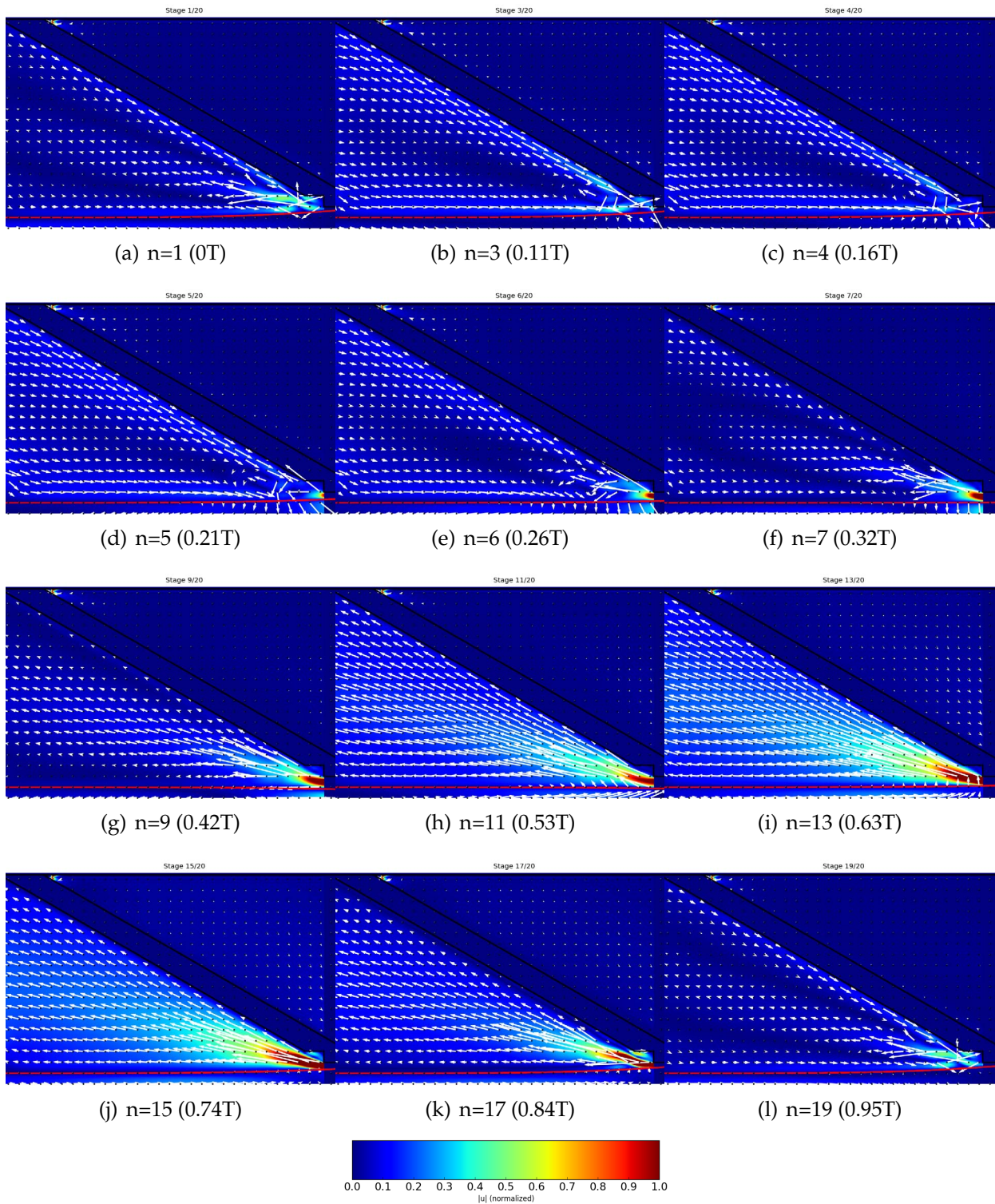


Figure 5.19 Long channel with a ditch: absolute velocity field u (background) and velocity vectors (white arrows) in mouthpiece.

closing stage, the direction of the flow motion is almost uniform in the middle of the mouthpiece chamber, and there is no obvious vortices. The influence of the ditch on the flow pattern in the major part of the mouthpiece chamber is negligible, but there is a weak vortex formed in the ditch area and the jet is slightly inclined to the upper surface due to the Coanda effect, which is observable at instances $0.74T$ and $0.84T$ in Fig. 5.19.

5.5.3.3 Zoomed-In Field Visualization in the Reed Channel

Figures 5.20, 5.21 and 5.22 provide a clear view of various phenomena observed in the reed channel during one duty cycle. The curl of the normalized velocity field is kept as the background from which the jet can be identified. On top of that, the white arrows present the direction and magnitude of the velocity vectors distributed at an interval of 5 cells in the x-direction. The green arrows plotted at an interval of every 3 cells along the reed surface present the normalized aerodynamic force exerting on the reed due to the pressure difference across both surfaces of the reed. Since the restitutive elastic force of the reed is not taken into account, the green arrows do not change directions during the duty cycle and are always positive. The mean value of the mouth pressure and the minimum and maximum values of the pressure in the mouthpiece during one duty cycle have been mapped to three horizontal thin black dashed lines, respectively, where their values for each geometry are provided in Table 5.6. Using the same mapping scale, the thick black dashed curve qualitatively illustrates the mean pressure profile in the reed channel and the nearby mouthpiece chamber delimited by the inner lay wall and the upper surface of the reed.

For the case of the short channel (Fig. 5.20), a jet is formed at the channel's entrance and is distinguished from the upper and bottom boundary layers during the opening stage (from $0T$ to $0.37T$). The different colors mapped on the boundary layers (blue and red) indicate the negative and positive velocity gradients of the fluid in the vicinity of the walls of the lay and the reed, respectively.

As the reed continues to move down ($dh/dt > 0$), there is a separation region consisting of cells with near zero velocities formed on the bottom of the reed channel right next to the entrance. This phenomenon has been discussed by van Zon et al. (1990) in the quasi-stationary model of flow where a separation is expected at the entrance of the reed channel if the edges of the mouthpiece and the reed are sharp. In the present simulation, however, the flow adheres to the upper lay wall where no separation occurs

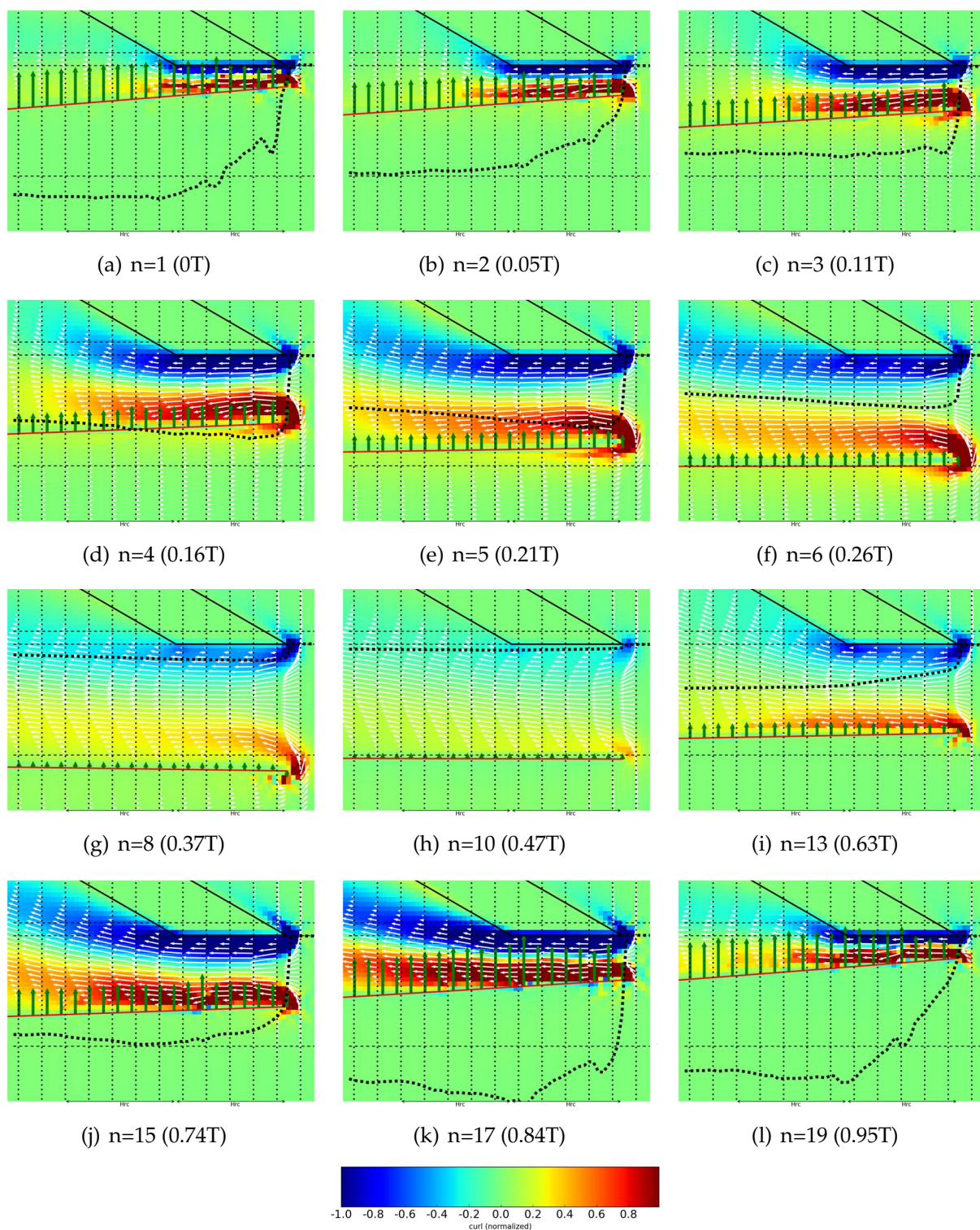


Figure 5.20 Short channel: the curl of velocity field (background), the velocity profile (white arrows), the pressure profile (thick dashed line) and the aerodynamic force profile on the reed (green arrows). Zoomed in in the vicinity of reed channel.

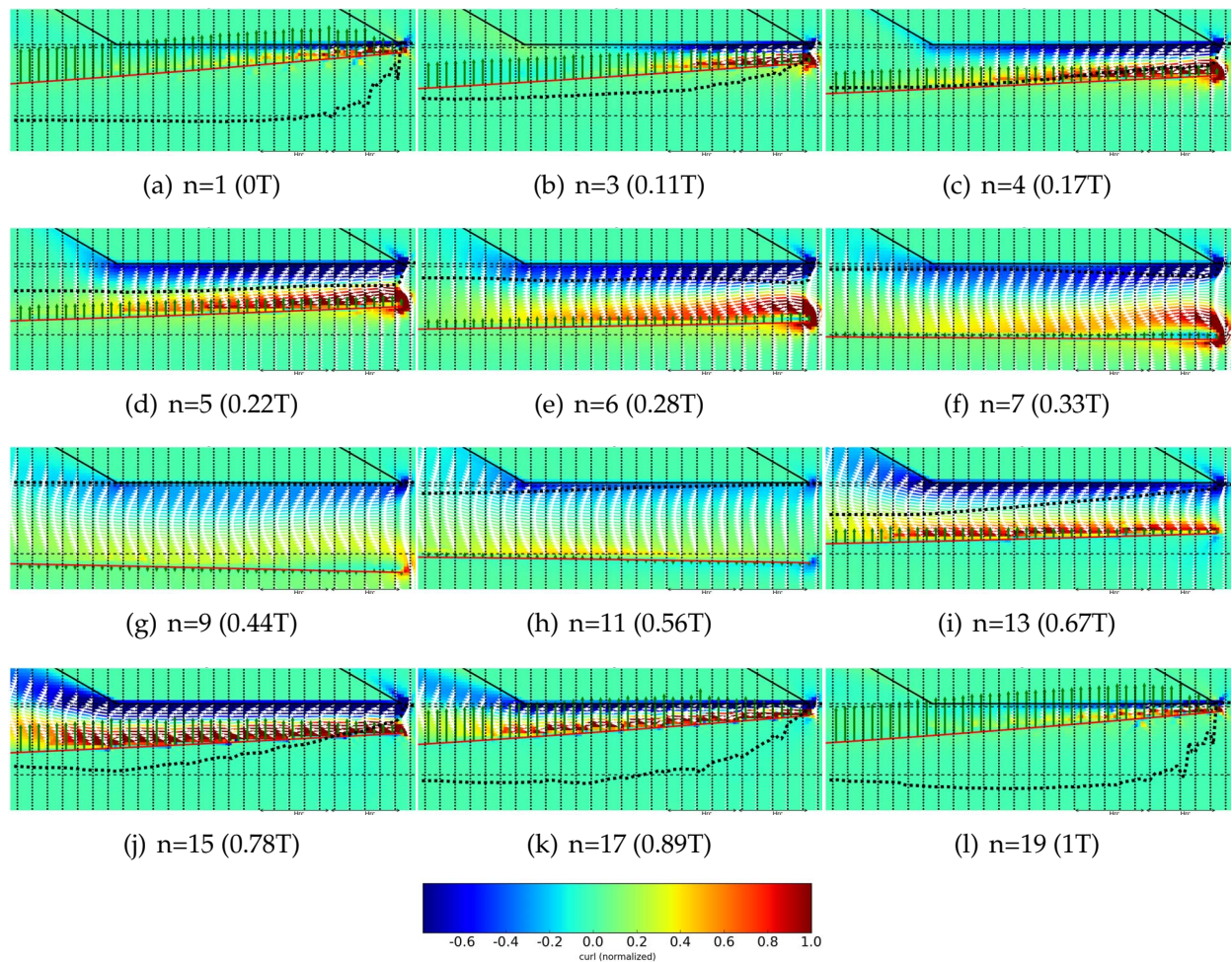


Figure 5.21 Long channel: the curl of velocity field (background), the velocity profile (white arrows), the pressure profile (thick dashed line) and the aerodynamic force profile on the reed (green arrows). Zoomed in in the vicinity of reed channel.

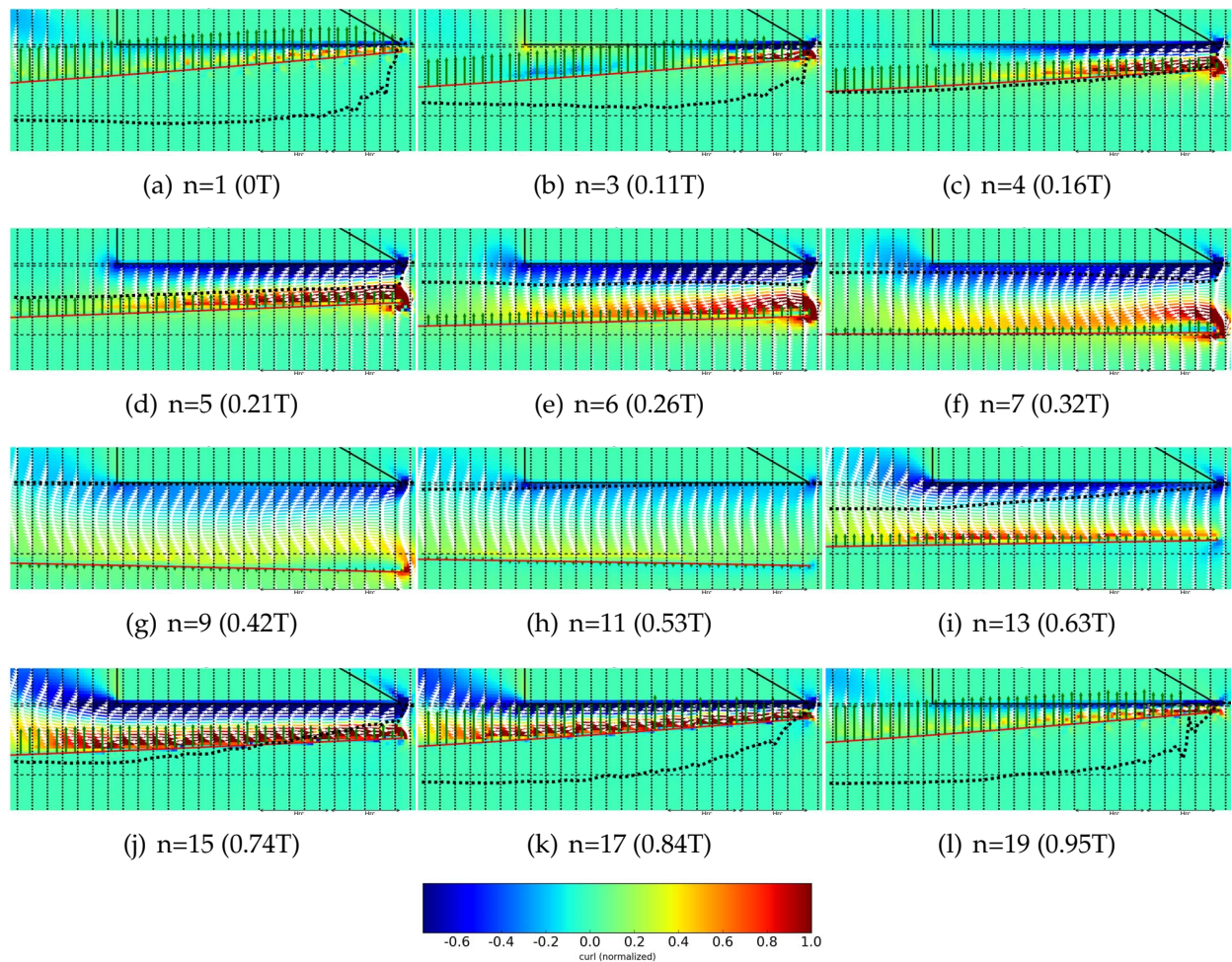


Figure 5.22 Long channel with a ditch: the curl of velocity field (background), the velocity profile (white arrows), the pressure profile (thick dashed line) and the aerodynamic force profile on the reed (green arrows). Zoomed in in the vicinity of reed channel.

on the rail tip, this is probably due to the thick edge of the mouthpiece tip. The same phenomenon of semi-detached flow is also reported by da Silva et al. (2007).

The quasi-stationary model assumes a uniform Bernoulli flow detached all the way through the short channel. The numerical results presented here are more complex. The flow can be described as uniform and fully detached from the reed only at the very beginning part of the reed channel. As the jet travels downstream, the separation region gradually shrinks due to the momentum transfer by viscosity from the jet to the separation region, known as the Coanda effect. Meanwhile, the uniform profile of the jet gradually grows into a parabolic shape and the jet eventually develops into a Poisseuille flow as it arrives at the end of the reed channel. As the jet is injected into the mouthpiece chamber, it is detached from both the reed and the inside wall of the lay due to the abrupt expansion of geometry.

During the closing stage (from $0.47T$ to $0.95T$), the separation region on the bottom of the reed channel disappears and the jet attaches to the reed's surface all the way throughout the reed channel. This phenomenon is also in contrast with the quasi-stationary model which assumes a constant fully separated flow. Actually, during the early part of the opening stage (from $0T$ to $0.11T$) and throughout the closing stage (from $0.63T$ to $0.95T$), the flow can be better described as a Poisseuille flow not only because of its parabolic velocity profile but also the gradient of the downstream pressure profile (the thick black dashed curve), which decreases downstream gradually though not linearly.

In general, the pressure gradient along the downstream direction inside the reed channel decreases as the reed channel aperture increases. For most instances during the duty cycle, the pressure profile in the reed channel is neither uniform nor smooth. At the channel entrance, there is a big drop between the pressure inside the reed channel and in the mouthpiece. After this initial drop, the pressure variation downstream in the reed channel is still not negligible, which decreases as the reed channel aperture increases. Consequently, the force distributed on the reed (depicted by the green arrows) is not uniform when the channel aperture is not very large.

For the long channel geometries (Figs. 5.21 and 5.22), a separation region also forms between the jet and the reed during the opening stage. Due to the Coanda effect, the flow reattaches to the reed at a distance of about $2H_{rc}$ from the channel entrance, where H_{rc} is the tip aperture at rest. This phenomenon is in accordance with the prediction of the quasi-stationary model. During the closing stage, the flow is developed into a

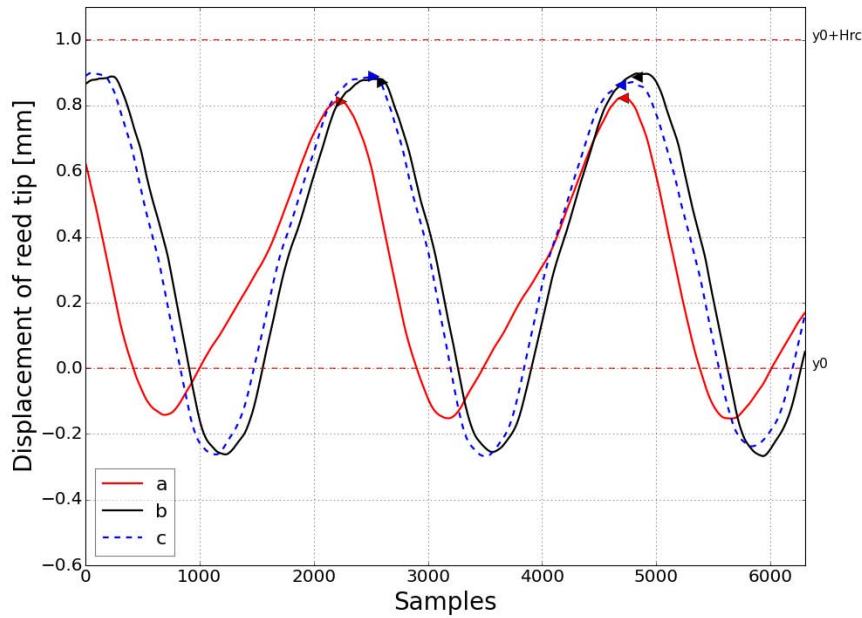


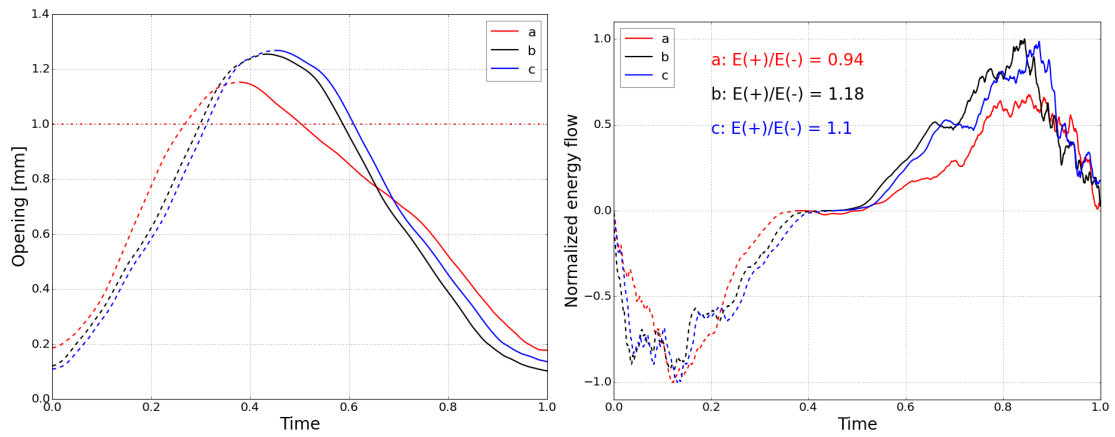
Figure 5.23 One duty cycle selected from time histories of reed tip for different geometries (a: short channel, b: long channel, c: long channel with a ditch).

Poiseuille flow featured by a parabolic velocity profile. The linear decreasing pressure profiles at the instances of $n = 13$ and 15 are typical for a Poiseuille flow.

Besides the longer distance between the reattachment point and the entrance found in the long channel, we also observe that the flow reattachment occurs at about $0.53 \sim 0.56T$ in the long channel, which is delayed compared to $\sim 0.47T$ for the case of the short channel. A similar phenomenon is also reported by da Silva et al. (2007) for the case of an anechoically terminated mouthpiece. This characteristic is explained by the combined effects of the inertia associated with different fluid volumes within the reed channel and the flow induced by the reed.

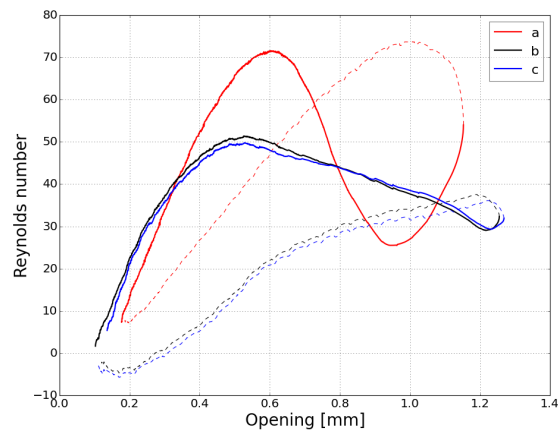
5.5.4 Characteristics of Dynamic Flows in One Duty Cycle

We now carry out further investigations regarding the dynamic characteristics in one single oscillation period. The one reed duty cycle has been selected based on the waveforms of the reed tip motion sampled at the period of $10 \times dt$. Figure 5.23 depicts the one duty cycle selected for all three cases of lay geometries, where the short channel, long



(a) Opening in one cycle.

(b) Energy flow in one cycle.



(c) Reynolds number as a function of opening.

Figure 5.24 Opening, Normalized energy flow and Reynolds number in one cycle for different geometries (a: short channel, b: long channel, c: long channel with a ditch).

channel and long channel with a ditch are represented by a (red solid line), b (black solid line) and c (blue dashed line), respectively. The two horizontal red dashed lines indicate the location of the rail tip ($y_0 + H_{rc}$) and the reed tip at rest (y_0), respectively. In the soft playing condition, the reed is not beating so the reed tip is always below the rail tip during the one duty cycle. Since there is no lip force engaged and the reed is relatively soft, the reed tip can move to a place lower than y_0 . The oscillation periods associated with the geometries of long channel are very close to each other by themselves and are about 5.3% shorter than that for the short channel.

Figures 5.24(a) and 5.24(b) depict the channel opening h and the normalized energy flow E as a function of normalized time during one single period of T . The opening stage and the closing stage are distinguished by the dashed line and the solid line, respectively. The energy flow is defined as $E = \frac{1}{M_r} \sum_{m=0}^{M_r-1} F(m) \cdot \dot{y}_r(m)$, where M_r is the total number of nodes of the distributed reed model, $F(m)$ stands for the aerodynamic force measured on the reed at m_{th} node and $\dot{y}_r(m)$ is the velocity measured on the reed at m_{th} node. A negative energy $E(-)$ indicates an opposite direction of the energy transfer, which means that the system is losing energy. A positive energy $E(+)$ indicates that the energy is transferred from the flow to the reed due to the work of the aerodynamic force. For all cases, the shift from negative to positive energy flow coincides with the maximum opening. The negative and positive energy regions are completely mapped to the opening stage and the closing stage, respectively, which is because the direction of aerodynamic force is almost always positive. Consequently the force is out of phase with the reed motion during the opening stage and in phase with the reed motion during the closing stage.

The net energy absorbed by the system can be evaluated by the ratio $E(+)/E(-)$, which has been calculated for each geometry and displayed in Fig. 5.24(b). The higher net energy absorbed in the cases of long channel explains their higher amplitude of reed oscillation in Fig. 5.24(a). Actually, the net energy ratio for the short channel case is less than one, which indicates a slightly damped oscillation which is not clearly observable in the waveform of $y_{r_{tip}}$ (Fig. 5.11) during the relatively short simulation time. For the cases of the two long channels, the slightly smaller value of the net energy ratio found for the geometry with a ditch is most likely caused by the extra energy dissipation in the ditch region.

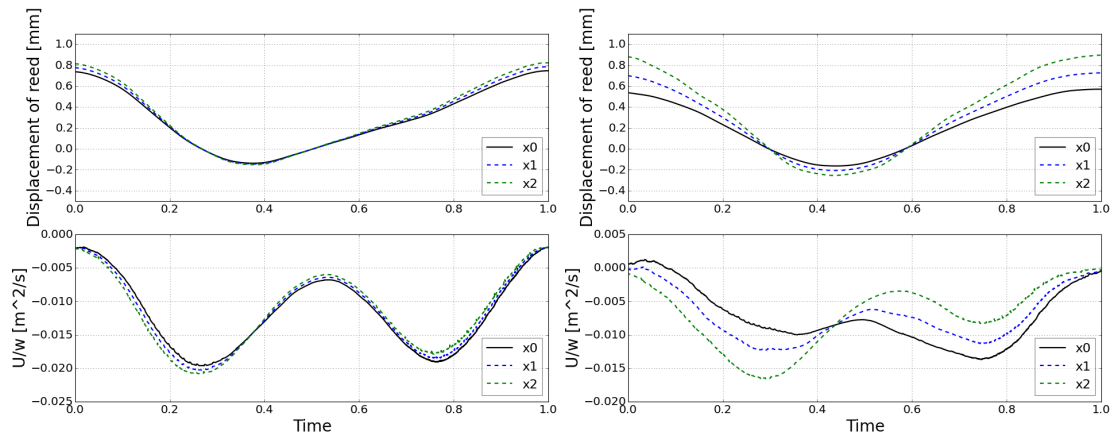
Figure 5.24(c) depicts the Reynolds number $Re = U/w\nu$ as a function of opening.

Strong hysteresis can be found in all cases, which is ascribed to the complex flow patterns which will be discussed later. Except for very small openings, the Reynolds number in general is larger than 10, which is sufficiently high for simulating the flow separation phenomenon (van Zon et al., 1990), as we have previously discovered in the field visualizations. However, due to the inherent limitation of maximum value of velocity, i.e. $M < 0.15$, that is allowed in the LBGK scheme simulating an incompressible fluid, the Reynolds number can not be much higher in the simulations. The very high Reynolds numbers (e.g., $Re > 1000$) reported in previous publications (da Silva et al., 2007, 2013) based on similar LBGK schemes are questionable and should be verified.

5.5.4.1 Dynamic Flow Behaviors in the Reed Channel

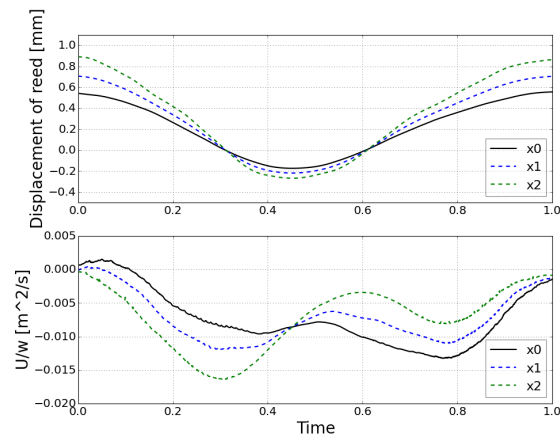
Here we carry out a further investigation on the dynamic flow behaviors in the reed channel. For all cases of lay geometry, the displacement of the reed and the volume flow per unit width (U/w) during one duty cycle probed at three different points (x_0 , x_1 and x_2 , see Fig. 5.10) are plotted in parallel in Fig. 5.25. The reed oscillations for all geometries are slightly asymmetric but close to sinusoidal, where the opening stage is about 40% and the closing stage is about 60%. The waveforms of volume flow during one duty cycle are rather complex and very different from sinusoidal. This phenomenon is due to the net effects of different components of the volume flow. In the dynamic regime and in the presence of acoustic coupling, the effective volume flow can be expressed as $U = U_{dp} + U_w + U_{ac}$, where U_{dp} is the flow driven by the pressure difference across the reed channel, U_w is the flow induced by the movement of reed and U_{ac} is the flow driven by the acoustic field accumulated inside the mouthpiece-bore system. The volume flow crossing the reed channel is not uniform but rather a function of x , this is particularly true for the geometries of the long channel. The contribution of acoustic flow is relatively stronger in the vicinity of the end of reed channel (x_0), while the influence of U_w is stronger in the upstream part (x_1 and x_2) of the reed channel. Moreover, the effect of U_w is stronger for the case of the long channel, especially at the instances near the closure of the channel when U_{dp} is very small. The volume flow U_{dp} also varies in the reed channel because it is influenced by the boundary layer on the walls and the separation region when it exists, where they are neither uniform in the reed channel nor consistent during the duty cycle.

Figures 5.26(a) and 5.26(b) depict the pressure difference across the reed channel dur-



(a) Short channel.

(b) Long channel.



(c) Long channel with a ditch.

Figure 5.25 Displacement of reed tip (top) and volume flow per unit width (bottom) probed at three locations (x_0 , x_1 , x_2) during one cycle for different geometries.

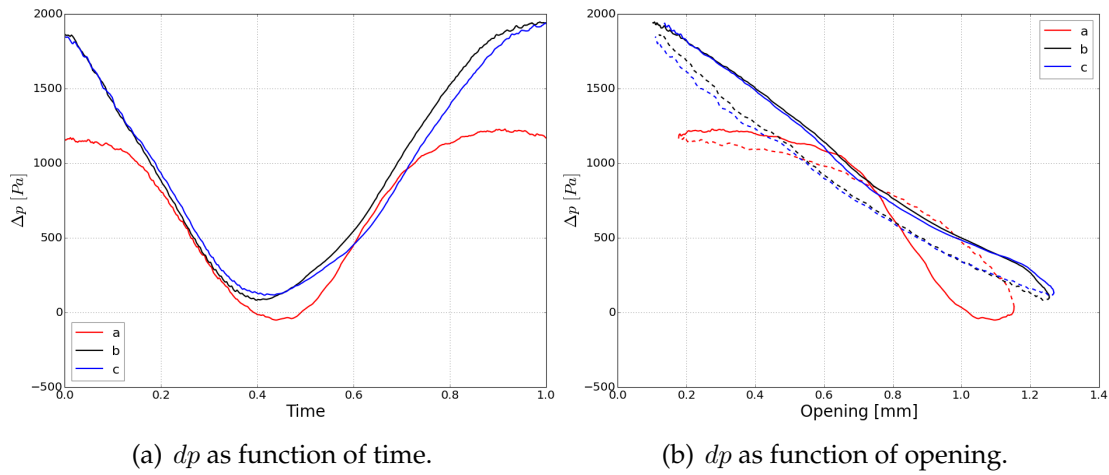


Figure 5.26 Pressure difference for different geometries.

ing one duty cycle as a function of time and opening, respectively. For geometries of the long channel, the pressure difference is always positive and is almost linearly related to the opening, although hysteresis exists due to the different flow behaviors at the opening stage and the closing stage. For the case of the short channel, the pressure difference is more complex.

Step	I	II	III	IV	V
Start	$0T$	$0.33T$	$0.44T$	$0.56T$	$0.75T$
End	$0.33T$	$0.44T$	$0.56T$	$0.75T$	$1T$

Table 5.7 Five steps during one duty cycle for the cases of long channel.

5.5.4.1.1 Long Channel Based on the measured results, we try to explain the characteristics of the volume flows measured at x_0 , x_1 and x_2 for the case of the long channel, namely U_0 , U_1 and U_2 . Because the ditch has little influence on the volume flow, we will only discuss the long channel without a ditch. For convenience, we roughly divide the one single duty cycle into five sequential steps. The start and end time of every step is shown in Table 5.7.

The range of Step I is from the beginning of the duty cycle ($0T$) to the instant when the reed tip reaches the equilibrium point ($\approx 0.33T$). During this period, the opening h increases and the pressure difference monotonically decreases. In general, the volume

flows measured at all three points accelerate over time t , i.e. $-dU/dt > 0$, where the minus sign indicates the direction of the flow is from right to left. We can also observe that the flows decelerate in the downstream direction, i.e. $-dU/(-dx) < 0$, due to not only the damping but also the net effects of $-U_w$ and $-U_{ac}$, where the minus sign indicates a negative contribution to the net flow.

The $-U_w$ has more influence on U_1 and U_2 . As the reed moves down, the influence of $-U_w$ compared to U_{dp} decreases over time, this enlarges the gap between U_0 and U_1 and U_2 over time, as we can find in Figs. 5.25(b) and 5.25(c).

The inverse acoustic flow $-U_{ac}$ coming from the mouthpiece has more influence near the end of the reed channel. The visualization of the velocity field in the mouthpiece chamber (Fig. 5.18) shows that the acoustic flow increases and reaches a local maximum at $\simeq 0.17T$ and then decreases and vanishes after $\simeq 0.33T$. The bump of the curve of U_0 at $\simeq 0.17T$ (Fig. 5.25(b)) is ascribed to the strong negative contribution of the acoustic flow at that instant. The influence of acoustic flow is also related to the relatively smaller magnitude of U_0 compared to U_1 and U_2 after $0.17T$, this phenomenon of flow slowing down can be directly observed from the velocity profile from $0T$ to $0.33T$, as depicted in Fig. 5.21. The flow slowing down is also related to the friction of walls in the long channel.

It is interesting that U_2 is always greater than U_1 during Step I in Fig. 5.25(b), despite the fact that the jet height at x_2 is smaller than that at x_1 due to the presence of the separation region in the upstream part of the reed channel. If we look at the gradient of the pressure profile at Step I in Fig. 5.21 (from $0T$ to $0.33T$), we will find significant pressure drops at the entrance (x_2), but only a very small amount of drops in the middle (x_1), this is particularly true for the instances after $0.22T$. So the main part of the flow at x_1 is not driven by the local pressure difference, but rather it is formed by the fluid particles from upstream due to inertia. Also, U_1 might be further weakened by the negative acoustic flow downstream. The influence of acoustic pressure can be observed at the instant $0.33T$ in Fig. 5.21, where despite the global positive pressure difference between the mouth pressure and the pressure in the mouthpiece chamber, the local pressure gradient inside the reed channel is actually in the opposite direction, i.e., $p(x_0) > p(x_1) > p(x_2)$.

Step II is defined in the range between $0.33T$ and $0.44T$, corresponding to the region where the reed tip moves from y_0 to the lowest point (or the instant of the biggest aperture). The flow pattern in Step II differs from that in Step I by the flow decelera-

tion over time ($-dU/dt < 0$), while the phenomenon of flow deceleration over space ($-dU/(-dx) < 0$) is similar. In this stage, the pressure difference decreases until slightly above zero. The contribution of $-U_w$ and $-U_{ac}$ is almost negligible. These combined factors explain the phenomenon that U_1 and U_2 quickly decrease and U_0 decreases relatively slowly.

The end of Step III is defined at $0.56T$, corresponding to the instant that the reed tip moves back to y_0 . The phenomenon of flow deceleration over time continues, but the flow across the reed channel switches to the acceleration mode ($-dU/(-dx) > 0$). During this step, although the pressure difference slightly increases, the local pressure differences at x_1 and x_2 are still very small and the contribution of U_w is very small, so U_1 and U_2 continue to decrease due to thermoviscous losses. The amount of U_0 is still relatively big because of inertia.

Step IV is defined in the range between $0.56T$ and $0.78T$ covering a large portion of the closing stage, where the aperture decreases and the pressure difference increases. The separation region between the jet and the reed vanishes at about $0.56T$. This stage is indicated by the flow acceleration over time ($-dU/dt > 0$) and the flow acceleration over space ($-dU/(-dx) > 0$). The increasing of U_0 , U_1 and U_2 is mainly driven by the pressure gradient across the reed channel, as shown in Fig. 5.21 at instances of $0.67T$ and $0.78T$. The pressure gradient is almost uniform in the reed channel ($dp/(-dx) \approx \text{constant}$), which helps to explain the same increasing rates for flows measured at all three places ($-dU_0/dt \approx -dU_1/dt \approx -dU_2/dt$).

Step V ranges from $0.78T$ to $1T$. During this stage, the opening is very small and U_w plays a more important role due to the smaller flow driven by the pressure difference. All flows measured at three places decrease because the amount of U_{dp} is restricted by the small opening, despite the fact that the pressure difference increases. At $\simeq 0.89T$, when the opening becomes very small, the flows decrease at a lower rate because of the positive contribution of U_w .

Step	I	II	III	IV	V
Start	$0T$	$0.25T$	$0.38T$	$0.52T$	$0.75T$
End	$0.25T$	$0.38T$	$0.52T$	$0.75T$	$1T$

Table 5.8 Five steps during one duty cycle for the case of short channel.

5.5.4.1.2 Short Channel A similar analysis is performed for the dynamic flow behavior in the short reed channel. The one single duty cycle for the short channel is divided into five steps in time, as shown in Table 5.8.

The range of Step I is from $0T$, the beginning of the opening stage, to $\simeq 0.25T$, when the reed tip arrives at the equilibrium point. Like the case of the long channel, the volume flows measured at all places accelerate over time, and the flow slows down along the downstream direction. Compared to the case of the long reed channel, there are two differences observed here. First, there is no inverse flow found during the early opening stage. The acoustic oscillation in the case of the short channel is weak due to a low mouth pressure. During Step I, the velocity field in the mouthpiece chamber shown in Fig. 5.17 is unstable and the flow driven by the acoustic oscillation is not stably formed in one direction. Consequently, the flow measured at the end of the reed channel is dominated by U_{dp} and is not much disturbed by U_{ac} . That said, the influence of the acoustic oscillation can still be observed through the positive gradient of pressure profile downstream ($dp/(-dx) > 0$) found in the short reed channel, as shown at the instances of $0.16T$, $0.21T$ and $0.26T$ in Fig. 5.20. Second, the difference between U_0 , U_1 and U_2 are much smaller than that found in the case of the long channel. This phenomenon is mainly explained by the reduced damping in a shorter distance and the simple uniform flow pattern formed in a short channel (Fig. 5.20) which, unlike what happens in the long channels (Figs. 5.21 and 5.22), is not altered by a flow reattachment in the middle of the channel.

Step II is defined in the range between $0.25T$ and $0.38T$, the latter corresponding to the instant of the biggest aperture and the smallest pressure difference. The phenomenon of flow deceleration in the downstream direction ($-dU/(-dx) < 0$) is similar to that in the case of the long channel, but to a less extent. During this stage, the pressure difference continuously decreases to about zero.

Step III is defined in the range between $\simeq 0.38T$ to $\simeq 0.52T$, corresponding to the period when the reed tip moves from the point of maximum opening back to the equilibrium point y_0 . In most time during this short period, the averaged pressure in the middle of mouthpiece chamber is slightly higher than the averaged mouth pressure. This negative pressure difference results in a slight deceleration of the volume flow in the upstream direction, but is not enough to switch the jet to an opposite direction due to the inertia of the fluid volume.

Step IV is defined in the range between $\simeq 0.52T$ to $\simeq 0.75T$ covering the main part of the closing stage. It is indicated by a decreasing opening and an increasing pressure difference. During this step, the jet is attached to the reed. A Poiseuille flow is fully developed all through the reed channel which can be confirmed by the velocity profiles and the linearly dropping pressure profiles, as shown in Fig. 5.20 at the instances of $0.63T$ and $0.74T$. This stage is indicated by the flow acceleration over time ($-dU/dt > 0$) and the flow acceleration in the downstream direction ($-dU/(-dx) > 0$). The very small differences between U_0 , U_1 and U_2 are attributed to the short channel length and the uniform boundary layers formed on both the upper lay wall and the reed wall.

Step V ranges from $\simeq 0.75T$ to $1T$. During this period, due to the lower mouth pressure, the pressure difference is significantly lower than that in the case of the long channel. Also, because the reed receives less energy from the fluid than that in the case of the long channel (see Fig. 5.24(b)), the aperture of the short channel in Step V is bigger than that of the long channel (see Fig. 5.24(a)). Thus, despite the lower dp , the volume flows measured in the short channel are actually higher than that measured in the long channel, because a bigger aperture allows more flow entering into the reed channel and a shorter channel has less damping.

5.5.4.1.3 Differences Between Short Channel and Long Channel Overall, the volume flow U in the short channel accelerates earlier into the mouthpiece chamber during the opening stage. This phenomenon is similar to that reported by da Silva et al. (2007) for the case of an anechoically terminated mouthpiece in the absence of acoustic coupling, where the earlier acceleration of volume flow helps the jet adhere on the reed surface earlier. This is also true for the present simulations with the acoustic coupling. The adhesion phenomenon in the short channel starts after $\simeq 0.47T$ (Fig. 5.20), and the same phenomenon occurs in the long channel after $\simeq 0.56T$ (Fig. 5.21). In all cases of the present simulations, the jet never detaches from the upper rail wall. This phenomenon was mentioned but not clearly observable in the visualizations in (da Silva et al., 2007) due to the low resolution.

The higher oscillation amplitudes in the geometries of the long channel is mainly due to the higher net energy measured by the ratio $E(+)/E(-)$, which is related not only to the lay geometry, but also to the higher mouth pressure. The aerodynamic forces shown in Figs. 5.20, 5.21 and 5.22 (green arrows) seem not significantly influenced by

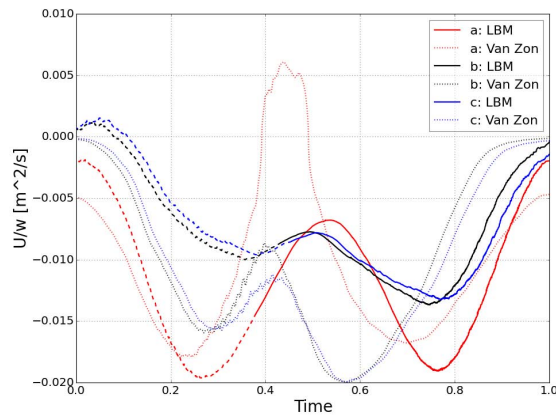
the attachment length, but only related to the mean pressure profile. This seems somewhat different from the results obtained by da Silva et al. (2007). In the latter case, the conditions were fairly different in that there was no acoustic feedback and the attachment/reattachment played a significant role. In the present study, however, there is an acoustic field inside the mouthpiece-bore system, and the force on the reed is mainly dominated by this effect.

5.5.5 Discussions

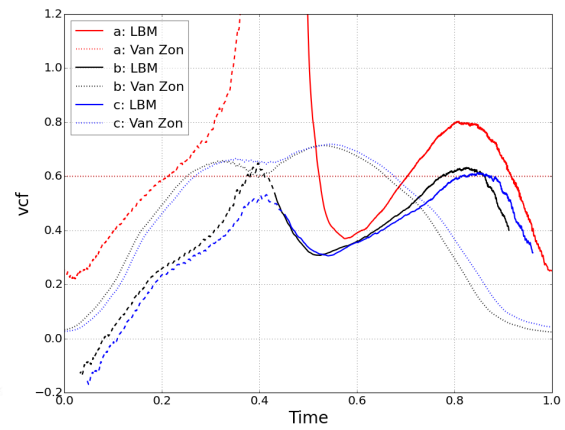
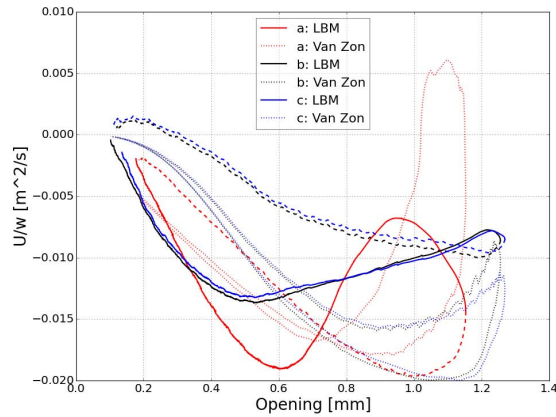
The numerical results show some fundamental discrepancies compared to the quasi-stationary predictions. As we have discovered in the field visualizations of the reed channel (Figs. 5.20, 5.21 and 5.22), the phenomenon of flow separation / reattachment in the dynamic regime are significantly different from the quasi-stationary predictions. In the short channel, the flow detached from the reed only in the opening stage but attached to the rail tip during the full duty cycle, which is in contrast with the fully separated flow assumed by the quasi-stationary theory. In the case of the long channel, the discrepancies are also obvious, where the separation and reattachment phenomenon only occurs during the opening stage, which is in contrast to the fixed reattachment point assumed by the quasi-stationary model. In general, the results obtained in the present dynamic simulations agree qualitatively to the dynamic results reported by da Silva et al. (2007).

Figure 5.27 compares the numerical volume flows U/w in the dynamic regime to the predictions of the quasi-stationary model by van Zon in one duty cycle for all three geometries. On the left side, the volume flows are presented as functions of time (top), opening (middle) and pressure difference (bottom), respectively. The vena contracta factors vcf are presented in parallel on the right side. For the numerical results, the opening stage and the closing stage are represented by the dashed line and the solid line, respectively. The dot line represents the theoretical predictions. The three geometries are distinguished by colors, i.e., a) short channel in red, b) long channel in black, c) long channel with a ditch in blue.

In Figs. 5.27(a) and 5.27(d), the curves of the numerical results of U/w and vcf as a function of time exhibit trends similar to the counterparts of the quasi-stationary model, though discrepancies in terms of phase delay and magnitude are clearly observable. The phase delay should be expected considering the existence of inertia of the fluid volume and the time associated with the acoustic wave propagation. Also, in Figs. 5.27(b) and



(a) Volume flow in one cycle.

(d) vcf in one cycle.

(b) Volume flow in function of opening.

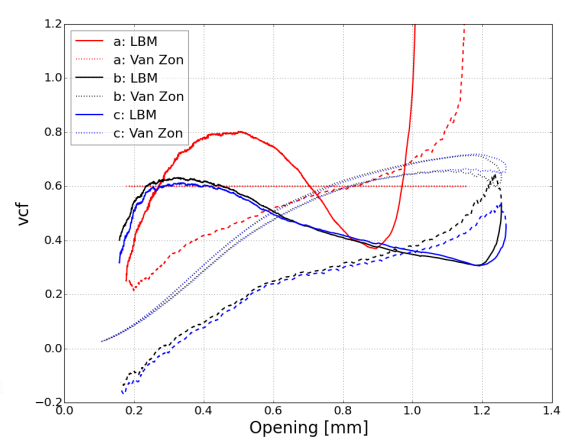
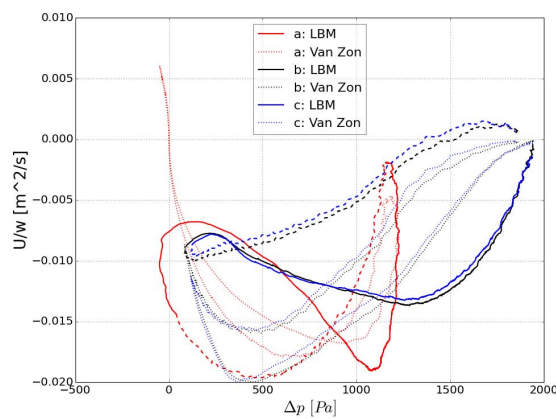
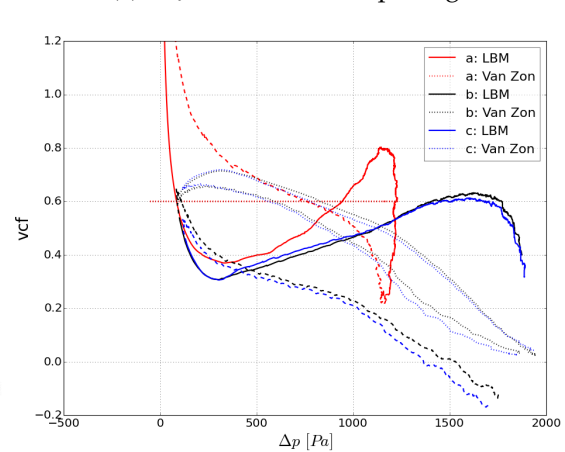
(e) vcf in function of opening.(c) Volume flow in function of dp .(f) vcf in function of dp .

Figure 5.27 Compare the numerical results with the theoretical predictions in terms of volume flow and vena contracta factor in one duty cycle for different geometries.

5.27(c), strong hysteresis is found in the numerical results in all geometries which is in stark contrast with the quasi-stationary predictions. Similar phenomena are observable in the results of vena contracta factors in Figs. 5.27(e) and 5.27(f).

Now we can take a close look in the case of the short channel. During the time span from $\simeq 0.38T$ to $\simeq 0.52T$, there is an inverse flow ($U/w > 0$) found in the quasi-stationary results, which is caused by the negative pressure difference at the instant of the biggest opening. This phenomenon is not found in the numerical results, though the trend of flow deceleration is similar. As previously discussed, this discrepancy is ascribed to the inertia of the fluid volume, which is not considered in the quasi-stationary model. As expected, the constant vcf predicted by the quasi-stationary model is not found in the numerical results. During the time span from $\simeq 0.1T$ to $\simeq 0.3T$ and from $\simeq 0.5T$ to $\simeq 0.95T$, or during $\simeq 0.65\%$ of the duty cycle, the numerical vcf fluctuates between 0.4 and 0.8, corresponding to a deviation of $\simeq 33\%$ from the theoretical prediction, which is larger compared to the deviation reported by da Silva et al. (2007) for the short channel.

Besides the large discrepancy found in the region of big opening and small pressure difference, another big discrepancy is found in the region of very small opening, which can be clearly observed in Figs. 5.27(e) and 5.27(f). In the early opening stage of the short channel, the opening is very small, i.e. $0.2 < h < 0.4$ or $2.5 < L/h < 5$, thus the geometry is similar to a long channel. The flow is not fully separated and is more like a Poiseuille flow, so the quasi-stationary model for the geometry of the short channel is not valid. This is also true for the late closing stage, where the Poiseuille-like flow in the reed channel attaches to both the rail tip and the reed. Due to the influence of the flow induced by the reed (U_w), the volume flow in the closing stage is slightly larger than that in the opening stage at the same opening, which explains the smaller deviation in the late closing stage and the hysteresis.

For the geometries of the long channel, the numerical results also exhibit prominent discrepancies compared to the quasi-stationary predictions. During the opening stage, the numerical volume flow is constantly lower than that predicted by the quasi-stationary model. This is probably due to the losses caused by the relatively high numerical viscosity and the friction between the fluid and the walls. Additionally, this is also due to inertial effects because the volume of fluid inside the long channel is bigger, which takes more force to accelerate. The discrepancy is slightly bigger during the period from $\simeq 0.25T$ to $\simeq 0.33T$, corresponding to a big opening between 0.8 and 1.1 mm.

This can be explained by the fact that the pressure profile in the reed channel during this period is almost flat (see, e.g., Figs. 5.21 at $0.28T$ and $0.33T$), consequently, the volume flow at the end of reed channel driven by the pressure difference is even weaker.

During the early closing stage between $\simeq 0.44T$ and $\simeq 0.7T$, the trend of a lower numerical volume flow continues until $\simeq 0.7T$, after then the numerical volume flow is higher than the theoretical prediction. Actually, the quasi-stationary model for the long channel does not hold in the late closing stage because the separation region vanishes and the reed channel is dominated by fully developed Poiseuille flow, which is in contrast to the phenomenon of separation / reattachment assumed by the theory.

5.6 Conclusion

In this chapter, we investigated the aeroacoustic aspects of a clarinet using a 2D hybrid numerical model. The fluid and the static walls were simulated using a GPU-accelerated parallel LB MRT model, which had been verified in Chpt. 4. The reed was simulated using the distributed model proposed by Avanzini and van Walstijn (2004). The interface integrating the reed model and the LB model was based on the technique developed by da Silva et al. (2007), which was re-implemented and parallelized on the GPU-PyCuda platform.

There were several improvements of the present numerical scheme compared to the one developed by da Silva et al. (2007). The numerical stability of the LB model was improved by the MRT scheme and the extrapolation scheme (Guo et al., 2002). The simulation speed was greatly improved by the parallelization of the LB model and the reed model implemented on the GPU platform, which was essential for the computationally intensive simulations involving acoustic oscillations which has a prolonged oscillating period and requires a longer transient period before the stable oscillation is obtained. The positive pressure source blowing into the mouth was a more realistic scheme than the negative pressure source at the outlet of the mouthpiece.

In the simulations of the quasi-stationary regime, the outlet of the mouthpiece was blocked by an absorbing boundary to thwart possible acoustic oscillations. We then investigated cases of both a fixed reed and a slowly moving reed and measured the complete non-linear characteristic curves including both the increasing and decreasing stages of mouth pressure. The influence of the geometry of reed channel was inves-

tigated, including the case of the short channel and the long channel. The numerical results were compared to the results predicted by the quasi-stationary model based on a simplified memoryless reed and the Bernoulli flow. In the case of the fixed reed, the vena contracta factor measured in the short channel was in good agreement with the theoretical counterpart, but the numerical volume flow measured in the long channel was underestimated, which was probably due to the higher damping in the long channel. In the case of the slowly moving reed, the numerical flow showed more hysteresis compared to the quasi-stationary model. We also found that the low spatial resolution reduced the accuracy of the measurement of the numerical volume flow and caused the staircase-like ripples in the results.

In the simulations of the dynamic regime, the outlet of the mouthpiece was attached to an axisymmetric cylindrical pipe with its other end open in a radiation domain. By fine tuning geometrical and numerical parameters of the hybrid model and using a soft reed, we were able to initiate the acoustic oscillation of the clarinet in a relatively short time span. Then we investigated the dynamic flow in the mouthpiece-reed system with three different lay geometries in the soft playing condition. Thanks to the high spatial resolution used in the dynamic simulations, the flow behaviors in the reed channel were visualized with high clarity.

The influence of the aerodynamic and acoustic oscillations on the velocity fields and pressure profiles were observed in both the mouthpiece chamber and the reed channel, which explained some fundamental discrepancies between the numerical results and the quasi-stationary predictions. For all geometries, the phenomena of flow separation / reattachment in the dynamic regime were similar to the results reported by da Silva et al. (2007) for the case of an anechoically terminated mouthpiece of clarinet in the dynamic regime without acoustic coupling, but were significantly different from the prediction of the quasi-stationary theory. Based on the high fidelity visualizations, we qualitatively discussed the evolution of volume flow measured at different places along the reed channel during the duty cycle, which would be very difficult, if not impossible, to investigate using traditional experimental approaches.

We then compared the volume flow measured at the end of reed channel in one duty cycle with the quasi-stationary predictions. The numerical volume flow and vcf as a function of time exhibited trends similar to the quasi-stationary predictions, but showed significant discrepancies in terms of phase delay, magnitude and hysteresis,

which were caused by inertia of the fluid volume and the complex influences due to the aerodynamic and acoustic oscillations. A noticeable inverse flow was found at the beginning of the opening stage for the long channel case in the present study and was explained by the influence of acoustic coupling. This phenomenon was not found in either quasi-stationary predictions or the numerical results obtained by da Silva et al. (2007).

The differences between the results of short / long channel were clearly observable in almost every aspect. To obtain the acoustic oscillation without the beating of reed, the mouth pressure prescribed to the short channel case was lower by 30% than that for the long channel cases. The spectrum of the results obtained from the short channel case was different from that of the long channel case by the smaller amplitude of the higher harmonics, which suggested a mellow tone. But it was not clear if this difference of timbre was just caused by the different mouth pressures or also due to the direct influence of lay geometries. The influence of the ditch was noticeable but not particularly strong in most results, though the ratio of absorbed energy in one cycle for the case of long channel with a ditch was slightly lower than the one without a ditch, which might suggest a little difference in terms of playability. In general, how the playability and timbre of a real clarinet is influenced by minor difference of lay geometries is an interesting topic.

Chapter 6

Conclusions and Future Research

6.1 Conclusions

In this thesis research, a customized numerical simulation system implementing the lattice Boltzmann method was developed to investigate acoustic problems involving complex static boundaries or dynamic boundaries and carrying a quiescent or non-zero subsonic mean flow. This system was first implemented on the Python-CPU platform and then parallelized and re-implemented on the PyCUDA-GPU platform using the GPU-accelerated computing technique. The GPU model achieved a speedup ratio of about 20 compared to the CPU model. The numerical stability under the conditions of complicated geometry, low fluid viscosity and non-zero mean flow was well maintained by using the multiple relaxation time scheme (d’Humières, 1994) and the extrapolated curved boundary condition (Guo et al., 2002). Subsequently, numerical investigations of a set of acoustic problems were carried out based on this simulation system.

Acoustic Systems with Static Boundaries

The investigation of acoustic systems with static boundaries was presented in Chpt. 4, which involved the acoustic transmission and radiation characteristics of axisymmetric waveguides terminated by different geometries, as well as the aeroacoustic behavior of whistles with complicated geometries. The accuracy and stability of the LBM simulation system was substantiated by a set of benchmark acoustic problems.

The first set of simulations was carried out to determine the acoustic transmission

properties at the open end of axisymmetric cylindrical waveguides in terms of reflection coefficient and length correction. The effects of geometrical parameters (the geometric profile of the termination) and flow parameters (the Mach number) were investigated. For the case of a cylindrical pipe immersed in a quiescent fluid domain, the numerical results were in good agreement with the theoretical predictions provided by Levine and Schwinger (1948). For the case of a cylindrical pipe carrying a subsonic non-zero mean flow in the range of $M \leq 0.15$, in general the numerical results were also in good agreement with the theoretical predictions provided by Munt (1990) and the experimental results provided by Allam and Åbom (2006), though a slight discrepancy was found for $ka < 0.2$ most likely due to the degraded accuracy of the two-microphone method in the low frequency limit. The effects of the horn extension with different profiles for both the quiescent flow case and the non-zero mean flow case were on par with the results provided by da Silva (2008).

The second set of simulations was carried out to determine the sound radiation directivity pattern at the open end of axisymmetric cylindrical waveguides. Also, the effects of horn extensions and non-zero mean flows were investigated. For the case of a cylindrical pipe carrying a quiescent flow, the numerical results were in excellent agreement with the theoretical predictions provided by Levine and Schwinger (1948) and the experimental results provided by Gorazd et al. (2012). For the case of a cylindrical pipe carrying a subsonic non-zero mean flow in the range of $0.036 \leq M \leq 0.15$, in general the numerical results were in good agreement with the available theoretical predictions and experimental results (Gabard and Astley, 2006; Gorazd et al., 2012), though discrepancies were found for the case of small angles ($\theta < 30^\circ$) and the highest flow speed ($M = 0.15$). The numerical results show that the directivity effect was reinforced by the horn extensions, where a big curvature radius of the horn resulted in a stronger directivity effect. A comparison between the signal measured in the far-field of the CPU model and of the GPU model showed that the sound radiation problem can be well represented by single precision (32-bit) floating-point numbers.

The third set of simulations was carried out to investigate the aeroacoustic behavior of whistles featuring complicated curved boundaries and relative high speed fluid flows, where the stability of the GPU model was well maintained during a long simulation time. However, the results show that the absorbing boundary conditions could not absorb the fluid vortices very well.

Acoustic Systems with Moving Boundaries

The investigation of acoustic systems with moving boundaries involved a clarinet-like system comprised of a mouthpiece of different geometries together with a dynamic moving reed. The reed's motion was described by the distributed model proposed by Avanzini and van Walstijn (2004) and the interaction of the moving boundary was solved by the extrapolated curved boundary condition proposed by Guo et al. (2002). Both the LBM scheme and the reed model have been parallelized on the PyCUDA-GPU platform.

The first set of simulations of the quasi-stationary regime were based on a relatively low spatial resolution ($dx = 8.5 \times 10^{-5} m$), where the outlet of the mouthpiece was blocked by an absorbing boundary and two different lay geometries were involved, namely the short channel and the long channel. The complete non-linear characteristic curves of the mouthpiece-reed system were measured and compared to the theoretic predictions provided by van Zon et al. (1990).

For the fixed reed, the numerical volume flow was in good agreement with the theoretical predictions in the short channel case but was significantly lower in the long channel case, likely due to the relatively higher damping effect. For both geometries, the vcf did not vary greatly over 80% of the duration, which suggests that a constant vcf used in the quasi-stationary model is a reasonable approximation for full reed channel openings.

For the slowly moving reed and both lay geometries, hysteresis was found in the numerical results, which was mainly due to the inertia of fluid volume. Also, the numerical vcf results were greater than unity in the region of high dp , which was in contrast with the quasi-stationary model and was explained by the non-uniform height across the reed channel and flow behaviors that deviated from the theoretical assumptions. The numerical results were limited by a low spatial resolution, which sometimes induced a staircase-like ripple in the measured volume flow.

The second set of simulations of the dynamic regime used a higher spatial resolution ($dx = 4.25 \times 10^{-5} m$). An axisymmetric cylindrical pipe with a length four times its diameter functioning as an acoustic resonator was attached to the outlet of the mouthpiece at one end and open in a radiation domain at the other end. The dynamic viscous flow in the mouthpiece-reed system with three different lay geometries in the soft playing condition was investigated.

Overall, there were fundamental discrepancies between the numerical results and the quasi-stationary predictions using the same geometrical parameters, which were mainly attributed to the unsteady flow associated with the aerodynamic and acoustic oscillations. The phenomena of flow separation /reattachment in the reed channel were similar to the results obtained by da Silva et al. (2007) in the absence of an acoustic oscillation, but were significantly different from the predictions of the quasi-stationary theory, which assumes a fully detached flow for the short channel geometry and a fixed reattachment point for the long channel geometry.

The effect of acoustic coupling was relatively strong at the outlet of the reed channel where a noticeable inverse flow was found at the beginning of a duty cycle for the long channel case. In general, for all geometries the pressure and velocity fields in the mouthpiece chamber and the reed channel were modulated by the acoustic perturbation, which were observable in the high resolution visualizations presented in this study. Consequently, the *vcf* in one single duty cycle deviated significantly from the prediction of quasi-stationary model, especially in the region of either a big opening or a very small opening of reed channel.

The effect of a varying channel length was clearly observable in many aspects. During one duty cycle, the volume flow in the short channel accelerated earlier due to the smaller fluid volume, which in turn helped the jet adhere to the reed surface earlier and helped to initiate the acoustic oscillation at a lower mouth pressure condition. The influence of the ditch was observable but not very strong, where the ratio of absorbed energy in one cycle was slightly reduced because of the extra energy dissipation due to the vortices formed in the vicinity of the ditch area.

6.2 Future Research

The investigation of the dynamic clarinet can be improved in several ways in the future. To compare the influence of the geometry in the soft playing condition, the same mouth pressure should be used for both the short channel case and the long channel case, which requires some further adjustments of simulation parameters. Using the same model, the investigation can be carried out in the hard playing conditions which may bring some new insights on nonlinear phenomena. Also, the investigation can be easily extended to various situations including different geometries (pipe length, minor geometry change

of the pipe end and the mouthpiece lay, etc.).

Another interesting new topic would be to find a more accurate modeling of the transient behavior of a clarinet, i.e., the quick variations at the onset of the oscillation. This problem can be investigated to some extent by observing the threshold of pressure oscillation, which is influenced by the mouth pressure, as well as the frequency of oscillation at the threshold. Previous studies on this topic assume an unrealistic constant flow and mouth pressure (Backus, 1963; Dalmont and Frappe, 2007). More recently, influences of time-varying pressures (Bergeot et al., 2014), reed motion induced flow (Silva et al., 2008), lip force and the player's vocal tract have been discussed. The simulation system developed for this research can be extended to include these aspects without major changes.

From the engineering aspect, the simulation can be improved by using a higher spatial resolution, which is generally limited by available computational and memory resources. To solve this problem, one option would be using a GPU cluster combined with the multiple block technique (Fan et al., 2004). Another option is to use the adaptive grid refinement technique (Rohde et al., 2006). Also, the performance of the present GPU model can be further improved by using various optimization techniques, such as those presented in (Ryoo et al., 2008; Tölke, 2010; Kuznik et al., 2010; Obrecht et al., 2011; Rinaldi et al., 2012; Habich et al., 2013).

One of the major limitations of the present LBM simulation system is its 2D representation, which cannot accurately describe the 3D real fluid behavior involving vortex motions and energy dissipation, as well as the energy transfer between flow and the acoustic field. The present D2Q9 LB model of the clarinet using a spatial resolution of $dx = 4.25 \times 10^{-5} m$ requires $\sim 4.25 \times 10^6$ cells. For a D3Q19 model using the same spatial resolution, the total number of cells would be $\sim 8.5 \times 10^9$, which is a big challenge for both computational power and memory capacity.

Appendix A

Benchmarks

Numerical Scheme

This section presents the benchmark results of a 2D Poiseuille flow problem solved by the GPU LBM model presented in Chpt. 3, which uses a single-precision presentation of floating-point numbers.

Figure A.1 depicts the numerical scheme of the benchmark simulation. The 2D flow evolves in a straight channel with a length of $L = 4a$. The lower and the upper wall are defined by $y = -a$ and $y = a$, respectively, upon which a no-slip condition for the velocity is enforced. The solid walls as well as all corner nodes are implemented in a generic way that works for all boundary conditions and for all types of flows. The flow is driven by a constant pressure drop along the channel produced by the SRC buffer at the inlet and the ABC buffer at the outlet of the channel. An extra ABC buffer adjacent to the left side of the SRC absorbs unwanted leakages. Both SRC and ABC are implemented by the same absorbing boundary condition proposed by Kam et al. (2006), where a SRC is distinguished from an ABC by a non-zero target velocity u_t . The width of the buffers of both SRC and ABC is set to 15 lattice cells.

The initial condition is the equilibrium distribution, using a constant density $\rho_0 = 1$ and a zero velocity. The steady-state at time step n is evaluated by

$$\text{Diff}(n) = \frac{\sum_i \sum_j |u_x(i, j, n) - u_x(i, j, n - 1)| + |u_y(i, j, n) - u_y(i, j, n - 1)|}{\sum_i \sum_j |u_x(i, j, n)| + |u_y(i, j, n)|}, \quad (\text{A.1})$$

where u_x and u_y are the velocity components on the x- and y-directions, i and j are the

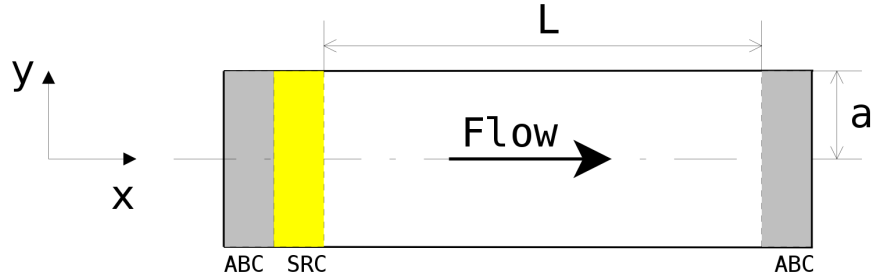


Figure A.1 2D Poiseuille flow channel.

space indices along the x - and y -directions.

The numerical error is evaluated by the l_2 -norm of the difference between the numerical velocities \mathbf{u} and the analytical velocities of the Poiseuille flow $\mathbf{u}^{(a)}$:

$$\text{Error}(n) = \sqrt{\sum_i \sum_j |\mathbf{u}(i, j) - \mathbf{u}^{(a)}(i, j)|^2 / P}, \quad (\text{A.2})$$

where the sum runs over all P nodes in the fluid domain.

The analytical velocity profile of 2D Poiseuille flow in a channel of width $2a$ is independent of location on the x -direction and is given by:

$$\begin{cases} u_x^{(a)} = u_0 \left(1 - \frac{y^2}{a^2}\right) \\ u_y^{(a)} = 0 \end{cases}, \quad (\text{A.3})$$

where u_0 is the peak velocity at the centerline. The Reynolds number is defined as

$$\text{Re} = \frac{u_0 N}{\nu}, \quad (\text{A.4})$$

where $N = 2a$ is the grid resolution, $\nu = (\frac{1}{\Omega} - 0.5) / 3$ is the kinematic viscosity and Ω is the relaxation parameter.

Results

The first set of simulations are designed for quickly comparing the numerical accuracy of the LBM SRT model to that of the LBM MRT model. The half width of the channel is set to $a = 5.5$ in lattice units, corresponding to a grid resolution of $N = 11$. The centreline

of the channel ($y = 0$) is on-grid and the upper / lower walls ($y = \pm 5.5$) are off-grid. The dimensionless target velocity of the SRC is set to a constant value ($M = 0.1$) for all simulations. Two different relaxation parameters ($\Omega = 1.6, 1.9$) have been used. The total number of numerical steps is $N_{sim} = 2000$.

Figures A.2, A.3 and A.4 present the time history of the Reynolds numbers, Diff and Error calculated from the numerical flow, respectively. The measured Reynolds numbers (Fig. A.2) indicate that the flow is in the laminar regime throughout all simulations. After about 1000 numerical steps, all simulations converge to a steady-state defined by $\text{Diff} \leq 10^{-5}$, as depicted in Fig. A.3. Figure A.4 shows that the accuracy of the LBM SRT model and the LBM MRT model is almost in the same level and the expected second-order accuracy is found for all cases. Also, the condition of a lower Reynolds number / higher viscosity results in a lower value of Error.

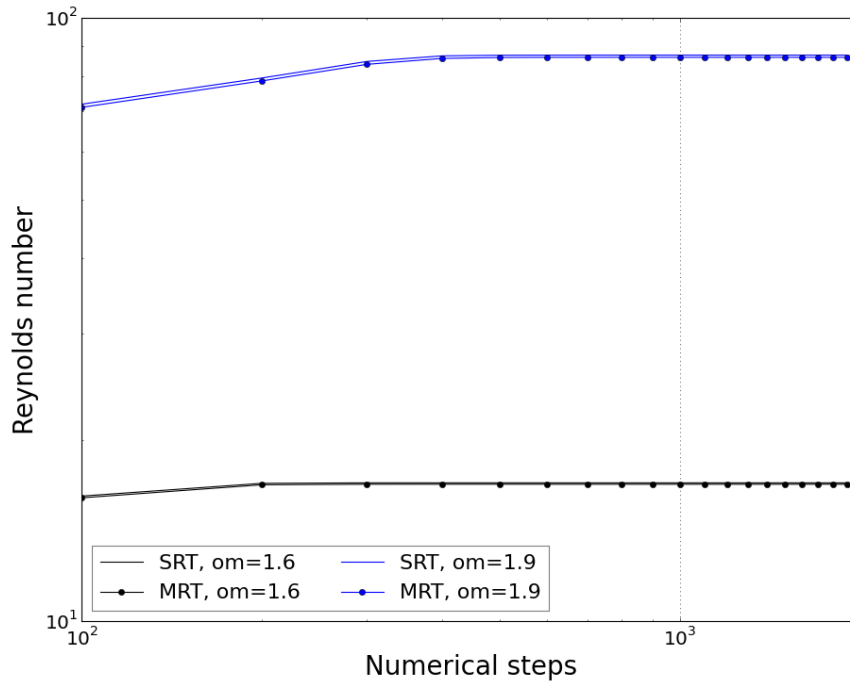


Figure A.2 Time history of *Reynolds number* for different collision modes (SRT vs. MRT) and relaxation parameters (Ω). Simulation parameters: $a = 5.5$, $M = 0.1$.

The second set of simulations are performed to investigate the accuracy of the LBM MRT model at different Reynolds numbers. The grid resolution is kept to a constant value of $N = 11$ or $a = 5.5$. The numerical viscosity is kept constant using $\Omega = 1.99$. The

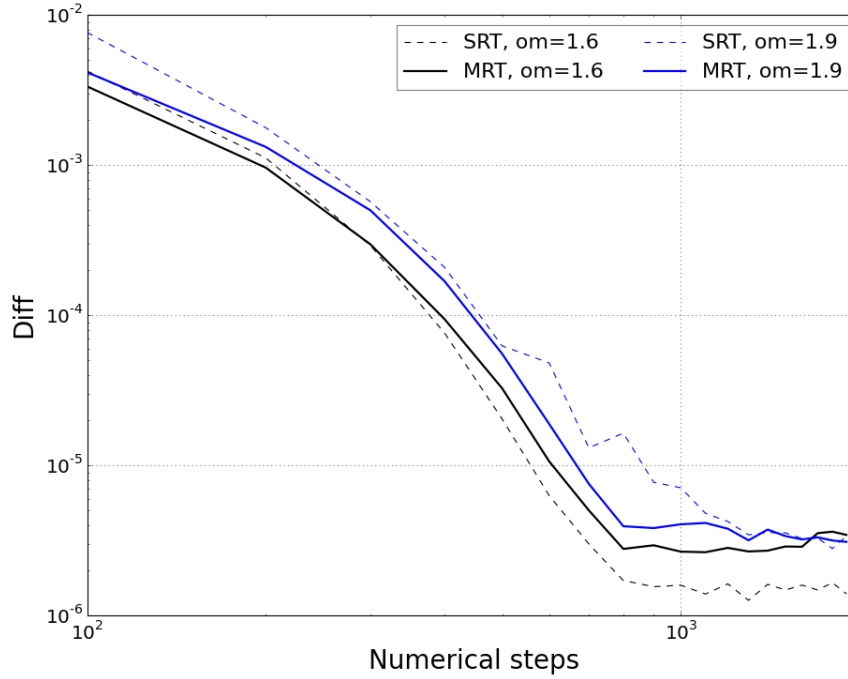


Figure A.3 Time history of $Diff$ for different collision modes (SRT vs. MRT) and relaxation parameters (Ω). Simulation parameters: $a = 5.5$, $M = 0.1$.

total number of simulation steps is $N_{sim} = 120,000$, which is big enough to ensure that the steady-state is reached for all simulations. To achieve a target Reynolds number in the steady state, the dimensionless velocity prescribed in the SRC is computed by

$$M_{target} = \frac{\sqrt{3}(2/\Omega - 1) Re_{target}}{6N}. \quad (\text{A.5})$$

In order to compensate the offset between the velocity u_m measured in the flow and the target velocity u_t prescribed in the SRC, a negative feedback loop described by Fig. A.5 is used.

The mean value of Error obtained in steady-state associated with different Reynolds number are depicted in Fig. A.6, which shows that the LBM MRT model is generally more accurate at lower Reynolds numbers. The numerical results are in second-order accuracy for $Re = 0.1, 1, 10, 100$. For the case of $Re = 1000$, Error is slightly higher than 1%.

The third set of simulations are performed to investigate how the accuracy of the LBM MRT model is influenced by grid resolution. The numerical viscosity is kept con-

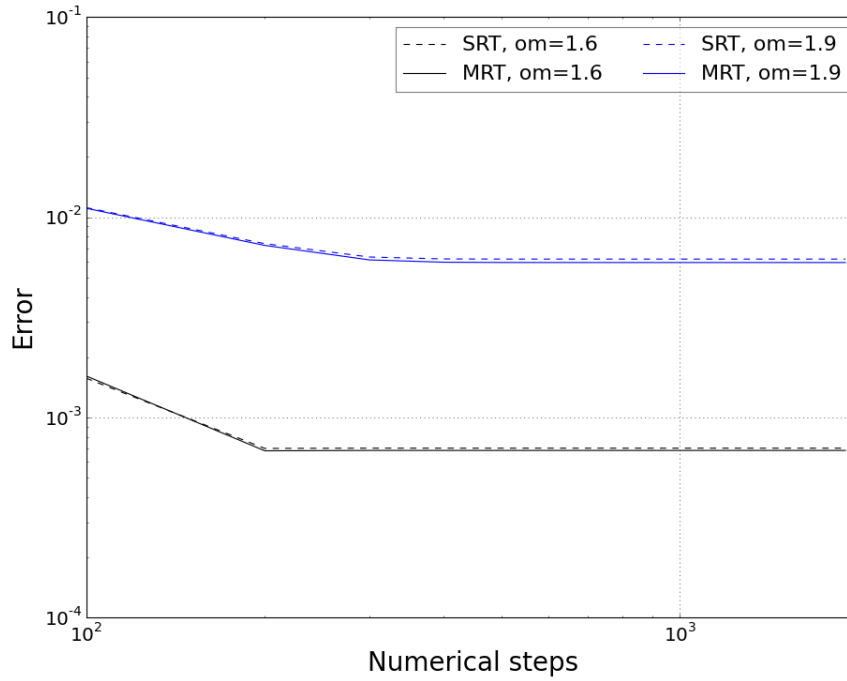


Figure A.4 Time history of *Error* for different collision modes (SRT vs. MRT) and relaxation parameters (Ω). Simulation parameters: $a = 5.5$, $M = 0.1$.

```

1  $u_m = u_t, u_t^{old} = u_t, u_t^{new} = u_t;$ 
2  $n = 0;$ 
3 while  $n \leq N_{sim}$  do
4   LBM iteration;
5   Measuring  $u_m$  from the flow;
6   if  $u_m < u_t \times 0.99$  then
7      $u_t^{new} = u_t^{old} * 1.01;$ 
8   end
9   if  $u_t > u_t \times 1.01$  then
10     $u_t^{new} = u_t^{old} * 0.99;$ 
11  end
12   $u_t^{old} = u_t^{new};$ 
13  Updating SRC by  $u_t^{new};$ 
14   $n = n + 1$ 
15 end

```

Figure A.5 Negative feedback loop for velocity correction.

stant using $\Omega = 1.6$. The total number of simulation steps is $N_{sim} = 120,000$. Seven different grid resolutions, $N = 5, 11, 21, 41, 81, 161$ and 321 , have been tested. To obtain

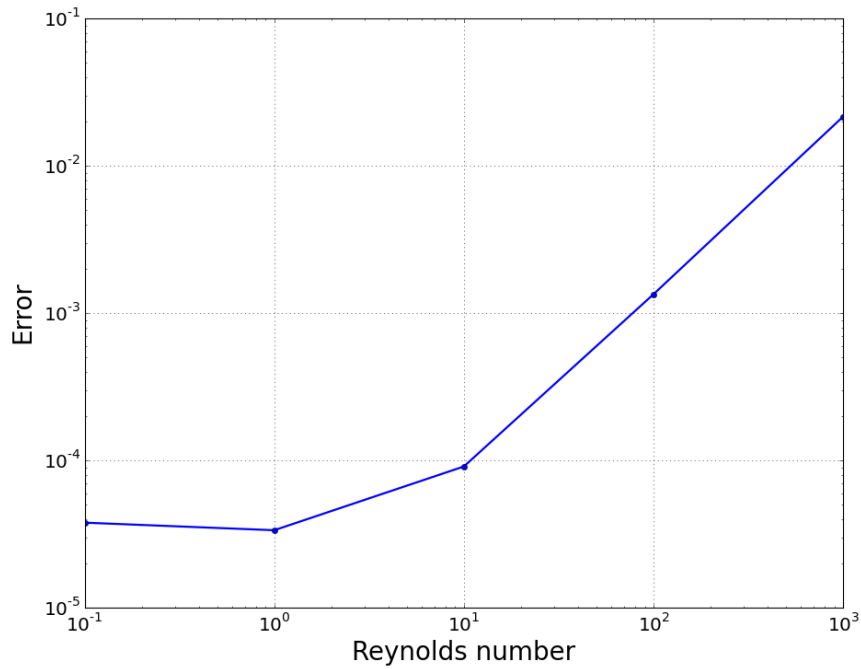


Figure A.6 The mean value of Error as a function of Reynolds number. Simulation parameters: $a = 5.5$, $\Omega = 1.99$.

a constant Reynolds number ($Re_{target} = 10$) for all simulations, the target dimensionless velocity in the SRC is computed by Eq. A.5 and the negative feedback loop described by Fig. A.5 is used. Figure A.7 shows that the LBM MRT model has a third-order accuracy for $N < 50$ and a fourth-order accuracy for $N > 50$. The model is generally more accurate using a larger grid resolution.

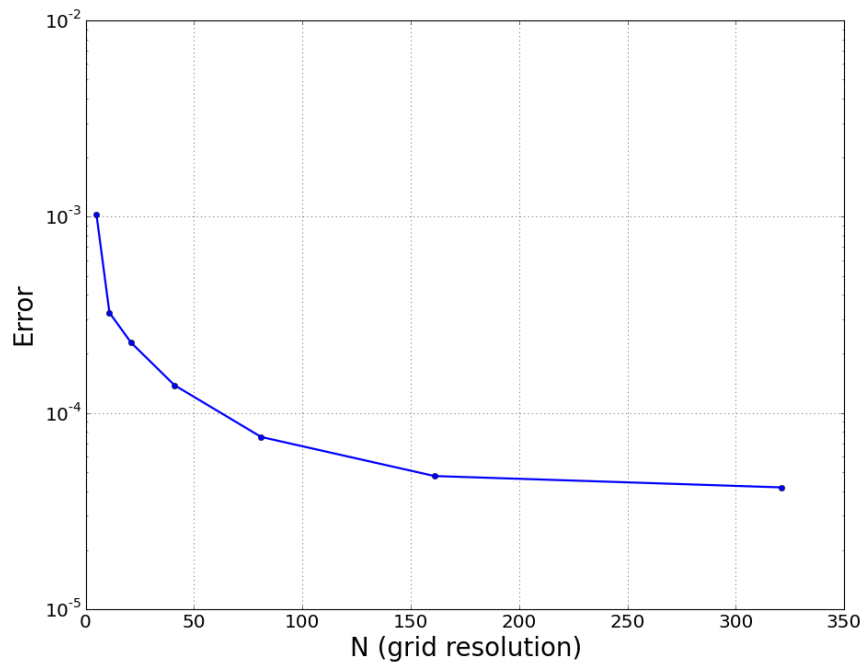


Figure A.7 The mean value of Error as a function of grid resolution. Simulation parameters: $\Omega = 1.6$, $\text{Re} = 10$.

References

- M. Åbom and H. Bodén. Error analysis of two-microphone measurements in ducts with flow. *Journal of the Acoustical Society of America*, 83(6):2429–2438, 1988.
- C. K. Aidun and J. R. Clausen. Lattice Boltzmann method for complex flows. *Annual Review of Fluid Mechanics*, 42:439–472, 2010.
- R. J. Alfredson and P. Davies. The radiation of sound from an engine exhaust. *Journal of Sound and Vibration*, 13(4):389–408, 1970.
- S. Allam and M. Åbom. Investigation of damping and radiation using full plane wave decomposition in ducts. *Journal of Sound and Vibration*, 292:519–534, 2006.
- A. Almeida, C. Vergez, and R. Caussé. Quasistatic nonlinear characteristics of double-reed instruments. *Journal of the Acoustical Society of America*, 121(1):536–546, 2007.
- Y. Ando. Experimental study of the pressure directivity and the acoustic centre of the circular pipe horn loud speaker. *Acoustica*, 20, 1968.
- Y. Ando. On the sound radiation from semi-infinite circular pipe of certain wall thickness. *Acoustica*, 22, 1969.
- M. Atig, J. P. Dalmont, and J. Gilbert. Termination impedance of open-ended cylindrical tubes at high sound pressure level. *Comptes Rendus Mécanique*, 332(4):299–304, 2004.
- F. Avanzini and M. van Walstijn. Modelling the mechanical response of the reed-mouthpiece-lip system of a clarinet. part 1. a one-dimensional distributed model. *Acta Acustica*, 90(3):537–547, 2004.
- J. Backus. Small-vibration theory of the clarinet. *Journal of the Acoustical Society of America*, 35(3):305–313, 1963.

- G. K. Batchelor. *An introduction to fluid dynamics*. Cambridge University Press., Cambridge, UK., 1967.
- J. P. Berenger. A perfectly matched layer for the absorption of electromagnetic waves. *Journal of Computational Physics*, 114(2):185–200, 1994.
- B. Bergeot, A. Almeida, B. Gazengel, C. Vergez, and D. Ferrand. Response of an artificially blown clarinet to different blowing pressure profiles. *Journal of the Acoustical Society of America*, 135(1):479–490, 2014.
- P. L. Bhatnagar, E. P. Gross, and M. Krook. A model for collision processes in gases. I. Small amplitude processes in charged and neutral one-component systems. *Physical Review*, 94(3):511, 1954.
- J. Bierkens. Calculations of the reflection coefficient of a jet pipe with subsonic jet flow. Technical report, Marcus Wallenberg Laboratory for Sound and Vibration Research of the Royal Institute of Technology, Sweden, 2002.
- H. Blasius. *Grenzschichten in Flüssigkeiten mit kleiner Reibung*. Druck von BG Teubner, 1907.
- N. N. Bogoliubov et al. Studies in statistical mechanics. *Studies in Statistical Mechanics I*, 1962.
- M. Bouzidi, M. Firdaouss, and P. Lallemand. Momentum transfer of a Boltzmann-lattice fluid with boundaries. *Physics of Fluids*, 13(11):3452–3459, 2001.
- G. B. Brown. The vortex motion causing edge tones. *Proceedings of the Physical Society*, 49(5):493, 1937a.
- G. B. Brown. The mechanism of edge-tone production. *Proceedings of the Physical Society*, 49(5):508, 1937b.
- G. B. Brown. Organ pipes and edge tones. *Nature*, 141:11–13, 1938.
- J. M. Buick, C. A. Greated, and D. M. Campbell. Lattice BGK simulation of sound waves. *EPL (Europhysics Letters)*, 43(3):235, 1998.

- J. M. Buick, C. L. Buckley, C. A. Greated, and J. Gilbert. Lattice Boltzmann BGK simulation of nonlinear sound waves: the development of a shock front. *Journal of Physics A: Mathematical and General*, 33:3917–3928, 2000.
- J. M. Buick, M. Atig, D. J. Skulina, D. M. Campbell, J. P. Dalmont, and J. Gilbert. Investigation of non-linear acoustic losses at the open end of a tube. *Journal of the Acoustical Society of America*, 129:1261, 2011.
- A. M. Cargill. Low-frequency sound radiation and generation due to the interaction of unsteady flow with a jet pipe. *Journal of Fluid Mechanics*, 121:59–105, 1982a.
- A. M. Cargill. Low frequency acoustic radiation from a jet pipe – a second order theory. *Journal of Sound and Vibration*, 83(3):339–354, 1982b.
- G. F. Carrier. Sound transmission from a tube with flow. *Quarterly of Applied Mathematics*, 13:457–461, 1956.
- A. Chaigne and V. Doutaut. Numerical simulations of xylophones. I. time-domain modeling of the vibrating bars. *Journal of the Acoustical Society of America*, 101(1):539–557, 1997.
- R. C. Chanaud. Aerodynamic whistles. *Scientific American*, 222:40–47, 1970.
- S. Chapman and T. G. Cowling. *The mathematical theory of non-uniform gases*. Cambridge University Press, 1960.
- S. Y. Chen and G. D. Doolen. Lattice Boltzmann method for fluid flows. *Annual Review of Fluid Mechanics*, 30:329–64, 1998.
- S. Y. Chen, D. Martinez, and R. W. Mei. On boundary conditions in lattice Boltzmann methods. *Physics of Fluids*, 8(9):2527–2536, 1996.
- X. X. Chen, X. Zhang, C. L. Morfey, and P. A. Nelson. A numerical method for computation of sound radiation from an unflanged duct. *Journal of Sound and Vibration*, 270: 573–586, 2004.
- J. B. Coelho. Study of the characteristics of acoustic elements in flow ducts, 1980.

- J. W. Coltman. Sounding mechanism of the flute and organ pipe. *Journal of the Acoustical Society of America*, 44(4):983–992, 1968.
- J. W. Coltman. Jet drive mechanisms in edge tones and organ pipes. *Journal of the Acoustical Society of America*, 60(3):725–733, 1976.
- E. Craig. *Perfectly Matched Layer Absorbing Boundary Conditions for the Discrete Velocity Boltzmann-BGK Equation*. PhD thesis, Old Dominion University, 2011.
- N. Curle. The mechanics of edge-tones. *Proceedings of the Royal Society of London. Series A. Mathematical and Physical Sciences*, 216(1126):412–424, 1953.
- A. R. da Silva. *Numerical Studies of Aeroacoustic Aspects of Wind Instruments*. PhD thesis, McGill University, Montreal, Canada, 2008.
- A. R. da Silva and G. P. Scavone. Lattice Boltzmann simulations of the acoustic radiation from waveguides. *Journal of Physics A: Mathematical and Theoretical*, 40:397–408, 2007.
- A. R. da Silva, G. P. Scavone, and M. van Walstijn. Numerical simulations of fluid structure-interactions in single-reed mouthpieces. *Journal of the Acoustical Society of America*, 122(3):1798–1810, 2007.
- A. R. da Silva, G. P. Scavone, and A. Lefebvre. Sound reflection at the open end of axisymmetric ducts issuing a subsonic mean flow: A numerical study. *Journal of Sound and Vibration*, 327:507–528, 2009.
- A. R. da Silva, G. P. Scavone, and A. Lenzi. Numerical investigation of the mean flow effect on the acoustic reflection at the open end of clarinet-like instruments. *Acta Acustica*, 96:959–966, 2010.
- A. R. da Silva, Y. Shi, and G. P. Scavone. Computational analysis of the dynamic flow in single-reed woodwind instruments. In *Proceedings of Meetings on Acoustics*, volume 19, page 035043. Acoustical Society of America, 2013.
- J. P. Dalmont and C. Frappe. Oscillation and extinction thresholds of the clarinet: Comparison of analytical results and experiments. *Journal of the Acoustical Society of America*, 122(2):1173–1179, 2007.

- J. P. Dalmont, C. J. Nederveen, and N. Joly. Radiation impedance of tubes with different flanges: numerical and experimental investigations. *Journal of Sound and Vibration*, 244(3):505–534, 2001.
- J. P. Dalmont, J. Gilbert, and S. Ollivier. Nonlinear characteristics of single-reed instruments: Quasistatic volume flow and reed opening measurements. *Journal of the Acoustical Society of America*, 114(4):2253–2262, 2003.
- P. O. A. L. Davies, J. B. Coelho, and M. Bhattacharya. Reflection coefficients for an unflanged pipe with flow. *Journal of Sound and Vibration*, 72(4):543–546, 1980.
- D. d’Humières. Generalized lattice Boltzmann equations. *Rarefied gas dynamics - Theory and simulations*, pages 450–458, 1994.
- J. H. M. Disselhorst and L. van Wijngaarden. Flow in the exit of open pipes during acoustic resonance. *Journal of Fluid Mechanics*, 99(02):293–319, 1980.
- E. Dokumaci. A note on transmission of sound in a wide pipe with mean flow and viscothermal attenuation. *Journal of Sound and Vibration*, 208(4):653–655, 1997.
- N. S. Dougherty, B. L. Liu, and J. M. O’Farrell. Numerical simulation of the edge tone phenomenon. Technical report, National Aeronautics and Space Administration, Office of Management, Scientific and Technical Information Program, 1994.
- Z. Fan, F. Qiu, A. Kaufman, and S. Yoakum-Stover. GPU cluster for high performance computing. In *Proceedings of the 2004 ACM/IEEE conference on Supercomputing*, page 47. IEEE Computer Society, 2004.
- N. H. Fletcher. Autonomous vibration of simple pressure-controlled valves in gas flows. *Journal of the Acoustical Society of America*, 93(4):2172–2180, 1993.
- N. H. Fletcher and T. D. Rossing. *The Physics of Musical Instruments*. Springer-Verlag, 1991.
- R. W. Fox, A. T. McDonald, and P. J. Pritchard. *Introduction to Fluid Mechanics*. John Wiley & Sons, Inc., 2004.
- U. Frisch, B. Hasslacher, and Y. Pomeau. Lattice-gas automata for the Navier-Stokes equation. *Phys. Rev. Lett.*, 56(14):1505–1508, 1986.

- U. Frisch, D. d'Humieres, B. Hasslacher, P. Lallemand, Y. Pomeau, and J.P. Rivet. Lattice gas hydrodynamics in two and three dimensions. *Complex Systems*, 1(4):649–707, 1987.
- G. Gabard and R. J. Astley. Theoretical model for sound radiation from annular jet pipes: Far- and near-field solutions. *Journal of Fluid Mechanics*, 549:315–341, 2006.
- J. Gilbert. *Étude des instruments de musique à anche simple (A Study of Single-reed Musical Instruments)*. PhD thesis, University of Maine, Maine, 1991.
- M. B. Giles. Nonreflecting boundary conditions for euler equations calculations. *AIAA Journal*, 28:2050–2058, 1990.
- N. Giordano. Direct numerical simulation of a recorder. *Journal of the Acoustical Society of America*, 133(2):1111–1118, 2013.
- N. Giordano. Simulation studies of a recorder in three dimensions. *Journal of the Acoustical Society of America*, 135(2):906–916, 2014.
- L. Gorazd, J. Jurkiewicz, and A. Snakowska. Experimental verification of the theoretical model of sound radiation from an unflanged duct with low mean flow. *Archives of Acoustics*, 37(2):227–236, 2012.
- Z. L. Guo and C. Shu. *Lattice Boltzmann Method and Its Applications in Engineering*. World Scientific Publishing, 2013. ISBN 978-9814508292.
- Z. L. Guo, C. G. Zheng, and B. C. Shi. An extrapolation method for boundary conditions in lattice Boltzmann method. *Physics of Fluids*, 14(6):2007–2010, 2002.
- K. Habibi, A. Najafi-Yazdi, P.T. Lew, and L. Mongeau. Simulation of sound radiated from turbulent heated jets using the lattice-Boltzmann method. In *17th AIAA/CEAS Aeroacoustics Conference (32nd AIAA Aeroacoustics Conference) AIAA 2011-2844 5-8 June 2011, Portland, Oregon, 2011*.
- J. Habich, C. Feichtinger, H. Köstler, G. Hager, and G. Wellein. Performance engineering for the lattice Boltzmann method on GPGPUs: Architectural requirements and performance results. *Computers & Fluids*, 80:276–282, 2013.
- I. Halliday, L. A. Hammond, C. M. Care, K. Good, and A. Stevens. Lattice Boltzmann equation hydrodynamics. *Phys. Rev. E.*, 64(011208):1–8, 2001.

- X. Y. He and L. S. Luo. Lattice Boltzmann model for the incompressible Navier–Stokes equation. *Journal of Statistical Physics*, 88(3-4):927–944, 1997.
- A. Hirschberg. *Aero-acoustics of wind instruments*. Springer Verlag, 1995.
- A. Hirschberg, J. C. Bruggeman, A. P. J. Wijnands, and N. Smits. The whistler nozzle and horn as aero-acoustic sound sources in pipe systems. *Acta Acustica*, 68(2):157–160, 1989.
- A. Hirschberg, R. W. A. van de Laar, J. P. Marrou-Mauriere, A. P. J. Wijnands, H. J. Dane, S. G. Kruijswijk, and A. J. M. Houtsma. A quasi-stationary model of air flow in the reed channel of single-reed wind instruments. *Acustica*, 70, 1990.
- A. Hirschberg, J. Gilbert, A. P. J. Wijnands, and A. M. C. Valkering. Musical aero-acoustics of the clarinet. *Le Journal de Physique IV*, 4(C5):C5–559, 1994.
- M. Hornikx, W. De Roeck, and W. Desmet. Simplified exhaust pipe noise radiation modelling using the Fourier PSTD method. In *International Conference on Noise and Vibration Engineering*. Leuven, Belgium, pages 20–22, 2010.
- M. S. Howe. Attenuation of sound in a low mach number nozzle flow. *Journal of Fluid Mechanics*, 91(02):209–229, 1979.
- M. S. Howe. The damping of sound by wall turbulent shear layers. *Journal of the Acoustical Society of America*, 98(3):1723–1730, 1995.
- F. Q. Hu. On absorbing boundary conditions for linearized Euler equations by a perfectly matched layer. *Journal of Computational Physics*, 129:201–219, 1996.
- F. Q. Hu. A stable, perfectly matched layer for linearized Euler equations in unsplit physical variables. *Journal of Computational Physics*, 173(2):455–480, 2001.
- F. Q. Hu. A perfectly matched layer absorbing boundary condition for linearized Euler equation with a non-uniform mean flow. *Journal of Computational Physics*, 208:469–492, 2005.
- F. Q. Hu. On the construction of PML absorbing boundary condition for the non-linear Euler equations. *AIAA paper 2006-0798*, 2006.

- F. Q. Hu, X. D. Li, and D. K. Lin. PML absorbing boundary conditions for non-linear aeroacoustics problems. *AIAA paper 2006-2521*, 2006.
- F. Q. Hu, X. D. Li, and D. K. Lin. Absorbing boundary conditions for nonlinear Euler and Navier-Stokes equations based on the perfectly matched layer technique. *Journal of Computational Physics*, 227(9):4398–4424, 2008.
- E. W. S. Kam, R. M. C. So, and R. C. K. Leung. Non-reflecting boundary conditions for one-step LBM simulation of aeroacoustics. In *27th AIAA Aeroacoustics Conference, 8-10 May 2006, Cambridge, Massachusetts*, 2006.
- E. W. S. Kam, R. M. C. So, S. C. Fu, and R. C. K. Leung. Finite difference lattice Boltzmann method applied to acoustic-scattering problems. *AIAA journal*, 48(2):354–371, 2010.
- J. Kergomard. Elementary considerations on reed-instrument oscillations. *Courses and Lectures-International Centre for Mechanical Sciences*, pages 229–290, 1995.
- J. Kergomard, S. Ollivier, and J. Gilbert. Calculation of the spectrum of self-sustained oscillators using a variable truncation method: Application to cylindrical reed instruments. *Acta Acustica*, 86(4):685–703, 2000.
- L. E. Kinsler, A. R. Frey, A. B. Coppens, and J. V. Sanders. *Fundamentals of Acoustics*. John Wiley & Sons, Inc., 2000.
- G. Kirchhoff. Ueber den einfluss der wärmeleitung in einem gase auf die schallbewegung. *Annalen der Physik*, 210(6):177–193, 1868.
- A. Klöckner, N. Pinto, Y. Lee, B. Catanzaro, P. Ivanov, and A. Fasih. PyCUDA and PyOpenCL: A scripting-based approach to GPU run-time code generation. *Parallel Computing*, 38(3):157–174, 2012.
- T. Kobayashi, T. Takami, M. Miyamoto, K. Takahashi, A. Nishida, and M. Aoyagi. 3D calculation with compressible LES for sound vibration of ocarina. *arXiv preprint arXiv:0911.3567*, 2009.
- H. Kühnelt. Simulating the mechanism of sound generation in flutes using the lattice Boltzmann method. In *Proceedings of the Stockholm Music Acoustics Conference*, 2003.

- H. Kühnelt. Simulating the sound generation in flutes and flue pipes with the lattice Boltzmann method. In *Proc. Int. Symp. Musical Acoustics, Nara, Japan, 2004*.
- H. Kühnelt. Simulation and analysis of the flow-acoustic interactions in the mouth of flute-like instruments. In *Forum Acusticum (European Conference on Acoustics), Budapest, pages 1–6, 2005*.
- H. Kühnelt. Vortex sound in recorder- and flute-like instruments: Numerical simulation and analysis. In *Proc. Int. Symp. Music. Acoust, 2007*.
- P. K. Kundu, I. M. Cohen, and D. R. Dowling. *Fluid Mechanics, Fifth Edition*. Elsevier Academic Press, Amsterdam, 2012.
- F. Kuznik, C. Obrecht, G. Rusaouen, and J.-J. Roux. LBM based flow simulation using GPU computing processor. *Computers & Mathematics with Applications*, 59(7):2380–2392, 2010.
- P. Lallemand and L. S. Luo. Theory of the lattice Boltzmann method: Dispersion, dissipation, isotropy, galilean invariance, and stability. *Physical Review E*, 61:6546–6562, 2000.
- P. Lallemand and L. S. Luo. Lattice Boltzmann method for moving boundaries. *Journal of Computational Physics*, 184:406–421, 2003.
- D. L. Lansing, J. A. Drischler, and C. G. Pusey. Radiation of sound from an unflanged circular duct with flow. *Journal of the Acoustical Society of America*, 48(1A):75–75, 1970.
- T. S. Lee, H. B. Huang, and C. Shu. An axisymmetric incompressible lattice BGK model for simulation of the pulsatile flow in a circular pipe. *International Journal for Numerical Methods in Fluids*, 49(1):99–116, 2005.
- A. Lefebvre and G. P. Scavone. Finite element modeling of woodwind instruments. In *20th International Symposium on Music Acoustics, Sydney and Katoomba, Australia, August 2010*. Associated Meeting of the International Congress on Acoustics.
- A. Lefebvre and G. P. Scavone. Characterization of woodwind instrument toneholes with the finite element method. *Journal of the Acoustical Society of America*, 131(4):3153–3163, 2012.

- H. Levine and J. Schwinger. On the radiation of sound from an unflanged circular pipe. *Physical Review*, 73(4):383–406, 1948.
- P. T. Lew, L. Mongeau, and A. Lyrintzis. Noise prediction of a subsonic turbulent round jet using the lattice Boltzmann method. *Journal of the Acoustical Society of America*, 128: 1118, 2010.
- W. Li, X. M. Wei, and A. Kaufman. Implementing lattice Boltzmann computation on graphics hardware. *The Visual Computer*, 19(7-8):444–456, 2003.
- X. M. Li, R. C. K. Leung, and R. M. C. So. One-step aeroacoustics simulation using lattice Boltzmann method. *AIAA journal*, 44(1):78–89, 2006.
- Y. B. Li and X. W. Shan. Lattice Boltzmann method for adiabatic acoustics. *Philosophical Transactions of the Royal Society A: Mathematical, Physical and Engineering Sciences*, 369 (1944):2371–2380, 2011.
- J. Liu. Simulation of whistle noise using computational fluid dynamics and acoustic finite element simulation. Masters thesis, University of Kentucky, Lexington, Kentucky, 2012.
- C. Y. Loh. On a non-reflecting boundary condition for hyperbolic conservation laws. *AIAA paper*, 3975:2003, 2003.
- V. Lorenzoni and D. Ragni. Experimental investigation of the flow inside a saxophone mouthpiece by particle image velocimetry. *Journal of the Acoustical Society of America*, 131(1):715–721, 2012.
- R. Maier, R. S. Bernard, and D. W. Grunau. Boundary conditions for the lattice Boltzmann method. *Physics of Fluids*, 8:1788–1801, 1996.
- R. Mani. Refraction of acoustic duct waveguide modes by exhaust jets. *Quarterly of Applied Mathematics*, 30:501–520, 1973.
- G. R. McNamara and G. Zanetti. Use of the Boltzmann equation to simulate lattice-gas automata. *Phys. Rev. Lett.*, 61(20):2332–2335, 1988.
- F. Mechel, W. Schlitz, and J. Dietz. Impedanuz einer luftdurchströmtem offnung. *Akustische*, 15:199–206, 1965.

- M. Miyamoto, Y. Ito, K. Takahashi, T. Takami, T. Kobayashi, A. Nishida, and M. Aoyagi. Applicability of compressible LES to reproduction of sound vibration of an air-reed instrument. In *Proceedings of the International Symposium on Musical Acoustics, Sydney and Katoomba, Australia*, 2010.
- M. Miyamoto, Y. Ito, T. Iwasaki, T. Akamura, K. Takahashi, T. Takami, T. Kobayashi, A. Nishida, and M. Aoyagi. Numerical study on acoustic oscillations of 2D and 3D flue organ pipe like instruments with compressible LES. *Acta Acustica*, 99(1):154–171, 2013.
- C. J. Moore. The role of shear-layer instability waves in jet exhaust noise. *Journal of Fluid Mechanics*, 80(02):321–367, 1977.
- R. M. Munt. The interaction of sound with a subsonic jet issuing from a semi-infinite cylindrical pipe. *Journal of Fluid Mechanics*, 83(4):609–640, 1977.
- R. M. Munt. Acoustic transmission properties of a jet pipe with subsonic jet flow: I. the cold jet reflection coefficient. *Journal of Sound and Vibration*, 142(3):413–436, 1990.
- A. Najafi-Yazdi and L. Mongeau. An absorbing boundary condition for the lattice Boltzmann method based on the perfectly matched layer. *Computers & fluids*, 68:203–218, 2012.
- C. J. Nederveen. *Acoustical Aspects of Woodwind Instruments*. PhD thesis, Technische Universiteit Te Delft (The Netherlands), 1969.
- C. J. Nederveen. *Acoustical aspects of woodwind instruments*. Northern Illinois University Press, 1998.
- X. D. Niu, C. Shu, and Y. T. Chew. An axisymmetric lattice Boltzmann model for simulation of Taylor–Couette flows between two concentric cylinders. *International Journal of Modern Physics C*, 14(06):785–796, 2003.
- A. N. Norris and I. C. Sheng. Acoustic radiation from a circular pipe with an infinite flange. *Journal of Sound and Vibration*, 135(1):85–93, 1989.
- Y. Obikane. Direct simulation on a fipple flute using the compressible Navier-Stokes equation. *World Acad. Sci., Eng. Technol*, 4:794–798, 2009.

- Y. Obikane. Computational aeroacoustics on a small flute using a direct simulation. In *Computational Fluid Dynamics 2010*, pages 435–441. Springer, 2011.
- Y. Obikane and K. Kuwahara. Direct simulation for acoustic near fields using the compressible Navier-Stokes equation. In *Computational Fluid Dynamics 2008*, pages 85–91. Springer, 2009.
- C. Obrecht, F. Kuznik, B. Tourancheau, and J.-J. Roux. A new approach to the lattice Boltzmann method for graphics processing units. *Computers & Mathematics with Applications*, 61(12):3628–3638, 2011.
- S. Ollivier, J.-P. Dalmont, and J. Kergomard. Idealized models of reed woodwinds. part I: Analogy with the bowed string. *Acta Acustica*, 90(6):1192–1203, 2004.
- S. Ollivier, J. Kergomard, and J.-P. Dalmont. Idealized models of reed woodwinds. part II: On the stability of. *Acta Acustica*, 91(1):166–179, 2005.
- H. F. Olson. *Acoustical Engineering*. Princeton, New Jersey: D. Van Nostrand Company, Inc., 1957.
- Y. Özyörük, E. Alpman, V. Ahuja, and L. N. Long. Frequency-domain prediction of turbofan noise radiation. *Journal of Sound and Vibration*, 270(4):933–950, 2004.
- P. Panhuis. Calculations of the acoustic end correction of a semi-infinite circular pipe issuing a subsonic cold or hot jet with co-flow. Technical report, Marcus Wallenberg Laboratory for Sound and Vibration Research of the Royal Institute of Technology, Sweden, 2003.
- M. C. A. M. Peters, A. Hirschberg, A. J. Reijnen, and A. P. J. Wijnands. Damping and reflection coefficient measurements for an open pipe at low Mach and low Helmholtz numbers. *Journal of Fluid Mechanics*, 256:499–534, 1993.
- A. D. Pierce. *Acoustics: An Introduction to its Physical Principles and Applications*. Acoustical Society of America, New York, 1989.
- R. A. Pinker and W. D. Bryce. The radiation of plane-wave duct noise from a jet exhaust, statically and in flight. In *American Institute of Aeronautics and Astronautics Conference*, volume 1, 1976.

- A. Powell. On the edgetone. *Journal of the Acoustical Society of America*, 33(4):395–409, 1961.
- Y. H. Qian, D. d’Humières, and P. Lallemand. Lattice BGK models for Navier-Stokes equation. *Europhysics Letters*, 17(6):479–484, 1992.
- L. Rayleigh and J. W. Strutt. *The Theory of Sound*. London: The Macmillan Company, 2nd edn. Reprinted 1945, New York: Dover Publications, 1896.
- S. W. Rienstra. A small Strouhal number analysis for acoustic wave-jet flow-pipe interaction. *Journal of Sound and Vibration*, 86(4):539–556, 1983.
- S. W. Rienstra. Acoustic radiation from a semi-infinite annular duct in a uniform subsonic mean flow. *Journal of Sound and Vibration*, 94:267–288, 1984.
- P. R. Rinaldi, E. A. Dari, M. J. Vénere, and A. Clausse. A lattice-Boltzmann solver for 3D fluid simulation on GPU. *Simulation Modelling Practice and Theory*, 25:163–171, 2012.
- M. Rohde, D. Kandhai, J. J. Derksen, and H. E. A. van den Akker. A generic, mass conservative local grid refinement technique for lattice-Boltzmann schemes. *International Journal for Numerical Methods in Fluids*, 51(4):439–468, 2006.
- D. Ronneberger. Experimentelle untersuchungen zum akustischen reflexionsfaktor von un stetigen querschnittsänderungen in einem luftdurchströmten rohr. *Acustica*, 19 (222-235):68, 1967.
- C. L. Rumsey, R. T. Biedron, and F. Farassat. Ducted-fan engine acoustic predictions using a Navier-Stokes code. *Journal of Sound and Vibration*, 213(4):643–664, 1998.
- S. Ryoo, C. I. Rodrigues, S. S. Baghsorkhi, S. S. Stone, D. B. Kirk, and W. M. W. Hwu. Optimization principles and application performance evaluation of a multithreaded GPU using CUDA. In *Proceedings of the 13th ACM SIGPLAN Symposium on Principles and practice of parallel programming*, pages 73–82. ACM, 2008.
- J. Saneyoshi, H. Teramura, and S. Yoshikawa. Feedback oscillations in reed woodwind and brasswind instruments. *Acta Acustica*, 62(3):194–210, 1987.
- S. D. Savkar. Radiation of cylindrical duct acoustic modes with flow mismatch. *Journal of Sound and Vibration*, 42(3):363–386, 1975.

- G. P. Scavone. *An Acoustic Analysis of Single-Reed Woodwind Instruments with an Emphasis on Design and Performance Issues and Digital Waveguide Modeling Technologies*. PhD thesis, Stanford University, 1997.
- R. H. Schlinker. The transmission of acoustic plane-waves at a jet exhaust. In *American Institute of Aeronautics and Astronautics, Aerospace Sciences Meeting, 15 th, Los Angeles, Calif, 1977*.
- A. Selamet, Z. L. Ji, and R. A. Kach. Wave reflections from duct terminations. *Journal of the Acoustical Society of America*, 109(4):1304–1311, 2001.
- Y. Shi, A. R. da Silva, and G. P. Scavone. Lattice Boltzmann simulations of sound directivity of a cylindrical pipe with mean flow. *Journal of Physics A: Mathematical and Theoretical*, 46(31):315501, 2013.
- F. Silva, J. Kergomard, C. Vergez, and J. Gilbert. Interaction of reed and acoustic resonator in clarinetlike systems. *Journal of the Acoustical Society of America*, 124(5):3284–3295, 2008.
- P. A. Skordos. Initial and boundary conditions for the lattice Boltzmann method. *Physical Review E*, 48:4823–4842, 1993.
- P. A. Skordos. *Modeling Flue Pipes: Subsonic Flow, Lattice Boltzmann, and Parallel Distributed Computers*. PhD thesis, Massachusetts Institute of Technology, 1995.
- J. O. Smith. Physical modeling using digital waveguides. *Computer Music Journal*, 16(4): 74–91, 1992.
- J. D. Sterling and S. Chen. Stability analysis of lattice Boltzmann methods. *Journal of Computational Physics*, 123(0016):196–206, 1996.
- S. Succi. *The lattice Boltzmann equation for fluid dynamics and beyond*. Oxford University Press, 2001.
- M. C. Sukop and D. T. Thorne. *Lattice Boltzmann modeling: An introduction for geoscientists and engineers*. Springer, 2006.
- C. K. W. Tam. Computational aeroacoustics - issues and methods. *AIAA Journal*, 33(10): 1788–1796, 1995.

- I. Tani. History of boundary layer theory. *Annual Review of Fluid Mechanics*, 9(1):87–111, 1977.
- K. W. Thompson. Time dependent boundary conditions for hyperbolic systems. *Journal of Computational Physics*, 68:1–24, 1987.
- K. W. Thompson. Time dependent boundary concepts for hyperbolic systems, II. *Journal of Computational Physics*, 89:439–461, 1990.
- J. Tölke. Implementation of a lattice Boltzmann kernel using the compute unified device architecture developed by nVIDIA. *Computing and Visualization in Science*, 13(1):29–39, 2010.
- V. Välimäki. *Discrete-time Modeling of Acoustic Tubes Using Fractional Delay Filters*. PhD thesis, Helsinki University of Technology, 1995.
- J. van Zon, A. Hirschberg, J. Gilbert, and A. P. J. Wijnands. Flow through the reed channel of a single reed music instrument. *Le Journal de Physique Colloques*, 51(C2): 821–824, 1990.
- E. M. Viggén. Viscously damped acoustic waves with the lattice Boltzmann method. *Philosophical Transactions of the Royal Society A: Mathematical, Physical and Engineering Sciences*, 369(1944):2246–2254, 2011.
- E. M. Viggén. Acoustic multipole sources for the lattice Boltzmann method. *Physical Review E*, 87(2):023306, 2013.
- V. L. Wells and R. A. Renaut. Computing Aerodynamically Generated Noise. *Annual Review of Fluid Mechanics*, 29(1):161–199, 1997.
- F. M. White. *Fluid Mechanics, Seventh Edition*. Mcgraw-Hill series in Mechanical Engineering, 2011.
- A. Wilde. Calculation of sound generation and radiation from instationary flows. *Computers & fluids*, 35(8):986–993, 2006.
- T. A. Wilson and G. S. Beavers. Operating modes of the clarinet. *Journal of the Acoustical Society of America*, 56(2):653–658, 1974.

-
- D. A. Wolf-Gladrow. *Lattice Gas Cellular Automata and Lattice Boltzmann Models: An Introduction. Lecture Notes in Mathematics*. Springer, Berlin / Heidelberg, 2004.
- W. E. Worman. *Self Sustained Oscillations in Clarinet Like Systems*. PhD thesis, Case Western University, 1971.
- X. Zhang, X. Chen, C. L. Morfey, and P. A. Nelson. Computation of spinning modal radiation from an unflanged duct. *AIAA Journal*, 42(9):1795–1801, 2004.